Molecular Simulations on the Colloidal Behaviors of Model Asphaltenes

by

Xiaoyu Sun

A thesis submitted in partial fulfillment of the requirements for the degree of

Doctor of Philosophy

in

Materials Engineering

Department of Chemical and Materials Engineering
University of Alberta

Abstract

Asphaltenes are the heaviest and most polar group of molecules in crude oil. Colloidal behaviors of asphaltenes, including the aggregation and interfacial behaviors, have impacts on many petroleum production processes. For example, the aggregation of asphaltenes can lead to problems such as clogging the pipelines and changing the wettability of oil reservoirs. Also, the interfacially adsorbed asphaltenes contributed to the stabilization of crude oil emulsions, which can cause severe corrosion problems. The colloidal behaviors of asphaltenes were under influence of the molecular structure of asphaltenes, the salinity in the aqueous phase, the solvent type, and the addition of demulsifiers.

In this dissertation, molecular dynamics (MD) simulations were performed to provide mechanistic understandings of the colloidal behaviors of asphaltenes at atomic level, where the first two topics were on the aggregation behaviors and the last two topics were on the interfacial properties. Firstly, the relations between aggregation and intramolecular deformation of archipelago type molecules were studied. A single archipelago asphaltene molecule favored unfolded state in water, while folded state was preferred in molecules in aggregates. In heptane and toluene, a single archipelago asphaltene or multiple asphaltenes in aggregates were flexible and could easily change between folded and unfolded states. In the co-aggregates of continental and archipelago asphaltenes, the archipelago molecules became less flexible in heptane, where the change was insignificant in toluene. Secondly, the effect of salinity (NaCl concentration) on the aggregation of continental asphaltenes with different side chain length was elucidated. With long side chains, the model asphaltenes molecules formed aggregate mainly through the hydrophobic interactions at the side chains. Due to the effect of salt on the hydrophobic interaction, the

aggregation of these model asphaltenes was enhanced at low salt concentration and then hindered at high salt concentration. For model asphaltenes with moderate side chain length, the interactions between core-core, core-chain, and chain-chain were under mutual influence of the salt concentration. The aggregation of model asphaltenes with the shortest side chain length was mainly driven by the core-core interactions, which were significantly affected by the salt concentration.

Thirdly, the interfacial adsorption of asphaltenes at the water/oil interface with the presence of model demulsifiers (PEO-PPO-PEO copolymer and Brij-93) was studied. A fraction of archipelago model asphaltenes were adsorbed and formed loosely structured aggregates at the water/oil interface. The addition of Brij-93 resulted in the desorption of archipelago model asphaltenes at water/toluene or heptane interface, while adding PEO-PPO-PEO copolymer led to desorption of archipelago model asphaltenes at the water/toluene interface but not at the water/heptane interface. The continental model asphaltenes had more adsorption and formed more compact aggregates at the water/oil interface than archipelago model asphaltenes. Thus, co-aggregation between continental asphaltenes and model demulsifiers, instead of desorption of asphaltenes, was observed at both water/toluene and water/heptane interface. Lastly, with model asphaltenes or model demulsifiers adsorbed at the water/toluene interface, the free energy of interaction between water droplets was calculated. When water droplets were far apart (over twice the droplet diameter), the dispersed asphaltenes contributed to the stability of water droplets that their coalescence was energetically unfavorable. At close proximity and before the merging of water droplets, the steric repulsion between the adsorbate films induced a large repulsive force between water droplets, which prevented the coalescence. The steric repulsion also contributed to the redistribution of adsorbate molecules at the surface of water droplets, and the water droplets in

the head-on direction were left with uncovered water molecules. Hydrogen bonds were formed between the uncovered water molecules, which gradually overcame the repulsive force and assisted the merging of water droplets. The copolymer had longer hydrophobic chains than Brij-93 and was more easily redistributed on the surface of water droplets, when the surface coverage on water droplets was high. Thus, the maximum repulsive force for water droplets coalescence was lower when copolymer was the adsorbate compared with Brij-93. Overall, the work in this dissertation provided fundamental understandings of the colloidal properties of asphaltenes, which can further help to solve the related problems in petroleum industries.

Preface

Chapter 3 of this thesis has been published as Sun, X., Zeng, H., & Tang, T. (2020). Molecular simulation of folding and aggregation of multi-core polycyclic aromatic compounds. *Journal of Molecular Liquids*, 113248. I was responsible for designing and conducting simulations, data collection and analysis as well as the manuscript drafting and revising. Dr. T. Tang and Dr. H. Zeng were the supervisory authors who contributed to concept formation, proofreading and revising the manuscript.

Chapter 4 of this thesis has been published as Sun, X., Jian, C., He, Y., Zeng, H., & Tang, T. (2018). Probing the effect of salt on asphaltene aggregation in aqueous solutions using molecular dynamics simulations. *Energy & Fuels*, *32*(8), 8090-8097. I was responsible for conducting simulations, data collection and analysis as well as the manuscript drafting and revising. Dr. C. Jian provided simulation models, assisted with simulation design and data analysis. K. He assisted with conducting the simulations. Dr. T. Tang and Dr. H. Zeng were the supervisory authors who contributed to concept formation, proofreading and revising the manuscript.

A version of Chapter 5 in this thesis has been published as Sun, X., Zeng, H., & Tang, T. (2021). Effect of non-ionic surfactants on the adsorption of polycyclic aromatic compounds at water/oil interface: A molecular simulation study. *Journal of Colloid and Interface Science*, *586*, 766–777. I was responsible for designing and conducting simulations, data collection and analysis as well as the manuscript drafting and revising. Dr. T. Tang and Dr. H. Zeng were the supervisory authors who contributed to concept formation, proofreading and revising the manuscript.

A version of Chapter 6 in this thesis is in preparation for publication as Sun, X., Zeng, H., & Tang, T. Free energy of interaction between adsorbate-stabilized water droplets. I was

responsible for designing and conducting simulations, data collection and analysis as well as the manuscript drafting and revising. Dr. T. Tang and Dr. H. Zeng were the supervisory authors who contributed to concept formation, proofreading and revising the manuscript.

Chapter 1, 2 and 7 are originally written by Xiaoyu Sun, and have never been previously published.

Acknowledgments

First and foremost, I would like to take this opportunity to express my sincere appreciation to my supervisors, Dr. Tian Tang and Dr. Hongbo Zeng for their insightful ideas and valuable guidance during my study and research. I also thank all the support from them, including the funding, time and encouragement. Their professional attitude in supervisory, education and research give good examples for my career and life.

I gratefully acknowledge the computing resources and technical support from the Western Canada Research Grid (WestGrid), and the financial support from the Natural Sciences and Engineering Research Council of Canada (NSERC) and the Future Energy Systems under the Canada First Research Excellence Fund.

I would also like to thank the University of Alberta for providing scholarships, including Doctoral Recruitment Scholarship and Graduate Research Assistantship Fellowship.

Special thanks to Dr. Cuiying Jian for sharing her knowledges and experience in research. Many thanks to my colleagues, Ms. Wenyuan Sun, Ms. Xiaohui Mao, Ms. Diling Yang, for their helpful discussions.

Finally, my deepest thanks go to my family for their love and support.

Table of Contents

List of Figures

List of Tables

Chapter 1. Introduction

Unconventional oil, such as heavy crude oil and bitumen, is becoming an important resource because of the increasing energy demand and the depletion of conventional oil. [1–3] Although abundant in nature, unconventional oil is difficult to extract from the oil sand, and a series of enhanced oil recovery techniques is required for the extraction. [1] The fraction of crude oil has been categorized as saturates, aromatics, resins and asphaltenes (SARA). Among them, asphaltenes are the heaviest and most aromatic components, which are soluble in aromatic solvents and insoluble in paraffinic solvents by definition. [4] Asphaltenes are complex mixtures of molecules with polycyclic aromatic hydrocarbons (PAH) and aliphatic chains, containing heteroatoms such as oxygen, sulfur and nitrogen. [5] It is important to investigate the aggregation and interfacial behavior of asphaltenes. Aggregation of asphaltene molecules were observed in various solvents, which may cause problems in petroleum production by precipitation and deposition. [6] With interfacially active features, asphaltenes tend to adsorb at the water-oil interface, which stabilizes the undesirable emulsions in petroleum industry. [7,8] Understanding the colloidal behaviors, including the aggregation and interfacial behaviors, of model asphaltenes is of great importance for solving the industrial problems.

1.1 Structure and Aggregation of Asphaltene

Several aspects of asphaltene molecules are under inconclusive debates, including the molecule weight, molecular architecture, etc. [9,10] In 1967, Dickie and Yen [11] studied the structure of asphaltene clusters based on various experimental methods, such as X-Ray diffraction and scattering, and mass spectroscopy. In the “Yen Model”, the asphaltene “molecules” consisted of individual sheets, associated into clusters and formed larger micelles. Molecular weights of

asphaltenes were said to vary from lower than 1000 to almost 10^9 Da. [11] Mullins et al. [9,10] then modified the Yen model, which showed the dominant molecule structure, nanoaggregation and clustering of asphaltene molecules. In the "Yen-Mullins Model", molecular weight of asphaltene molecules is on average around 750 Da and ranging between 500-1000 Da. [9,10] Typically, the architecture of asphaltene is categorized as continental type and archipelago type, as shown in Fig. 1.1. A continental (island) type asphaltene, as shown in Fig. 1.1a-c, has a single large PA core with peripheral side chains [12–14]. As proposed by the Yen-Mullins model [12], the continental type is the dominant structure of asphaltenes. An archipelago type asphaltene molecule consists of multiple PA cores with interconnecting alkane chains [15,16], as shown in Fig. 1.1d-e. Based on nuclear magnetic resonance (NMR) experiments, Durand et al. [17] and Chacón-Patiño et al. [18] suggested that asphaltenes contained both archipelago and continental types, while Athabasca asphaltenes might contain more archipelago type [17]. In more recent works, a new classification, "aryl-linked core", is defined by Schuler et al. [19,20] based on their observation from scanning tunneling microscope (STM) and atomic force microscopy (AFM) experiments. In this new classification, the PA cores are connected by one or more aryl linkages, which can be a secondary feature in continental and archipelago type molecules. [19]

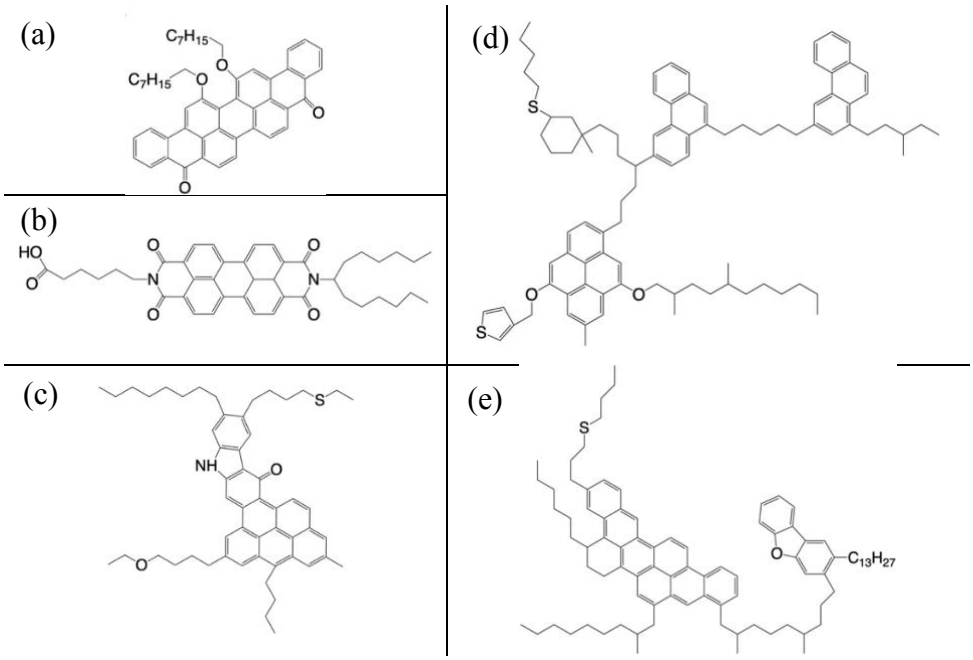

Figure 1.1 Molecular structures for (a-c) continental (island) type and (d-e) archipelago type model asphaltenes. (a: Violanthrane-79 (VO-79) [21]; b: C5Pe [22]; c [23], d [24] and e [25]: other model asphaltene molecules.)

Asphaltene aggregation and precipitation have attracted extensive interest due to their importance in the petroleum production processes. On one hand, the aggregation of asphaltene is highly undesirable because it causes severe problems, such as clogging pipelines, settling in transportation and storage tanks, and deactivating catalysts. [17] On the other hand, solvent-induced precipitation is an essential step in some heavy oil processes, including partial deasphalting and froth treatment. [26] Spontaneous aggregation of asphaltenes is mostly studied in toluene, in which the asphaltenes are by definition soluble. As shown in Fig. 1.2a-b, asphaltene molecules formed nanoaggregates when the concentration is above the critical nanoaggregate concentration (on the order of 100 mg/L). [12,13] Such nanoaggregates contain an average of six molecules, which formed stacking driven by the π–π interactions [27]. Heteroatoms, such as S, N, O, in the PA cores can change the strength of π-electron cloud, thus impacting the π–π interaction.

[28] Peripheral chains also play important roles in the aggregation of asphaltenes, which impose steric repulsion in toluene and hinder the association of PA cores. [29] Simulations have confirmed the π–π interaction as a driving force for asphaltene aggregation in toluene and steric repulsion as a negative contribution [30]. The hydrophobic interactions between side chains make additional contribution for asphaltene aggregation in aqueous solutions. [30,31] Side chains may also contain heteroatoms and the asphaltene molecules are mildly polar. Hydrogen bonding between the polar groups provides an alternative driving force for the association of asphaltene molecules. The mechanism of aggregation is therefore largely dependent on the structures of asphaltene molecules and the nature of the solvent. Compared with continental type molecules, archipelago type asphaltenes have internal rotational degree of freedom at the interconnecting chains, which makes the core-core interaction less favorable. [17]

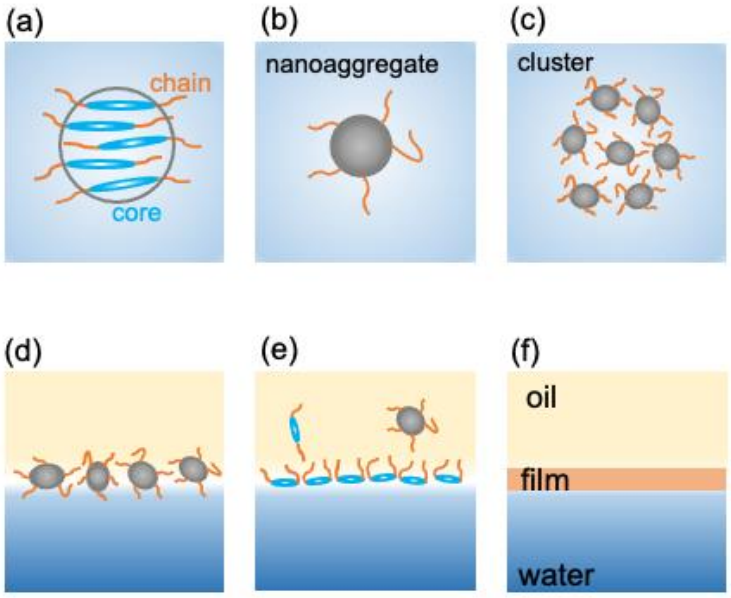

Figure 1.2 Schematics for (a) association between asphaltene molecules through π–π interaction; (b) nanoaggregate and (c) cluster of asphaltene; adsorption of (d) asphaltene nanoaggregates and

(e) monomers at water/oil interface; (f) formation of film at water/oil interface. (subfigure (a-c) are adapted from Mullins et al. [10].)

Asphaltene molecules associate into larger aggregates when their concentration reaches several g/L. In most cases, the larger aggregates or clusters are fractal gathering of the pre-formed nanoaggregates [13,32], as shown Fig. 1.2c. The clusters may exhibit other shapes, such as vesicles [33] and disks [34]. The binding energy between the clusters is smaller than that within the nanoaggregates. Clustering is sensitive to parameters such as temperature, asphaltene concentration, and solvent properties, which then affects the viscosity and rheological properties of asphaltene solutions. The clusters have various sizes, as small as 6 nm and up to tens of nanometers or more [12]. The smallest clusters are stably suspended in crude oil and toluene, while larger ones can become unstable and grow into flocs, which will then separate the asphaltene phase from the surrounding. From microscopic observations, the aggregate size of asphaltenes increases with the decrease of solvent aromaticity [35] and the increase of heptane content [36].

Using molecular dynamics (MD) simulations, Jian et al. [37] observed that Violanthrone-78 (VO-78), a model of continental type asphaltene, formed short cylinder-like aggregates in toluene and longer rod-like aggregates in n-heptane through π–π interactions. By simulating hypothetical model asphaltenes in MD, Headen et al. [38] investigated the nanoaggregation of continental and archipelago type model asphaltenes in toluene and heptane. For both types of asphaltenes, the aggregates were observed to be larger and more stable in heptane than in toluene. Unlike continental type asphaltenes, the archipelago type asphaltenes could form aggregates without the association of PA cores [38]. The authors then performed MD simulations on archipelago, continental and their mixtures in toluene and heptane [39]. For continental type

asphaltenes, a larger aggregate was formed in heptane than in toluene. [39] The difference was smaller for archipelago type. [39] The mixture of archipelago and continental types (50:50 weight ratio) had intermediate aggregate size compare to systems with a single type of molecules [39]. Kuznicki et al. [40] performed MD simulations on a mixture of 12 continental and 12 archipelago model asphaltenes, dispersed in water, toluene and heptane. Aggregation was found to be most significant in water, followed by heptane and then toluene. [40] The authors reported self-stacking of archipelago type asphaltenes in the aggregates, similar to folding proposed by Acevedo et al. [41].

1.2 Stabilization of W/O Emulsions by Asphaltenes

Crude oil emulsions are categorized into water-in-oil (W/O) emulsion, oil-in-water (O/W) emulsion and multiple emulsions. W/O emulsion corresponds to water droplets dispersed in the continuous phase of oil, while O/W emulsion contains oil droplets dispersed in the continuous phase of water. Multiple emulsions are complex water-in-oil-in-water and oil-in-water-in-oil emulsions where small droplets of phase A are suspended in a larger drop of phase B which in turn is suspended in the continuum form of phase A. Among the emulsions, W/O emulsions are most commonly encountered in the oil and gas industry. Based on their size, the water droplets during the crude oil production process were classified into three groups as: emulsified water with droplet diameter < 10 μm, dispersed water with droplet diameter 10 to 60 μm, and free water with droplet diameter greater than 60 μm. [42] The free water could settle instantly and the dispersed water could be removed by sedimentation or centrifugation, while the emulsified water was stable due to the presence of interfacial active components in crude oil, such as asphaltene, resin, wax and so on. [42] The adsorption of asphaltene is the main contributor to the formation a rigid protective film at the water/oil interface, which stabilizes the W/O emulsions. [43] These emulsions are

desirable in food processing, cosmetics industries, etc., but mostly undesirable in the petroleum industry. For example, W/O emulsion causes severe corrosion problem during the storage and transportation processes in petroleum production.

1.2.1 Adsorption of asphaltene and stabilization of W/O emulsions

Asphaltene shows surface-active features and tends to be adsorbed at the water/oil interface. Sjöblom et al. measured the interfacial tension (IFT) of water/decane interface with presence of asphaltenes and resins extracted from crude oil. [44] The IFT was reduced in presence of asphaltene, with linear correlation between IFT ($\gamma_{w/o}$) and ln C (C is the asphaltene concentration in crude oil). The adsorption of asphaltene followed the Gibbs adsorption equation for a single component as [45]:

$$\frac{d\gamma}{d(lnC)} = -\Gamma RT \tag{1.1}$$

where Γ is the surface excess (molecules per unit area), R is the gas constant, and T is the temperature. The stability of water/oil interface has been commonly attributed to the lowered IFT caused by the adsorption of asphaltenes. [44]

Several subfractions of asphaltene have been explored based on their adsorption on the water/oil interface. For example, Qiao et al. [46] categorized the subfractions of asphaltenes into two groups, the remaining asphaltenes (RA) in the oil supernatant and the interfacial-active asphaltenes (IAA) that were adsorbed on the water droplets after a procedure of treatment. The IAA was only a small fraction (2% wt.) in the whole asphaltene, while played a dominant role in the stabilization of W/O emulsion. [46] With the presence of sulfoxide groups, the IAA were highly interfacial active and tended to form rigid films that interacted strongly with water. [46] Liu et al. [47] identified asphaltenes by their polarities, which was higher if the proportion of aliphatic

chains was lower. The asphaltene with higher polarity was proposed to be adsorbed as nanoaggregates on the interface, [47] as shown in Fig. 1.2d. While the asphaltenes with lower polarity was adsorbed in a less aggregated form. [47] For the subfraction with lower polarities, the asphaltenes had higher tendency to be dispersed in oil phase. [47] The dispersed asphaltenes had higher adsorption rate onto the interface. [47] However, the low polarity in asphaltenes also enhanced the migration rate of asphaltenes at the interface so that the asphaltene films were more likely to be deformed, which was indicated by the low dilatational modulus at the interface. [47] The emulsion stability was higher if the adsorption rate of asphaltenes was higher and the migration rate of asphaltene on the interface was lower, which reached maximum with moderate polarities of asphaltene subfraction. [47]

Other adsorption mechanism of asphaltene at water/oil interface has been proposed by Rane et al. [48]. They measured the IFT of water/ Nexbase 2000 series oil and found it independent with the aging time and asphaltene concentration. [48] From Langmuir equation of state, the correlation between IFT and the surface coverage was fitted when the surface excess coverage was 3.2 molecules/nm^2. [48] It suggested that the asphaltene were adsorbed as monomers on the interface, as shown in Fig. 1.2e, instead of adsorbed as nanoaggregates. Overall, it is commonly accepted that the water/oil interface is stabilized by the formation of rigid solid film, as shown in Fig. 1.2f, which is under influence of various parameters, such as the solvent type, asphaltene structure, the composition of crude oil, and so on. [49]

Adsorption of asphaltene at the water/oil interface is affected by various factors including the solvent type, the composition of oil, and so on. Facilitated by the dynamic IFT measurement, Mohammadi et al. [50] studied the adsorption kinetics of asphaltene at the heptol/water interface with various heptane-toluene ratio and asphaltene concentration. At the heptol/water interface,

adding asphaltene resulted in the reduction of equilibrium IFT at the interface, where the reduction increased with the increase of asphaltene concentration. [50] At a given asphaltene concentration, the reduction of equilibrium IFT was more significant when heptol had higher heptane/toluene ratio. [50] The authors concluded that the initial stage of asphaltene adsorption was controlled by the diffusion of asphaltene from bulk heptol phase to the interface, in a form of monomers instead of nanoaggregates. [50] Their results also indicated that the higher ratio of heptane in heptol contributed to a faster and more adsorption of asphaltene on the interface. [50] Interaction force between water droplets was studied by Shi et al. [51] using drop probe AFM, where the micrometer-sized water droplets were aged in asphaltene solutions and then immersed in organic solvents. The solvent types were varied between toluene, heptane and heptol with different ratio of heptane and toluene, and the asphaltene solution had different concentrations ranging up to 500 mg/L. [51] In pure toluene, the water droplets had a steric repulsion due to the hydrodynamic force during the coalescence when there was no asphaltene. [51] With asphaltene adsorbed, the coalescence was not initiated with the maximum force of 2 nN. [51] When water droplets contacted and then separated by the probe, there was adhesion between asphaltene film on the two different water droplets, which was attributed to the aggregation of interfacial asphaltenes. [51] With the increase of heptane in the solvent, the aggregation of interfacially adsorbed asphaltene was enhanced, [51] which ultimately contributed to the coalescence of water droplets in pure heptane. Mouraille and Sjöblom et al. studied the stability of water in crude oil emulsion by using separation/sedimentation tests and high voltage destabilization test. [52] Different solutions were used to represent the oil phase, such as toluene, heptane, and heptol (mixture of toluene and heptane). [52] The solvation state of asphaltene played important roles in the stability of water in crude oil emulsion. [52] For example, asphaltene was dispersed in toluene instead of being

adsorbed on water/toluene interface. [52] For heptane as solvent, the asphaltene had low solubility and tended to form aggregated structure, which made it difficult to cover the entire water/heptane interface. [52] Thus, water/oil interface was less stable when pure toluene or heptane was used as solvent than the case with heptol as solvent. [52] While the above studies have focused on the toluene, heptane and their mixtures as organic solvents, researchers also investigated the adsorption of asphaltenes at pentol (mixture of pentane and toluene)/water interface [53], xylene/water interface [54], and so on.

Compositions of crude oil also affect the adsorption of asphaltene and the stability of emulsion. For example, Liu et al. [55] investigated the properties of water/oil interface and the W/O emulsion stability in the binary system with both asphaltenes and resin and the single systems with asphaltenes or resin, respectively. It was concluded that asphaltene played important role in the stabilization of W/O emulsion, while adding resin (in binary system) enhanced the migration of asphaltenes and further improved the emulsion stability. [55] Wen et al. [56] estimated the correlation between emulsion stability and four parameters of the oil compositions, including c_{a+r} (content of asphaltene and resin), c_{w+m} (content of wax and mechanical impurities), AV (acid value), and CN (average carbon number in crude oil). Emulsification experiments were performed on eight crude oils with various parameters, and the correlation between emulsification and parameters were obtained by data regression. [56] The stability of water-in-paraffin based crude oil emulsion was enhanced by higher values of the four parameters. [56] The influence of the parameters from the highest to lowest was $CN > c_{a+r} > AV > c_{w+m}$, which again emphasized the importance of solvent environment and the content of asphaltene and resin on the stability of emulsions. [56] Zhang et al. studied the water droplets coalescence by using microfluidic flow-focusing geometry [57]. Water droplets were introduced into the collision chamber filled with

model oil solution, which contained asphaltene from crude oil or asphaltene-like molecules, VO-79 or coronene. [57] The coalescence rate was calculated based on the number of coalescence events monitored and recorded by camera. [57] At certain concentration of asphaltenes, water droplets in solution containing real asphaltene had lowest coalescence rate compared to the case with VO-79 or coronene. [57] The coalescence rate tended to decrease with the increase of the concentration for asphaltene or asphaltene-like molecules. [57] It indicated that the model asphaltene molecules could not fully mimic the real asphaltene when the stabilization of water droplets was considered. [57]

1.2.2 Simulation studies

Simulation studies have provided atomic or molecular level insights into the adsorption and interfacial properties of asphaltene at water/oil interface [58]. Nanoaggregation of model asphaltene molecules at the water/oil (represented by toluene and heptane) interface was investigated by Mikami et al. [59] The asphaltene molecules adsorbed more on the water/heptane interface than on the water/toluene interface, because asphaltenes had high solubility in toluene and tended to be dispersed in bulk toluene. [59] With only small amount of asphaltene adsorbed, the reduction of IFT at water/oil interface was insignificant. [59] While the IFT was reduced by 12 mN/m at water/heptane interface when asphaltene molecules were abundant and formed a complete film. [59] Jian et al. used [60] MD simulation to study the reduction of IFT at water/toluene (or heptane) interface with presence of asphaltene and compared the results with experimental measurements. It suggested that the reduction of IFT at water/oil interface was dependent on the surface concentration instead of the bulk concentration of asphaltene. [60] Using MD simulation Gao et al. [61] investigated the adsorption of model asphaltenes, N-(1-hexylheptyl)-N'-(5-carbonylicpentyl) perylene-3,4,9,10-tetracarboxylic bisimide (C5Pe) and

anionic C5Pe, at the water/model crude oil interface. The anionic C5Pe molecules had high affinity to the water/oil interface due to the formation of H-bond between their oxygen functionality and water phase. [61] While the majority of the electroneutral C5Pe molecules were in bulk oil phase with only a small proportion adsorbed on the interface. [61]

In another simulation work of Jian et al. [62], two identical water droplets surrounded by model asphaltene, Violanthrone-79 (VO-79), were placed in toluene or heptane. At equilibrium state, protective films of asphaltenes were formed at the surface of water droplet, which was stabilized in the organic solvent without spontaneous coalescence. [62] In toluene, the adsorption of asphaltene was less pronounced than in heptane. [62] The dispersed asphaltene in toluene phase could also contribute the stabilization of water droplets. [62] Duan et al. [63] investigated water droplet in toluene with the adsorption of asphaltenes/polyacrylamide (PAM) by using dissipative particle dynamics (DPD). They identified the layer-by-layer assembly of asphaltene and PAM where PAM was adsorbed as the inner layer and asphaltene as the outer layer. [63] The simulation studies provided fundamental understanding on the stabilization mechanism of W/O emulsion.

1.3 Destabilization of W/O Emulsions

W/O emulsion is highly undesirable in petroleum industry because they increase the corrosion of equipment and pipelines, reduce the transportation efficiency, and pose environmental concerns. [64,65] It is necessary to separate water from the stable emulsions before further transportation and processing of crude oil. Various demulsification techniques are employed to destabilize the W/O emulsion, including chemical, physical and biological methods. Frequently, combinations of these techniques are applied in order to achieve the best demulsification outcome. Typical physical methods include sedimentation, centrifugation, application of electrical field or magnetic field, thermal treatment [66,67], freeze/thaw method [68], membrane separation [69–71], etc. Biological

methods apply biosurfactants produced from bacteria and microbial cell surface to destabilize the emulsion. [72–74] Chemical demulsifier has been extensively used because of their advantages such as adaptability, rapid demulsification and cost efficiency. [75]

1.3.1 Chemical demulsifiers

Chemical demulsifiers are categorized into three groups: polymeric surfactants, ionic liquid and nanoparticles. [76] Effective chemical demulsifiers are more interfacially active than the components in the rigid film which stabilize the emulsion. [64,76] As mentioned in section 1.2, W/O emulsions are stabilized by the formation of rigid, solid film by interfacial active components in crude oil, as shown in Fig. 1.3a. In contrary, demulsifiers break the stable emulsion and promote the flocculation or coalescence of water droplets. The typical mechanism of chemical demulsification is proposed to have the following steps: (1) the chemical demulsifiers have higher interfacial affinity and adsorb readily on the surface of water droplets, as shown in Fig. 1.3b [77,78]; (2) the adsorbed layers of demulsifiers are commonly loosely packed and less ordered than the rigid film formed by the surface active components in crude oil; (3) the demulsifier films are adsorbed as the inner layer and protective films are replaced and become thinner; (4) the water droplets are less stable and started to flocculate as shown Fig. 1.3c or coalesce as shown in Fig. 1.3d.

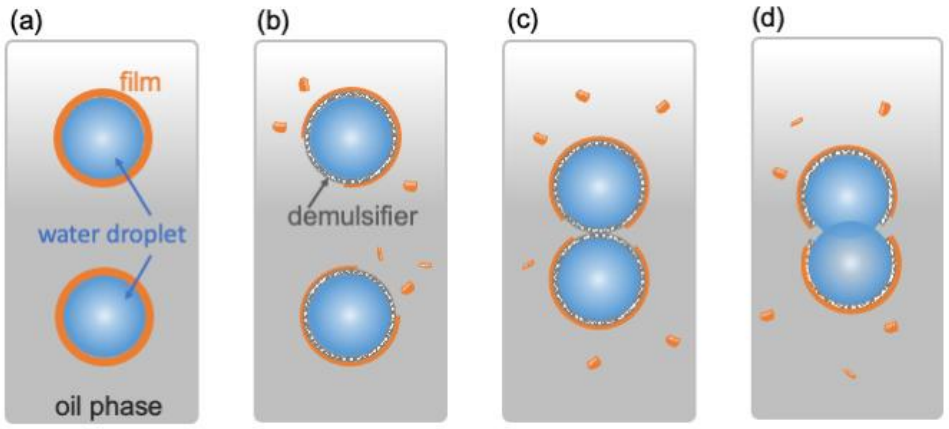

Figure 1.3 Schematics of demulsification mechanism: (a) water droplets stabilized by interfacial films; (b) demulsifiers penetrate into the films and become adsorbed at the surface of water droplets; (c) flocculation and (d) coalescence of water droplets.

Among chemical demulsifiers, polypropylene oxide (PPO)-polyethylene oxide (PEO) block copolymers are commercially available and have been extensively studied. [79–81] These copolymers show amphiphilic features with PEO as the hydrophilic group and PPO as the hydrophobic group. [49] Triblock polymers $[PEO]_m$-$[PPO]_n$-$[PEO]_m$ is commercially available as Poloxamer with the brand name of Pluronic. The amphiphilic character of the triblock copolymers is described by the hydrophilic-lipophilic balance (HLB), which can be calculated from *m* and *n* as [82]:

$$HLB = -\frac{36n}{2m+n} + 33 \tag{1.2}$$

Zhang et al. [83] synthesized and characterized triblock copolymers with different molecular weight and HLB. From demulsification tests where water separated from emulsion was recorded with time, triblock copolymers with higher HLB resulted in lower dehydration speed than

those with lower HLB, but similar ultimate dehydration. [83] Researchers have also synthesized and investigated the copolymers with other structural isomers, including multibranch isomer, star isomer, and linear isomer. [49] Hernandez et al. [84] applied PPO-PEO copolymers with different number (1-5) of branches to destabilize water-in-crude oil emulsion. The traditional triblock copolymers had linear structure with two PEO branches, which represented the case of two-branch copolymers in their work. [84] At low dosage of demulsifiers (500 ppm), the two-branch copolymer reached better water removal than the other copolymers. [84] Likewise, Pacheco et al. [85] compared linear PPO-PEO copolymers (one branch) and three-branch copolymers and concluded that the three-branch copolymer resulted in better demulsification performance. Kailey et al. [86] proposed that five-branch PPO-PEO copolymers contributed to higher dehydration efficiency than three-branch copolymers. Cendejas et al. [87] investigated water removal from super-heavy crude oil by PEO-PPO-PEO triblock copolymers and their functionalized forms with amine groups attached to PEO groups. The functionalized copolymers had higher demulsification performance than the non-functionalized copolymers, due to the higher affinity of the functionalized groups to the water phase. [87]

Beside structural properties, the concentration of demulsifiers has also been frequently studied as an important parameter for demulsification performance. Hernandez et al. [84] found that the water removal by using two-branch copolymer was suppressed when the demulsifier concentration increased from 500 ppm to 1000 ppm. [84] The performance at optimal concentration (500 ppm) was attributed to the complete coverage of the interface by demulsifiers. [84] Similarly, in Cendejas et al.'s study [87], the demulsification performance increased with the increase of concentration for the functionalized copolymers until the optimal dose, at which the saturation of polymeric chains at the water/oil interface was reached. [87] The demulsification

performance was dependent on the demulsifier concentration. Pensini et al. [88] used bottle tests and micropipette experiments to investigate the destabilization of water droplets in toluene with the presence of C5 asphaltenes, where the optimal concertation for star-like PEO-PPO copolymer was determined to be 2.3 ppm. [88]

Many polymeric demulsifiers share similarity with the PPO-PEO copolymers, such as PEO-PDMS-PEO with two terminal PEO groups and poly(dimethyl)siloxane (PDMS) as central group. [77,89] From the microscopic image in Lobato et al. [89], the asphaltene films were disrupted by the PEO-PDMS-PEO copolymer at low dosage of 100 ppm. Le Follotec et al. [77] studied the demulsification efficiency of PEO-PDMS-PEO copolymer by using measurement of light backscattering and transmission. With higher PEO/PDMS ratio, the demulsifiers were more hydrophilic and more efficient for destabilizing water-in-crude oil emulsion. [77] Thus, the authors proposed the demulsification mechanism as that a hole nucleated in the oil films and the water droplets could contact and merge. [77] The curvature of the hole was opposite to the spontaneous curvature of the copolymer monolayer at the water/oil interface if the copolymer had long hydrophobic chain. [77] Thus, the copolymer with long hydrophobic chain was ineffective in destabilizing the water droplets. [77] Beside PPO-PEO and similar copolymers, other demulsification agents have been identified and widely studied, including non-ionic surfactants [90], ethyl cellulose (EC) [91,92], dendritic molecules [93], etc. Efforts have been made on developing novel demulsifiers, such as multibranch tannic acid phenol-amine polyether [94] and Fe_3O_4 based micro-spheres [95]. Along with the development of demulsifiers, mechanistic investigations on the destabilization of water/oil interface and W/O emulsion are in demand in order to improve the demulsification efficiency. [49]

1.3.2 Simulation studies

In the aforementioned section 1.2.2, the interfacial behavior of asphaltene have been extensively investigated through simulations, while interfaces with co-existence of asphaltene and demulsifiers are less discussed. Without asphaltenes, the interfacial behavior of PEO-PPO-PEO triblock copolymer was studied by Ballal et al. [96] using modified interfacial statistical associating fluid theory. PEO-PPO-PEO copolymers with different molecular weight and EO/PO ratio was applied at water/toluene interface. [96] By adding copolymers, the IFT of water/toluene interface was reduced, and reached minimum if copolymer had a 1:1 EO/PO ratio. [96] The architecture of PEO-PPO-PEO was more effective in reducing IFT than the reverse structure of PPO-PEO-PPO. [96] This work suggested higher affinity of PPO-PEO copolymer to the interface was obtained if it had the PEO-PPO-PEO architecture and EO/PO at 1:1. [96] The co-existence of model asphaltene and demulsifier was studied by Niu et al. [97] using MD simulation. Three-branch PEO-PPO copolymers were placed near water-xylene interface with C5Pe. [97] When the C5Pe layer was closer to the water phase and the copolymers layer was farther, the copolymer molecules penetrated into the C5Pe layer and adsorbed on the water surface. On the contrary, when the copolymer layer was initially closer to water phase than C5Pe, the C5Pe molecules were not able to replace the copolymers. It indicated a higher affinity of the copolymer than C5Pe. [97]

The destabilization of water droplets with presence of asphaltene and demulsifiers were investigated at atomic level. For example, using MD simulations, Liu et al. [98] studied the adsorption of model asphaltenes at the surface of water droplets in toluene, and subsequent addition of EC molecules. A protective film of asphaltene was formed on the water droplet. [98] By adding EC, the adsorbed asphaltenes were attracted by the dispersed EC in toluene, forming interaction between EC and asphaltenes in toluene phase. [98] The observation was different from

the mechanism proposed earlier where the demulsifiers would penetrate into the film of asphaltenes. Using DPD, Song et al. [99] studied multiple water droplets in model crude oil (SARA) with polyether demulsifiers. The asphaltene and demulsifiers were both adsorbed on the surface of water droplet by forming patched films with mixing components. [99] The coalescence of water droplets was initiated by the bridging of the interfacial films. [99]

1.4 Effect of Salinity

Brine water always co-exists with crude oil during petroleum production. [100-101] Brine water with various salinity was injected into oil reservoir, where low salinity water could result in higher oil recovery than high salinity water (seawater and formation water). [102–104] Salinity of the aqueous phase is an important parameter throughout the investigations on the aggregation, adsorption, and interfacial properties of asphaltenes. The stability of W/O emulsion is highly dependent on the salinity, which ultimately affects the demulsification efficiency.

The precipitation of asphaltenes from crude oil was measured by Ameri et al. [105], where water with different salinity was added into the crude oil. Adding water at all salinity resulted in precipitation, while the amount of precipitation first decreased with the increase of salinity and then increased. [105] The interfacial adsorption of asphaltene is commonly studied by analyzing the IFT, as introduced in section 1.2.1. At water/pentol interface stabilized by asphaltene, increasing the concentration of NaCl in water from 0 to 3 M contributed to the increase of IFT. [53] At the interface of water and crude oil, the IFT had a non-monotonic trend, first decreasing and then increasing, as the salinity increased from low (10 and 2 times diluted seawater) to high (seawater and formation water). [103] Compared with pure water, the reduction of IFT was observed for all salinity level. [103] The authors attributed the IFT reduction to the adsorption of asphaltene at the interface, which reached maximum when the minimum IFT was observed (with

2 times diluted seawater). [103] With further increase of salinity, the cations accumulated at the interface and decreased the interaction between water and polar asphaltene molecules. [103] Thus, the adsorption of asphaltene was suppressed and IFT was increased when the salinity increased from 2 times diluted seawater to seawater and then formation water. [103] Similar observation was obtained in the work of Moeini et al. [106], where the IFT at brine/ heavy oil (from Iranian oil reservoirs) interface was correlated to the NaCl concentration (up to 200,000 ppm) in brine. IFT was reduced by the addition of low concentration of salt and reached a minimum at NaCl concentration of ~ 40,000 ppm and then increased with further increase of NaCl concentration. [106]

The emulsion prepared with heavy oil and different seawater samples was observed by Maaref et al. [107] using microscopic imaging. The water droplets had larger size when the salinity of water phase was higher, which indicated a higher coalescence rate of water droplets and lower stability of emulsion. [107] However, Ling et al. [108] studied their sample of brine in crude oil emulsion and found out that the long-term stability of emulsion was increasing with the increase of salinity. Similarly, Wang et al. [109] found that having salt in water phase was beneficial for the stability of water-in-crude oil emulsion. The effect of salinity on demulsification is a more complex topic, as interfacial behavior of both demulsifiers and interface-active components in crude oil should be taken into account. Zaki et al. [110] investigated the demulsification efficiency of PPO-PEO copolymers on water-in-benzene emulsion with presence of petroleum asphaltene. The demulsification efficiency decreased with the increase of NaCl concentration from 0 to 1 M. [110] While, Borges et al. proposed that the increase of salinity enhanced the demulsification efficiency of non-ionic demulsifiers by increasing their adsorption at the interface [111].

Using MD simulations, Yassen et al. [100] studied the aggregation of model asphaltene molecules in oil phase (ortho-xylene) by water flooding with high salinity brine (25% wt. NaCl). Salting-in effect was observed where the aggregation of asphaltene was hindered by the high salinity brine compared with pure water. [100] At water/toluene interface without model asphaltenes, the IFT of water/pure toluene interface was reported by Jian et al. to increase upon the increase of NaCl concentration from 0 to 28 % wt. [21] Adding model asphaltene, VO-79, caused the reduction of IFT at the water/toluene interface, and the reduction increased with the increase of NaCl concentration. [21] The larger IFT reduction was attributed to the increase of H-bonding between asphaltene and water phase. [21] For water droplets, the increase of asphaltene-water interaction by adding NaCl was more pronounced when the size of water droplets was small. [112]

1.5 Motivations and Objectives

Asphaltenes are complex mixtures of molecules with various structures, which is categorized into continental and archipelago types. The continental model asphaltenes have been frequently studied, while the aggregation of archipelago model asphaltenes and their coaggregation with continental model asphaltenes have been less investigated. An archipelago type asphaltene contains multiple PAH cores and may undergo intramolecular flexibility that will impact its aggregation behaviors. There is a lack of studies on the relation between intramolecular flexibility of archipelago asphaltene and the aggregation of model asphaltenes.

As introduced in Section 1.4, salinity is an importance parameter that affects the aggregation behavior and interfacial properties of asphaltenes. The effect of salinity on the interfacial properties of water/oil interface has been commonly studied from experimental work. While mechanistic studies have not been carried out on the aggregation of asphaltenes under

influence of salinity. As the aggregation behavior of asphaltenes varies by their molecular structures, studying the effect of salinity on the aggregation of various model asphaltene is in demand.

Water/oil interface is commonly stabilized by the adsorption of asphaltene, which is influenced by many factors, including the molecular structure of asphaltenes, the solubility of asphaltene in oil phase, and the addition of demulsifiers. In order to understand the stabilization and destabilization of water/oil interface, it is demanding to study the adsorption of asphaltenes and the co-existence of asphaltenes and demulsifiers. Though experiments have proposed various demulsification mechanism by measuring interfacial properties at the water/oil interface, molecular level investigation on the interaction between asphaltenes and demulsifiers have not been obtained by solely experimental work.

Interaction force between water droplets is a direct indicator of the stability of W/O emulsion. Though experimental measurements, such as AFM, have been used to measure the interaction force between water droplets with adsorption of asphaltene. To the best of my knowledge, similar measurements has not been performed on water droplets with adsorption of model demulsifiers, such as PEO-PPO copolymers. Thus, it is important to quantitatively study the water droplets coalescence with adsorption and demulsifiers, which will provide understanding on the stabilization and destabilization of the problematic W/O emulsions.

In this thesis, the aggregation and interfacial properties of asphaltenes will be investigated at atomic level by using MD simulations. The studies on asphaltene aggregation will address the following two questions: firstly, the colloidal behaviors of archipelago asphaltenes and continental/archipelago mixtures; secondly, the effect of salinity on the aggregation of asphaltenes. Investigation on the interfacial properties of asphaltene will focus on two fields: firstly, the

interfacial adsorption of asphaltenes, and the co-existence of asphaltenes and demulsifiers in various solvents and interfaces; secondly, the water droplets coalescence with presence of model asphaltenes and demulsifiers. Overall, the research in this thesis aims to fulfill the following four objectives through MD simulations: (1) understand the relation between the intramolecular flexibility in archipelago model asphaltenes and aggregation and coaggregation of model asphaltenes; (2) illustrate the effect of salt on the aggregation of model asphaltenes with various structures; (3) unveil the effect of demulsifiers on the adsorption of model asphaltenes at the water/organic solvent interface; and (4) probe the free energy for coalescence of water droplet adsorbed model asphaltene and demulsifiers.

1.6 Outline

In Chapter 2, the simulation methodology is reviewed, including the force field, equation of motion, temperature and pressure coupling, cut-off and long-range interactions, the concepts of radial distribution function and potential of mean force.

Chapter 3 presented the folding and aggregation of archipelago type model asphaltene, and the coaggregation of archipelago and continental type model asphaltenes in water, heptane and toluene. MD simulations were performed to illustrate the intramolecular conformational changes and intermolecular aggregation of archipelago type model asphaltenes, and the subsequent effect on their aggregation behavior in different solutions.

In Chapter 4, a series of MD simulations was performed to study the aggregation of model asphaltenes in aqueous solutions with various concentration of NaCl, compared to the case of pure water without adding NaCl. Molecular structures of the model compounds were varied in order to investigate the effect of side chain length of the model asphaltenes. The aggregation behavior of

model asphaltenes under the influence of NaCl concentration was studied, and the driving force for the aggregation was identified.

In Chapter 5, the effect of demulsifiers on the adsorption of asphaltenes at water/organic solvent interfaces was investigated by using MD simulations. Various parameters were varied and studied, including the solvent type to represent the oil phase, the molecule structure of asphaltenes, the type and concentration of demulsifiers. The adsorption of asphaltenes was correlated to their aggregation form at the interface, their solubility in organic phase and their interaction with demulsifiers at the water/organic solvent interface.

Chapter 6 presented the water droplets coalescence with the adsorption of model asphaltene and demulsifiers. Quantitative probing of interaction forces was facilitated by MD simulation with potential of mean force calculation by umbrella sampling. The surface coverage of molecules on the water droplets was studied as an important parameter. Intermolecular interactions between the water droplets and the adsorbed molecules were observed at atomic level. The destabilization mechanism of water droplets in oil phase was provided.

In Chapter 7, overall conclusions were summarized, and future perspectives were given.

References

[1] S. Zhao, W. Pu, B. Sun, F. Gu, L. Wang, Comparative Evaluation on the Thermal Behaviors and Kinetics of Combustion of Heavy Crude Oil and its SARA Fractions, Fuel. 239 (2019) 117–125.

[2] C. Wu, A. De Visscher, I.D. Gates, On Naphthenic Acids Removal from Crude Oil and Oil Sands Process-Affected Water, Fuel. 253 (2019) 1229–1246.

[3] D. Wang, Z. Zhao, C. Qiao, W. Yang, Y. Huang, P. McKay, D. Yang, Q. Liu, H. Zeng, Techniques for Treating Slop Oil in Oil and Gas Industry: A Short Review, Fuel. 279 (2020) 118482.

[4] J.G. Speight, Petroleum Asphaltenes - Part 1: Asphaltenes, Resins and the Structure of Petroleum, Oil Gas Sci. Technol. 59 (2004) 467–477.

[5] B. Schuler, Y. Zhang, F. Liu, A.E. Pomerantz, A.B. Andrews, L. Gross, V. Pauchard, S. Banerjee, O.C. Mullins, Overview of Asphaltene Nanostructures and Thermodynamic Applications, (n.d.) 24.

[6] K.L. Gawrys, G.A. Blankenship, P.K. Kilpatrick, Solvent Entrainment in and Flocculation of Asphaltenic Aggregates Probed by Small-Angle Neutron Scattering, Langmuir. 22 (2006) 4487–4497.

[7] M. Fortuny, C.B.Z. Oliveira, R.L.F.V. Melo, M. Nele, R.C.C. Coutinho, A.F. Santos, Effect of Salinity, Temperature, Water Content, and pH on the Microwave Demulsification of Crude Oil Emulsions †, Energy Fuels. 21 (2007) 1358–1364.

[8] J.D. McLean, P.K. Kilpatrick, Effects of Asphaltene Solvency on Stability of Water-in-Crude-Oil Emulsions, J. Colloid Interface Sci. 189 (1997) 242–253.

[9] O.C. Mullins, The Modified Yen Model, Energy Fuels. 24 (2010) 2179–2207.

[10] O.C. Mullins, H. Sabbah, J. Eyssautier, A.E. Pomerantz, L. Barré, A.B. Andrews, Y. Ruiz-Morales, F. Mostowfi, R. McFarlane, L. Goual, R. Lepkowicz, T. Cooper, J. Orbulescu, R.M. Leblanc, J. Edwards, R.N. Zare, Advances in Asphaltene Science and the Yen–Mullins Model, Energy Fuels. 26 (2012) 3986–4003.

[11] J.P. Dickie, T.Fu. Yen, Macrostructures of the Asphaltic Fractions by Various Instrumental Methods, Anal. Chem. 39 (1967) 1847–1852.

[12] O.C. Mullins, The Modified Yen Model †, Energy Fuels. 24 (2010) 2179–2207.

[13] O.C. Mullins, H. Sabbah, J. Eyssautier, A.E. Pomerantz, L. Barré, a. B. Andrews, Y. Ruiz-Morales, F. Mostowfi, R. McFarlane, L. Goual, R. Lepkowicz, T. Cooper, J. Orbulescu, R.M. Leblanc, J. Edwards, R.N. Zare, Advances in Asphaltene Science and the Yen–Mullins Model, Energy Fuels. 26 (2012) 3986–4003.

[14] H.H.F. Koolen, A.F. Gomes, L.G.M. de Moura, F. Marcano, F.M.R. Cardoso, C.F. Klitzke, R. Wojcik, J. Binkley, J.S. Patrick, R.F. Swarthout, P.T.V. Rosa, F.C. Gozzo, Integrative Mass Spectrometry Strategy for Fingerprinting and Tentative Structural Characterization of Asphaltenes, Fuel. 220 (2018) 717–724.

[15] O.P. Strausz, T.W. Mojelsky, F. Faraji, E.M. Lown, P. Peng, Additional Structural Details on Athabasca Asphaltene and Their Ramifications, Energy Fuels. 13 (1999) 207–227.

[16] O.P. Strausz, T.W. Mojelsky, E.M. Lown, The Molecular Structure of Asphaltene: An Unfolding Story, Fuel. 71 (1992) 1355–1363.

[17] E. Durand, M. Clemancey, J.-M. Lancelin, J. Verstraete, D. Espinat, A.-A. Quoineaud, Effect of Chemical Composition on Asphaltenes Aggregation, Energy Fuels. 24 (2010) 1051–1062.

[18] M.L. Chacón-Patiño, S.M. Rowland, R.P. Rodgers, Advances in Asphaltene Petroleomics. Part 1: Asphaltenes Are Composed of Abundant Island and Archipelago Structural Motifs, Energy Fuels. 31 (2017) 13509–13518.

[19] B. Schuler, Y. Zhang, F. Liu, A.E. Pomerantz, A.B. Andrews, L. Gross, V. Pauchard, S. Banerjee, O.C. Mullins, Overview of Asphaltene Nanostructures and Thermodynamic Applications, Energy Fuels. (2020).

[20] B. Schuler, G. Meyer, D. Peña, O.C. Mullins, L. Gross, Unraveling the Molecular Structures of Asphaltenes by Atomic Force Microscopy, J. Am. Chem. Soc. 137 (2015) 9870–9876.

[21] C. Jian, M.R. Poopari, Q. Liu, N. Zerpa, H. Zeng, T. Tang, Mechanistic Understanding of the Effect of Temperature and Salinity on the Water/Toluene Interfacial Tension, Energy Fuels. 30 (2016) 10228–10235.

[22] Z. Niu, X. Ma, R. Manica, T. Yue, Molecular Destabilization Mechanism of Asphaltene Model Compound C5Pe Interfacial Film by EO-PO Copolymer: Experiments and MD Simulation, J. Phys. Chem. C. 123 (2019) 10501–10508.

[23] X. Zhu, D. Chen, G. Wu, Molecular Dynamic Simulation of Asphaltene Co-Aggregation with Humic Acid During Oil Spill, Chemosphere. 138 (2015) 412–421.

[24] T.F. Headen, M.P. Hoepfner, Predicting Asphaltene Aggregate Structure from Molecular Dynamics Simulation: Comparison to Neutron Total Scattering Data, Energy Fuels. 33 (2019) 3787–3795.

[25] T.F. Headen, E.S. Boek, G. Jackson, T.S. Totton, E.A. Müller, Simulation of Asphaltene Aggregation through Molecular Dynamics: Insights and Limitations, Energy Fuels. 31 (2017) 1108–1125.

[26] J.A. Duran, Y.A. Casas, L. Xiang, L. Zhang, H. Zeng, H.W. Yarranton, Nature of Asphaltene Aggregates, Energy Fuels. 33 (2019) 3694–3710.

[27] C.A. Hunter, J.K.M. Sanders, The Nature of .pi.-.pi. Interactions, J. Am. Chem. Soc. 112 (1990) 5525–5534.

[28] M. Sedghi, L. Goual, W. Welch, J. Kubelka, Effect of Asphaltene Structure on Association and Aggregation Using Molecular Dynamics, J. Phys. Chem. B. 117 (2013) 5765–5776.

[29] E. Buenrostro-Gonzalez, H. Groenzin, C. Lira-Galeana, O.C. Mullins, The Overriding Chemical Principles that Define Asphaltenes, Energy Fuels. 15 (2001) 972–978.

[30] C. Jian, T. Tang, S. Bhattacharjee, Probing the Effect of Side-Chain Length on the Aggregation of a Model Asphaltene Using Molecular Dynamics Simulations, Energy Fuels. 27 (2013) 2057–2067.

[31] C. Jian, T. Tang, S. Bhattacharjee, Molecular Dynamics Investigation on the Aggregation of Violanthrone78-Based Model Asphaltenes in Toluene, Energy Fuels. 28 (2014) 3604–3613.

[32] L. Barré, J. Jestin, A. Morisset, T. Palermo, S. Simon, Relation between Nanoscale Structure of Asphaltene Aggregates and their Macroscopic Solution Properties, Oil Gas Sci. Technol. – Rev IFP. 64 (2009) 617–628.

[33] G. Porte, H. Zhou, V. Lazzeri, Reversible Description of Asphaltene Colloidal Association and Precipitation, Langmuir. 19 (2003) 40–47.

[34] K.L. Gawrys, P.K. Kilpatrick, Asphaltenic Aggregates are Polydisperse Oblate Cylinders, J. Colloid Interface Sci. 288 (2005) 325–334.

[35] P.M. Spiecker, K.L. Gawrys, P.K. Kilpatrick, Aggregation and Solubility Behavior of Asphaltenes And Their Subfractions, J. Colloid Interface Sci. 267 (2003) 178–193.

[36] J.A. Duran, Y.A. Casas, L. Xiang, L. Zhang, H. Zeng, H.W. Yarranton, Nature of Asphaltene Aggregates, Energy Fuels. 33 (2019) 3694–3710.

[37] C. Jian, T. Tang, Molecular Dynamics Simulations Reveal Inhomogeneity-Enhanced Stacking of Violanthrone-78-Based Polyaromatic Compounds in n-Heptane-Toluene Mixtures., J. Phys. Chem. B. 119 (2015) 8660–8.

[38] T.F. Headen, E.S. Boek, N.T. Skipper, Evidence for Asphaltene Nanoaggregation in Toluene and Heptane from Molecular Dynamics Simulations †, Energy Fuels. 23 (2009) 1220–1229.

[39] T.F. Headen, E.S. Boek, G. Jackson, T.S. Totton, E.A. Müller, Simulation of Asphaltene Aggregation through Molecular Dynamics: Insights and Limitations, Energy Fuels. 31 (2017) 1108–1125.

[40] T. Kuznicki, J.H. Masliyah, S. Bhattacharjee, Molecular Dynamics Study of Model Molecules Resembling Asphaltene-Like Structures in Aqueous Organic Solvent Systems, Energy Fuels. 22 (2008) 2379–2389.

[41] S. Acevedo, A. Castro, E. Vásquez, F. Marcano, M.A. Ranaudo, Investigation of Physical Chemistry Properties of Asphaltenes Using Solubility Parameters of Asphaltenes and Their Fractions A1 and A2, Energy Fuels. 24 (2010) 5921–5933.

[42] F. Rao, Q. Liu, Froth Treatment in Athabasca Oil Sands Bitumen Recovery Process: A Review, Energy Fuels. 27 (2013) 7199–7207.

[43] P.-C. Schorling, D.G. Kessel, I. Rahimian, Influence of the Crude Oil Resin / Asphaltene Ratio on The Stability of Oil / Water Emulsions, Colloids Surf. Physochemical Eng. Asp. 152 (1999) 95–102.

[44] J. Sjöblom, L. Mingyuan, A.A. Christy, T. Gu, Water-in-Crude-Oil Emulsions from The Norwegian Continental Shelf 7. Interfacial Pressure and Emulsion Stability, Colloids Surf. 66 (1992) 55–62.

[45] T. Tadros, Gibbs Adsorption Isotherm, in: T. Tadros (Ed.), Encycl. Colloid Interface Sci., Springer Berlin Heidelberg, Berlin, Heidelberg, 2013: pp. 626–626.

[46] P. Qiao, D. Harbottle, P. Tchoukov, J. Masliyah, J. Sjoblom, Q. Liu, Z. Xu, Fractionation of Asphaltenes in Understanding Their Role in Petroleum Emulsion Stability and Fouling, Energy Fuels. 31 (2017) 3330–3337.

[47] D. Liu, C. Li, X. Zhang, F. Yang, G. Sun, B. Yao, H. Zhang, Polarity Effects of Asphaltene Subfractions on the Stability and Interfacial Properties of Water-In-Model Oil Emulsions, Fuel. 269 (2020) 117450.

[48] J.P. Rane, V. Pauchard, A. Couzis, S. Banerjee, Interfacial Rheology of Asphaltenes at Oil–Water Interfaces and Interpretation of the Equation of State, Langmuir. 29 (2013) 4750–4759.

[49] D. Wang, D. Yang, C. Huang, Y. Huang, D. Yang, H. Zhang, Q. Liu, T. Tang, M. Gamal El-Din, T. Kemppi, B. Perdicakis, H. Zeng, Stabilization Mechanism and Chemical Demulsification of Water-In-Oil and Oil-In-Water Emulsions in Petroleum Industry: A Review, Fuel. 286 (2021) 119390.

[50] M. Mohammadi, M. Zirrahi, H. Hassanzadeh, Adsorption Kinetics of Asphaltenes at the Heptol–Water Interface, Energy Fuels. 34 (2020) 3144–3152.

[51] C. Shi, L. Zhang, L. Xie, X. Lu, Q. Liu, J. He, C.A. Mantilla, F.G.A. Van den berg, H. Zeng, Surface Interaction of Water-in-Oil Emulsion Droplets with Interfacially Active Asphaltenes, Langmuir. 33 (2017) 1265–1274.

[52] O. Mouraille, T. Skodvin, J. Sjöblom, J.-L. Peytavy, Stability of Water-In-Crude Oil Emulsions: Role Played by The State of Solvation of Asphaltenes and by Waxes, J. Dispers. Sci. Technol. 19 (1998) 339–367.

[53] L. Xie, Q. Lu, X. Tan, Q. Liu, T. Tang, H. Zeng, Interfacial Behavior and Interaction Mechanism of Pentol/Water Interface Stabilized with Asphaltenes, J. Colloid Interface Sci. 553 (2019) 341–349.

[54] D. Pradilla, S. Simon, J. Sjöblom, Mixed Interfaces of Asphaltenes and Model Demulsifiers Part I: Adsorption and Desorption of Single Components, Colloids Surf. Physicochem. Eng. Asp. 466 (2015) 45–56.

[55] D. Liu, C. Li, F. Yang, G. Sun, J. You, K. Cui, Synergetic Effect of Resins and Asphaltenes on Water/Oil Interfacial Properties and Emulsion Stability, Fuel. 252 (2019) 581–588.

[56] J. Wen, J. Zhang, Z. Wang, Y. Zhang, Correlations between Emulsification Behaviors of Crude Oil-Water Systems and Crude Oil Compositions, J. Pet. Sci. Eng. 146 (2016) 1–9.

[57] Z. Zhang, J. Song, Y.-J. Lin, X. Wang, S.L. Biswal, Comparing the Coalescence Rate of Water-in-Oil Emulsions Stabilized with Asphaltenes and Asphaltene-like Molecules, Langmuir. 36 (2020) 7894–7900.

[58] T. Kuznicki, J.H. Masliyah, S. Bhattacharjee, Aggregation and Partitioning of Model Asphaltenes at Toluene−Water Interfaces: Molecular Dynamics Simulations, Energy Fuels. 23 (2009) 5027–5035.

[59] Y. Mikami, Y. Liang, T. Matsuoka, E.S. Boek, Molecular Dynamics Simulations of Asphaltenes at the Oil–Water Interface: From Nanoaggregation to Thin-Film Formation, Energy Fuels. 27 (2013) 1838–1845.

[60] C. Jian, M.R. Poopari, Q. Liu, N. Zerpa, H. Zeng, T. Tang, Reduction of Water/Oil Interfacial Tension by Model Asphaltenes: The Governing Role of Surface Concentration, J. Phys. Chem. B. 120 (2016) 5646–5654.

[61] F. Gao, Z. Xu, G. Liu, S. Yuan, Molecular Dynamics Simulation: The Behavior of Asphaltene in Crude Oil and at the Oil/Water Interface, Energy Fuels. 28 (2014) 7368–7376.

[62] C. Jian, Q. Liu, H. Zeng, T. Tang, Effect of Model Polycyclic Aromatic Compounds on the Coalescence of Water-in-Oil Emulsion Droplets, J. Phys. Chem. C. 121 (2017) 10382–10391.
[63] M. Duan, X. Song, S. Zhao, S. Fang, F. Wang, C. Zhong, Z. Luo, Layer-by-Layer Assembled Film of Asphaltenes/Polyacrylamide and Its Stability of Water-in-Oil Emulsions: A Combined Experimental and Simulation Study, J. Phys. Chem. C. 121 (2017) 4332–4342.
[64] Z. Grenoble, S. Trabelsi, Mechanisms, Performance Optimization and New Developments in Demulsification Processes for Oil and Gas Applications, Adv. Colloid Interface Sci. 260 (2018) 32–45.
[65] R. Zolfaghari, A. Fakhru'l-Razi, L.C. Abdullah, S.S.E.H. Elnashaie, A. Pendashteh, Demulsification Techniques of Water-In-Oil and Oil-In-Water Emulsions in Petroleum Industry, Sep. Purif. Technol. 170 (2016) 377–407.
[66] S.M. Abed, N.H. Abdurahman, R.M. Yunus, H.A. Abdulbari, S. Akbari, Oil Emulsions and The Different Recent Demulsification Techniques in The Petroleum Industry - A Review, IOP Conf. Ser. Mater. Sci. Eng. 702 (2019) 012060.
[67] Y.N. Romanova, T. Maryutina, N.S. Musina, E. V Yurtov, B.Y. Spivakov, Demulsification of Water-In-Oil Emulsions by Exposure to Magnetic Field, J. Pet. Sci. Eng. 179 (2019) 600–605.
[68] X. Yang, W. Tan, Y. Bu, Demulsification of Asphaltenes and Resins Stabilized Emulsions via the Freeze/Thaw Method, Energy Fuels. 23 (2009) 481–486.
[69] M. Kukizaki, M. Goto, Demulsification of Water-In-Oil Emulsions by Permeation Through Shirasu-Porous-Glass (SPG) Membranes, J. Membr. Sci. 322 (2008) 196–203.
[70] N.M. Kocherginsky, C.L. Tan, W.F. Lu, Demulsification of Water-In-Oil Emulsions Via Filtration Through A Hydrophilic Polymer Membrane, J. Membr. Sci. 220 (2003) 117–128.
[71] D. Sun, X. Duan, W. Li, D. Zhou, Demulsification of Water-In-Oil Emulsion by Using Porous Glass Membrane, J. Membr. Sci. 146 (1998) 65–72.
[72] X. Huang, K. Peng, L. Lu, R. Wang, J. Liu, Carbon Source Dependence of Cell Surface Composition and Demulsifying Capability of Alcaligenes sp. S-XJ-1, Environ. Sci. Technol. 48 (2014) 3056–3064.
[73] N. Hou, D. Li, F. Ma, J. Zhang, Y. Xu, J. Wang, C. Li, Effective Biodemulsifier Components Secreted by Bacillus Mojavensis XH-1 and Analysis of The Demulsification Process, Biodegradation. 25 (2014) 529–541.

[74] Q. Cai, Z. Zhu, B. Chen, B. Zhang, Oil-in-Water Emulsion Breaking Marine Bacteria for Demulsifying Oily Wastewater, Water Res. 149 (2019) 292–301.

[75] Z. Zhang, G.Y. Xu, F. Wang, S.L. Dong, Y.M. Li, Characterization and Demulsification of Poly(Ethylene Oxide)–Block–Poly(Propylene Oxide)–Block–Poly(Ethylene Oxide) Copolymers, J. Colloid Interface Sci. 277 (2004) 464–470.

[76] F. Shehzad, I.A. Hussein, M.S. Kamal, W. Ahmad, A.S. Sultan, M.S. Nasser, Polymeric Surfactants and Emerging Alternatives used in the Demulsification of Produced Water: A Review, Polym. Rev. 58 (2018) 63–101.

[77] A. Le Follotec, I. Pezron, C. Noik, C. Dalmazzone, L. Metlas-Komunjer, Triblock Copolymers as Destabilizers of Water-In-Crude Oil Emulsions, Colloids Surf. Physicochem. Eng. Asp. 365 (2010) 162–170.

[78] S. An, Z. Li, H. Chen, Z. Yan, Y. Tan, Proanthocyanidin-Based Polyether Demulsifiers for the Treatment of Aging Oil Emulsions, Energy Fuels. 34 (2020) 5788–5797.

[79] E.B. Zamora, F. Vázquez, E.I. Hernández, F. Álvarez, G. Zavala, A. López, C.A. Flores-Sandoval, Triblock Copolymers Functionalized with Quaternary Ammonium Salts as Dehydrating Agents for Heavy and Extra-Heavy Crude Oils, J. Dispers. Sci. Technol. 39 (2018) 1502–1509.

[80] M. Acosta, L.H. Reyes, J.C. Cruz, D. Pradilla, Demulsification of Colombian Heavy Crude Oil (W/O) Emulsions: Insights into the Instability Mechanisms, Chemical Structure, and Performance of Different Commercial Demulsifiers, Energy Fuels. 34 (2020) 5665–5678.

[81] W. Kang, G. Jing, H. Zhang, M. Li, Z. Wu, Influence of Demulsifier on Interfacial Film Between Oil and Water, Colloids Surf. Physicochem. Eng. Asp. 272 (2006) 27–31.

[82] A. Goliaei, E.Y. Lau, U. Adhikari, E. Schwegler, M.L. Berkowitz, Behavior of P85 and P188 Poloxamer Molecules: Computer Simulations Using United-Atom Force-Field, J. Phys. Chem. B. 120 (2016) 8631–8641.

[83] Z. Zhang, G.Y. Xu, F. Wang, S.L. Dong, Y.M. Li, Characterization and Demulsification of Poly(Ethylene Oxide)–Block–Poly(Propylene Oxide)–Block–Poly(Ethylene Oxide) Copolymers, J. Colloid Interface Sci. 277 (2004) 464–470.

[84] E.I. Hernández, L.V. Castro-Sotelo, J.R. Avendaño-Gómez, C.A. Flores, F. Alvarez-Ramírez, F. Vázquez, Synthesis, Characterization, and Evaluation of Petroleum Demulsifiers of Multibranched Block Copolymers, Energy Fuels. 30 (2016) 5363–5378.

[85] V.F. Pacheco, L. Spinelli, E.F. Lucas, C.R.E. Mansur, Destabilization of Petroleum Emulsions: Evaluation of the Influence of the Solvent on Additives, Energy Fuels. 25 (2011) 1659–1666.

[86] I. Kailey, X. Feng, Influence of Structural Variations of Demulsifiers on their Performance, Ind. Eng. Chem. Res. 52 (2013) 785–793.

[87] G. Cendejas, F. Arreguín, L.V. Castro, E.A. Flores, F. Vazquez, Demulsifying Super-Heavy Crude Oil with Bifunctionalized Block Copolymers, Fuel. 103 (2013) 356–363.

[88] E. Pensini, D. Harbottle, F. Yang, P. Tchoukov, Z. Li, I. Kailey, J. Behles, J. Masliyah, Z. Xu, Demulsification Mechanism of Asphaltene-Stabilized Water-in-Oil Emulsions by a Polymeric Ethylene Oxide–Propylene Oxide Demulsifier, Energy Fuels. 28 (2014) 6760–6771.

[89] M.D. Lobato, J.M. Pedrosa, S. Lago, Effects of Block Copolymer Demulsifiers on Langmuir Films of Heavy and Light Crude Oil Asphaltenes, Energy Fuels. 28 (2014) 745–753.

[90] J. Wu, Y. Xu, T. Dabros, H. Hamza, Effect of Demulsifier Properties on Destabilization of Water-in-Oil Emulsion, Energy Fuels. 17 (2003) 1554–1559.

[91] F. Yang, P. Tchoukov, P. Qiao, X. Ma, E. Pensini, T. Dabros, J. Czarnecki, Z. Xu, Studying Demulsification Mechanisms of Water-In-Crude Oil Emulsions Using A Modified Thin Liquid Film Technique, Colloids Surf. Physicochem. Eng. Asp. 540 (2018) 215–223.

[92] Z. Chen, J. Peng, L. Ge, Z. Xu, Demulsifying Water-In-Oil Emulsions by Ethyl Cellulose Demulsifiers Studied Using Focused Beam Reflectance Measurement, Chem. Eng. Sci. 130 (2015) 254–263.

[93] P. Zhang, H. Wang, X. Liu, X. Shi, J. Zhang, G. Yang, K. Sun, J. Wang, The Dynamic Interfacial Adsorption and Demulsification Behaviors of Novel Amphiphilic Dendrimers, Colloids Surf. Physicochem. Eng. Asp. 443 (2014) 473–480.

[94] Z. Li, H. Geng, X. Wang, B. Jing, Y. Liu, Y. Tan, Noval Tannic Acid-Based Polyether as An Effective Demulsifier for Water-In-Aging Crude Oil Emulsions, Chem. Eng. J. 354 (2018) 1110–1119.

[95] X. Mao, L. Gong, L. Xie, H. Qian, X. Wang, H. Zeng, Novel Fe3O4 based Superhydrophilic Core-Shell Microspheres for Breaking Asphaltenes-Stabilized Water-In-Oil Emulsion, Chem. Eng. J. 358 (2019) 869–877.

[96] D. Ballal, R. Srivastava, Modeling the Interfacial Properties of Poly(Ethylene Oxide-Co-Propylene Oxide) Polymers At Water-Toluene Interface, Fluid Phase Equilibria. 427 (2016) 209–218.

[97] Z. Niu, X. Ma, R. Manica, T. Yue, Molecular Destabilization Mechanism of Asphaltene Model Compound C5Pe Interfacial Film by EO-PO Copolymer: Experiments and MD simulation, J. Phys. Chem. C. 123 (2019) 10501–10508.

[98] J. Liu, Y. Zhao, S. Ren, Molecular Dynamics Simulation of Self-Aggregation of Asphaltenes at an Oil/Water Interface: Formation and Destruction of the Asphaltene Protective Film, Energy Fuels. 29 (2015) 1233–1242.

[99] X. Song, P. Shi, M. Duan, S. Fang, Y. Ma, Investigation of Demulsification Efficiency in Water-In-Crude Oil Emulsions Using Dissipative Particle Dynamics, RSC Adv. 5 (2015) 62971–62981.

[100] S. Yaseen, G.A. Mansoori, Asphaltene Aggregation Onset During High-Salinity Waterflooding of Reservoirs (A Molecular Dynamic Study), Pet. Sci. Technol. 36 (2018) 1725–1732.

[101] P.C. Myint, A. Firoozabadi, Thin Liquid Films in Improved Oil Recovery from Low-Salinity Brine, Curr. Opin. Colloid Interface Sci. 20 (2015) 105–114.

[102] P. Zhang, M.T. Tweheyo, T. Austad, Wettability Alteration and Improved Oil Recovery in Chalk: The Effect of Calcium in the Presence of Sulfate, Energy Fuels. 20 (2006) 2056–2062.

[103] P. Rostami, M.F. Mehraban, M. Sharifi, M. Dejam, S. Ayatollahi, Effect of Water Salinity on Oil/Brine Interfacial Behaviour During Low Salinity Waterflooding: A Mechanistic Study, Petroleum. 5 (2019) 367–374.

[104] T.E. Chávez-Miyauchi, A. Firoozabadi, G.G. Fuller, Nonmonotonic Elasticity of the Crude Oil–Brine Interface in Relation to Improved Oil Recovery, Langmuir. 32 (2016) 2192–2198.

[105] A. Ameri, F. Esmaeilzadeh, D. Mowla, Effect of Low-Salinity Water on Asphaltene Precipitation, J. Dispers. Sci. Technol. 39 (2018) 1031–1039.

[106] F. Moeini, A. Hemmati-Sarapardeh, M.-H. Ghazanfari, M. Masihi, S. Ayatollahi, Toward Mechanistic Understanding of Heavy Crude Oil/Brine Interfacial Tension: The Roles of Salinity, Temperature and Pressure, Fluid Phase Equilibria. 375 (2014) 191–200.

[107] S. Maaref, S. Ayatollahi, The Effect of Brine Salinity on Water-In-Oil Emulsion Stability Through Droplet Size Distribution Analysis: A Case Study, J. Dispers. Sci. Technol. 39 (2018) 721–733.

[108] N.N.A. Ling, A. Haber, B.F. Graham, Z.M. Aman, E.F. May, E.O. Fridjonsson, M.L. Johns, Quantifying the Effect of Salinity on Oilfield Water-in-Oil Emulsion Stability, Energy Fuels. 32 (2018) 10042–10049.

[109] X. Wang, V. Alvarado, Effects of Aqueous-Phase Salinity on Water-in-Crude Oil Emulsion Stability, J. Dispers. Sci. Technol. 33 (2012), 165-170.

[110] N.N. Zaki, M.E. Abdel-Raouf, A.-A.A. Abdel-Azim, Propylene Oxide-Ethylene Oxide Block Copolymers as Demulsifiers For Water-In-Oil Emulsions, II. Effects Of Temperature, Salinity,Ph-Value, And Solvents On The Demulsification Efficiency, Monatshefte Für Chem. - Chem. Mon. 127 (1996) 1239–1245.

[111] B. Borges, M. Rondón, O. Sereno, J. Asuaje, Breaking of Water-in-Crude-Oil Emulsions. 3. Influence of Salinity and Water−Oil Ratio on Demulsifier Action, Energy Fuels. 23 (2009) 1568–1574.

[112] J. Qiao, S. Cheng, W. Song, C. Jian, W. Wang, D. Zhang, Y. Xu, Probing the Effect of NaCl Concentrations on a Model Asphaltene Adsorption onto Water Droplets of Different Sizes, Energy Fuels. 33 (2019) 3881–3890.

Chapter 2. Simulation Methodology

Molecular dynamics (MD) is an atomic-level simulation method based on the classical statistical mechanics, which was first introduced in the 1950s. [1] Its applications have been widely explored, ranging from physics, materials science, to biological systems. [2] In MD simulations, atoms interact with each other through inter-atomic potentials defined in a force field. The motions of the atoms are obtained by numerically integrations of the classical equations of motion by an algorithm. [1–4] Possible conformational profiles and dynamics of the molecules are simulated at molecular level, which are usually impossible to reach by real experiments. Nowadays, many software packages are available to carry out MD simulations, such as Assisted Model Building with Energy Refinement (AMBER), Chemistry at Harvard Macromolecular Mechanics (CHARMM), GROningen MAchine for Chemical Simulations (GROMACS), GROningen MOlecular Simulation (GROMOS), Nanoscale Molecular Dynamics (NAMD), Large-scale Atomic/Molecular Massively Parallel Simulator (LAMMPS), etc. In this thesis, MD simulations are mainly performed by using GROMACS software package due to its various advantages. GROMACS is versatile to simulate systems with up to millions of particles from a variety of molecules, including biomedical molecules and polymers. Moreover, it is suitable to perform calculations with complex bonded interactions and provides extremely fast calculation on non-bonded interactions. [5]

2.1 Force Field

Force field is a collection of equations that specify the potential energy of a system in terms of atomic coordinates. [2,6] In general, the potential is the summation of various interaction terms,

including two body interaction, three body interaction, four body interaction, and so on. [3] A typical functional form for the potential is expressed as [2,7]:

$$U(\boldsymbol{r}) = \sum_{bonds} \frac{k_{i,l}}{2}\left(l_i - l_{i,0}\right)^2 + \sum_{angles} \frac{k_{i,\theta}}{2}\left(\theta_i - \theta_{i,0}\right)^2 + \sum_{torsions} \frac{V_{i,n}}{2}(1 + cos(n\omega_i - \gamma))^2 +$$

$$\sum_{improper} \frac{k_{i,\eta}}{2}\left(\eta_i - \eta_{i,0}\right)^2 + \sum_{i=1}^{N}\sum_{j=i+1}^{N} 4\varepsilon_{ij}\left[\left(\frac{\sigma_{ij}}{r_{ij}}\right)^{12} - \left(\frac{\sigma_{ij}}{r_{ij}}\right)^{6}\right] + \sum_{i=1}^{N}\sum_{j=i+1}^{N} \frac{q_i q_j}{4\pi\epsilon_0 \epsilon r_{ij}} \quad (2.1)$$

where $U(\boldsymbol{r})$ is the potential energy, $\boldsymbol{r}$ represents the position of N atoms in the system. The first four terms on the right side of the equation are the bonded potential between a fixed list of atoms. Specifically, the first term represents the bonded energy between pairs of atoms, e.g. A-B. It is the harmonic potential as the bond stretches from the equilibrium reference $l_{i,0}$ to length l_i with force constant $k_{i,l}$. The second term is a harmonic angle potential summing over all the bond-angles between three atoms, e.g. A- B- C, as angle θ_i deviates from the equilibrium value $\theta_{i,0}$ with force constant $k_{i,\theta}$. The third term represents the potential of proper dihedrals between four atoms A-B-C-D, where ω_i is the torsional angle, n is a multiplicity coefficient, $V_{i,n}$ is the height of the potential barrier and γ is the phase factor (0 or 180°). The fourth term is the simplest form of improper dihedral potential, which is used to keep the planar structure of certain atom groups or to prevent the flipping-over of molecules. $k_{i,\eta}$ is the force constant, η_i the angle between two planes and $\eta_{i,0}$ is the equilibrium value of the dihedral angle. The fifth and sixth terms are the non-bonded potentials, describing the interaction between pairs of atoms i and j in different molecules or in the same molecule but are at least three bonds apart from each other. Specifically, the fifth term is the Lennard-Jones potential for van der Waals interactions, where variable r_{ij} is the distance between atoms i and j, parameters ε_{ij} is the depth of the potential energy and σ_{ij} is the collision diameter. The sixth term is potential for the electrostatic interaction based on the Coulomb's law, with partial atomic charges q_i and q_j, dielectric constant ϵ and the permittivity of free space ϵ_0. [2]

A force field is defined by both the functional form of the potential energy and the associated set of parameters. As the force field is *empirical*, the optimal force field for a system is usually obtained by evaluating the accuracy and computational efficiency. [2] With certain functional form chosen, the parameterization of the force field is implemented by comparing data to experimental results or quantum mechanics calculations. [2] Usually, the structure properties for some molecules, including geometry of molecular structure, conformational energies and thermodynamic properties, are difficult to obtain from experimental measurements. [2] Quantum mechanics calculations are more commonly used to optimize the force field. The force fields are further optimized by two traditional approaches, trial and error assessment and least square fitting, or automated approach such as machine learning methods. [2] In the traditional approaches, the parameters for an individual molecule from experimental data or quantum mechanics calculations are used as input, which may require fragmentation of large molecules. Then, the feature properties of the molecules are characterized and fitted by human and computer efforts, which ultimately lead to the force field parameterization. The process might be less efficient than the automated approaches such as machine learning. [2]

2.2 Equation of Motion

The general form for classical equations of motion is expressed as [8]:

$$\dot{\boldsymbol{q}}_{\boldsymbol{i}} = \frac{\boldsymbol{p}_{\boldsymbol{i}}}{m_i}, \quad \dot{\boldsymbol{p}}_{\boldsymbol{i}} = \boldsymbol{f}_{\boldsymbol{i}}, \tag{2.2}$$

where $\boldsymbol{q}_i$ is the coordinate, $\boldsymbol{p}_i$ is the conjugate momentum, and m_i is the mass of particle i; $\boldsymbol{f}_i$ is the force on particle i. The total energy, or Hamiltonian H, of the system is the summation of kinetic energy K and potential energy U, as [1]:

$$H = K(\boldsymbol{p}) + U(\boldsymbol{q}) = \sum_i \frac{\boldsymbol{p}_i^2}{2m_i} + U(\boldsymbol{q}) \tag{2.3}$$

Then equation 2.2 is rewritten as:

$$\dot{\boldsymbol{q}}_{\boldsymbol{i}} = \frac{\partial H}{\partial \boldsymbol{p}_{\boldsymbol{i}}}, \quad \dot{\boldsymbol{p}}_{\boldsymbol{i}} = -\frac{\partial H}{\partial \boldsymbol{q}_{\boldsymbol{i}}} \tag{2.4}$$

MD simulations are implemented by solving the equations of motion step-by-step. The Verlet algorithm is one simple and commonly used method, which is expressed as follows [8]:

$$\boldsymbol{p}_{\boldsymbol{i}}(t + \tfrac{1}{2}\Delta t) = \boldsymbol{p}_{\boldsymbol{i}}(t) + \tfrac{1}{2}\Delta t \boldsymbol{f}_{\boldsymbol{i}}(t), \tag{2.5a}$$

$$\boldsymbol{q}_{\boldsymbol{i}}(t + \Delta t) = \boldsymbol{q}_{\boldsymbol{i}}(t) + \Delta t \boldsymbol{p}_{\boldsymbol{i}}(t + \tfrac{1}{2}\Delta t)\frac{1}{m_i}, \tag{2.5b}$$

$$\boldsymbol{p}_{\boldsymbol{i}}(t + \Delta t) = \boldsymbol{p}_{\boldsymbol{i}}(t + \tfrac{1}{2}\Delta t) + \tfrac{1}{2}\Delta t \boldsymbol{f}_{\boldsymbol{i}}(t + \Delta t), \tag{2.5c}$$

where t is the time and Δt is the time step. As shown in equation 2.5a, the momenta are first advanced by half of a time step. Then, the coordinates are moved forward by one time step calculated from the new momenta, as shown in the equation 2.5b. Lastly, the force at $t + \Delta t$ is evaluated and used towards the calculation of momenta at $t + \Delta t$, as shown in equation 2.5c. The Verlet/leapfrog algorithm has various advantages, such as time reversibility, simplicity, and stability. [1,8]

In MD simulation, the intermolecular bonds have high oscillation frequency, which limits the length of time step. Constraints are usually applied to fix the bonds to certain lengths in order to improve the calculation efficiency. [2] In a system with constraints, Lagrange multipliers are added to the Hamiltonian and solved by algorithms. The first scheme for applying constraints under the leapfrog algorithm is called SHAKE. More recently, LINCS (linear constraint solver) is another algorithm to apply constraints, which reduced the constraint equations to a linear matrix equation. [8]

2.3 Temperature and Pressure Coupling

An ensemble is a collection of systems in identical macroscopic states but different microscopic states. [3] If the systems are closed and have fixed volume V and total internal energy E, it is called a microcanonical (NVE) ensemble. Canonical (NVT) ensemble represents the case where systems exchange heat with the surrounding environment through a heat bath to maintain a constant temperature T. If the systems could exchange heat and volume with the surrounding environment but have a constant pressure p, they form the isothermal-isobaric (NpT) ensemble.

Among the ensembles, the NVT ensemble is the more commonly used. The internal energy is $E_i(N,V)$ for quantum state i, and repeated based on its degeneracy. At thermodynamics equilibrium, the statistical properties, including energy, pressure, etc., of systems can be described by the partition function, which has the form of [3]:

$$Q(N,V,T) = \sum_i e^{-E_i(N,V)/k_B T} \tag{2.6}$$

where k_B is the Boltzmann constant. The Helmholtz free energy is expressed as:

$$A(N,V,T) = k_B T \ln Q(N,V,T) \tag{2.7}$$

In practice, the absolute free energy of a system is difficult to be calculated, while the free energy difference between two different states can be obtained in MD simulations [9,10].

In order to obtain constant temperature of the systems, various thermostats have been introduced, including Nosé-Hoover thermostat, Berendsen thermostat, etc. The Berendsen thermostat uses a weak coupling to a heat bath at temperature T_0, which corrects the first order deviation of system temperature by:

$$\frac{dT}{dt} = \frac{T_0 - T}{\tau_T} \tag{2.8}$$

where τ_T is a time constant. The advantage of Berendsen thermostat is that the temperature could be equilibrated in a short time, while the fluctuations of kinetic energy are suppressed, which compromises the accuracy in calculating fluctuation-related properties. [11] The velocity-rescaling thermostat modifies the Berendsen coupling by adding a stochastic term to correct the probability distribution of kinetic energy. Canonical ensemble is properly produced with this thermostat, with the same efficiency as Berendsen coupling. [11]

Beside thermostat, the isothermal-isobaric (NpT) ensemble requires pressure coupling to a pressure bath. Different pressure coupling methods are available, such as Berendsen and Parrinello-Rahman barostats, which are compatible with many temperature coupling methods. The Berendsen pressure coupling uses the same concept as the temperature coupling, which rescales the pressure p according to

$$\frac{dp}{dt} = \frac{p_0 - p}{\tau_p} \tag{2.9}$$

where τ_p is a time constant and p_0 is the reference pressure. Berendsen barostat also results in a fast equilibration of pressure but does not reproduce the exact NpT ensemble. If the fluctuation in volume is of interest, the weak-coupling scheme of Berendsen algorithm is not suitable, and more exact albeit less efficient barostats such as Parrinello-Rahman pressure coupling should be used. [11]

2.4 Cut-off and Long-Range Interactions

Due to the computational cost for large systems, the size of the simulation systems is limited. Periodic boundary conditions (PBC) are commonly applied so that the primitive simulation box is surrounded by its identical replicas in all directions. [1] In the calculation, one particle may leave the primitive box and will be replaced by its periodic image entering the box. [2]

Computing the energy and forces is time consuming if all pairwise interactions were looped over. [2] Cut-off is applied to the non-bonded interactions in order to reduce the calculation cost. A switch function $f(r_{ij})$ is used to simply truncate the non-bonded interactions, which is expressed as [2]:

$$f(r_{ij}) = \begin{cases} 1, & r_{ij} < R_c \\ 0, & r_{ij} > R_c \end{cases} \tag{2.10}$$

where r_{ij} is the distance between atom i and j, and R_c is the cut-off. As an example, the non-bonded interactions, such as Lennard-Jones interaction $V_{LJ}(r_{ij})$ and electrostatic interaction $V_{Elec}(r_{ij})$, between atoms i and j are adjusted to [2]:

$$V_{LJ}(r_{ij}) + V_{Elec}(r_{ij}) = f(r_{ij})\left[4\varepsilon_{ij}\gamma_{ij}^{LJ}\left[\left(\frac{\sigma_{ij}}{r_{ij}}\right)^{12} - \left(\frac{\sigma_{ij}}{r_{ij}}\right)^{6}\right] + \gamma_{ij}^{Elec}\frac{q_i q_j}{4\pi\epsilon_0\epsilon r_{ij}}\right] \tag{2.11}$$

where γ_{ij}^{LJ} and γ_{ij}^{Elec} are scaling factors defined at the beginning of simulations.

The distance between pairs of atoms is examined and only the interaction for the nearby atoms will be calculated. Verlet scheme suggests a fast way to examine the pair separation using the so-called neighboring list. [8] In this scheme, a list is constructed for the neighboring atoms within a distance r_{list} of the atom of interest, where r_{list} is slightly greater than R_c. In the next time step, only the atoms on the list will be examined. The lists are updated during the time evolution, and the frequency to update the list is negatively correlated to the size of the list. [2]

Long-range interactions, such as electrostatic interaction, is subjected to contribution from long-range images in the periodic boxes. [2] The Ewald summation provides a way to integrate the electrostatic interaction in the primitive simulation box and the infinite periodic images. [2] The particle-meshed-Ewald (PME) method further increases the efficiency of calculating the reciprocal sum in Eward summation. In PME method, the charges are assigned to each point on a

grid by interpolation. [2] The reciprocal summation is done by looping over the grid transformed by Fast Fourier Transformation (FFT) algorithm. The PME method is considered to be both accurate and computational efficient.

2.5 Radial Distribution Function

Radial distribution function (RDF) describes the probability of finding particles at certain distance *r* from a reference particle. [3] As shown in Fig. 2.1, the RDF for particle type B (marked in blue) with respect to particle type A (marked in gray) is a function of the distance *r*. The system is divided into spherical shells with thickness of *dr*. If the center of mass of a type B particle is in the shell, it is counted towards the average particle density $\langle \rho_B(r) \rangle$ at distance *r*, as shown in blue filled circles in Fig. 2.1. The RDF *g*(*r*) of particle type B with respect to type A is obtained from the following expression [12]:

$$g_{AB}(r) = \frac{\langle \rho_B(r) \rangle}{\langle \rho_B \rangle_{local}} = \frac{1}{\langle \rho_B \rangle_{local}} \frac{1}{N_A} \sum_{i \in A}^{N_A} \sum_{j \in B}^{N_B} \frac{\delta(r_{ij} - r)}{4\pi r^2 dr} \tag{2.12}$$

where N_A and N_B are the number of type A and type B particles, respectively. The normalization factor $\langle \rho_B \rangle_{local}$ is the density of type B particles averaged over all spherical shells with radius up to r_{max}, which is commonly half of the box length. And r_{ij} is the distance between particle $i \in A$ and $j \in B$. For any pair of particles *i* and *j*, the distribution $\delta(r_{ij} - r)$ of particle *j* in the shell is quantified by:

$$\text{if } r < r_{ij} < (r + dr),\ \delta(r_{ij} - r) = 1 \tag{2.13}$$

which means that if particle *j* was located in the shell with bin width of δr at distance *r* from particle *i*, then the distribution of particle *j* was counted as 1. The shell has a volume of

$$V_{shell} = \frac{4}{3}\pi(r + dr)^3 - \frac{4}{3}\pi r^3 = 4\pi r^2 dr \tag{2.14}$$

Equation 2.12 has two summations: one is the summation over all particles in B around any particle in A; the other summations is over all particles in A.

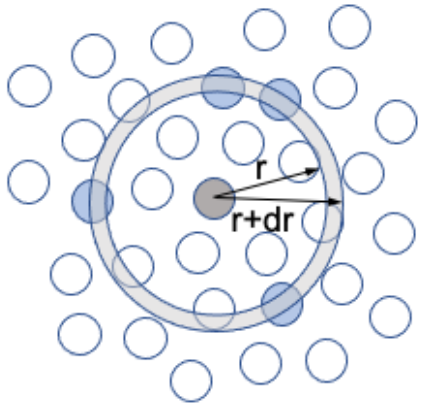

Figure 2.1 Schematic of calculating radial distribution function.

2.6 Free Energy Calculation

Potential of mean force (PMF) calculation is a quantitative way to describe the free energy profile of the system along a reaction coordinate (ξ). In mechanics, a conservative force $\boldsymbol{F}(\xi)$ is equal to the negative gradient of a potential $W(\xi)$, as:

$$\boldsymbol{F}(\xi) = -\nabla W(\xi) \tag{2.15}$$

In the simulation, the potential of mean force can be calculated from the average distribution function $P(\xi)$, expressed as:

$$W(\xi) = W(\xi_0) - \frac{1}{\beta} ln\left[\frac{P(\xi)}{P(\xi_0)}\right] \tag{2.16}$$

where β is $1/k_B T$, ξ_0 is the reference reaction coordinate where $W(\xi_0)$ is defined as zero, $P(\xi_0)$ is the reference value of distribution function.

To calculate PMF in MD simulations, umbrella sampling (US) method has been commonly used to obtain the approximate PMF with a set of histograms over the range of reaction coordination. For an umbrella simulation indexed by *i* in a set of N_w sampling windows, the biasing potential applied on the reaction coordinate is given by [13]:

$$w_i(\xi) = \frac{K_i}{2}\left(\xi - \xi_i\right)^2, \quad (i = 1, \ldots, N_w) \tag{2.17}$$

which represents a harmonic potential restraining the reaction coordinate to position ξ_i with force constant K_i. Adding the biasing potential $w_i(\xi)$ to the system, the biased probability distribution $P_i^b(\xi)$ along ξ is represented by a histogram $h_i(\xi)$ in each umbrella sampling window. The PMF is then calculated by the weighted histogram analysis method (WHAM), in which the unbiased probability distribution $P(\xi)$ is given by

$$P(\xi) = \frac{\sum_{i=1}^{N_w} x_i^{-1} h_i(\xi)}{\sum_{j=1}^{N_w} n_j x_j^{-1} e^{-\beta[w_j(\xi) - f_j]}} \tag{2.18}$$

and

$$e^{-\beta f_j} = \int d\xi e^{-\beta w_j(\xi)} P(\xi) \tag{2.19}$$

where n_j is the number of data points in umbrella sampling window *j;* x_i and x_j are the statistical inefficiency as a function of the autocorrelation time, which can be canceled if the autocorrelation is identical in different umbrella windows; f_j is the free energy constant of an umbrella sampling window *j*. In WHAM, the above two equations are solved iteratively to computes f_j and $P(\xi)$.

References

[1] E.R. Hernández, L.M.M. Zetina, G.T. Vega, M.G. Rocha, L.F.R. Ochoa, R.L. Fernandez, Molecular Dynamics: from basic techniques to applications (A Molecular Dynamics Primer), in: AIP Conference Proceedings, AIP, Mexico City, (Mexico), 2008: pp. 95–123.

[2] H. Kamberaj, Molecular Dynamics Simulations in Statistical Physics: Theory and Applications, Springer International Publishing, Cham, 2020.

[3] C.C.M. Rindt, S.V. Gaastra-Nedea, Modeling thermochemical reactions in thermal energy storage systems, in: Advances in Thermal Energy Storage Systems, Elsevier, 2015: pp. 375–415.

[4] J. Polanski, Chemoinformatics, in: Comprehensive Chemometrics, Elsevier, 2009: pp. 459–506.

[5] H.J.C. Berendsen, D. van der Spoel, R. van Drunen, GROMACS: A Message-Passing Parallel Molecular Dynamics Implementation, Computer Physics Communications. 91 (1995) 43–56.

[6] E. Chow, J.L. Klepeis, C.A. Rendleman, R.O. Dror, D.E. Shaw, 9.6 New Technologies for Molecular Dynamics Simulations, in: Comprehensive Biophysics, Elsevier, 2012: pp. 86–104.

[7] A.R. Leach, A.R. Leach, Molecular Modelling: Principles and Applications, Pearson Education, 2001.

[8] Gustav-Stresemann-Institut e.V. für Übernationale Bildung und Europäische Zusammenarbeit, John von Neumann-Institut für Computing, Johannes Gutenberg-Universität Mainz, Max-Planck-Institut für Biophysikalische Chemie, Max-Planck-Institut für Polymerforschung, eds., Computational soft matter: from synthetic polymers to proteins, NIC, Jülich, 2004.

[9] W.F. van Gunsteren, X. Daura, A.E. Mark, Computation of Free Energy, Helvetica Chimica Acta. 85 (2002) 17.

[10] V. Gapsys, S. Michielssens, J.H. Peters, B.L. de Groot, H. Leonov, Calculation of Binding Free Energies, in: A. Kukol (Ed.), Molecular Modeling of Proteins, Springer New York, New York, NY, 2015: pp. 173–209.

[11] H.J.C. Berendsen, Transport Properties Computed by Linear Response through Weak Coupling to a Bath, in: M. Meyer, V. Pontikis (Eds.), Computer Simulation in Materials Science, Springer Netherlands, Dordrecht, 1991: pp. 139–155.

[12] M. Abraham, D. Van der Spoel, E. Lindahl, B. Hess, the GROMACS development team, GROMACS user manual, version 2016, 2018.

[13] J.S. Hub, B.L. de Groot, D. van der Spoel, g_wham—A Free Weighted Histogram Analysis Implementation Including Robust Error and Autocorrelation Estimates, J. Chem. Theory Comput. 6 (2010) 3713–3720.

Chapter 3. Molecular Simulation of Folding and Aggregation of Multi-Core Polycyclic Aromatic Compounds

3.1 Introduction

Flexible molecules in colloidal systems undergo dynamic motion and conformational changes driven by many non-covalent interactions, such as hydrogen bonding, van der Waals forces, π-π interactions, electrostatic interactions, etc. Internally, different parts of the same molecule can interact forming interesting configurations [1]. One such example is the folding of biomacromolecules such as protein [2–4]. Molecular folding has also been studied in many other applications, including biomedical [5,6], environmental [7,8], food science [9,10], and chemical engineering [11,12]. On the other hand, interactions among different molecules can lead to aggregation and even assembly of ordered structures in colloidal systems, which has found applications in a number of areas [13,14]. In this work we investigate a class of interesting molecules, polycyclic aromatic compounds (PACs), which are susceptible to both intramolecular conformational changes and intermolecular aggregation.

PAC has two subgroups: polycyclic aromatic hydrocarbon which has two or more fused benzene rings with only carbon and hydrogen atoms, and heterocyclic aromatic hydrocarbons which contain heteroatoms [15,16]. A large fraction of PACs exists naturally in coal, oil, wood, tar, etc. [17], while some have been synthesized for nanotechnology applications [18–21]. It is known that PACs tend to stack through intermolecular π−π interactions between their polyaromatic (PA) cores [22,23]. In fact, self-assembly of PACs into columnar superstructures has led to intriguing nanostructures [24–26] that can function as optical and electronic devices [24,27–29]. The PA cores in a PAC can have different sizes and structures, such as acenaphthene, fluoranthene,

pyrene, etc. [15,24] In addition, a PAC can contain one large PA core, or multiple small cores connected by aliphatic linkers. For example, structures of asphaltenes, a component of crude oil, are typically categorized as continental type (single-core) and archipelago type (multi-core). Adamson et al. [30], using tandem mass spectrometry, detected aliphatically-bridged multi-core PACs in sooting flames. Alvariño et al. [25] synthesized metallacycles of PACs with multiple aromatic regions and matched the dimension of cavity to dinuclear receptors, which was of interest for applications such as drug delivery. Pisula et al. [22] studied columnar assembly of disk-like PA cores in electronic applications; by attaching side chains with or without other PA cores, the mobility of charge carrier could be tuned. Mativetsky et al. [31] synthesized self-assembled monolayer of multi-core bridged PACs that could be applied as a new donor-acceptor dyad. While the intermolecular aggregation or self-assembly have been frequently studied for single-core PACs [32–35], much less attention has been paid to multi-core PACs [22,25,30,31]. Furthermore, compared with single-core PACs, multi-core PACs are usually more flexible and susceptible to internal structural changes. This has motived the present study, where we investigate both aggregation and folding, the stacking between the cores within the same molecule, of multi-core PACs.

Studies on the colloidal behaviours of multi-core PACs have been limited. Acevedo et al. [36] calculated the solubility parameter of PACs in 57 organic solvents and found multi-core PACs to be more difficult to aggregate than single-core PACs [36]. To explain, the authors hypothesized that multi-core PACs may have folding and unfolding features due to their rotational degree of freedom at the interconnection between the cores, although no direct evidence was provided [36]. Kuznicki et al. [37] performed molecular dynamics (MD) simulations on a mixture of both single-core and multi-core PACs, dispersed in water, toluene and heptane. The observation of "self-

stacking" was reported for multi-core PACs, similar to the folding proposed by Acevedo et al. [36] Recently, an interesting work by Wang et al. studied the aggregation and folding of multi-core PACs in toluene, n-heptane and their mixtures, using coarse-grained MD simulation and nonlinear machine learning [38]. Folding of these PACs was demonstrated to depend on the molecular structure, for example, extended (unfolded) configuration was energetically favorable for a model with two linearly connected PA cores and a model with three mutually connected PA cores, whereas a model that contained three linearly connected PA cores showed a complex free energy landscape that was concentration dependent [38]. Although different concentrations were simulated, mechanistically how the folding of individual molecules was impacted by aggregation was not addressed.

Based on the state of the literature, the present work investigated the folding of multi-core PACs and for the first time, addressed the relationship between folding and aggregation. Three commonly used solvents: water (polar), heptane (aliphatic) and toluene (aromatic), were applied to examine the potential effect of solvent. In addition, single-core PACs were introduced to study the impact of heteroaggregation on the folding of multi-core PACs. Our work contributed to the fundamental understanding of molecules in a colloidal system which are simultaneously susceptible to intramolecular conformational changes and intermolecular aggregation. The results illustrated the connections between the intra- and intermolecular behaviors, as well as the impact of surrounding environment (i.e., solvent), which may provide insights into the investigation of other complex colloidal systems.

3.2 Method

3.2.1 Models and systems

Two molecular models were constructed to represent multi-core (model archipelago asphaltene) and single-core PACs (model continental asphaltene), respectively, and their chemical structures are shown in Fig. 3.1. The multi-core PAC is a hypothetical model that contains three aromatic cores connected by short aliphatic chains (Fig. 3.1a), which will be hereafter referred to as model "M". The initial structure of model M was drawn in ChemDraw Prime 16.0. The geometry of the entire molecule was optimized using Gaussian16 [39] at B3LYP/3-31G + (d,p) level [40], and then submitted to Automated Topology Builder (ATB) [41,42] to produce the topology compatible with the GROMOS96 [43–45] united-atom force field. The partial atomic charges were calculated using Gaussian16 at B3LYP/6-31G + (d,p) level [46–49] with CHELPG (CHarges from ELectrostatic Potentials using a Grid based method) , and manually assigned to the topology generated from ATB [8,50,51]. This procedure of developing the force field parameters is well-established and used extensively in the literature [40–42,46–49]. The creation of model M originated from a chemical structure proposed by Nexen Energy ULC to represent pentane-insoluble asphaltenes [52,53] in Athabasca bitumen. MD simulations were performed to calculate the density of M molecules in solid state and size of their aggregates in organic solvents, which compared well with experimental study of asphaltene samples (see Appendix A1 for details). However, it should be emphasized that it is not the purpose of the present work to determine the quality of model M in representing asphaltenes, which is still highly debated. Rather, our focus is to investigate its folding and the interplay between folding and aggregation. The single-core PAC (Fig. 3.1b) is based on the compound Violanthrone-79 (VO-79) and will be hereafter referred to as model "S". This model has been simulated in the past and its force field parameters were directly adopted [54,55].

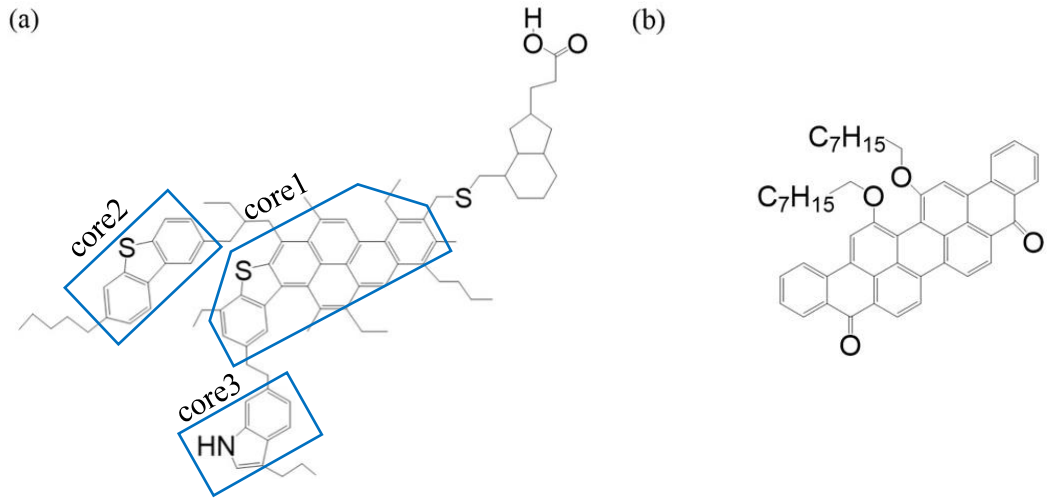

Figure 3.1 Molecular structure of (a) molecule "M"; and (b) molecule "S" (VO-79).

Three types of solvents were selected to study folding and aggregation of PACs in colloidal systems. The first is water since PACs are common water contaminants and their behaviors in aqueous solution are of wide interest [56–58]. The other two are organic solvents, respectively aliphatic (heptane) and aromatic (toluene) in nature. They were chosen because like most of the PACs, the models in Fig. 3.1 contain both aromatic and aliphatic units. In fact, heptane and toluene have both been extensively used as solvents for PACs [59–65]. SPC model was used for water, while force field parameters for heptane and toluene were adopted from previous publications of Lan et al. from our group [54,55].

A single model M molecule was solvated in water, heptane and toluene respectively, which formed systems 1, 2 and 3 as shown in Table 3.1. Solutions containing multiple M molecules were simulated as systems 4, 5 and 6 respectively in water, heptane and toluene. A mixture of M and S molecules were also simulated in water, heptane and toluene (systems 7, 8 and 9).

Table 3.1 Details of simulated systems

sys.	# of M	# of S	solvent	# of solvent molecules	initial box length (nm)
1	1	0	water	7039	6
2	1	0	heptane	1063	6
3	1	0	toluene	1132	6
4	12	0	water	56786	12
5	12	0	heptane	8450	12
6	12	0	toluene	9920	12
7	6	18	water	56542	12
8	6	18	heptane	8500	12
9	6	18	toluene	9793	12

3.2.2 Simulation details

All simulations were performed using GROMACS package [45,66–68] (version 5.0.7) with GROMOS 96 force field 53A6 parameter sets [69]. Each system first underwent a static structure optimization via energy minimization. Then, NVT simulation was carried out for 100 ps where non-hydrogen atoms of the model PAC molecules were restrained by a harmonic potential with constant 1000 kJ/(mol·nm^2). The restraint was removed, and full dynamics simulation was carried out in NpT ensemble at 300 K and 1 bar. The pressure was controlled by Parrinello-Rahman barostat and the temperature was controlled by velocity rescaling thermostat. LINCS algorithm and Particle Mesh Ewald method for full electrostatics [70] were applied. The cut-off for non-bonded (van der Waals and electrostatic) interactions was set to 1.4 nm. Periodic boundary conditions were applied in all directions. All simulations had a time step of 2 fs and simulation time of 60 ns.

3.3 Results and Discussion

3.3.1 Folding of a single M molecule

Systems 1 to 3 examine the conformation changes of a single M molecule in the three solvents. From the root-mean-square deviation (RMSD) of the molecule (Appendix A2), in the last 50 ns, configuration of the single M molecule became relatively stable in water, while the molecule in heptane or toluene underwent more dynamic but reversible conformational changes. Data in the last 50 ns representing dynamic equilibrium were analyzed. Because the interconnecting chains in the M molecule allow for internal degree of freedom, it was observed that sometimes during the simulation trajectory, two aromatic cores within the molecule could approach each other and exhibit stacking or parallel alignment. An example for such a configuration is shown in Fig. 3.2a and b. The aromatic cores may also stay un-stacked, as shown in Fig. 3.2c and d. Dynamic conversion between the two types of configurations, i.e., folding and unfolding of the molecule, was observed.

In order to quantify folding and unfolding, the distance (D) between the centers of geometry (COGs) of core1 and core2 (see Fig. 3.1a for definition) was calculated, along with the angle (θ) between the two cores. As shown in Fig. 3.1a, core1 contains 6 aromatic rings, core2 contains 2 aromatic rings, whereas core3 only has one aromatic ring. It is therefore expected that among the three cores, the interaction between core1 and core2 is the strongest and plays dominant role in folding. This was confirmed by the generally larger distance between core3 and core1 than that between core2 and core1 (see Appendix A3 for details). To calculate D and θ, each core was approximated by a plane defined by three atoms, two carbon atoms shown in cyan and one sulfur shown in yellow in Fig. 3.2. The COG of these three atoms was calculated to represent the COG of each core. θ was calculated as the angle between the positive normal of the two planes. Therefore,

when θ is close to 0 or 180° the two cores are nearly parallel to each other (see Appendix A4 for more details). In Fig. 3.2c-d, D = 1.0 nm and θ = 137°, whereas in Fig. 3.2a-b, D = 0.4 nm and θ = 173°. The reduction in separation along with θ approaching 180° is an indication of stacking between the two cores, i.e., folding of the molecule.

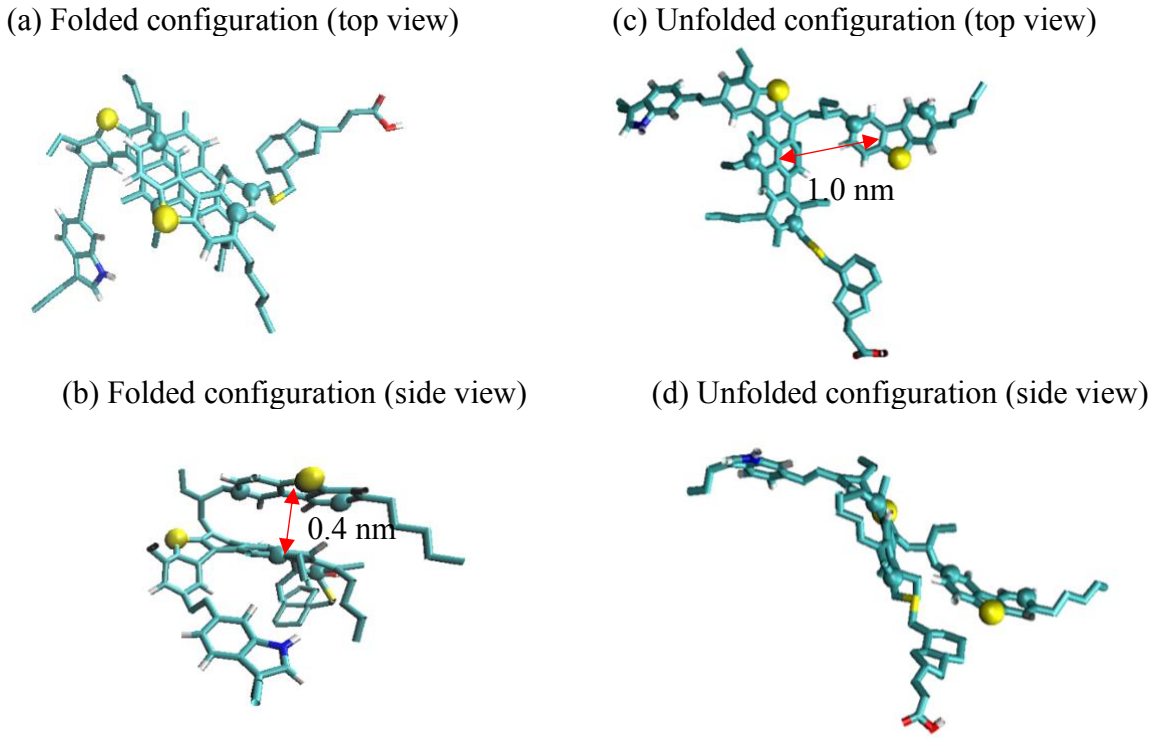

Figure 3.2 Left panel: a representative folded configuration of the M molecule in toluene (a) top view, (b) side view. Right panel: a representative unfolded configuration for the same molecule (c) top view, (d) side view. Distance between core1 and core2 are indicated in (b) and (c), and three atoms defining the plane of each core are highlighted in each subfigure.

D and θ values were collected along the simulation trajectory for the last 50 ns (one data every 10 ps, 5000 data points in total) and plotted against each other in Fig. 3.3. For D, the data naturally separates into groups that are either slightly smaller than 0.55 nm, or greater than 0.55 nm. For θ, separation of data can be observed at around 140°. As stated earlier, angles close to

180° or 0° represent nearly parallel stacking of core1 and core2. Considering symmetry, in this work the molecule will be defined to be in a folded state when $D \leq 0.55$ nm and θ is either <40° or >140°. If $D \leq 0.55$ nm but θ is between 40° and 140°, the two cores have close contact but are not parallel, and we describe the molecule as being in a partially folded state. The molecule is in an unfolded state if $D > 0.55$ nm. Further explanation on using 0.55 nm as the criterion is given in Appendix A5.

In water, Fig. 3.3a shows two distinct bands for the collected data (highlighted by black lines): one with D slightly below 0.75 nm and θ in the range of 20° to 100°, representing the unfolded state; and the other with D slightly below 0.55 nm and θ in the range of 140° to 180°, representing the folded state. There is a clear gap between $\theta = 100°$ and $\theta = 140°$ where few data points exist, suggesting an energy barrier for the transition between folded and unfolded states. Additional evidence for this barrier is shown in Appendix A6 where the molecule stayed in the unfolded state for the first 56 ns, then became folded and stayed in such state for the rest of the simulation. The folded configuration is favored by the π–π interaction between the hydrophobic PA cores, while the unfolded configuration is favored by the release of stress in the linkers connecting the cores as well as the entropy gain from the dissociation of cores. Dynamic motion of the small water molecules also tends to destabilize the folded configuration of a single molecule. Consequently, the M molecule spends the majority of the time in the unfolded state.

In heptane, as shown in Fig. 3.3b, a band near $\theta = 180°$ (highlighted by black line) can be recognized as the molecule being in the folded state. This band is continuous with another band (highlighted by another black line) where D =~0.55 nm and θ is between 50° and 140°, corresponding to partially folded state. There are also considerable amounts of data for the folded

state near $\theta = 0°$. Compared with water, data corresponding to the unfolded state do not form a narrow band. Instead, there is a cloud-like distribution spanning a large range of D (from 0.55 nm to 1 nm). The molecule shows much more flexibility in heptane, which can also be seen from the larger fluctuations in θ (Appendix A6) along the simulation trajectory. Data in toluene (Fig. 3.3c) exhibit similar features as in heptane, except that partial folding of the molecule is almost absent. The lack of partial folding could be caused by the interaction between the aromatic cores of toluene and PA cores on the M molecule, which tends to destabilize a partially folded configuration.

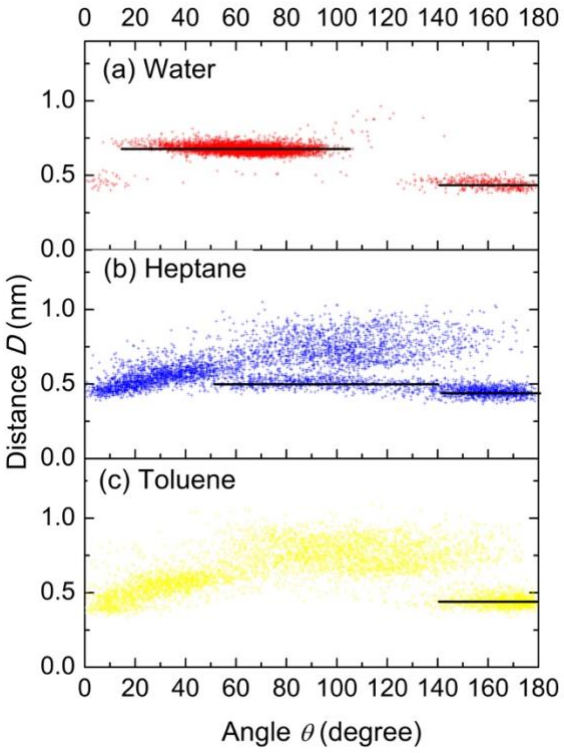

Figure 3.3 Distance D between COGs of core1 and core2 versus angle θ between the two cores. Data are from simulations of a single M molecule in (a) water, (b) heptane and (c) toluene.

Based on the criteria introduced above, the numbers of folded, unfolded and partially folded states were counted from the 5000 frames in the last 50 ns of the simulations, from which

the probability of each state was calculated, as shown in Table 3.2. The free energy change from state 1 to state 2 was then be estimated from [71]:

$$\Delta G = \mathrm{G}(2) - \mathrm{G}(1) = -\mathrm{kTln}[P_2/P_1] \quad (3.1)$$

where k = 1.38×10^{-23} J/K is the Boltzmann constant, T = 300 K is the simulation temperature, P_2 is the probability for one M molecule to be in state 2, and P_1 is the corresponding probability in state 1. Table 3.2 also shows ΔG for the transition from unfolded to partially folded states, and from unfolded to folded states. ΔG in water (system 1) has greater values than those in heptane (system 2) and toluene (system 3), confirming the larger energy barrier for the M molecule to transit from unfolded to folded states in water as discussed in Fig. 3.3.

Table 3.2 Probabilities that one M molecule is in unfolded, partially folded and folded states, as well as the free energy change estimated from the probabilities.

sys.	solvent	probability (%)			free energy change (kJ/mol)	
		unfolded	partially folded	folded	unfolded to partially folded	unfolded to folded
1	water	91.1	0.9	8.0	11.5	6.1
2	heptane	50.5	15.1	34.4	3.0	1.0
3	toluene	61.4	3.1	35.4	7.4	1.4
4	water	27.1	16.7	56.2	1.2	-1.8
5	heptane	58.8	10.0	31.2	4.4	1.6
6	toluene	61.7	14.3	24.0	3.6	2.4
7	water	78.9	2.6	18.5	8.5	3.6
8	heptane	87.4	6.4	6.1	6.5	6.6
9	toluene	65.3	15.7	19.1	3.6	3.1

The above results show that compared with in heptane and toluene, the M molecule is less flexible in water, has lower probability of being in the folded state and is more likely to be "locked" in the unfolded state due to the energy barrier. Acevedo et al. [36] hypothesized that multi-core PAC molecules would unfold in very good solvents due to solute-solvent affinity. The aromatic nature of toluene usually renders itself as a better solvent than water for PAC molecules. However, the M molecule in our simulations exhibited more likelihood to be unfolded in water than in toluene, which seems contradictory to Acevedo et al.'s hypothesis. One reason is that water can interact with the carboxyl group on the M molecule (evidence in Appendix A7) which suppresses folding. More importantly, Acevedo et al. considered a PAC solution, not a single PAC molecule as discussed in this section. The folding behaviors of multiple molecules in a solution will be studied next to reveal the relations between folding, flexibility and solubility.

3.3.2 Folding under homoaggregation

The number of molecules in the largest aggregate for systems with 12 M molecules is shown in Fig. 3.4a, for the last 10 ns of the simulations. The cut-off minimum distance for two molecules to be considered in an aggregate was set to be 0.35 nm (see Appendix A8 for detailed explanation on this criterion). A large stable aggregate containing 6 molecules was formed in water, which did not change its size in the last 10 ns. The size of the largest aggregate in heptane fluctuated between 2 and 4 molecules, with an average of 2.6. In toluene, the largest aggregate had up to 3 molecules (average 1.8) and its fluctuation was more frequent. The solubility of M molecules is clearly lowest in water and slightly higher in toluene than in heptane. Snapshots of the largest aggregate in the three solvents are shown in Fig. 3.4b-d. It should be pointed out that all the 4 molecules in heptane and all the 3 molecules in toluene are shown in the snapshots, although as seen in Fig. 3.4a some of them detached from the largest aggregates during the simulation. The largest aggregate in water

(Fig. 3.4b) had a spherical shape and the carboxyl tails were located at the surface of the aggregate. In heptane (Fig. 3.4c), close contact between carboxyl groups was observed in the aggregate, as highlighted by black circles. In toluene (Fig. 3.4d), the three molecules were considered forming an aggregate based on the minimum distances between them. However, the structure of the aggregate was very loose, and there was no clear evidence for the association of PA cores or carboxyl groups.

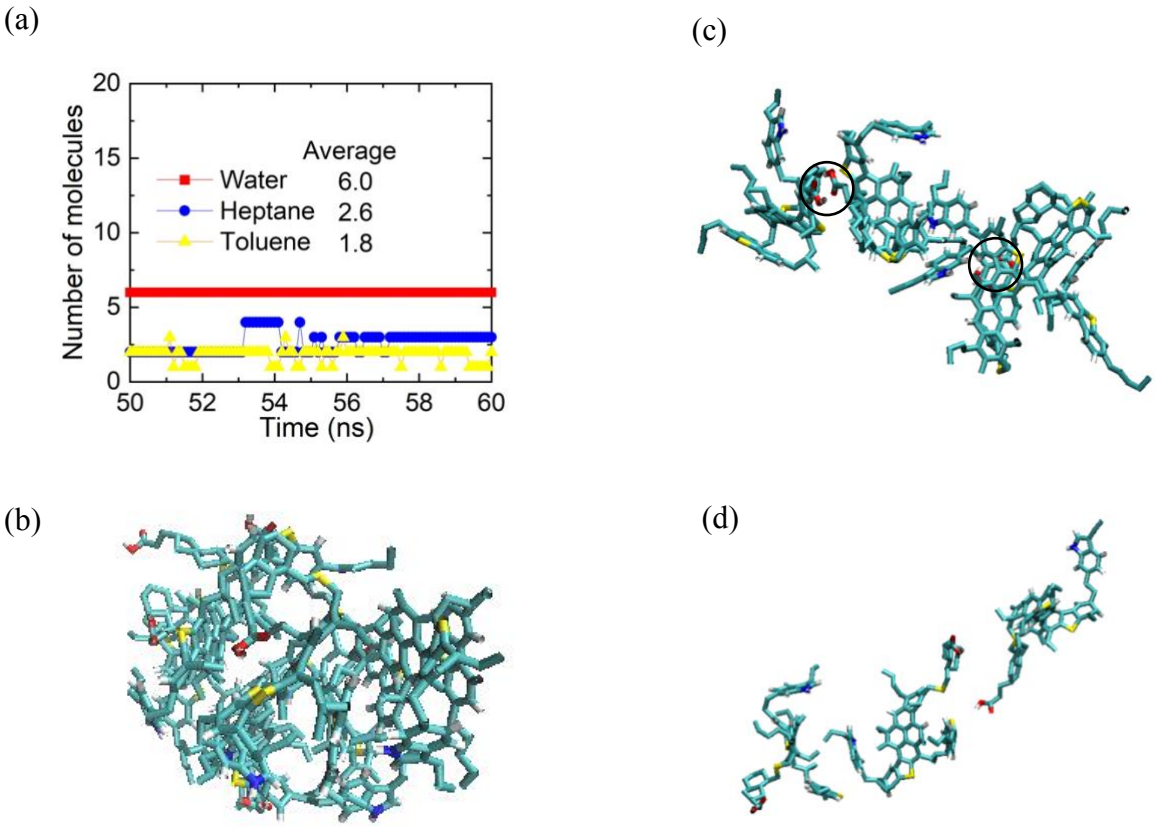

Figure 3.4 (a) Number of molecules in the largest aggregates over the last 10 ns, for systems with 12 M molecules in water, toluene and heptane. Snapshots of the largest aggregate for systems in (b) water, (d) heptane and (d) toluene.

To investigate the roles of PA cores and carboxyl tails in the aggregation, radial distribution functions (RDFs) between PA cores and carboxyl groups are plotted in Fig. 3.5a and 5b respectively. RDFs in Fig. 3.5a were calculated for the COG distance between core1 (see Fig. 3.1a for its definition) of any two M molecules. Compared with core2 which has 2 aromatic rings, core1 contains 6 rings and is dominant in the π−π interaction between two molecules. To obtain the RDFs in Fig. 3.5b, each carboxyl group was represented by the COG of its two oxygen atoms. Results for the system in water are shown as red curve in Fig. 3.5a and b. In Fig. 3.5a, the first and most prominent peak is located at 0.8 nm, which corresponds to a T-shaped stacking where the two cores are nearly perpendicular (see a snapshot in Appendix A9). In water, there is no evidence of association between carboxyl groups as the curve stays close to zero in Fig. 3.5b. This is consistent with the fact that the carboxyl groups were located at the outer surface of the sphere-like aggregate (Fig. 3.4b) with large separation between them. The curve (blue) for heptane in Fig. 3.5a has a distinct peak at ~1.0 nm. Meanwhile the RDF for the carboxyl groups in Fig. 3.5b has its first peak located at a much closer distance (~0.28 nm). The result implies that hydrogen bonding between the carboxyl groups made dominant contribution to the aggregation of M molecules in heptane, whereas the interaction between PA cores was limited at close proximity (see a snapshot in Appendix A9). For toluene (yellow curve in Fig. 3.5a), there is no obvious peak in the RDF of PA cores. There is a peak in the RDF of the carboxyl groups at a similar location (~ 0.28 nm) to heptane, but the peak value is much smaller. The results suggest that the aggregation of the M molecules in toluene is driven mainly by interaction between carboxyl groups. Interaction between cores is weak, and as such the formed structure is looser compared with those in water and heptane, as seen in Fig. 3.4d.

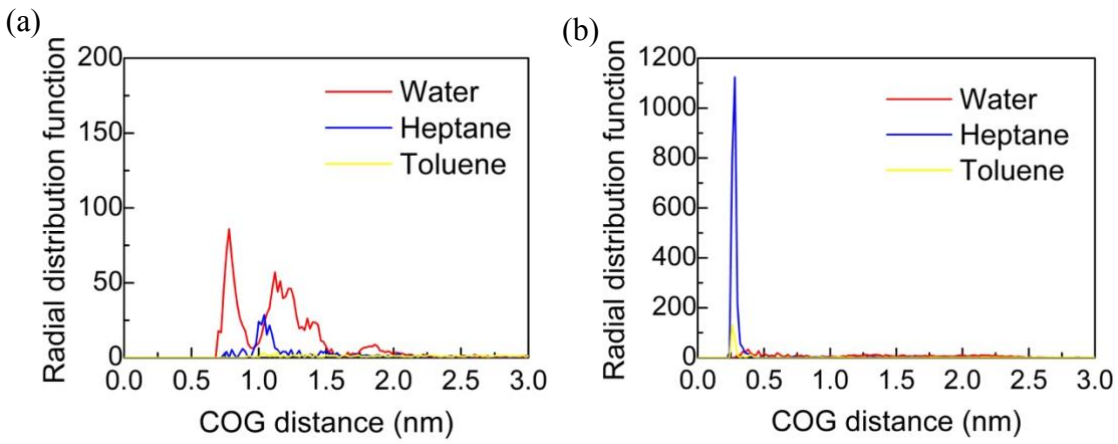

Figure 3.5 (a) RDFs for the COG distance between core1 (see Fig. 3.1a for its definition) of any two M molecules; (b) RDFs for the distance between the carboxyl groups of any two M molecules, where each carboxyl group is represented by the COG of the two oxygen atoms. Data are for systems with 12 M molecules and different curves in each subfigure correspond to different solvents (water, toluene and heptane).

Folding behavior of the molecules in the largest aggregates was investigated and shown in Fig. 3.6. D and θ values were collected along the simulation trajectory for the last 50 ns and plotted against each other. Each subplot corresponds to one molecule. In water, there were 6 molecules in the largest aggregates, labeled as W1 to W6. All 4 molecules in heptane and 3 molecules in toluene shown in Fig. 3.4c-d were analyzed in Fig. 3.6. They were labeled as H1 to H4 in heptane, and T1 to T3 in toluene. Among the 6 molecules in water, W2, W3, W4 were mainly in the folded state, and W6 was mainly in the partially folded state. With all of their D values close to 0.55 nm, these molecules had almost zero probability of being in the unfolded state. On the contrary, W5 was exclusively in the unfolded state. Only W1 exhibited both folded and unfolded states throughout the simulation. ΔG for the transition between states is shown in Table A2 (Appendix A10) for these 6 individual molecules, while the overall ΔG determined from probabilities using data for all 6

molecules is given in Table 3.2. As described in Fig. 3.3, there was an energy barrier for a single M molecule in water to switch between folded and unfolded states. With the presence of multiple molecules, it was still difficult for individual M molecules to overcome this barrier (see Appendix A10 for details), and the transition was lacking for 5 out of the 6 molecules in the largest aggregate. Upon homoaggregation, the internal motions of the molecules within were further restricted, and the molecules were more likely to be "locked" in one of the configuration states. Another interesting observation, from the comparison of Fig. 3.6 with Fig. 3.3, is that when a single M molecule was in water the unfolded state was preferred, while in an aggregate the folded state was dominant. This can also be seen in Table 3.2 where the averaged ΔG from unfolded to folded states is positive for system 1 but negative for system 4. The interactions between the M molecules significantly altered the folding behavior of individual molecules in water. The situation is different in heptane, where the *D*-θ distributions in Fig. 3.6 are similar to those shown in Fig. 3.3 and aggregation did not introduce significant alteration of the folding behaviors. ΔG values in Table 3.2 further confirm this, showing similar magnitude for systems 2 and 5. Influence of aggregation on folding was also small in toluene, but partial folding which was lacking in Fig. 3.3 can now be observed for all the molecules in the largest aggregate. Consequently, system 6 has a smaller ΔG from unfolded to partially folded states compared to system 3, as shown in Table 3.2.

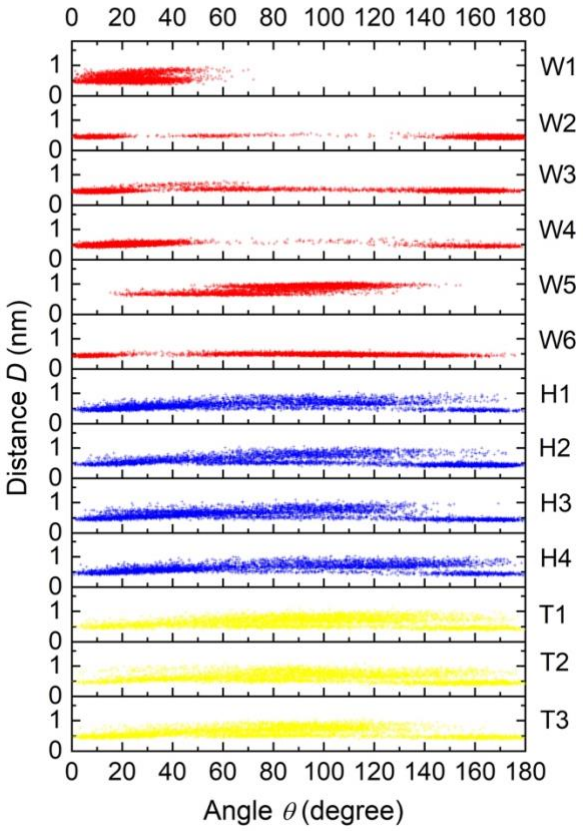

Figure 3.6 Distance between COGs of core1 and core2 versus angle between the two cores. Data are for individual M molecules in the largest aggregate in water (W1~W6), heptane (H1~H4), and toluene (T1~T3).

A closer look at the interactions between polyaromatic cores and between carboxyl groups (Fig. 3.5) allows us to further investigate the relation between homoaggregation and folding. In water, the hydrophobic polyaromatic cores repelled water while interacting strongly within the aggregate (Fig. 3.5a). The tendency to form a compact structure that minimizes core-water interaction and maximizes carboxyl tail-water interaction enhanced folding, changing the dominant configuration from unfolded (for a single molecule) to folded (for molecules in the aggregate). In heptane, the aggregation was achieved mainly through the strong carboxyl-carboxyl

association (Fig. 3.5b). Core-core interactions were not strong enough to have significant contribution to the aggregation. Such interactions left the molecules in the aggregate with sufficient flexibility to switch between the folded and unfolded configurations. In toluene, the core-core interactions were almost absent, and the carboxyl-carboxyl interactions were much weaker than in heptane as seen in Fig. 3.5. Such weak interactions also allowed the molecules to be flexible and easily switch between folded and unfolded states. On the other hand, the presence of interactions between multiple M molecules, although small, could still shield some interaction between M molecules and toluene so that partially folded configurations could be stabilized. As discussed in Section 3.1, a single M molecule unfolded more in water than in toluene, whereas Acevedo et al. [36] hypothesized that multi-core PAC molecules tended to unfold in good solvent. Here we see that when multiple M molecules were present in water, their folding behavior was significantly altered, with folded configuration being dominant. The molecules in toluene did not experience such a change, and more unfolding is now observed in "good" solvent (toluene) than in "bad" solvent (water), consistent with the hypothesis of Acevedo et al. [36]. Our results not only demonstrate the effects of solvent on the folding of multi-core PACs (see Appendix A11 for a comparison to folding of multi-core PACs in vacuum), but also highlight the dependence of such effects on the aggregated state of the PAC molecules.

3.3.3 Folding under heteroaggregation

Since single-core PACs are more prone to aggregation than multi-core PACs, simulations were performed to investigate the effect of adding model S molecules on aggregation, and consequently on the folding of M molecules. Fig. 3.7 shows the number of molecules in the largest aggregate in systems with a mixture of 6 M molecules and 18 S molecules. In water, all the PAC molecules formed a single large aggregate, which was stable in the last 10 ns of the simulation. There were

much more molecules in the largest aggregate in heptane (average 7.1) than in toluene (average 2.5), in agreement with the distinct solubility of single-core PACs in toluene and in heptane [72,73]. Near the end of the simulations, the largest aggregate in heptane contained 1 M and 5 S molecules, while the largest aggregate in toluene contained 1 M and 1 S molecules.

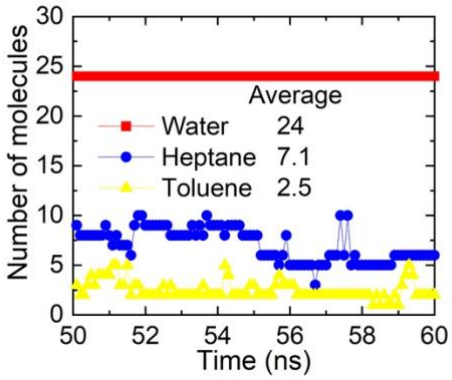

Figure 3.7 Number of molecules in the largest aggregate of systems containing 6 M molecules and 18 S molecules during the last 10 ns.

D-θ distributions for the M molecules in the largest aggregates are plotted in Fig. 3.8. In water, W1 to W3 were mainly in the unfolded state (over 89% probability, see Appendix A10), whereas W4 to W6 had 19.7% to 52.6% of probability to be in the folded states as shown in SI10. The presence of both folded and unfolded states for 3 out of the 6 molecules (W4, W5, W6), as compared to only 1 out of the 6 molecules in Fig. 3.6, suggests that the M molecules in system 7 were more flexible than those in system 4 which contained only M molecules. Normally, higher flexibility and larger conformation change of individual molecules are detrimental to the stability of aggregation. However, the aggregate in water was large and very stable here due to the presence of S molecules, which dictates the dominating role of S molecules in the heteroaggregation. In fact, the folding characteristics of the M molecules was altered by the aggregation driven by S

molecules. Unlike in system 4, the folded state was no longer preferred in system 7, and ΔG from unfolded to folded states was positive as shown in Table 3.2. The S molecules also influenced the behavior of M molecules in heptane. Firstly, the interaction between M molecules was suppressed and there was only one M molecule in the largest aggregate. Secondly, unlike in system 5 where the M molecules had frequent transitions between folded and unfolded states, the M molecule in the largest aggregate in system 8 was almost exclusively in the unfolded state, which had large ΔG values for the transition out of the unfolded state (Table 3.2). The interactions between M and S molecules reduced the flexibility of the M molecule, which favored aggregation. Different from that in water and heptane, when S molecules were introduced to toluene, no significant changes were observed for the folding behavior of the M molecules in the aggregates. ΔG from unfolded state to folded or partially folded states were similar between systems 9 and system 6, as shown in Table 3.2. This can be understood by comparing the degree of homoaggregation (Fig. 3.4) with that of heteroaggregation (Fig. 3.7). While the presence of S molecules significantly changed the degree of aggregation in water and in heptane, their influence on the aggregation in toluene was minor. Our findings therefore underline the significant interplay between aggregation and folding.

While previous studies observed self-stacking of multi-core PACs as they aggregate [36,37], the only in-depth investigation on the intramolecular conformational changes of this type of molecules was provided by Wang et al. [38], where a mechanistic connection between aggregation and folding was still absent. Our work, for the first time, compared the folding behaviors of multi-core PACs in isolation vs. in aggregated states, and addressed the effect of aggregation on folding. Homoaggregation and heteroaggregation had different effects, as well changing the type of solvents led to different folding characteristics within the aggregates, which was not studied in previous literatures.

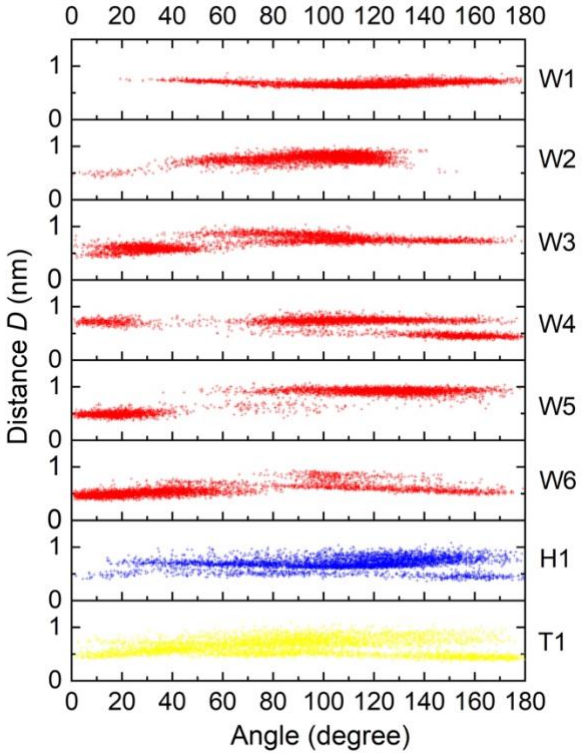

Figure 3.8 Distance between COGs of core1 and core2 versus angle between the two cores. Data are for individual M molecules in the largest aggregate in systems with a mixture of M and S molecules: in water (W1 to W6), in heptane (H1) and in toluene (T1).

3.4 Conclusion

This work investigated the folding and aggregation of multi-core polycyclic aromatic compounds (PAC). Solvent was shown to have a strong influence on the structural flexibility of the multi-core PAC molecules. In water, a single dispersed multi-core PAC molecule had small internal flexibility, evidenced by an energy barrier separating folded and unfolded states. The unfolded configuration was dominant, and the molecule had a high probability of being "locked" in such a state. When several multi-core PAC molecules were in water and aggregated, the folded state replaced the unfolded state to become dominant, due to the tendency to form a compact structure where the

exposure of polyaromatic cores to water was minimized. Introduction of single-core PAC molecules further changed the folding characteristics of multi-core PAC molecules in water due to heteroaggregation. The flexibility of the multi-core PAC molecules was enhanced, and there was more frequent exchange between the folded and unfolded states. In both heptane and toluene, the multi-core PAC molecules were flexible and could easily switch between folded and unfolded states, whether they were dispersed as individual molecules, or in aggregated form. Single-core PAC molecules also altered the folding behavior of multi-core PAC molecules in heptane, making them less flexible, while such effect was not seen in toluene.

References

[1] D.J. Hill, M.J. Mio, R.B. Prince, T.S. Hughes, J.S. Moore, A Field Guide to Foldamers, Chem. Rev. 101 (2001) 3893–4012.

[2] V.P. Jain, C. Maldarelli, R.S. Tu, Modeling the Dynamic Folding and Surface-Activity of a Helical Peptide Adsorbing to a Pendant Bubble Interface, J. Colloid Interface Sci. 331 (2009) 364–370.

[3] A. Steinchen, K. Sefiane, A. Sanfeld, Nano-Encapsulation as High Pressure Devices for Folding–Unfolding Proteins, J. Colloid Interface Sci. 355 (2011) 509–511.

[4] C.M. Dobson, Protein Folding and Misfolding, Nat. Lond. 426 (2003) 884–90.

[5] W. Zhao, W. Chiuman, J.C.F. Lam, S.A. McManus, W. Chen, Y. Cui, R. Pelton, M.A. Brook, Y. Li, DNA Aptamer Folding on Gold Nanoparticles: From Colloid Chemistry to Biosensors, J. Am. Chem. Soc. 130 (2008) 3610–3618.

[6] F.M. Menger, L. Shi, S.A.A. Rizvi, Self-Assembling Systems: Mining a Rich Vein, J. Colloid Interface Sci. 344 (2010) 241–246.

[7] R. von Wandruszka, Humic Acids: Their Detergent Qualities and Potential Uses in Pollution Remediation, Geochem. Trans. 1 (2000) 10.

[8] T. Lan, H. Wang, J. Liao, Y. Yang, Z. Chai, N. Liu, D. Wang, Dynamics of Humic Acid and Its Interaction with Uranyl in the Presence of Hydrophobic Surface Implicated by Molecular Dynamics Simulations, Environ. Sci. Technol. 50 (2016) 11121–11128.

[9] R. Mezzenga, P. Schurtenberger, A. Burbidge, M. Michel, Understanding Foods as Soft Materials, Nat. Mater. 4 (2005) 729–740.

[10] R. Mezzenga, P. Fischer, The Self-Assembly, Aggregation and Phase Transitions of Food Protein Systems in One, Two and Three Dimensions, Rep. Prog. Phys. 76 (2013) 046601.

[11] R.J.B.M. Delahaije, P.A. Wierenga, M.L.F. Giuseppin, H. Gruppen, Improved Emulsion Stability by Succinylation of Patatin is Caused by Partial Unfolding Rather Than Charge Effects, J. Colloid Interface Sci. 430 (2014) 69–77.

[12] E. Sheppard, N. Tcheurekdjian, Monolayer Studies: Iv. Surface Films of Emulsion Latex Particles, J. Colloid Interface Sci. 28 (1968) 481–486.

[13] A. Cornellas, L. Perez, F. Comelles, I. Ribosa, A. Manresa, M.T. Garcia, Self-Aggregation and Antimicrobial Activity of Imidazolium and Pyridinium Based Ionic Liquids in Aqueous Solution, J. Colloid Interface Sci. 355 (2011) 164–171.

[14] M.Y. Lin, H.M. Lindsay, D.A. Weitz, R.C. Ball, R. Klein, P. Meakin, Universality in Colloid Aggregation, Nature. 339 (1989) 360–362.

[15] H.I. Abdel-Shafy, M.S. Mansour, A Review on Polycyclic Aromatic Hydrocarbons: Source, Environmental Impact, Effect on Human Health and Remediation, Egypt. J. Pet. 25 (2016) 107–123.

[16] C. Achten, J.T. Andersson, Overview of Polycyclic Aromatic Compounds (PAC), Polycycl. Aromat. Compd. 35 (2015) 177–186.

[17] D. Zhang, T.K. Ronson, R. Lavendomme, J.R. Nitschke, Selective Separation of Polyaromatic Hydrocarbons by Phase Transfer of Coordination Cages, J. Am. Chem. Soc. 141 (2019) 18949–18953.

[18] V. Rajeshkumar, M. Courté, D. Fichou, M.C. Stuparu, Synthesis and Properties of Large Polycyclic Aromatic Hydrocarbons with Planar and Non-Planar Structural Motifs, Eur. J. Org. Chem. 2016 (2016) 6010–6014.

[19] C. Aumaitre, J.-F. Morin, Polycyclic Aromatic Hydrocarbons as Potential Building Blocks for Organic Solar Cells, Chem. Rec. 19 (2019) 1142–1154.

[20] K. Müllen, J.P. Rabe, Nanographenes as Active Components of Single-Molecule Electronics and How a Scanning Tunneling Microscope Puts Them to Work, Acc. Chem. Res. 41 (2008) 511–520.

[21] J. Wu, W. Pisula, K. Müllen, Graphenes as Potential Material for Electronics, Chem. Rev. 107 (2007) 718–747.

[22] W. Pisula, X. Feng, K. Müllen, Tuning the Columnar Organization of Discotic Polycyclic Aromatic Hydrocarbons, Adv. Mater. 22 (2010) 3634–3649.

[23] G. Wu, C.-Y. Wang, T. Jiao, H. Zhu, F. Huang, H. Li, Controllable Self-Assembly of Macrocycles in Water for Isolating Aromatic Hydrocarbon Isomers, J. Am. Chem. Soc. 140 (2018) 5955–5961.

[24] F.S. Kim, G. Ren, S.A. Jenekhe, One-Dimensional Nanostructures of π-Conjugated Molecular Systems: Assembly, Properties, and Applications from Photovoltaics, Sensors, and Nanophotonics to Nanoelectronics †, Chem. Mater. 23 (2011) 682–732.

[25] C. Alvariño, E. Pía, M.D. García, V. Blanco, A. Fernández, C. Peinador, J.M. Quintela, Dimensional Matching of Polycyclic Aromatics with Rectangular Metallacycles: Insertion Modes Determined by [C-H···π] Interactions, Chem. – Eur. J. 19 (2013) 15329–15335.

[26] Z. Zhang, D.S. Kim, C.-Y. Lin, H. Zhang, A.D. Lammer, V.M. Lynch, I. Popov, O.Š. Miljanić, E.V. Anslyn, J.L. Sessler, Expanded Porphyrin-Anion Supramolecular Assemblies: Environmentally Responsive Sensors for Organic Solvents and Anions, J. Am. Chem. Soc. 137 (2015) 7769–7774.

[27] S. Origuchi, M. Kishimoto, M. Yoshizawa, S. Yoshimoto, A Supramolecular Approach to the Preparation of Nanographene Adlayers Using Water-Soluble Molecular Capsules, Angew. Chem. Int. Ed. 57 (2018) 15481–15485.

[28] A. Narita, X.-Y. Wang, X. Feng, K. Müllen, New Advances in Nanographene Chemistry, Chem. Soc. Rev. 44 (2015) 6616–6643.

[29] D. Wasserfallen, M. Kastler, W. Pisula, W.A. Hofer, Y. Fogel, Z. Wang, K. Müllen, Suppressing Aggregation in a Large Polycyclic Aromatic Hydrocarbon, J. Am. Chem. Soc. 128 (2006) 1334–1339.

[30] B.D. Adamson, S.A. Skeen, M. Ahmed, N. Hansen, Detection of Aliphatically Bridged Multi-Core Polycyclic Aromatic Hydrocarbons in Sooting Flames with Atmospheric-Sampling High-Resolution Tandem Mass Spectrometry, J. Phys. Chem. A. 122 (2018) 9338–9349.

[31] J.M. Mativetsky, M. Kastler, R.C. Savage, D. Gentilini, M. Palma, W. Pisula, K. Müllen, P. Samorì, Self-Assembly of a Donor-Acceptor Dyad Across Multiple Length Scales: Functional Architectures for Organic Electronics, Adv. Funct. Mater. 19 (2009) 2486–2494.

[32] K. Hąc-Wydro, K. Połeć, M. Broniatowski, The Impact of Selected Polycyclic Aromatic Hydrocarbons (pahs) on the Morphology, Stability and Relaxation of Ternary Lipid Monolayers Imitating Soil Bacteria Membrane, J. Mol. Liq. 276 (2019) 409–416.

[33] A. Tirjoo, B. Bayati, H. Rezaei, M. Rahmati, Molecular Dynamics Simulation of the Effect of Ions in Water on the Asphaltene Aggregation, J. Mol. Liq. 277 (2019) 40–48.

[34] J.A. González, M. Zawadzki, U. Domanska, Thermodynamics of Mixtures Containing Polycyclic Aromatic Hydrocarbons, J. Mol. Liq. 143 (2008) 134–140.

[35] H. Jin, W. Ding, B. Chen, B. Bai, Q. Zhao, C. Cao, A Molecular Dynamics Simulation Investigation on the Solubility of Polycyclic Aromatic Hydrocarbons in Supercritical Water, J. Mol. Liq. 301 (2020) 112464.

[36] S. Acevedo, A. Castro, E. Vásquez, F. Marcano, M.A. Ranaudo, Investigation of Physical Chemistry Properties of Asphaltenes Using Solubility Parameters of Asphaltenes and Their Fractions A1 and A2, Energy Fuels. 24 (2010) 5921–5933.

[37] T. Kuznicki, J.H. Masliyah, S. Bhattacharjee, Molecular Dynamics Study of Model Molecules Resembling Asphaltene-Like Structures in Aqueous Organic Solvent Systems, Energy Fuels. 22 (2008) 2379–2389.

[38] J. Wang, M. Gayatri, A.L. Ferguson, Coarse-Grained Molecular Simulation and Nonlinear Manifold Learning of Archipelago Asphaltene Aggregation and Folding, J. Phys. Chem. B. 122 (2018) 6627–6647.

[39] M.J. Frisch, G.W. Trucks, H.B. Schlegel, G.E. Scuseria, M.A. Robb, J.R. Cheeseman, G. Scalmani, V. Barone, G.A. Petersson, H. Nakatsuji, et al., Gaussian 16 Rev. C.01, Wallingford, CT, 2016.

[40] A.B. Andrews, A. McClelland, O. Korkeila, A. Demidov, A. Krummel, O.C. Mullins, Z. Chen, Molecular Orientation of Asphaltenes and PAH Model Compounds in Langmuir−Blodgett Films Using Sum Frequency Generation Spectroscopy, Langmuir. 27 (2011) 6049–6058.

[41] A.K. Malde, L. Zuo, M. Breeze, M. Stroet, D. Poger, P.C. Nair, C. Oostenbrink, A.E. Mark, An Automated Force Field Topology Builder (ATB) and Repository: Version 1.0, J. Chem. Theory Comput. 7 (2011) 4026–4037.

[42] G. Heerdt, I. Tranca, A.J. Markvoort, B.M. Szyja, N.H. Morgon, E.J.M. Hensen, Photoisomerization Induced Scission of Rod-Like Micelles Unravelled with Multiscale Modeling, J. Colloid Interface Sci. 510 (2018) 357–367.

[43] J.A. Lemkul, D.R. Bevan, Assessing the Stability of Alzheimer's Amyloid Protofibrils Using Molecular Dynamics, J. Phys. Chem. B. 114 (2010) 1652–1660.

[44] J.A. Lemkul, W.J. Allen, D.R. Bevan, Practical Considerations for Building GROMOS-Compatible Small-Molecule Topologies, J. Chem. Inf. Model. 50 (2010) 2221–2235.

[45] D.V.D. Spoel, E. Lindahl, B. Hess, G. Groenhof, A.E. Mark, H.J.C. Berendsen, GROMACS: Fast, flexible, and free, J. Comput. Chem. 26 (2005) 1701–1718.

[46] J. Liu, X. Li, W. Jia, Z. Li, Y. Zhao, S. Ren, Demulsification of Crude Oil-in-Water Emulsions Driven by Graphene Oxide Nanosheets, Energy Fuels. 29 (2015) 4644–4653.

[47] C.M. Breneman, K.B. Wiberg, Determining Atom-Centered Monopoles from Molecular Electrostatic Potentials. the Need for High Sampling Density in Formamide Conformational Analysis, J. Comput. Chem. 11 (1990) 361–373.

[48] R.J. Ferreira, M.-J.U. Ferreira, D.J.V.A. dos Santos, Insights on P-Glycoprotein's Efflux Mechanism Obtained by Molecular Dynamics Simulations, J. Chem. Theory Comput. 8 (2012) 1853–1864.

[49] N.E. Jackson, K.L. Kohlstedt, B.M. Savoie, M. Olvera de la Cruz, G.C. Schatz, L.X. Chen, M.A. Ratner, Conformational Order in Aggregates of Conjugated Polymers, J. Am. Chem. Soc. 137 (2015) 6254–6262.

[50] P.R. Arantes, M.D. Polêto, E.B.O. John, C. Pedebos, B.I. Grisci, M. Dorn, H. Verli, Development of GROMOS-Compatible Parameter Set for Simulations of Chalcones and Flavonoids, J. Phys. Chem. B. 123 (2019) 994–1008.

[51] C. Jian, T. Tang, S. Bhattacharjee, Probing the Effect of Side-Chain Length on the Aggregation of a Model Asphaltene Using Molecular Dynamics Simulations, Energy Fuels. 27 (2013) 2057–2067.

[52] J. Dufour, J.A. Calles, J. Marugán, R. Giménez-Aguirre, J.L. Peña, D. Merino-García, Influence of Hydrocarbon Distribution in Crude Oil and Residues on Asphaltene Stability †, Energy Fuels. 24 (2010) 2281–2286.

[53] J.M. Sheremata, M.R. Gray, H.D. Dettman, W.C. McCaffrey, Quantitative Molecular Representation and Sequential Optimization of Athabasca Asphaltenes, Energy Fuels. 18 (2004) 1377–1384.

[54] T. Lan, H. Zeng, T. Tang, Understanding Adsorption of Violanthrone-79 as a Model Asphaltene Compound on Quartz Surface Using Molecular Dynamics Simulations, J. Phys. Chem. C. 122 (2018) 28787–28796.

[55] T. Lan, H. Zeng, T. Tang, Molecular Dynamics Study on the Mechanism of Graphene Oxide to Destabilize Oil/Water Emulsion, J. Phys. Chem. C. 123 (2019) 22989–22999.

[56] X. Zhu, G. Wu, D. Chen, Molecular Dynamics Simulation of Cyclodextrin Aggregation and Extraction of Anthracene from Non-Aqueous Liquid Phase, J. Hazard. Mater. 320 (2016) 169–175.

[57] A. Srivastava, K. Ismail, Solubilization of Polycyclic Aromatic Hydrocarbons in Aqueous Sodium Dioctylsulfosuccinate Solutions, J. Mol. Liq. 195 (2014) 105–109.

[58] C. Wu, A. De Visscher, I.D. Gates, Molecular Interactions Between 1-Butyl-3-Methylimidazolium Tetrafluoroborate and Model Naphthenic Acids: A DFT Study, J. Mol. Liq. 243 (2017) 462–471.

[59] M. Maes, M. Trekels, M. Boulhout, S. Schouteden, F. Vermoortele, L. Alaerts, D. Heurtaux, Y.-K. Seo, Y.K. Hwang, J.-S. Chang, I. Beurroies, R. Denoyel, K. Temst, A. Vantomme, P. Horcajada, C. Serre, D.E. De Vos, Selective Removal of N-Heterocyclic Aromatic Contaminants from Fuels by Lewis Acidic Metal–Organic Frameworks, Angew. Chem. Int. Ed. 50 (2011) 4210–4214.

[60] H. Sharghi, R. Khalifeh, A.R. Salimi Beni, Synthesis of New Lariat Ethers Containing Polycyclic Phenols and Heterocyclic Aromatic Compound on Graphite Surface Via Mannich Reaction, J. Iran. Chem. Soc. 7 (2010) 275–288.

[61] J. Taheri-Shakib, N. Saadati, A. Esfandiarian, S.A. Hosseini, M. Rajabi-Kochi, Characterizing the Wax-Asphaltene Interaction and Surface Morphology Using Analytical Spectroscopy and Microscopy Techniques, J. Mol. Liq. 302 (2020) 112506.

[62] C. Jian, T. Tang, One-Dimensional Self-Assembly of Polyaromatic Compounds Revealed by Molecular Dynamics Simulations, J. Phys. Chem. B. 118 (2014) 12772–12780.

[63] R.N. Nagrimanov, A.A. Samatov, B.N. Solomonov, Additive Scheme of Solvation Enthalpy for Linear, Cyclic and Branched-Chain Aliphatic Compounds at 298.15 K, J. Mol. Liq. 292 (2019) 111365.

[64] R. Dutta Majumdar, T. Montina, O.C. Mullins, M. Gerken, P. Hazendonk, Insights into Asphaltene Aggregate Structure Using Ultrafast MAS Solid-State 1 H NMR Spectroscopy, Fuel. 193 (2017) 359–368.

[65] J. Eyssautier, P. Levitz, D. Espinat, J. Jestin, J. Gummel, I. Grillo, L. Barré, Insight into Asphaltene Nanoaggregate Structure Inferred by Small Angle Neutron and X-Ray Scattering, J. Phys. Chem. B. 115 (2011) 6827–6837.

[66] B. Hess, P-LINCS: A Parallel Linear Constraint Solver for Molecular Simulation, J. Chem. Theory Comput. 4 (2008) 116–122.

[67] E. Lindahl, B. Hess, D. van der Spoel, GROMACS 3.0: A Package for Molecular Simulation and Trajectory Analysis, J. Mol. Model. 7 (2001) 306–317.

[68] H.J.C. Berendsen, D. van der Spoel, R. van Drunen, GROMACS: A Message-Passing Parallel Molecular Dynamics Implementation, Comput. Phys. Commun. 91 (1995) 43–56.

[69] C. Oostenbrink, A. Villa, A.E. Mark, W.F.V. Gunsteren, A Biomolecular Force Field Based on the Free Enthalpy of Hydration and Solvation: The GROMOS Force-Field Parameter Sets 53a5 and 53a6, J. Comput. Chem. 25 (2004) 1656–1676.

[70] U. Essmann, L. Perera, M.L. Berkowitz, T. Darden, H. Lee, L.G. Pedersen, A Smooth Particle Mesh Ewald Method, J. Chem. Phys. 103 (1995) 8577–8593.

[71] W.F. van Gunsteren, X. Daura, A.E. Mark, Computation of Free Energy, Helv. Chim. Acta. 85 (2002) 3113–3129.

[72] C. Jian, T. Tang, Molecular Dynamics Simulations Reveal Inhomogeneity-Enhanced Stacking of Violanthrone-78-Based Polyaromatic Compounds in *n* -Heptane–Toluene Mixtures, J. Phys. Chem. B. 119 (2015) 8660–8668.

[73] Y. Aray, R. Hernández-Bravo, J.G. Parra, J. Rodríguez, D.S. Coll, Exploring the Structure–Solubility Relationship of Asphaltene Models in Toluene, Heptane, and Amphiphiles Using a Molecular Dynamic Atomistic Methodology, J. Phys. Chem. A. 115 (2011) 11495–11507.

Chapter 4. Probing the Effect of Salt on Asphaltene Aggregation in Aqueous Solutions Using Molecular Dynamics Simulations

4.1 Introduction

Asphaltenes are the heaviest components in crude oil. [1] Their aggregation and interfacial activities pose serious problems during oil production, such as changing the wettability of oil reservoir, choking the pore throats, and stabilizing the interface between water and oil. [2–12] Spontaneous aggregation of asphaltenes is mostly studied in toluene, in which asphaltenes are by definition soluble. It was observed that above the critical nanoaggregate concentration (CNAC), on the order of 100 mg/L, nanoaggregates are formed each containing a small number of molecules (<10). At higher concentrations (several g/L), the nanoaggregate can associate into clusters. [13,14] The clusters have various sizes, as small as 6 nm and up to tens of nanometers or more. [15]

The most well-known model that describes the aggregation behavior of asphaltenes is the Yen-Mullins model, [14,16] which considers the continental-type asphaltene that consists of a polycyclic aromatic (PA) core attached with peripheral hydrocarbon chains. [17,18] Supported by many experiments, [13,19] the nanoaggregate in the Yen-Mullins model has a stack of PA cores surrounded by aliphatic side chains. The aggregation is mostly attributed to the π–π interaction between the PA cores, while the side chains exhibit steric repulsion in toluene and hinder the association of PA cores. [20,21] In aqueous solutions, however, the hydrophobic association between side chains becomes another driving force for asphaltene aggregation. [21,22] In the molecular dynamics (MD) simulations by Jian et al., [21] hydrophobic interaction contributed significantly to the aggregation of model compounds with long side chains. By reducing the length of the side chains, the size of the aggregates decreased due to the reduced degree of side chain

association. Only when the side chains were sufficiently small the aggregation could be enhanced again due to the diminishing interference of the side chains with the π-π interaction. The mechanisms of aggregation are therefore largely dependent on the structures of asphaltene molecules and the nature of the solvents.

Salt is another factor that can influence the behaviors of asphaltenes, since water or brine water is widely applied in water-flooding during the recovery process. [23–25] In carbonate reservoirs, the salt in water can reach a concentration as high as 250 000 ppm, [26] which impacts the viscosity of crude oil, interfacial tension between water and oil, and wettability of oil reservoirs. [27] It is therefore important to understand the role of salinity during the oil production processes. Rezaeidoust et al. discovered that the solubility of asphaltene in low salinity water was significantly decreased by increasing salt concentration, [25,28] which could in turn promote the aggregate of asphaltene molecules. They attributed the observation to the salting-out effect, viz., the cations (Na^+, Ca^{2+}) interfered with the water structure around the organic molecules, thus decreasing their solubility. Chaala et al. also found that salt deposits in flooding water promoted the flocculation of asphaltenes. [29] Liu et al. [30] and Zhang, et al. [31] measured the interfacial forces between asphaltene films in aqueous solutions by an atomic force microscope (AFM) and surface forces apparatus (SFA), respectively. The results suggested that the adhesion force between asphaltene films was slightly increased upon the addition of 100 mM KCl [30] or 100 mM NaCl, which was more significantly enhanced upon the addition of 1-100 mM $CaCl_2$ [31]. Previous studies also investigated the effect of salt on the behaviors of asphaltenes adsorbed on water/oil interfaces, since the accumulation of asphaltenes on the interfaces tends to cause a reduction in the interfacial tension (IFT). [32] In the presence of low salinity water, asphaltene accumulation on the water/oil interface is prominent, and several independent works reported a

reduction of IFT. [11,23,33–35] When the salt concentration is sufficiently high (~40,000 ppm), Moeini et al. observed that the IFT started to increase with further addition of salt. This reversed trend was attributed to the salting-out effect, which decreased the solubility of asphaltene in water, increased its solubility in oil, and reduced asphaltene accumulation on the interface. [34]

Despite the above experimental work, mechanistic understanding on the effect of salinity on asphaltene aggregation is not yet completely clear, especially at the molecular level. Such effect is likely dependent on the molecular structure of the asphaltenes, which has not been investigated. Motivated by these, we performed a series of MD simulations to study the aggregation of model asphaltene compounds in water with the presence of salt (NaCl). Below the saturation concentration of NaCl (26% wt. at 20°C), we selected three different concentrations (5% wt., 10% wt. and 15% wt.), in addition to the case of pure water (no salt). Variations in the molecular structures of the model compounds were also studied. This work provides new insights into how salinity impacts the asphaltene aggregation and the interplay between salinity and different moieties (PA core, side chains) on the asphaltenes.

4.2 Simulation Methods

4.2.1 Molecular models

The model asphaltene compounds simulated in this work are based on Violantrone-78 ($C_{70}H_{84}O_6$, VO-78), [36] shown in Fig. 4.1a. It has the typical structure and properties of continental-type asphaltene, containing a polyaromatic core and aliphatic side chains, and has been employed widely as a model compound to study the aggregation behaviour of asphaltenes. [12,21,22,37–40] In order to investigate the effect of molecular structure, three models were constructed in addition to the original VO-78, by varying the side chain length. These models are shown in Fig. 4.1b to d, where the number of carbon atoms in each side chain attached to –COO- is reduced from 16 in

VO-78 to 12, 8 and 4, respectively. The four models will be denoted as VO-16C, VO-12C, VO-8C and VO-4C in this work.

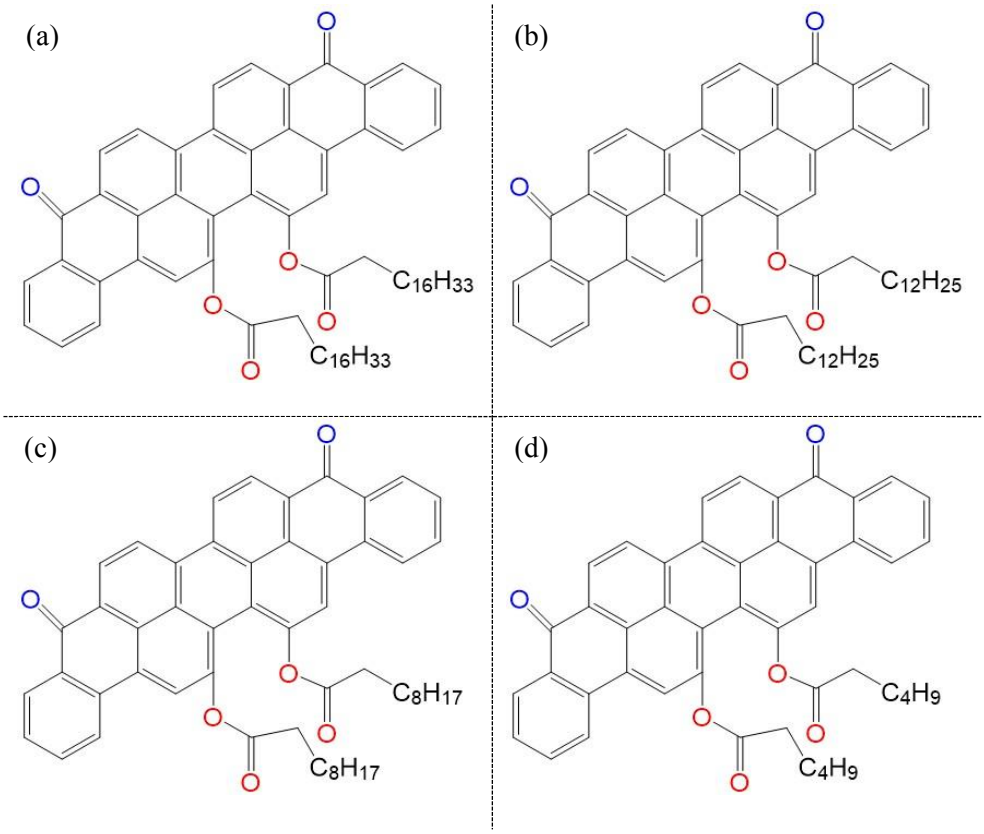

Figure 4.1 Molecular structures of (a) VO-16C, (b) VO-12C, (c) VO-8C and (d) VO-4C. The 2 oxygen atoms bonded to the core are colored blue, and the 4 oxygen atoms on the side chains are colored red.

The molecular structure of VO-16C was generated using the Chem3D Ultra 10.0 software. By manually adjusting the number of carbon atoms on the side chains, the structures of VO-12C, VO-8C and VO-4C were obtained. The coordinate files of each model were submitted to GlycoBioChem PRODRG2 server, [41] which generated the corresponding topology files. The partial charges and charge groups in the topology were manually modified in order to be compatible with the force field GROMOS96 53A6 [42]. Appendix B1 shows the partial atomic

charges of the model compounds, which were proposed and validated in our previous studies [21,22,39,40,43].

4.2.2 Simulation details

In each simulation, 24 molecules of a particular type of model compound were introduced into a cubic box with side length of 12 nm in the form of a 2 × 3 × 4 array. The box was large enough to ensure all solute molecules were at least 1.8 nm from the edge of the box. The box was then filled with simple-point-charge (SPC) water, which has been proven suitable to simulate the interaction between water and asphaltene molecules. [44–46] The concentration of asphaltenes was around 20 g/L so nanoaggregates were expected to be formed.

To investigate the effect of salinity, different amount of NaCl was added to the water box to reach salt concentrations of 5% wt. 10% wt. and 15% wt. respectively. All systems simulated in this work are listed in Table 4.1, where each system is named by the concentration of NaCl and the type of asphaltene models. For example, 5%-4C represents the system with 24 VO-4C molecules in 5% wt. NaCl solution.

Table 4.1 Details of simulated systems.

System	NaCl concentration (mM)	Model compounds
5%-16C	854.5	VO-16C
5%-12C	856.3	VO-12C
5%-8C	858.2	VO-8C
5%-4C	862.2	VO-4C
10%-16C	1755.3	VO-16C
10%-12C	1763.3	VO-12C
10%-8C	1772.1	VO-8C
10%-4C	1777.1	VO-4C
15%-16C	2712.0	VO-16C
15%-12C	2715.6	VO-12C
15%-8C	2731.0	VO-8C
15%-4C	2735.2	VO-4C

MD simulations were performed using the GROMACS (version 5.0.6) package. [47–50] In all simulations, periodic boundary conditions and a time step of 2 fs were used. Long range electrostatics was handled with particle mesh Ewald summation method, [51] while short range non-bonded interactions were calculated with a cutoff distance of 1.4 nm. The SETTLE algorithm was used to constrain all bonds in water molecules and the LINCS algorithm was applied to constrain all bonds of solute molecules. In each simulation, the total potential energy was first minimized by static structure optimization. Then, the solvent molecules were relaxed for 1 ns (300 K, 1 bar) around the solutes whose heavy atoms were restrained with a harmonic potential (coefficient = 1000 kJ/(mol nm^2)). After removing the restraint, an NpT ensemble simulation was performed for 80 ns. Full trajectory was obtained by recording the coordinates every 10 ps.

4.3 Results

In the last 10 ns of the simulation, a large stable aggregate is observed in each of the 12 systems, along with a few smaller aggregates in some systems. The time evolution of number of molecules in the largest aggregates is shown in Fig. B2 (Appendix B2), which remains the same in the last 10 ns. The radial distribution functions (RDFs) for the center of geometry (COG) separation between PA cores are shown in Fig. B3 (Appendix B3). The RDF curves obtained from averages in different 2 ns time windows overlap with each other, which further supports the stability of the aggregates and the attainment of equilibrium. The number of molecules in the largest aggregate quantifies the size of the largest aggregate and the averaged value over last 10 ns is plotted in Fig. 4.2, where data in pure water (0% salt) is adopted from Jian et al. [21] Depending on the length of the side chain, the size of the largest aggregate shows different trend with the salt concentration. Starting with the VO-16C systems, the largest aggregate in 5% salt solution is of the same size as in pure water (all 24 molecules fully aggregated). With further increase of salt, the size decreases to 15 molecules in 10% solution and increases slightly (to 17 molecules) in 15% solution. The trends in the systems containing VO-12C and VO-8C are similar: the largest aggregate is relatively small in pure water (13 and 10 for VO-12C and VO-8C respectively), while the 24 molecules become fully aggregated in 5% and 10% solution; with increase of salt concentration to 15%, the size of the largest aggregate reduces again (to 23 molecules in 15%-12C and 17 molecules in 15%-8C). In the systems containing VO-4C, the aggregate size is 24 in pure water, decreases to 13 with 5% salt addition, increases to 24 again in 10% solution, and finally decreases to 18 at the highest concentration of salt in 15%-4C.

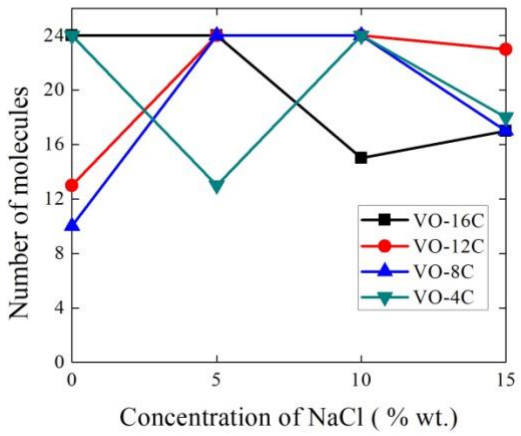

Figure 4.2 Number of molecules in the largest aggregates plotted against % wt of NaCl in the solution. Data for 0% wt salt (i.e. pure water) were adopted from Jian et al. 2013. [21]

It is clear from the results above that the extent of aggregation can have a non-monotonic dependence on the salt concentration, which differs from the monotonic increasing trend reported by Rezaeidoust et al. [28] The dependence is further sensitive to the molecular structure of the solutes, i.e., the different side chain lengths here. In pure water, the full aggregation of VO-16C molecules was attributed to the mutual association of the long side chains caused by hydrophobic interactions, whereas with the short side chains the full aggregation of VO-4C molecules was due to the stacking of PA cores. [21] The smaller degree of aggregation of VO-8C and VO-12C was caused by the interactions between cores and side chains, which interfered with the core-core stacking. [21] To understand the different trends observed in Fig. 4.2 for different molecules, and whether such difference is caused by different forces driving the aggregation, we quantify the interactions between the model asphaltene molecules via their two regions: the PA core and the side chains.

To do so, each molecule was separated into the two regions, and for any two molecules we calculated: 1) the minimum distance (d_{min}) between the two PA cores, 2) d_{min} between the core region of one molecule and the side chain region of the other molecule, and 3) d_{min} between the two side-chain regions. A π-π contact is said to be formed if d_{min} between the two core regions is ≤ 0.5 nm, a θ−θ contact is recorded if d_{min} between the two side chain regions is ≤ 0.5 nm, and a π−θ contact is said to be present if d_{min} between one core region and one side chain region is ≤ 0.5 nm. The criteria of 0.5 nm was chosen because it corresponds to the distance at which the radial distribution function between the centers of geometry of two PA cores shows the first and most prominent peak in pure water. [21] For a pair of molecules, there can be at most one π−π contact and one θ−θ contact. However, two π−θ contacts can potentially be formed: one between the core of molecule 1 and side chains of molecule 2, and the other between the core of molecule 2 and side chains of molecule 1. Consequently, in any system the maximum possible number of π−θ contacts is twice the maximum possible numbers of π−π and θ−θ contacts. To make a fair comparison, the calculated number of π−θ contacts is divided by two to obtain a scaled value.

Counts of π−π, π−θ (scaled) and θ−θ contacts as functions of time are presented in Fig. B4 (Appendix B4). In the last 10 ns, the numbers for all 12 systems become stable, and the average values are plotted in Fig. 4.3. As shown in Figure 4.3a, the number of θ−θ contacts in all 4 systems containing VO-16C is not only 2-3 times the number of π−π contacts, but also much greater than that of π−θ contacts. It is clear that it is the hydrophobic association of the side chains that dominates the aggregation of VO-16C molecules in water. The change of θ−θ contacts with salt concentration also correlates well with the trend of aggregation size shown in Fig. 4.2. Specifically, the number of θ−θ contacts is about the same in pure water and 5% solution, decreases in 10% solution and remains almost the same at 15%. Consistently, Fig. 4.2 also shows the aggregation

size at 10% and 15% to be comparable, which is smaller than the aggregates at 0% and 5% (fully aggregated).

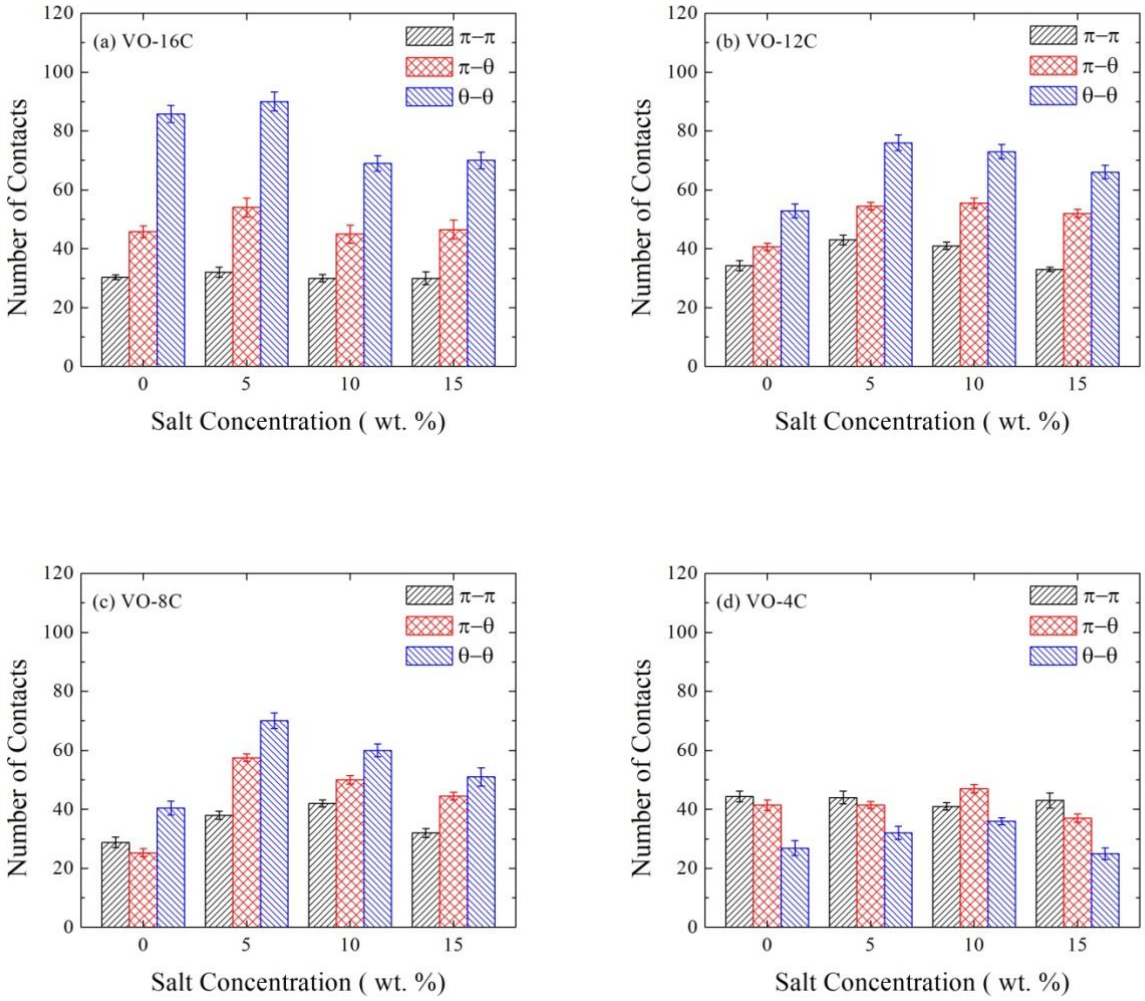

Figure 4.3 Numbers of π−π, π−θ (scaled) and θ−θ contacts averaged over last 10 ns of simulation for the systems containing: (a) VO-16C, (b) VO-12C, (c) VO-8C, (d) VO-4C. Data for 0% salt are adopted from Jian *et al.* 2013. [21]

Compared with VO-16C, in systems containing VO-12C (Fig. 4.3b), the count of θ−θ contacts have reduced due to the length reduction of the side chains. However, it still appears to

be the most important among the three interactions. As the salt concentration increases from 0% to 5%, θ−θ contacts experience a sharp increase; further increase in salt concentration causes it to decrease but very gradually. This again aligns well with results shown in Fig. 4.2, where for systems containing VO-12C, the aggregate increases its size significantly from pure water to 5% solution and becomes fully aggregated, remains fully aggregated at 10% and only decreases slightly at 15%.

Since side chain association plays the most significant role in aggregating VO-16C and VO-12C molecules, the trend observed in Fig. 4.2 for systems containing these two types of molecules can be understood by considering the effect of salt on the aggregation of hydrophobic entities. Zangi *et al.* performed such a study [52] and found that increasing ions with low charge density in a solution promoted the aggregation of hydrophobic particles at low salt concentration but suppressed it at high concentration. Their results were explained by recognizing that the low charge ions behave like co-solutes to the hydrophobic particles at low salt concentration. They increase the aggregation of the hydrophobic particles by withdrawing water from them and adhere to the formed aggregates. When too much salt was introduced, however, the dielectric constant of the solution was significantly decreased, making the hydrophobic particles more soluble in water. The increase of solubility resulted in a reduced tendency for aggregation. That is, there exists a salt concentration at which the salt ions transition from being “co-solute” to being “co-solvent”, and the aggregation of hydrophobic particles is maximized at this transition concentration. Interestingly, the transition concentration was found to depend on the number of hydrophobic particles in the solution. [52] With more hydrophobic particles, the ions became “co-solvent” at a lower concentration, i.e., the transition concentration is smaller.

If we consider each side chain in the model compounds simulated here as a collection of hydrophobic particles (carbon atoms), the aggregation behaviors observed earlier for VO-16C and VO-12C systems can be explained by the findings of Zangi et al. [52] In the systems containing VO-16C, significant reduction in aggregation (Fig. 4.2) as well as in side chain θ−θ interaction (Fig. 4.3a) occurs after the salt concentration is increased beyond 5%. That is, the transition concentration is around 5% for VO-16C. The side chains in VO-12C are shorter, i.e., the hydrophobic carbon atoms in the systems containing VO-12C are fewer than in those containing VO-16C. It can then be hypothesized that the transition salt concentration may be higher in the VO-12C systems. Indeed, the aggregation size for VO-12C (Fig. 4.2) starts decreasing only after reaching 10%. Although the side chain association (θ−θ contact in Fig. 4.3b) shows signs of decreasing from 5% to 10%, the decrease is very limited and almost negligible if standard deviation in the data is taken into account. More noticeable reduction in the θ−θ contact also occurs after 10%.

While the aggregation of VO-16C and VO-12C is mainly governed by side chain association, and the role of salt can be explained by its effect on the aggregation of carbon atoms, it is not the case for the systems containing VO-8C. If we only considered the aggregation of carbon atoms on the side chains, the smaller number of carbon atoms in VO-8C systems would suggest an even higher transition concentration compared with the VO-12C systems (i.e., at least and possibly beyond 10%). However, in Fig. 4.3c we see a clear decreasing trend in the number of θ−θ contacts initiated at 5%. In addition, from Figure 4.3b to Fig. 4.3c we see that the number of θ−θ contacts has further decreased and is comparable to the number of π−θ contacts. The above result implies that the aggregation of VO-8C may also be affected by the interactions involving the core region.

In order to examine the effect of salt addition on the PA cores alone, individual PA cores were created by removing the side chains from the molecules in Fig. 4.1 and MD simulations were carried out on systems containing 6 PA cores in pure water, 5%, 10% and 15% NaCl solutions. The details of the simulations can be found in Appendix B5. Each system was simulated for 20 ns, which became stable in the last 3 ns. As shown in Fig. 4.4a, in pure water a 4-molecules aggregate (shown in dashed square) and a dimer are formed, which are separated without mutual interactions. The aggregate has a very ordered structure, with the 4 PA cores stacking to each other in perfect parallel. In 5% solution as shown in Fig. 4.4b, all 6 PA cores form a single aggregate. Five out of the six PA cores are stacked together in parallel fashion while the last one is perpendicular, i.e., forming a T-stacking. When the salt concentration is increased to 10% (Fig. 4.4c), there are one dimer and one 4-molecular aggregate. However, unlike in Fig. 4.4a, only three PA cores in the aggregate form parallel stacking while the other forms a T-stacking (Fig. 4.4c). In 15% solution (Fig. 4.4d), a large aggregate is formed again with 5 molecules in perfect parallel, along with a single dispersed molecule. Clearly the presence of 10% salt has weakened the ability of the PA cores to form parallel stacking. To quantify parallel stacking, the number of direct parallel stacking (DPS) pairs has been calculated. A DPS between two cores is the configuration in which the distance of their geometry centers is within 0.50 nm and the angle between the two cores is near zero (cosine of the angle greater than 0.90). [21] Fig. 4.5 shows the relationship between the number of DPS pairs and salt concentration, where for the core-only systems minimum number of DPS pairs is found in 10% solution.

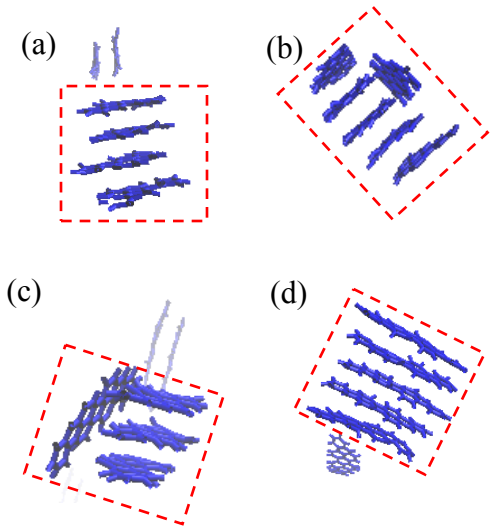

Figure 4.4 Snapshot of 6 polyaromatic cores in (a) pure water, (b) 5%, (c) 10% and (d) 15% NaCl solutions at the end of 20 ns simulations. Largest aggregates are shown in dashed rectangle.

One possible explanation to this non-monotonic dependence of parallel stacking on salt concentration is the interaction between salt ions and the heteroatoms on the PA cores (Oxygen here). It is well known that the parallel stacking of large aromatic moieties is driven by the interaction between positive σ-framework and negative π-electron cloud. [20] The presence of heteroatoms withdraws the π-electron clouds to reduce the π-π electron repulsion, further enhancing the parallel stacking. [53] When salt ions are introduced, they can establish interactions with the heteroatoms. Our analysis on the distribution of Na^+ ions around the model compounds in Fig. B6 (Appendix B6) in fact shows that they interact with the oxygen atoms on the PA cores at short distance while having little interaction with the oxygen atoms in the side chains. The attraction between Na^+ ions and oxygen atoms on the cores can reduce the stacking-enhancing effect of the oxygen atoms and negatively impact parallel stacking of the PA cores. The results in Fig. 4.4 seem to suggest that this influence of the salt is little at 5% salt but becomes noticeable at

10%. With more salt added (15%), the negative impact of salt is diminished again, possibly due to the strong screening of the electric field under such a high concentration, which has reduced the π-π electron repulsion.

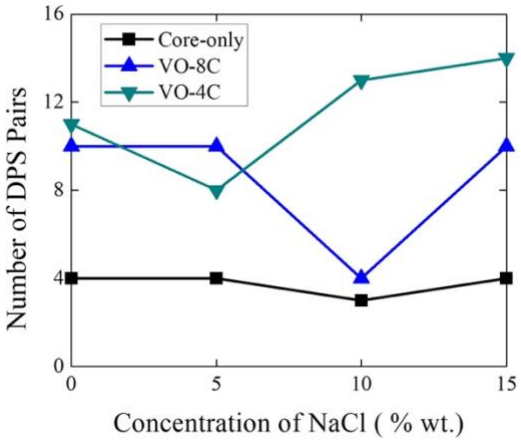

Figure 4.5 Number of direct parallel stacking pairs for the core-only systems and systems containing VO-8C and VO-4C.

Through the above analysis, it has been demonstrated that the addition of salt can promote aggregation by increasing side chain association (up to a "co-solute" to "co-solvent" transition concentration); meanwhile it can reduce aggregation by decreasing parallel stacking of the cores for intermediate concentration. In the systems containing VO-8C, the number of DPS pairs shows the same trend as the core-only systems (Fig. 4.5). Although the effect of salt on hydrophobic association of side chains, if isolated, would have predicted higher intermolecular interactions at 10% than at 5%, the reduced capability of forming parallel stacking at 10% has led to the decrease in the numbers of π−θ and θ−θ contacts as the salt concentration changes from 5% to 10% (Fig. 4.3c). The results also indicate that there are mutual influences of the core-core, chain-chain and

core-chain interactions in VO-8C, because the length of side chains is comparable to the size of the PA core.

Interestingly, the reduced parallel stacking at 10% did not cause the overall π–π contacts to decrease. Instead, the number of π–π contacts in Fig. 4.3c increases as the salt concentration changes from 5% to 10%. The reason for this seemingly contradictory observation is that while the capability of forming parallel stacking is weaker at 10%, T-stacking between cores increases (see Fig. 4.4). T-stacking is able to compensate for the loss of parallel stacking, which leads to the same aggregation size at 10% as the size at 5% (Fig. 4.2). However, the aggregate structures are less compact with T-stacking (as shown in Appendix B7). T-stacking also limits the core-chain and chain-chain interactions at 10%, as shown in Fig. 4.3c.

Finally, in VO-4C systems (Fig. 4.3d), the side chains are so short that the θ–θ interaction becomes the smallest among the three. The aggregation through hydrophobic interaction becomes less dominant. On the other hand, despite the short side chains, the aggregation of VO-4C molecules is not entirely controlled by core-core interaction. In fact, the trend of aggregation size shown in Fig. 4.2 is not the same as that of π–π contacts in Fig. 4.3d. The counting of DPS pairs shows that the smallest number of DPS pairs occurs at 5%, as shown in Fig. 4.5. This is different from the VO-8C systems, as well as the systems without side chains (Fig. 4.5); in both cases the DPS is weakest at 10%. Given that the side chains in VO-4C are the shortest; its behaviors would have been expected to be closest to the model without side chains. The counterintuitive results we observed suggest that the role of the rather short side chains in VO-4C is not negligible in the presence of salt, although the exact mechanism still remains inconclusive and to be further explored. Nevertheless, the smallest DPS at 5% does agree with the smallest aggregation size at 5% for VO-4C (Fig. 4.2), even though the number of π–π contacts (Fig. 4.3d) is not reduced at

5%. T-stacking in this case appears to be incapable of compensating for the loss of DPS, as it did for the VO-8C systems. As for the decreased aggregation size again at 15% (Fig. 4.2), it is similar to the cases of VO-12C and VO-8C and is caused by the significant reduction in of π−θ and θ−θ interactions from 10% to 15% (Fig. 4.3d)), possibly due to the transition of salt from "co-solute" to "co-solvent".

4.4 Discussion

It is worth commenting on our results in comparison to two experimental works that studied the effect of salt on asphaltene accumulation on oil/water interface. Verruto et al. [54] observed that the salt addition delayed the formation and consolidation of asphaltene film at heptol/water interface. Chávez-Miyauchi et al. [55] reported a non-monotonic relationship between the elasticity of asphaltene film on crude oil/water interface and salt concentration. Both works attributed the effect of salt to the screening of electrostatic interactions between asphaltenes. Compared with these studies, the electrostatic interaction in our work is expected to be weaker. Firstly, the model compounds simulated in this work (based on VO-78) are likely to be less polar than real asphaltenes used in the experiments. As shown in Fig. B1 (Appendix B1), the model compounds have partial charges at the oxygen atoms and their neighboring carbon atoms, while the rest of the molecules carry zero or negligible partial charges. Furthermore, the two studies considered oil/water interface, which can be negatively charged and provide a strong electrostatic driving force. Such an interface is absent in our systems. As a result, the electrostatic interaction in our work is weaker and is manifested via the core-core interaction. The added salt interacts with the heteroatoms (oxygen) on the cores, which in turn affects the core-core interaction.

On the other hand, in bulk water the hydrophobic association of side chains provides another mechanism for the aggregation. Rankin et al. [56] studied the interaction between small

hydrocarbon groups (CH_3OH and $C_4H_{10}O$) in water and reported the contact between them to be random rather than hydrophobic. In our work, however, the hydrophobic moieties are much larger. Even VO-4C, with shortest side chain length, contains 5 hydrocarbon groups on each side chain. There is strong evidence of association of side chains, as shown by the stable θ−θ contacts found in the last stage of simulation (Fig. B4 in Appendix B4). Studying modified VO-78 with different side chain lengths has allowed us to address the role of side chain association, and their joint effect with the electrostatic interaction among the cores. There has been a large body of simulation work [57–61] that has provided fundamental understanding of interaction between hydrophobic entities, including quantification of the interaction between two hydrophobic solutes using the potential of mean force (PMF). Similar PMF calculation for our model compounds is of interest but performing constraint MD simulations to obtain the PMF is out of the scope of this work.

Asphaltenes are known to absorb onto oil/water interface and stabilized the oil-in-water or water-in-oil emulsion. Many researchers have reported the accumulation of asphaltene at the oil/water interface in the form of aggregates. [54,55] Molecular arrangement in the aggregates can affect the rheological properties of the asphaltene films, thereby influencing the emulsion stability. The presence of salt can affect the interfacial adsorption of asphaltenes via two ways. Firstly, it can change the amount of asphaltenes accumulation on the interface. For instance, the MD simulation performed by Jian et al. [62] reported that salt addition increased the accumulation of asphaltene onto toluene/water interface. Secondly, the presence of salt can affect the interaction among asphaltene aggregates, thus affect the structure of asphaltene film. [54,55] The model compound (VO-79) simulated by Jian et al. [62] has a similar structure to VO-8C studied in the present work. Our results have shown that the aggregate size of VO-8C has non-monotonic dependence on salt concentration, reaching a maximum at intermediate concentration. One could

then hypothesize that intermediate salt concentration might be most detrimental in terms of stabilizing the emulsion, since it will lead to not only large amount of adsorption, but also large aggregates that form a rigid film. Confirming this hypothesis, however, would require a series of simulations with different salt concentration applied to a water/oil/asphaltene system.

4.5 Conclusions

Using molecular dynamics simulations, we studied the aggregations of 4 types of asphaltene model compounds, VO-16C, VO-12C, VO-8C and VO-4C, in aqueous solution with different NaCl concentrations. Our results, for the first time, revealed complex non-monotonic relationship between the aggregation size and salt concentration. In addition, the four compounds, having the same polyaromatic core but different side chain length, exhibited different dependence on salt addition. Hydrophobic association between side chains are the predominant driving force for aggregation in systems containing VO-16C and VO-12C molecules which have longer side chain length. The change of aggregation size with salt concentration is positively correlated to the effect of salt on hydrophobic interaction: it promotes the hydrophobic interaction at low concentration but suppresses it at high concentration. In systems with VO-8C molecules, which have intermediate side chain length, the aggregation is not only dependent on the hydrophobic association between chains, but also influenced by core-core and core-side chain interactions. In systems containing VO-4C with shortest side chain, while salt addition has a significant effect on the core-core interaction, the short side chains still play a non-negligible role in aggregation with the presence of salt.

References

[1] J.G. Speight, Petroleum Asphaltenes - Part 1: Asphaltenes, Resins and the Structure of Petroleum, Oil & Gas Science and Technology. 59 (2004) 467–477.

[2] M. Fortuny, C.B.Z. Oliveira, R.L.F. V. Melo, M. Nele, R.C.C. Coutinho, A.F. Santos, Effect of Salinity, Temperature, Water Content, and pH on the Microwave Demulsification of Crude Oil Emulsions †, Energy & Fuels. 21 (2007) 1358–1364.

[3] B. Borges, M. Rondón, O. Sereno, J. Asuaje, Breaking of Water-in-Crude-Oil Emulsions. 3. Influence of Salinity and Water−Oil Ratio on Demulsifier Action, Energy & Fuels. 23 (2009) 1568–1574.

[4] E. Byambajav, Y. Ohtsuka, Cracking Behavior of Asphaltene in the Presence of Iron Catalysts Supported on Mesoporous Molecular Sieve with Different Pore Diameters, Fuel. 82 (2003) 1571–1577.

[5] A.Y. Zekri, S.A. Shedid, The Effect of Fracture Characteristics on Reduction of Permeability by Asphaltene Precipitation in Carbonate Formation, Journal of Petroleum Science and Engineering. 42 (2004) 171–182.

[6] N.H.G. Rahmani, T. Dabros, J.H. Masliyah, Evolution of Asphaltene Floc Size Distribution in Organic Solvents Under Shear, Chemical Engineering Science. 59 (2004) 685–697.

[7] J. Sayyad Amin, E. Nikooee, S. Ayatollahi, A. Alamdari, Investigating Wettability Alteration Due to Asphaltene Precipitation: Imprints in Surface Multifractal Characteristics, Applied Surface Science. 256 (2010) 6466–6472.

[8] J.D. Mclean, P.K. Kilpatrick, Effects of Asphaltene Solvency on Stability of Water-in-Crude-Oil Emulsions, Journal of Colloid and Interface Science. 189 (1997) 242–253.

[9] A.L. Nenningsland, B. Gao, S. Simon, J. Sjöblom, Comparative Study of Stabilizing Agents for Water-In-Oil Emulsions, Energy and Fuels. 25 (2011) 5746–5754.

[10] L. Zhang, C. Shi, Q. Lu, Q. Liu, H. Zeng, Probing Molecular Interactions of Asphaltenes in Heptol Using a Surface Forces Apparatus: Implications on Stability of Water-in-Oil Emulsions, Langmuir. 32 (2016) 4886–4895.

[11] C. Shi, L. Zhang, L. Xie, X. Lu, Q. Liu, C.A. Mantilla, F.G.A. Van Den Berg, H. Zeng, Interaction Mechanism of Oil-in-Water Emulsions with Asphaltenes Determined Using Droplet Probe AFM, Langmuir. 32 (2016) 2302–2310.

[12] C. Jian, Q. Liu, H. Zeng, T. Tang, Effect of Model Polycyclic Aromatic Compounds on the Coalescence of Water-in-Oil Emulsion Droplets, The Journal of Physical Chemistry C. 121 (2017) 10382–10391.

[13] L. Barré, J. Jestin, A. Morisset, T. Palermo, S. Simon, Relation between Nanoscale Structure of Asphaltene Aggregates and their Macroscopic Solution Properties, Oil & Gas Science and Technology – Rev. IFP. 64 (2009) 617–628.

[14] O.C. Mullins, H. Sabbah, J. Eyssautier, A.E. Pomerantz, L. Barré, A. B. Andrews, Y. Ruiz-Morales, F. Mostowfi, R. McFarlane, L. Goual, R. Lepkowicz, T. Cooper, J. Orbulescu, R.M. Leblanc, J. Edwards, R.N. Zare, Advances in Asphaltene Science and the Yen–Mullins Model, Energy & Fuels. 26 (2012) 3986–4003.

[15] O.C. Mullins, The Modified Yen Model †, Energy & Fuels. 24 (2010) 2179–2207.

[16] B. Schuler, G. Meyer, D. Peña, O.C. Mullins, L. Gross, Unraveling the Molecular Structures of Asphaltenes by Atomic Force Microscopy, Journal of the American Chemical Society. 137 (2015) 9870–9876.

[17] H. Groenzin, O.C. Mullins, Asphaltene Molecular Size and Structure, The Journal of Physical Chemistry A. 103 (1999) 11237–11245.

[18] H. Groenzin, O.C. Mullins, Molecular Size and Structure of Asphaltenes from Various Sources, Energy. (2000) 677–684.

[19] J. Eyssautier, P. Levitz, D. Espinat, J. Jestin, J. Gummel, I. Grillo, L. Barré, Insight into Asphaltene Nanoaggregate Structure Inferred by Small Angle Neutron and X-Ray Scattering, Journal of Physical Chemistry B. 115 (2011) 6827–6837.

[20] C.A. Hunter, J.K.M. Sanders, The Nature of .pi.-.pi. Interactions, Journal of the American Chemical Society. 112 (1990) 5525–5534.

[21] C. Jian, T. Tang, S. Bhattacharjee, Probing the Effect of Side-Chain Length on the Aggregation of a Model Asphaltene Using Molecular Dynamics Simulations, Energy & Fuels. 27 (2013) 2057–2067.

[22] C. Jian, T. Tang, S. Bhattacharjee, Molecular Dynamics Investigation on the Aggregation of Violanthrone78-Based Model Asphaltenes in Toluene, Energy & Fuels. 28 (2014) 3604–3613.

[23] M. Lashkarbolooki, S. Ayatollahi, M. Riazi, Effect of Salinity, Resin, and Asphaltene on the Surface Properties of Acidic Crude Oil/Smart Water/Rock System, Energy & Fuels. 28 (2014) 6820–6829.

[24] A.Z. Hezave, S. Dorostkar, S. Ayatollahi, M. Nabipour, B. Hemmateenejad, Investigating the Effect Of Ionic Liquid (1-Dodecyl-3-Methylimidazolium Chloride ([C12mim] [Cl])) On The

Water/Oil Interfacial Tension As A Novel Surfactant, Colloids and Surfaces A: Physicochemical and Engineering Aspects. 421 (2013) 63–71.

[25] J.J. Sheng, Critical Review of Low-Salinity Waterflooding, Journal of Petroleum Science and Engineering. 120 (2014) 216–224.

[26] S.F. Shariatpanahi, S. Strand, T. Austad, Initial Wetting Properties of Carbonate Oil Reservoirs: Effect of The Temperature and Presence of Sulfate in Formation Water, Energy and Fuels. 25 (2011) 3021–3028.

[27] M. Lashkarbolooki, S. Ayatollahi, Effect of Asphaltene And Resin on Interfacial Tension of Acidic Crude Oil/ Sulfate Aqueous Solution: Experimental study, Fluid Phase Equilibria. 414 (2016) 149–155.

[28] A. Rezaeidoust, T. Puntervold, S. Strand, T. Austad, Smart Water as Wettability Modifier in Carbonate and Sandstone: A Discussion of Similarities/Differences in The Chemical Mechanisms, Energy and Fuels. 23 (2009) 4479–4485.

[29] A. Chaala, B. Benallal, S. Hachelef, Investigation on the Flocculation of Asphaltenes and the Colloidal Stability of the Crude Oil Fraction, The Canadian Journal of Chemical Engineering. 72 (1994) 1036–1041.

[30] J. Liu, L. Zhang, Z. Xu, J. Masliyah, Colloidal Interactions between Asphaltene Surfaces in Aqueous Solutions, Langmuir. 22 (2006) 1485–1492.

[31] L. Zhang, L. Xie, C. Shi, J. Huang, Q. Liu, H. Zeng, Mechanistic Understanding of Asphaltene Surface Interactions in Aqueous Media, Energy & Fuels. 31 (2017) 3348–3357.

[32] Y. Mikami, Y. Liang, T. Matsuoka, E.S. Boek, Molecular Dynamics Simulations of Asphaltenes at the Oil–Water Interface: From Nanoaggregation to Thin-Film Formation, Energy & Fuels. 27 (2013) 1838–1845.

[33] M. Lashkarbolooki, M. Riazi, S. Ayatollahi, A. Zeinolabedini Hezave, Synergy Effects of Ions, Resin, And Asphaltene On Interfacial Tension of Acidic Crude Oil and Low-High Salinity Brines, Fuel. 165 (2016) 75–85. https://doi.org/10.1016/j.fuel.2015.10.030.

[34] F. Moeini, A. Hemmati-Sarapardeh, M.H. Ghazanfari, M. Masihi, S. Ayatollahi, Toward Mechanistic Understanding of Heavy Crude Oil/Brine Interfacial Tension: The Roles of Salinity, Temperature and Pressure, Fluid Phase Equilibria. 375 (2014) 191–200.

[35] S. Sakthivel, S. Velusamy, V.C. Nair, T. Sharma, J.S. Sangwai, Interfacial Tension of Crude Oil-Water System with Imidazolium and Lactam-Based Ionic Liquids and Their Evaluation for Enhanced Oil Recovery Under High Saline Environment, Fuel. 191 (2017) 239–250.

[36] A.B. Andrews, A. McClelland, O. Korkeila, A. Demidov, A. Krummel, O.C. Mullins, Z. Chen, Molecular Orientation of Asphaltenes and PAH Model Compounds in Langmuir−Blodgett Films Using Sum Frequency Generation Spectroscopy, Langmuir. 27 (2011) 6049–6058.

[37] Manuel F. González, Clementina Sosa Stull, A. Francisco López-Linares, P. Pereira-Almao*, Comparing Asphaltene Adsorption with Model Heavy Molecules over Macroporous Solid Surfaces, Energy & Fuels. 21 (2007) 234–241.

[38] C. Jarne, V.L. Cebolla, L. Membrado, K. Le Mapihan, P. Giusti, High-Performance Thin-Layer Chromatography Using Automated Multiple Development for the Separation of Heavy Petroleum Products According to Their Number of Aromatic Rings, Energy & Fuels. 25 (2011) 4586–4594.

[39] C. Jian, T. Tang, Molecular Dynamics Simulations Reveal Inhomogeneity-Enhanced Stacking of Violanthrone-78-Based Polyaromatic Compounds in n-Heptane-Toluene Mixtures., The Journal of Physical Chemistry. B. 119 (2015) 8660–8.

[40] C. Jian, T. Tang, One-dimensional Self-Assembly of Polyaromatic Compounds Revealed by Molecular Dynamics Simulations, Journal of Physical Chemistry B. 118 (2014) 12772–12780.

[41] A.W. Schüttelkopf, D.M.F. van Aalten, IUCr, *PRODRG* : A Tool for High-Throughput Crystallography of Protein–Ligand Complexes, Acta Crystallographica Section D Biological Crystallography. 60 (2004) 1355–1363.

[42] C. Oostenbrink, A. Villa, A.E. Mark, W.F. Van Gunsteren, A Biomolecular Force Field Based on The Free Enthalpy of Hydration and Solvation: The GROMOS Force-Field Parameter Sets 53A5 and 53A6, Journal of Computational Chemistry. 25 (2004) 1656–1676.

[43] C. Jian, T. Tang, S. Bhattacharjee, A Dimension Map for Molecular Aggregates, Journal of Molecular Graphics and Modelling. 58 (2015) 10–15.

[44] T. Kuznicki, J.H. Masliyah, S. Bhattacharjee, Molecular Dynamics Study of Model Molecules Resembling Asphaltene-Like Structures in Aqueous Organic Solvent Systems, Energy & Fuels. 22 (2008) 2379–2389.

[45] T. Kuznicki, J.H. Masliyah, S. Bhattacharjee, Aggregation and Partitioning of Model Asphaltenes at Toluene−Water Interfaces: Molecular Dynamics Simulations, Energy & Fuels. 23 (2009) 5027–5035.

[46] X. Zhu, D. Chen, G. Wu, Molecular Dynamic Simulation of Asphaltene Co-Aggregation with Humic Acid During Oil Spill, Chemosphere. 138 (2015) 412–421.

[47] B. Hess, P-LINCS: A Parallel Linear Constraint Solver for Molecular Simulation, Journal of Chemical Theory and Computation. 4 (2008) 116–122.

[48] D. Van Der Spoel, E. Lindahl, B. Hess, G. Groenhof, A.E. Mark, H.J.C. Berendsen, GROMACS: Fast, Flexible, and Free, Journal of Computational Chemistry. 26 (2005) 1701–1718.

[49] E. Lindahl, B. Hess, D. van der Spoel, GROMACS 3.0: A Package for Molecular Simulation and Trajectory Analysis, Journal of Molecular Modeling. 7 (2001) 306–317.

[50] H.J.C. Berendsen, D. van der Spoel, R. van Drunen, GROMACS: A Message-Passing Parallel Molecular Dynamics Implementation, Computer Physics Communications. 91 (1995) 43–56.

[51] U. Essmann, L. Perera, M.L. Berkowitz, T. Darden, H. Lee, L.G. Pedersen, A Smooth Particle Mesh Ewald Method, The Journal of Chemical Physics. 103 (1995) 8577–8593.

[52] R. Zangi, B.J. Berne, Aggregation and Dispersion of Small Hydrophobic Particles in Aqueous Electrolyte Solutions, Journal of Physical Chemistry B. 110 (2006) 22736–22741.

[53] M. Sedghi, L. Goual, W. Welch, J. Kubelka, Effect of Asphaltene Structure on Association and Aggregation Using Molecular Dynamics, The Journal of Physical Chemistry B. 117 (2013) 5765–5776.

[54] V.J. Verruto, R.K. Le, P.K. Kilpatrick, Adsorption and Molecular Rearrangement of Amphoteric Species at Oil-Water Interfaces, The Journal of Physical Chemistry B. 113 (2009) 13788–13799.

[55] T.E. Chávez-Miyauchi, A. Firoozabadi, G.G. Fuller, Nonmonotonic Elasticity of the Crude Oil-Brine Interface in Relation to Improved Oil Recovery, Langmuir. 32 (2016) 2192–2198.

[56] B.M. Rankin, D. Ben-Amotz, S.T. Van Der Post, H.J. Bakker, Contacts between Alcohols in Water are Random rather than Hydrophobic, Journal of Physical Chemistry Letters. 6 (2015) 688–692.

[57] N. Choudhury, On the manifestation Of Hydrophobicity at The Nanoscale, Journal of Physical Chemistry B. 112 (2008) 6296–6300.

[58] N. Choudhury, B.M. Pettitt, On the Mechanism of Hydrophobic Association of Nanoscopic Solutes, Journal of the American Chemical Society. 127 (2005) 3556–3567.

[59] N. Choudhury, B.M. Pettitt, The Dewetting Transition and The Hydrophobic Effect, Journal of the American Chemical Society. 129 (2007) 4847–4852.

[60] A. Wallqvist, B.J. Berne, Molecular Dynamics Study of the Dependence of Water Solvation Free Energy on Solute Curvature and Surface Area, J. Phys. Chem. 99 (1995) 2885–2892.

[61] X. Huang, C.J. Margulis, B.J. Berne, Dewetting-induced Collapse of Hydrophobic Particles, Proceedings of the National Academy of Sciences. 100 (2003) 11953–11958.

[62] C. Jian, M.R. Poopari, Q. Liu, N. Zerpa, H. Zeng, T. Tang, Mechanistic Understanding of the Effect of Temperature and Salinity on the Water/Toluene Interfacial Tension, Energy & Fuels. 30 (2016) 10228–10235.

Chapter 5. Effect of Non-ionic Surfactants on the Adsorption of Polycyclic Aromatic Compounds at Water/Oil interface: A Molecular Simulation Study

5.1 Introduction

Understanding the adsorption of surface-active components at liquid/liquid interfaces is essential for many colloidal processes and industrial applications. [1,2] Transportation of surface-active components from one liquid phase to another plays important roles in extraction and separation processes, which involves the important step of interfacial adsorption. [3–5] Interfacially adsorbed molecules with functional groups could form well-organized aggregates, which are suitable as catalysts, biosensors, drug delivery agent, etc. [6–8] Emulsification occurs when the interface between two immiscible liquids (e.g., water and oil) is stabilized by the adsorption of surface-active components. [9] Stable emulsions are desirable in applications such as food, pharmaceutical, and cosmetic industries. [10–14] On the other hand, water/oil emulsification is highly undesirable in petroleum industry because it causes difficulty in oil/water separation, increases the corrosion of equipment and pipelines, and reduces the transportation efficiency. [15–17]

The adsorption of polycyclic aromatic compounds (PACs) on the water/oil interface has attracted wide attention in environmental [18–23] and industrial research [24–27]. PACs, naturally present in fossil fuel, contain polycyclic aromatic hydrocarbon (PAH) core(s) and aliphatic chains, which generally have functional groups with heteroatoms such as sulfur, oxygen and nitrogen. These molecules exhibit amphiphilic and surface-active features and can be adsorbed at the water/oil interface. Consequently, they become organic contaminates and accumulate in soil and ocean as oil spills [18–23]. For example, Zhu et al. [23] studied the co-existence of PAH (anthracene) and cyclodextrin on water/chloroform interface, as a means to extract PAH pollutants

from the oil phase. The cyclodextrin was found to be able to transport spontaneously from water phase to the water/oil interface, indicated by the negative free energy change. The PAH preferred to be included into the cyclodextrin aggregates on the water/oil interface instead of in bulk oil. The same authors [28] reported the co-aggregation of humic acid and PACs at water/toluene interface, and suggested that the co-aggregation increased the retainment of the oil contaminants in aqueous environments. [28] Various non-ionic surfactants have been explored for remediation of PACs from contaminated soil or water [20,21], as they increased the dissolution rate and solubility of PACs in the aqueous phase and promoted the efficiency of groundwater flushing [29].

Beside pollutant treatment, non-ionic surfactants were frequently applied as destabilisers for unwanted emulsions stabilized by PACs. [30] Water and oil emulsification was commonly attributed to the formation of a stable and rigid film of surface-active components at the water/oil interface, [15–17] among which the PACs were a main contributor. The water and oil emulsions include water-in-oil (W-O), oil-in-water (O-W), and more complex cases like water-in-oil-in-water (W-O-W) emulsions, where the W-O emulsion is the predominant type. To break up the W-O emulsion, various non-ionic surfactants have been used for chemical demulsification. [30–32] The experiments of Li et al. [33] studied the demulsification of water-in-aging-crude-oil emulsion by novel tannic acid phenol-amine polyether with multiple branches. They proposed that the hydrophilic branches entered the interior of the water droplets while the hydrophobic parts stayed on the surface, which had the strong interaction with the PACs in the protective film and could partially break up the film. [33] PEO-PPO copolymers, a group of non-ionic surfactants, have been commonly synthesized and used for W-O demulsification processes. [34–37] Their demulsification performance, i.e. the water removal efficiency, was affected by many factors such as the number of copolymer branches [34], molecular weight, PPO/PEO ratio [36], and

concentration [35]. For example, Cendejas et al. [35] attributed the optimal water separation from water-in-crude-oil emulsion at certain concentration of PEO-PPO copolymer to the saturation of polymeric chains at the water/oil interface. The desorption mechanism of PACs from water/xylene interface by PEO-PPO co-polymer, as well as Brij-93, was investigated by Pradilla et al. [38,39] They added the non-ionic surfactants to the water/xylene interface with already adsorbed PACs and carried out interfacial tension measurement to assess the desorption of PACs at the interface. [38,39] The composition of non-ionic surfactants and PACs on the mixed interface was calculated using the Langmuir equation of state. [38,39] At low concentration of non-ionic surfactants (10 ppm for Brij-93 and 0.5 ppm for PPO-PEO co-polymers), interaction between non-ionic surfactants and PACs was detected on the interface, while the PAC desorption was partial or negligible. [38] At 2500 ppm Brij-93 and 100 ppm PPO-PEO co-polymers, the PACs were completely replaced from the interface and had no interaction with the surfactants. [38] The authors proposed that the desorption of PACs was initiated by the interaction between the non-ionic surfactants and PACs, followed by the formation of complex structure between them, and finally the displacement of PACs by the surfactants. [38] While experimental studies frequently attributed the demulsification mechanisms to the interactions of PACs with non-ionic surfactants on the interface, molecular-level evidence of the interactions was difficult to obtain by experimental approach alone.

Theoretical investigations, by the means of molecular simulations, have provided direct observations on the interfacial adsorption and interaction of PACs and surfactants, and contributed to the understanding of demulsification mechanisms. Many studies have been carried out on water/oil interface with solely PACs [40–42] or non-ionic surfactants [2,43]; few works simulated the co-existence of PACs and surfactants. For example, molecular dynamics (MD) simulation was

carried out by Niu et al. [44] on water/xylene interface with adsorbed C5Pe, a model PAC molecule, by adding a PEO-PPO triblock copolymer. The copolymer was found to be more surface active than C5Pe and could form stronger hydrogen bonding with water. [44] The adsorbed copolymers replaced C5Pe molecules and broke up the rigid C5Pe film at the water-xylene interface, which would ultimately assist the coalescence of water droplets. [44]

In spite of experimental and theoretical approaches to understand the demulsification mechanism by non-ionic surfactants, molecular level investigation on the intermolecular interactions between PACs and non-ionic surfactants on the water/oil interface is still in demand. Especially, there is a lack of systematic theoretical investigation on the factors that affect the demulsification process. For example, various non-ionic surfactants have been applied as destabilizers and the demulsification mechanisms can vary greatly. [30,45,46] While many reports studied the popular PEO-PPO copolymers, other non-ionic surfactants have been much less discussed, such as the Brij group which has been compared with PEO-PPO copolymers in experiments [38,39]. Additionally, PACs have complex structures that yield different surface-activity [47]. For example, it was suggested that PACs with moderate polarity could be adsorbed readily at the water/oil interface to stabilize the emulsion, while the stability was reduced when PACs with low or high polarity were adsorbed. [48] Mixtures of PACs were generally used in experimental studies, and there is a lack of comparison between different PAC structures in the demulsification by non-ionic surfactants. Also, the oil phase could be represented by various organic solvents, among which the aromatic solvent (toluene) and aliphatic solvent (heptane) were commonly compared. The emulsion was generally less stable with PACs on water/heptane interface than on water/toluene interface, which was attributed to the change in the aggregation

state of PACs on the interface. [15] It remains unclear how the solvent type would affect the demulsification by non-ionic surfactants at the molecular level.

This work aims to use MD simulations to provide a comprehensive understanding on the effect of non-ionic surfactant on the adsorption of PACs at water/oil interface, by considering several factors, such as PAC architecture, solvent types, structures and concentration of non-ionic surfactants. To achieve this objective, model PAC molecules with a single polyaromatic (PA) core and multiple PA cores were simulated. The effect of solvent types was studied by representing the oil phase with two different organic solvents: one aromatic (toluene) and the other aliphatic (heptane). A model PEO-PPO copolymer, $(EO)_5(PO)_{10}(EO)_5$, was introduced to examine its capability of desorbing the PACs from the oil/water interface. Comparison was made with another widely used non-ionic surfactant from Brij family, Brij-93 [38,39]. Finally, each of the two non-ionic surfactants was applied into the organic phase at two concentrations. The interactions between PACs, non-ionic surfactants and interface were analyzed at the molecular level, to provide mechanistic insights into the stabilization and destabilization of water/oil interfaces.

5.2 Methods

5.2.1 Molecular modelling

Two PAC model molecules were used in this work, one of which had multiple PA cores (model archipelago asphaltene) and the other had a single PA core (model continental asphaltene). The PAC with multiple PA cores, referred to as "PacM", was hypothesized based on C5-insoluble asphaltenes [49,50] from Athabasca bitumen, as shown in Fig. 5.1a. PacM has a molecular weight (MW) of 1303 g/mol and chemical composition as: C 81.12; H 7.97; N 1.07; O 2.46; S 7.38 (%wt.). There are six heteroatoms including 2 oxygen atoms, 3 sulfur atoms and 1 nitrogen atom. The other PAC with a single PA core, Violenthrane-79 (VO-79), has been extensively studied [51,52]

and is referred to as "PacS" in this work. PacS has a chemical formula of $C_{50}H_{48}O_4$ with MW of 712 g/mol, as shown in Fig. 5.1b. One of the non-ionic surfactants used was polyethylene glycol oleyl ether $C_{22}H_{44}O_3$ (Brij-93) with average MW of 357 g/mol (Fig. 5.1c), which is referred to as NisB in this work. The other model non-ionic surfactant simulated was $(EO)_5(PO)_{10}(EO)_5$ (referred to as NisP, MW: 1039 g/mol), a typical triblock copolymer with equal number of EO and PO branches as shown in Fig. 5.1d.

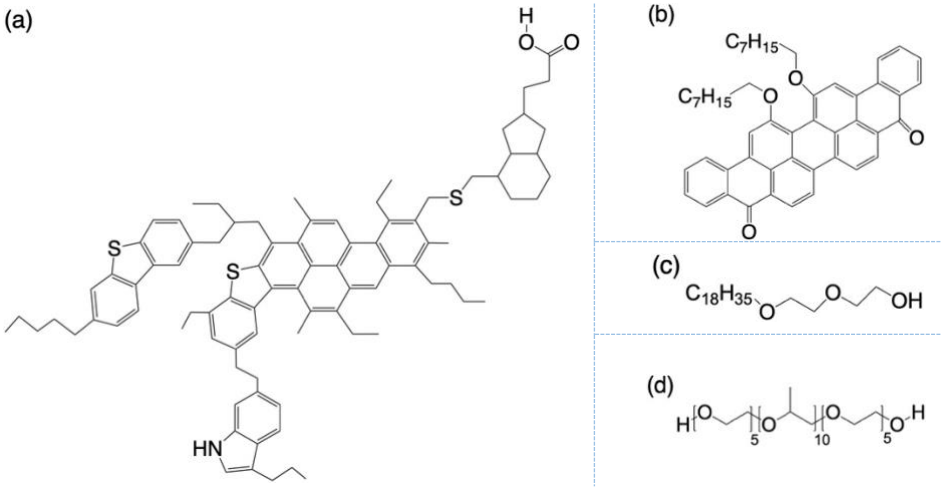

Figure 5.1 Molecular structures of (a) PacM (archipelago model asphaltene), (b) PacS (VO-79), (c) NisB (Brij-93), and (d) NisP ($(EO)_5(PO)_{10}(EO)_5$).

Initial chemical structure of PacM was drawn in ChemDraw Prime 16.0. Geometry optimization of PacM was first performed by density functional theory (DFT) calculation at B3LYP/6-31G + (d,p) level [53]. The obtained geometry was further optimized using Automated Topology Builder (ATB) [54], in order to generate force field parameters compatible with the GROMOS96 parameter sets [55]. The partial atomic charges were determined from the electrostatic potential calculated at B3LYP /6-31G + (d,p) level, with the CHELPG (CHarges from ELectrostatic Potentials using a Grid based method) [56] method. The partial charges were then manually mapped to the topology generated from ATB. The parameters for NisB and NisP were

obtained following the same procedure. All quantum-chemical calculations were carried out using the Gaussian 16 software package [57]. Models for PacS, toluene and heptane were adopted from previous publications in our group [58]; the parameterization steps were identical except the use of def2-SV(P) basis set. Single point charge (SPC) model was used for water molecules, which has been extensively applied and validated. [59] The density of pure PACs (PacM, PacS) and non-ionic surfactants (NisB, NisP) were further validated against the experimental data in the literature, as explained in Appendix C1.

5.2.2 Simulated systems

A total of 20 systems were simulated, with details given in Table 5.1. The name of each system starts with a letter of T or H, corresponding to toluene and heptane being the organic solvent (oil phase), respectively. The second letter indicates the type of PAC molecules: M for PacM and S for PacS. The non-ionic surfactants, NisB and NisP, are labeled as B and P after the type of PACs. The label is finally followed by "low" or "high", which corresponds to relatively low and high concentrations of the surfactants. Sys. 1, 6, 11 and 16 do not contain any non-ionic surfactants and are used as control systems. Each system contained 32 PAC molecules. In the system with PacM and a low concentration of NisB, 32 NisB molecules were introduced, leading to the same molar concentration between NisB and PacM. A high concentration of NisB corresponded to 124 NisB molecules, which had a mass concentration comparable to PacM. The number of NisP molecules were also decided to render comparable molar (low concentration) or mass (high concentration) ratios between NisP and PacM. The same number of non-ionic surfactants were added to systems containing PacS.

Table 5.1 Details of simulated systems. (sys. 1 TM, sys. 6 HM, sys. 11 TS, and sys. HS are control systems without adding non-ionic surfactants)

Sys.	Name	Solvent	no. of PacM	no. of PacS	no. of NisB	no. of NisP	Molar ratio (PAC/NIS)	Mass ratio (PAC/NIS)
1	TM	Toluene	32	-	-	-	-	
2	TM-B-low	Toluene	32	-	32	-	1:1	1:0.27
3	TM-B-high	Toluene	32	-	128	-	1:4	1:1.1
4	TM-P-low	Toluene	32	-	-	24	1:0.75	1:0.6
5	TM-P-high	Toluene	32	-	-	48	1:1.5	1:1.2
6	HM	Heptane	32	-	-	-		
7	HM-B-low	Heptane	32	-	32	-	1:1	1:0.27
8	HM-B-high	Heptane	32	-	128	-	1:4	1:1.1
9	HM-P-low	Heptane	32	-	-	24	1:0.75	1:0.6
10	HM-P-high	Heptane	32	-	-	48	1:1.5	1:1.2
11	TS	Toluene	-	32	-	-		
12	TS-B-low	Toluene	-	32	32	-	1:1	1:0.5
13	TS-B-high	Toluene	-	32	128	-	1:4	1:2
14	TS-P-low	Toluene	-	32	-	24	1:0.75	1:1.1
15	TS-P-high	Toluene	-	32	-	48	1:1.5	1:2.2
16	HS	Heptane	-	32	-	-		
17	HS-B-low	Heptane	-	32	32	-	1:1	1:0.5
18	HS-B-high	Heptane	-	32	128	-	1:4	1:2
19	HS-P-low	Heptane	-	32	-	24	1:0.75	1:1.1
20	HS-P-high	Heptane	-	32	-	48	1:1.5	1:2.2

5.2.3 Simulation details

To construct the initial configuration for the control systems, a box with dimension of 12×12×12 nm^3 was filled with water [60]. As shown in Fig. 5.2a, the box was then extended in z direction to

24 nm, where the PacM/S were aligned in an array of 4×4×2 next to the water box. The extended box containing PacM/S molecules was then filled by organic solvent (toluene or heptane), which formed the initial configuration for the control systems, as shown in Fig. 5.2b. After equilibration, the final configuration of PacM/S adsorbed at the interface was obtained, as shown in Fig. 5.2c. This was used to construct the initial configuration for systems with non-ionic surfactants (NisB/P) by the following steps in Fig. 5.2: removing the solvent (Fig. 5.2d), adding NisB/P (Fig. 5.2e), and filling the right side of the simulation box with organic solvent (Fig. 5.2f).

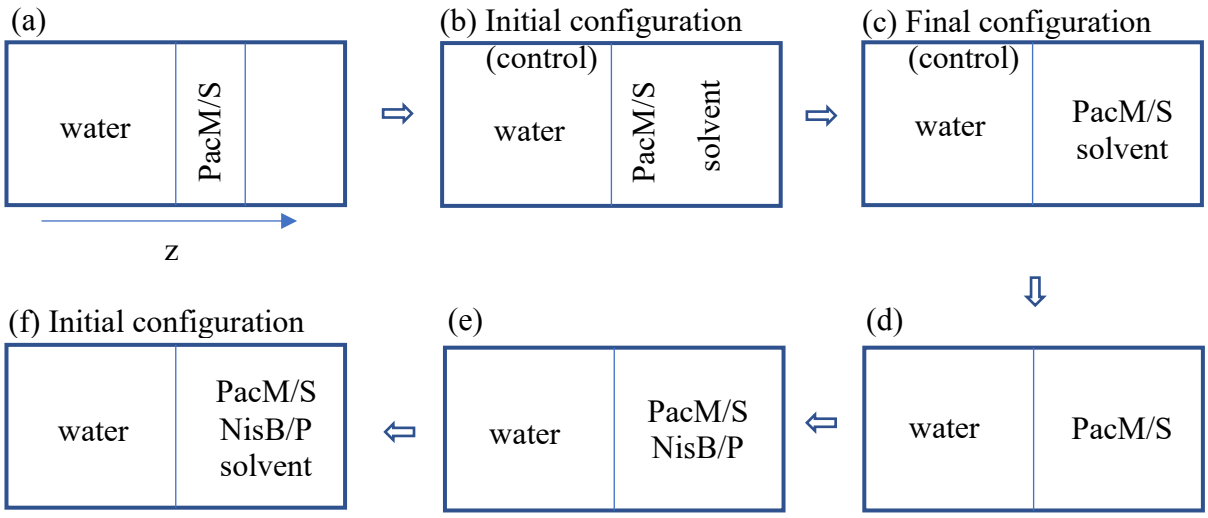

Figure 5.2 Schematic representation of the construction of initial configurations.

All simulations were performed by using GROMACS package [61–63] (version 5.0.7) with GROMOS 96 force field parameter set 53A6 [64]. Each simulation underwent an energy minimization process for static structure optimization. Then, a short *NVT* simulation was carried out with position-restraints on the non-hydrogen atoms of PAC, using a harmonic potential of force constant 1000 kJ/(mol·nm^2). The restraint was removed, and full dynamics simulation was carried out in NpT ensemble at 300 K and 1 bar. The pressure was controlled by isotropic Parrinello-

Rahman barostat with time constant τ_p of 1 ps and compressibility of 4.5×10^{-5} bar^{-1}. The temperature was controlled by velocity rescaling thermostat with time constant τ_T of 0.1 ps. For each simulation, LINCS [65] algorithm and Particle Mesh Ewald method for full electrostatics [66] were applied. The cut-off for non-bonded (van der Waals and electrostatic) interactions was set to 1.4 nm. Periodic boundary conditions in all three directions were applied. All simulations had a time step of 2 fs, and the total simulation time was 60 ns for each system, except sys. 1 which was simulated for 120 ns.

5.3 Results and Discussion

5.3.1 Adsorption and desorption of PacM

Control systems with PacM on water/toluene (sys. 1) and water/heptane (sys. 6) interfaces were simulated before adding the non-ionic surfactants. Density profiles of water, organic solvent and PacM are shown in Fig. 5.3a and b, respectively for sys. 1 and 6, with final configurations of the systems above the plot. The density profiles were averaged over the last 5 ns when the adsorption of PACs was stable, as shown in Appendix C2. Compared with Fig. 5.2, the simulation boxes in Fig. 5.3 were each translated by 6 nm along -z direction, in order to better show the interfaces between water and organic solvent. For the rest of this paper and in the SI, the same translation was applied to all figures containing snapshots and density profiles. Due to the periodic boundary condition, each system had two interfaces, obtained from the intersection of the density profiles for water and toluene (or heptane), which were marked by blue arrows. The left interface was located at z = ~6 nm, referred to as interface-L. The right interface, referred to as interface-R, was located around 18 nm for sys. 1 and 11, and around 20 nm for sys. 6 and sys. 16. The density profile of PacM in each system had two peaks each near one of the interfaces, indicating the adsorption of PacM molecules. Also shown in Fig. 5.3a, PacM had non-zero density in the bulk

toluene phase, consistent with the snapshot where many PacM molecules were dispersed in bulk toluene. On the contrary, in Fig. 5.3b the density of PacM was close to zero in bulk heptane, and the vast majority of the PacM molecules were located close to the interfaces.

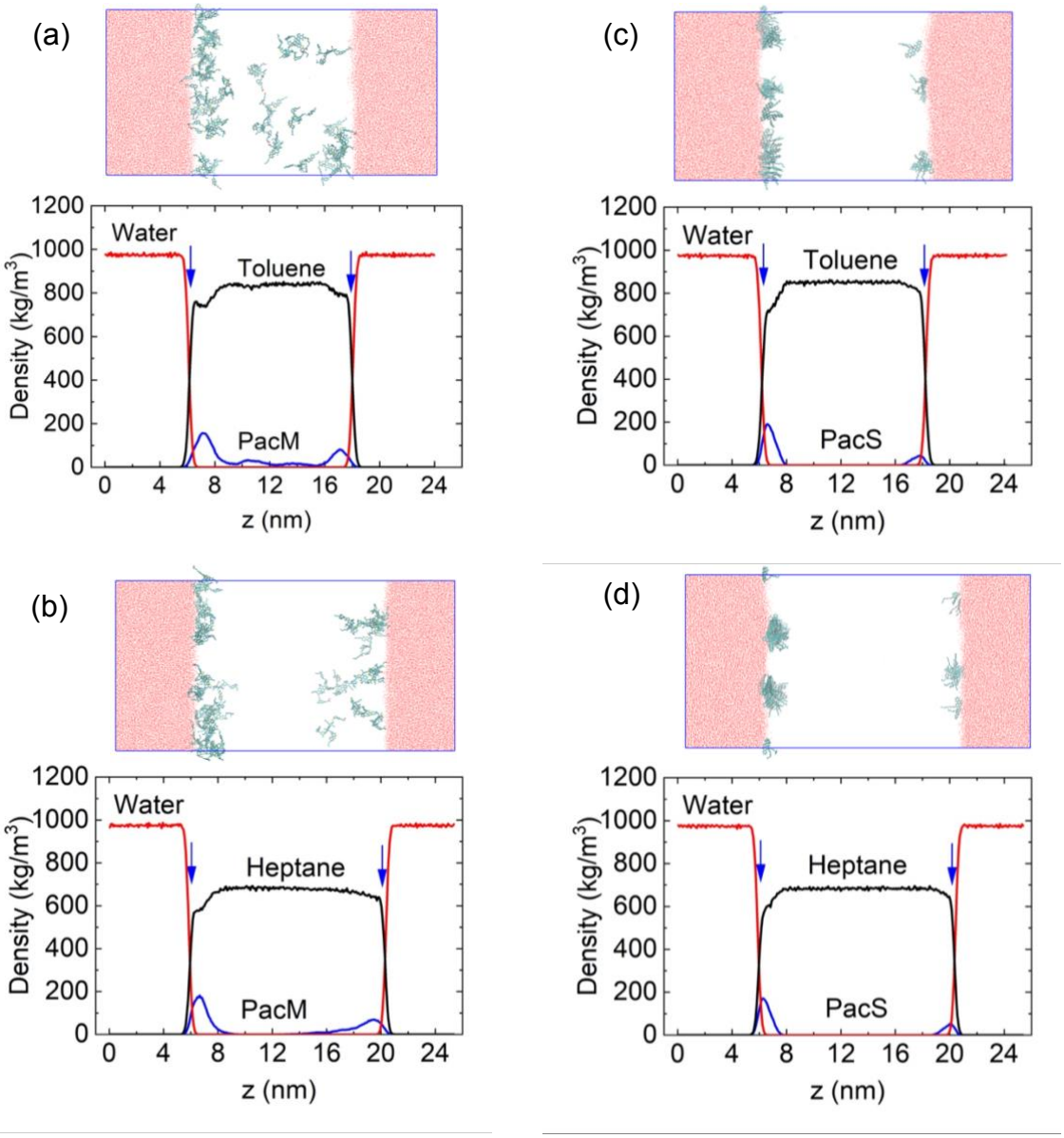

Figure 5.3 Density profiles of water, toluene or heptane, and PacM or PacS, averaged over the last 5 ns of the simulations for the control systems without non-ionic surfactants (a) sys. 1 (water/toluene with PacM); (b) sys. 6 (water/heptane with PacM); (c) sys. 11 (water/toluene with

PacS); (d) sys. 16 (water/heptane with PacS). Above each subfigure is the snapshot of final configuration for the corresponding system (water molecules shown in red; heptane or toluene molecules removed for clarity; PacM or PacS molecules shown in cyan).

The number of adsorbed PAC molecules was quantified by the criterion that the minimum distance between PAC and the water phase was below 0.35 nm, as explained in Appendix C3. For all systems involving PacM molecules (sys. 1 to 10), the number of adsorbed PacM were stable over the last 5 ns of the simulations (see Appendix C4) and the averages are plotted in Fig. 5.4 (one decimal of the average value was kept). On the water/toluene interface, without non-ionic surfactants (sys. 1, shown as "None" in black symbol), the average number of adsorbed PacM molecules was 22.8. By adding NisB, the number of adsorbed PacM decreased to 18.2 at both low and high concentrations, indicating that the effect of NisB concentration was negligible. Adding NisP also resulted in a reduction of adsorbed PacM at water/toluene interface, but the effect of concentration was more significant. Lower concentration of NisP resulted in more desorption of the PacM, with 16.8 PacM remaining adsorbed as compared to 19.9 at high NisP concentration. On the water/heptane interface, as shown in Fig. 5.4 by red symbols, adding NisB reduced the number of adsorbed PacM molecules from 25.5 to 23.9 at lower concentration and to 23.6 at higher concentration. The difference caused by different NisB concentrations was again negligible. Interestingly, more PacM became adsorbed at the water/heptane interface with the addition of NisP, where lower concentration of NisP led to 26.2 adsorbed molecules and higher NisP concentration further increased the number to 28.5.

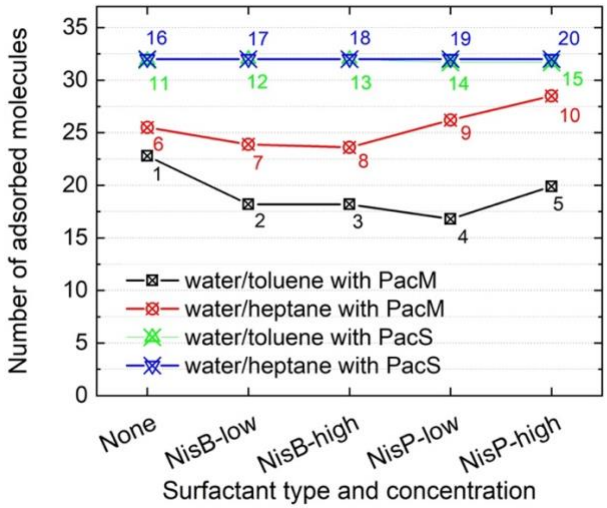

Figure 5.4 Number of adsorbed PAC molecules at organic solvent/water interface averaged over the last 5 ns of simulation. Water/toluene with PacM (black), water/heptane with PacM (red), water/toluene with PacS (green), water/heptane with PacS (blue). Horizontal labeling: (None) control systems without adding surfactants, sys. 1, 6, 11, 16; (NisB-low) adding NisB at low concentration, sys. 2, 7, 12, 17; (NisB-high) adding NisB at high concentration, sys. 3, 8, 13, 18; (NisP-low) adding NisP at low concentration, sys. 4, 9, 14, 19; (NisP-high) adding NisP at high concentration, sys. 5, 10, 15, 20. System number shown beside each symbol.

5.3.2 Role of non-ionic surfactants: competition vs. co-adsorption

The destabilization of water/oil interface by non-ionic surfactants have been frequently attributed to the competitive adsorption between non-ionic surfactants and PACs, where the non-ionic surfactants were more surface active and replaced the adsorbed PAC molecules [38,39, 44,67,68]. Generally, if some adsorption sites were occupied by one component causing fewer adsorption sites available for other components, the situation was considered competitive adsorption. [69] In this work, competitive adsorption was identified if desorption of PACs was observed along with

simultaneous adsorption of non-ionic surfactants. On the other hand, the intermolecular interaction between non-ionic surfactants and PACs might assist their adsorption together on the interface, which represents co-adsorption [70].

The adsorptions of PACs and non-ionic surfactants were analyzed through their density distribution at equilibrium. Density profiles for PacM and NisB/P were averaged over the last 5 ns of simulation and plotted in Fig. 5.5a for sys. 2-5 (PacM in toluene) and Fig. 5.5b for sys. 7-10 (PacM in heptane). Two dashed lines in each system corresponded to the locations of interface-L and interface-R determined from the intersection of water and toluene (or heptane) density profiles. In each system, the curve for PacM or NisB/P had two peaks located near the interfaces, indicating the interfacial adsorption of both PacM and NisB/P. The black dot curve in each plot was the density profile of PacM in the corresponding control system, in absence of non-ionic surfactants. It should be noted that the locations of the two interfaces in systems with non-ionic surfactants were slightly different from the control systems, due to the change in box dimensions during the NpT simulation. In Appendix C5, the actual locations of the two interfaces in each system were given, along with locations of the peaks in the PacM density profiles. These data allowed us to calculate the distance between each PacM density peak and the nearest interface, as a measure of the proximity of PacM adsorption. By adding NisB at low concentration (sys. 2), the peak of PacM at interface-L was lowered but the peak at interface-R had no significant change. The curve for NisB had one peak on each interface, with zero values in bulk toluene, indicating their complete adsorption on the interfaces. Most of the NisB molecules were adsorbed at interface-L, where there was evident competitive adsorption between NisB and PacM. For sys. 3 with NisB at high concentration, the peak of PacM at interface-L was also lowered and both peaks shifted toward bulk toluene (see Appendix C5 for more details). Meanwhile, NisB showed two pronounced peaks

at the two interfaces. The adsorption of NisB also competed with the adsorption of PacM, pushing them towards the bulk. When NisP were added instead of NisB, sys. 4 and sys. 5 were found to behave similarly to sys. 3.

As shown in Fig. 5.5b, on the water/heptane interface, adding NisB at low concentration (sys. 7) did not have obvious effect on the peak of PacM near interface-L but slightly narrowed the peak near interface-R. The peaks of NisB at the two interfaces were weak and non-zero densities were found in bulk heptane, suggesting that the adsorption of NisB was incomplete. The adsorbed NisB competed with PacM, but the competition was very mild and only seen by the slight narrowing of the PacM peak at interface-R. Meanwhile, the dispersed NisB and PacM had interaction in bulk heptane, as shown in Appendix C6. For sys. 8, the PacM peak at interface-L was lowered and shifted towards bulk heptane, while the peak at interface-R was narrowed but moved closer to the water phase (see Appendix C5 for more details). By adding NisP at low concentration (sys. 9), the changes in the PacM peaks were negligible. With NisP completely adsorbed at the interfaces, co-adsorption between NisP and PacM was observed. In sys. 10, the PacM peaks near both interfaces increased compared with the control system, signifying considerable co-adsorption of NisP and PacM.

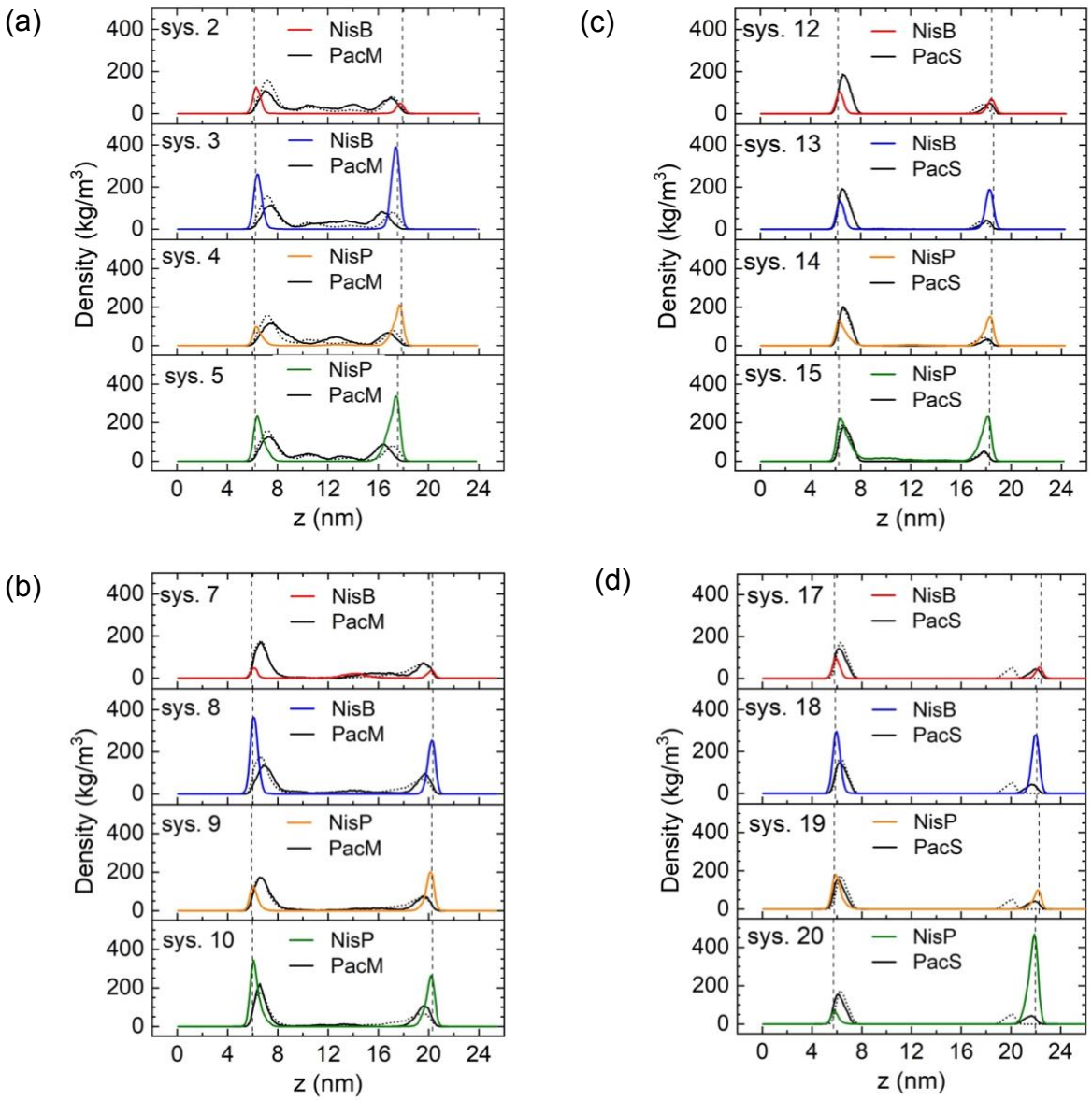

Figure 5.5 Density profiles for PacM/S and NisB/P averaged over last 5 ns for (a) sys. 2-5, PacM on water/toluene interface; (b) sys. 7-10, PacM on water/heptane interface; (c) sys. 12-15, PacS on water/toluene interface; and (d) sys. 17-20, PacS on water/heptane interface. In each plot, vertical dashed lines indicate the locations of the two interfaces, and the black dot curve is the density profile of PacM/S in the corresponding control systems.

The co-adsorption of PacM and NisB/P might be attributed to their intermolecular interactions, which was analyzed through the radial distribution function (RDF) of the atoms in NisB/P with respect to the atoms in PacM, as plotted in Fig. 5.6a for sys. 2-5 (water/toluene interface) and in Fig. 5.6b for sys. 7-10 (water/heptane interface). RDF represents the probability of finding a particle at a certain radial distance from the reference particle, which is useful to identify interparticle structural correlations. [71] For example, de Oliveira et al. [72] simulated polyethylene glycol (PEG) polymers in water and chloroform solvents, and calculated the RDF between PEG groups in different polymers. The first peak in the RDF was located at 0.48 nm, corresponding to direct PEG-PEG interaction. The second peak was located at 0.59 nm, corresponding to PEG-PEG interaction mediated by solvent molecules. [72] The two non-ionic surfactants simulated in this work were not PEG but share some similarities at the end groups. On the other hand, the RDFs in Fig. 5.6 used the PAC atoms as the reference particles. The PACs do not have linear structures and may not be able to interact with the surfactants at distances as close as those reported in de Oliveira et al. [72] In Fig. 5.6a, the first RDF peaks in sys. 2-5 (PacM in toluene) was located at 0.56 - 0.58 nm. The intensity of the first peak was quite low (around 1-2), indicating weak interaction between PacM and non-ionic surfactants. As shown in Fig. 5.6b, the first RDF peaks for sys. 7-10 were located at 0.54 - 0.56 nm, with low intensity (~ 3) for sys. 7-8 and higher intensity (~ 4.5-5.5) for sys. 9-10. The higher intensity for sys. 9-10 indicated a stronger correlation between PacM and NisP than between PacM and NisB in sys. 7-8. From the comparison of the first RDF peaks, the strength of short-range interaction between PacM and non-ionic surfactants was characterized as weak (intensity of peak: 1-2) in sys. 2-5, moderate (intensity of peak: 2-4) in sys. 7-8, and strong (intensity of peak over 4) in sys. 9-10. As mentioned in Fig. 5.5a-b, competitive adsorption was observed in sys. 2-5 and sys. 7-8, while co-adsorption was

more dominant in sys. 9-10, which was correlated with the stronger interaction between PacM and non-ionic surfactants in sys. 9-10.

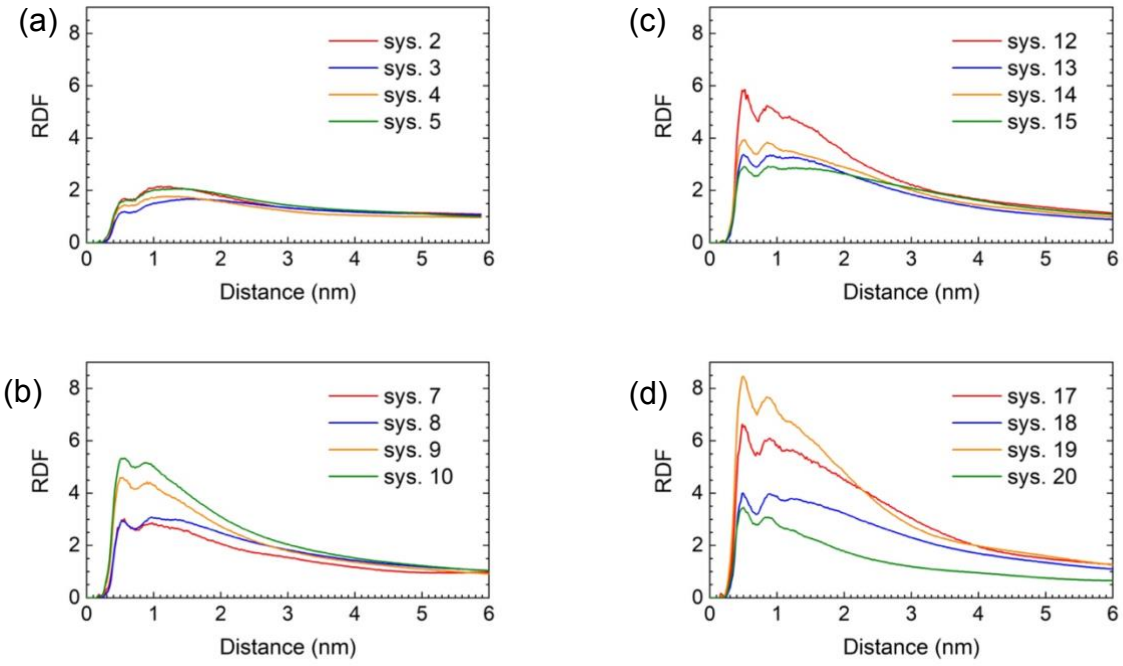

Figure 5.6 Radial distribution functions (RDFs) of all atoms in NisB/P molecules with respect to all atoms in PacM/S molecules, averaged over the last 5 ns, for (a) sys. 2-5, PacM on water/toluene interface; (b) sys. 7-10 PacM, on water/heptane interface; (c) sys. 12-15, PacS on water/toluene interface; and (d) sys. 17-20, PacS on water/heptane interface.

5.3.3 Co-adsorption between PacS and non-ionic surfactants

For the control systems with PacS, the density profiles stayed zero in bulk toluene (Fig. 5.3c) and heptane (Fig. 5.3d), indicating that all molecules were completely adsorbed at the interface. By introducing non-ionic surfactants into the water/toluene systems (sys. 12-15), as shown in Fig. 5.4, the number of adsorbed PacS molecules had no obvious change. It was consistent with the

observation in Fig. 5.5c that the density profiles for PacS in sys. 12-15 with non-ionic surfactants almost overlapped with the curve for the control system (sys. 11). There was even a slight shift of the PacS peaks towards bulk water at interface-R for sys. 12-14, and at interface-L for sys. 15 (see Appendix C5 for more details). As shown in Fig. 5.6c, the first RDF peaks for sys. 12-15 had intensity of ~ 2.5-6.0, indicating that the interaction between PacS and NisB/P was moderate (sys. 13-15) to strong (sys. 12). At water/heptane interface (sys. 17-20), Fig. 5.5d shows considerable shift of the PacS peaks towards the water phase, however this was mainly due to the change in the simulation box (see Appendix C5 for details). Nevertheless, the interaction between PacS and NisB/P (Fig. 5.6c) was moderate (sys. 18, sys. 20) to strong (sys. 17, sys. 19), and co-adsorption of NisB/P with PacS was evident.

5.3.4 Discussion

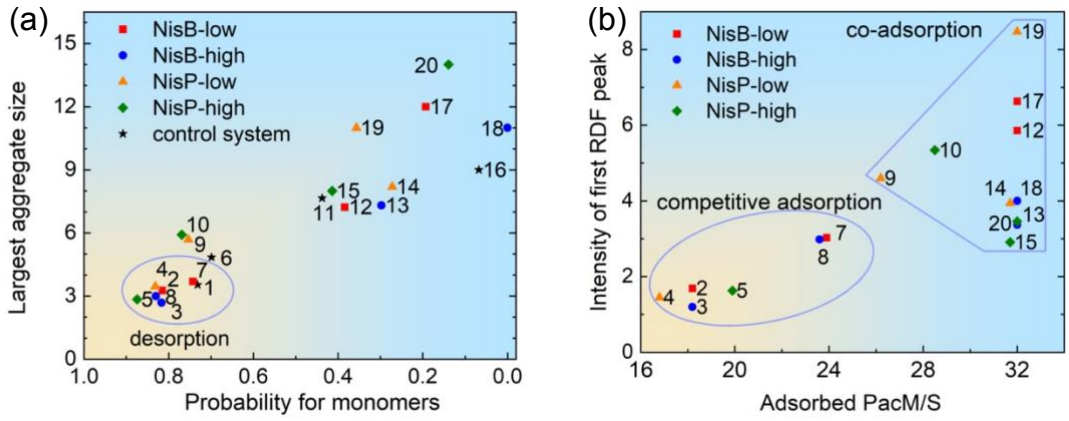

Figure 5.7 Summary of (a) the largest aggregate size vs. the probability of monomers; (b) the interaction between PacM/S and NisB/P vs. the number of adsorbed PacM/S molecules, where the interaction is represented by the intensity of the first RDF peaks in Fig. 5.6. Label on each symbol indicates the system number given in Table 5.1. All systems are mapped onto these two

diagrams (control systems are excluded in (b)), based on data from the last 5 ns of the simulations.

Stable W-O emulsions were frequently attributed to the adsorption of PACs on the water/oil interface, which had certain correlation with the aggregation of PACs. [73–75] For example, Spiecker et al. [73] investigated the effect of resin on the aggregate size of PACs, and the stability of W-O emulsion. With the increase of resin concentration, the aggregate size of PACs in mixtures of toluene and heptane, measured by small-angle neutron scattering, became smaller. [73] And the stability of W-O emulsion was lowered, due to the strong interaction between resin and PACs that interrupted the aggregation of PACs. [73] In our work, adding non-ionic surfactant also affect the aggregation of PACs. The aggregate size was quantified by the number of PAC molecules in the aggregate, which was determined by the criterion that any two PAC molecules in the aggregate had minimum distance less than 0.35 nm. The size of PAC aggregates was recorded over the last 5 ns of the simulations, and the probability distributions were plotted in Appendix C7. In addition, the size of the largest aggregates in each system was averaged over the last 5 ns of the simulations and reported in Appendix C8. Using the data from Appendix C7 and 8, the aggregation of PAC molecules is compared in Fig. 5.7a through two aspects, the probability that PAC molecules existed as monomers (x axis) and the size of the largest aggregates (y axis). It was reported that compared with PacS, individual PacM molecules possessed intramolecular flexibility and could transition between folded and unfolded state in bulk toluene and heptane, which hindered aggregation [76]. As shown in Fig. 5.7a, PacM molecules also formed small aggregates (2-6 molecules in sys. 1-10), whereas PacS molecules formed larger aggregates (7-14 molecules in sys. 11-20). Also, compared with PacM for which the aggregates were loosely structured, the structure of PacS aggregates were more compact due to π–π stacking (see Appendix C9).

As Anton et al. [77] suggested, larger aggregates on the water/oil interface were more difficult to desorb than smaller aggregates. Among the systems containing PacM which formed smaller aggregates than PacS, desorption was observed in sys. 2-5 (PacM at water/toluene interface with NisB or NisP) and 7-8 (PacM at water/heptane interface with NisB), as marked in the blue circle in Fig. 5.7a. In these systems, the probability of monomers increased, and the size of the largest aggregate decreased compared with the control systems, sys. 1 (PacM only on water/toluene interface) and sys. 6 (PacM only on water/heptane interface). This result implies the correlation between desorption and aggregation: desorption was more likely to occur upon the reduction of aggregate size and the increase of monomers, caused by adding non-ionic surfactants, as observed in sys. 2-5 and 7-8. In sys. 9-10, the largest aggregate size was increased by adding NisP on water/heptane interface, and desorption was not observed, which confirmed that larger aggregates were more difficult to desorb from the interface. It should be noted that all 32 PAC molecules were analyzed in Fig. 5.7a, and PAC monomers or the largest aggregates could be on the interface or dispersed in bulk organic phase. In fact, the largest aggregates were always observed on the interface except for sys. 2-3 where the largest aggregates were in bulk toluene. Large and compact aggregates formed by PacS were more difficult to desorb from the interface, and no desorption of PacS was observed for sys. 12-15 and 17-20 as shown in Fig. 5.7a.

Beside the effect of PAC structure, the aggregation and adsorption form of PAC at the interface also depended on the type of organic solvent. The PACs molecules had higher solubility in aromatic solvent (toluene) than in the aliphatic solvent (heptane). [58,76] Larger PAC aggregates could be formed in bulk heptane due to the solvent-solute incompatibility. [73] As shown in Fig. 5.7a, there were more PAC molecules in the largest aggregates on water/heptane interface. Also, more PacM molecules was adsorbed on the water/heptane interface than on

water/toluene interface, which can be seen from Fig. 5.7b where the intensity of the first RDF peak from Fig. 5.6 is plotted against the number of adsorbed PAC molecules from Fig. 5.4. Mikami et al. [78] observed through MD simulations that their model single-core PACs had more adsorption on water/heptane interface than on water/toluene interface. The finding was similar to the case of PacM molecules in our work where there was more adsorption at water/heptane interface. In this work, PacS molecules were completely adsorbed on both water/toluene and water/heptane interfaces, which was consistent with the simulation work from Lan et al. [58], but different from Mikami et al. [78]. One possible explanation is that the single core PAC model in Mikami's work had only one heteroatom, sulfur, located in the side chain, whereas the PacS molecule in our work had two oxygen atoms at the PA core, which could interact strongly with water phase and promote the adsorption of PacS molecules, as shown in Appendix C9.

The role of non-ionic surfactants is summarized in Fig. 5.7b. For sys. 2-3, and 7-8 marked in the blue circle, there was competitive adsorption between PacM and NisB. As discussed in Fig. 5.5a-b, all NisB were completely adsorbed in sys. 2, 3, and 8, while the adsorption of NisB in sys. 7 was incomplete due to their interaction with dispersed PacM in bulk heptane (Appendix C6). The adsorbed NisB molecules competed with PacM and caused desorption of PacM. Several factors contributed to the desorption of PacM by NisB. Firstly, NisB had hydrophilic ethyl oxide groups and chain-like structure with low molecular weight, which enabled the entire NisB molecule to be adsorbed close to the water phase, as shown in Fig. 5.5a-b and illustrated in Appendix C10. PacM molecules were larger and interacted with water mainly at the point of carboxyl group, while the rest of the molecule could be far from the water phase, as shown in Appendix C9 and C10. With the adsorption of NisB, the interaction between PacM and water might be interrupted. Secondly, the interaction between NisB and PacM (Fig. 5.7b, y-axis) was

weak for sys. 2-3 and moderate for sys. 7-8, thus the co-adsorption was insignificant. Thirdly, the adsorbed NisB interfered with the loosely structured PacM aggregates and promoted the dissociation of the aggregates into monomers. As discussed in Fig. 5.7a, the reduction of aggregate size and increase of monomers contributed to the desorption of PacM. It is important to mention that in our simulations, the concentration of NisB did not make significant difference in the desorption of PacM. On the water/oil interface, the interfacial tension was governed by the surface concentration of PACs and not the bulk concentration, as pointed out by Jian et al. [41] In our work, while the bulk concentration of the solute was high (over 10,000 ppm) due to the small size of the simulation box, the maximum surface concentration possible was (32+128)/(2*144) = 0.56 molecules/nm^2, assuming all solutes were adsorbed. This concentration was less than half of the saturation surface concentration for single-core PAC on water/oil interface: 1.32 molecules/nm^2. [41] The insignificant effect of the concentration of non-ionic surfactants was likely caused by the fact that the interface was well below saturation.

The desorption of a mixture of PACs from water/xylene interface by adding Brij-93 were investigated by Pradilla et al. through interfacial tension measurement. [38,39] From Langmuir adsorption isotherm, they analyzed the composition on the interface and proposed the interaction between non-ionic surfactants and PACs. At low concentration of Brij-93 (10 ppm), there were interaction between Brij-93 and PACs and the partial desorption of PACs from the interface. [38] At higher concentration of Brij-93 (100 ppm), the PACs were almost completely desorbed from the interface and the interaction between Brij-93 and PACs diminished. [38] In our case, the interface with mixtures of PACs and NisB was below saturation, which corresponded to low concentration in the experiment. The low concentration scenario from Pradilla et al. [38] was consistent with our observation that there was weak (sys. 2-3) to moderate (sys. 7-8) interaction

between Brij-93 (named NisB in this work) and PacM, and PacM molecules were partially desorbed from the interface. Other observation was obtained in this work for PacS molecules on water/toluene (sys. 12-13) and water/heptane (sys. 17-18) interfaces with the presence of NisB. The PacS molecules were difficult to desorb due to their large and compact aggregate structure, close contact with water phase, and moderate to strong interaction (Fig. 5.7b) with NisB.

In Pradilla et al.'s work [38,39], PE8100, a PEO-PPO copolymer, was shown to have better desorption capability than Brij-93, in that less amount of PE8100 was required to obtain similar degree of PAC desorption by Brij-93. At low concentration of PE8100 (0.5 ppm), strong interaction between PE8100 and PACs was observed and there was negligible desorption of PACs. [38,39] At high concentration of PE8100 (100 ppm), there was no interaction between PACs and PE8100, and PACs were completely desorbed. [38,39] The low concentration scenario in Pradilla et al.'s work was similar to sys. 9-10 in our work, where there was strong interaction between PacM and NisP, and co-adsorption was dominant on water/heptane interface, as shown in Fig. 5.7b. While for sys. 4-5 with PacM on water/toluene interface, the desorption of PacM by NisP could be attributed to the close contact between NisP and water phase, the small and loose structure of PacM aggregates, and the weak interaction between NisP and PacM. The effect of NisP concentration was more significant than NisB, probably due to the higher surface activity and molecular weight of NisP [38,39]. Increasing NisP concentration from sys. 4 to sys. 5, the desorption became less significant. And from sys. 9 to sys. 10, the co-adsorption of PacM and NisP was enhanced. The increased adsorption of PacM correlated with the increase of interaction between PacM and NisP (Fig. 5.7b). For systems with PacS (sys. 14-15, 19-20), co-adsorption between PacS and NisP was observed, similar to systems where NisB was added (sys. 12-13, 17-18).

In a previous simulation study, Niu et al. [44] placed a complete film of PEO-PPO copolymer and C5Pe, a model single-core PAC molecule, on water/xylene interface. They reported that the PEO-PPO copolymer could penetrate into and destroy the film formed by C5Pe. [44] Pradilla et al. [38,39] reported that with high concentration of non-ionic surfactants (2500 ppm of Brij-93 and 100 ppm of PE8100), the PACs could be completely displaced and there was no interaction between PACs and non-ionic surfactant. Such complete desorption was not observed in our work, most likely due to the relatively low surface concentration of PACs and surfactants. While the bulk concentration of PACs can be assigned at the beginning of the simulations, their adsorption and hence surface coverage of the interface cannot be controlled. All of our simulations showed many of the PACs adsorbed in aggregated form, and even when they adsorbed in monomer form, their polyaromatic cores tended to be perpendicular or slant, instead of parallel, to the interface. Such configurations led to limited surface coverage of the interface, even though the bulk concentration was quite high. As shown in the Appendix C11, the surface coverage fraction was 15% for sys. 1, 18% for sys. 6, and 11% for both sys. 11 and sys. 16. The surface coverage fraction was less than 20% in all cases, leave ample exposed interface where the non-ionic surfactants could adsorb and co-exist with the PACs. Although higher surface coverage was obtained for control systems with PacM than with PacS, the difference is small and the different desorption behaviors observed between PacM and PacS were mainly due to their different solubility, aggregation characteristics and interaction with the non-ionic surfactants. Our work shed light onto the different roles played by non-ionic surfactants on the adsorption of PAC on water/oil interface, which depend on PAC architecture, solvent and surfactant property. Competitive adsorption and desorption of the PACs may not be the only way to destabilize W-O emulsions; in fact, co-adsorption and subsequent bridging of small droplets have been proposed to

be an alternative way of demulsification [58]. Understanding the roles of non-ionic surfactants is crucial to the design of chemical demulsifiers and control of their performance.

5.4 Conclusion

Molecular dynamics simulations were employed to investigate the adsorption of multi-core (PacM) and single-core (PacS) PACs at water/oil interfaces, in the presence of non-ionic surfactants (NisB and NisP). Different PAC architectures, solvent types, non-ionic surfactants and surfactant concentrations were used to investigate their influences. PacM tended to form smaller and more loosely structured aggregates at the interface, while the aggregates for PacS was larger and more compact. [76,78] There was more adsorption of PacM on water/heptane interface than on water/toluene interface, due to the lower solubility in heptane, whereas PacS molecules were completely adsorbed at both interfaces. [52,58,78,79]

NisB molecules were adsorbed closer to the water phase than PacM molecules due to the strong interaction between the hydrophilic EO group of NisB and water. The adsorbed NisB interfered with the interaction between PacM and water, as well as the interaction within the loosely structured PacM aggregates, causing them to dissociate into monomers that were easier to desorb [77]. For the surface concentrations obtained in this work, the bulk concentration of NisB did not have significant effect on the desorption of PacM, which was likely caused by the fact that the interface was well below saturation [41]. When NisP were added to the systems containing PacM and water/toluene interface, desorption was also observed. While on water/heptane interface, the interaction between NisP and PacM promoted the adsorption of PacM. The effect of NisP concentration was more significant than NisB, probably due to the higher surface activity and molecular weight of NisP [38,39], with the increase of NisP concentration favoring adsorption. Adding NisB or NisP did not induce the desorption of PacS, due to the large size and compact

structure of PacS aggregates, the interaction between PacS and water, and the interactions between PacS and non-ionic surfactants.

This work identified two opposite roles of non-ionic surfactants on the adsorption of PACs, namely, competition and co-adsorption. While it was traditionally believed that competitive adsorption of non-ionic surfactants and their displacement of PACs were necessary for demulsification [44,80], our results showed that co-adsorption could also occur when there were strong interactions between PACs and the surfactants. This phenomenon may not be detrimental to demulsification, and in fact suggests an alternative way of demulsification, by co-adsorption and subsequent bridging of small droplets into bigger ones which are then easier to be separated from the bulk phase [58]. To our best knowledge, this is the first atomistic-level study that comprehensively addressed the adsorption and interaction of PACs and non-ionic surfactants at water/oil interface under the influence of many important factors, such as PAC structure, solvent type, as well as structure and concentration of non-ionic surfactants. This work provided useful insights into the fundamental understanding of how non-ionic surfactants may modulate oil/water interfaces with adsorbed PACs, especially when they are used as chemical demulsifiers to treat water-in-oil emulsions. Future work will explore the coalescence or adhesion of water droplets with the presence of non-ionic surfactants, and a combined experimental and theoretical investigation on the stability of water-in-oil and oil-in-water emulsions with PACs and non-ionic surfactants.

References

[1] A.G. Volkov, Liquid Interfaces in Chemical, Biological and Pharmaceutical Applications, CRC Press, 2001.

[2] N. Somekawa, A. Yamauchi, K. Eda, T. Osakai, Computational Prediction of Adsorption Equilibrium for Nonionic Surfactants at the Oil/Water Interface, Langmuir. 35 (2019) 11345–11350.

[3] D. Lavabre, V. Pradines, J.-C. Micheau, V. Pimienta, Periodic Marangoni Instability in Surfactant (CTAB) Liquid/Liquid Mass Transfer, J. Phys. Chem. B. 109 (2005) 7582–7586.

[4] N. Paul, P. Schrader, S. Enders, M. Kraume, Effects of Phase Behaviour on Mass Transfer in Micellar Liquid/Liquid Systems, Chem. Eng. Sci. 115 (2014) 148–156.

[5] M.A. Fulazzaky, Determining the Resistance of Mass Transfer for Adsorption of The Surfactants onto Granular Activated Carbons from Hydrodynamic Column, Chem. Eng. J. 166 (2011) 832–840.

[6] A. Wu, F. Lu, P. Sun, X. Gao, L. Shi, L. Zheng, Photoresponsive Self-Assembly of Surface Active Ionic Liquid, Langmuir. 32 (2016) 8163–8170.

[7] J. Penfold, R.K. Thomas, H.-H. Shen, Adsorption and Self-Assembly of Biosurfactants Studied by Neutron Reflectivity and Small Angle Neutron Scattering: Glycolipids, Lipopeptides And Proteins, Soft Matter. 8 (2012) 578–591.

[8] B. Dong, N. Li, L. Zheng, L. Yu, T. Inoue, Surface Adsorption and Micelle Formation of Surface Active Ionic Liquids in Aqueous Solution, Langmuir. 23 (2007) 4178–4182.

[9] J.P. Rane, V. Pauchard, A. Couzis, S. Banerjee, Interfacial Rheology of Asphaltenes at Oil–Water Interfaces and Interpretation of the Equation of State, Langmuir. 29 (2013) 4750–4759.

[10] A. Sarkar, D.S. Horne, H. Singh, Interactions of Milk Protein-Stabilized Oil-In-Water Emulsions with Bile Salts in A Simulated Upper Intestinal Model, Food Hydrocoll. 24 (2010) 142–151.

[11] C. Shi, L. Zhang, L. Xie, X. Lu, Q. Liu, C.A. Mantilla, F.G.A. van den Berg, H. Zeng, Interaction Mechanism of Oil-in-Water Emulsions with Asphaltenes Determined Using Droplet Probe AFM, Langmuir. 32 (2016) 2302–2310.

[12] C.-C. Chang, I. Williams, A. Nowbahar, V. Mansard, J. Mecca, K.A. Whitaker, A.K. Schmitt, C.J. Tucker, T.H. Kalantar, T.-C. Kuo, T.M. Squires, Effect of Ethylcellulose on the Rheology

and Mechanical Heterogeneity of Asphaltene Films at the Oil–Water Interface, Langmuir. 35 (2019) 9374–9381.

[13] H. Katepalli, A. Bose, T.A. Hatton, D. Blankschtein, Destabilization of Oil-in-Water Emulsions Stabilized by Non-ionic Surfactants: Effect of Particle Hydrophilicity, Langmuir. 32 (2016) 10694–10698.

[14] B. Khadem, N. Sheibat-Othman, Modeling of Double Emulsions Using Population Balance Equations, Chem. Eng. J. 366 (2019) 587–597.

[15] C. Shi, L. Zhang, L. Xie, X. Lu, Q. Liu, J. He, C.A. Mantilla, F.G.A. Van den berg, H. Zeng, Surface Interaction of Water-in-Oil Emulsion Droplets with Interfacially Active Asphaltenes, Langmuir. 33 (2017) 1265–1274.

[16] L. Zhang, L. Xie, X. Cui, J. Chen, H. Zeng, Intermolecular and Surface Forces at Solid/Oil/Water/Gas Interfaces in Petroleum Production, J. Colloid Interface Sci. 537 (2019) 505–519.

[17] L. Xie, C. Shi, X. Cui, H. Zeng, Surface Forces and Interaction Mechanisms of Emulsion Drops and Gas Bubbles in Complex Fluids, Langmuir. 33 (2017) 3911–3925.

[18] W. Zhou, L. Zhu, Distribution of Polycyclic Aromatic Hydrocarbons in Soil–Water System Containing A Nonionic Surfactant, Chemosphere. 60 (2005) 1237–1245.

[19] X. Li, M. Yoneda, Y. Shimada, Y. Matsui, Effect of Surfactants on The Aggregation and Stability of TiO2 Nanomaterial in Environmental Aqueous Matrices, Sci. Total Environ. 574 (2017) 176–182.

[20] J. Long, L. Li, Y. Jin, H. Sun, Y. Zheng, S. Tian, Synergistic Solubilization Of Polycyclic Aromatic Hydrocarbons by Mixed Micelles Composed of a Photoresponsive Surfactant and A Conventional Non-Ionic Surfactant, Sep. Purif. Technol. 160 (2016) 11–17.

[21] Z. Zheng, J.P. Obbard, Effect of Non-Ionic Surfactants on Elimination of Polycyclic Aromatic Hydrocarbons (PAHs) In Soil-Slurry by Phanerochaete Chrysosporium, J. Chem. Technol. Biotechnol. 76 (2001) 423–429.

[22] S.Y. Yuan, S.H. Wei, B.V. Chang, Biodegradation of Polycyclic Aromatic Hydrocarbons by A Mixed Culture, Chemosphere. 41 (2000) 1463–1468.

[23] X. Zhu, G. Wu, D. Chen, Molecular Dynamics Simulation of Cyclodextrin Aggregation and Extraction of Anthracene from Non-Aqueous Liquid Phase, J. Hazard. Mater. 320 (2016) 169–175.

[24] P. Tchoukov, F. Yang, Z. Xu, T. Dabros, J. Czarnecki, J. Sjöblom, Role of Asphaltenes in Stabilizing Thin Liquid Emulsion Films, Langmuir. 30 (2014) 3024–3033.

[25] D.M. Sztukowski, M. Jafari, H. Alboudwarej, H.W. Yarranton, Asphaltene Self-Association and Water-In-Hydrocarbon Emulsions, J. Colloid Interface Sci. 265 (2003) 179–186.

[26] S. Zhang, L. Zhang, X. Lu, C. Shi, T. Tang, X. Wang, Q. Huang, H. Zeng, Adsorption Kinetics of Asphaltenes at Oil/Water Interface: Effects of Concentration and Temperature, Fuel. 212 (2018) 387–394.

[27] D. Wang, Z. Zhao, C. Qiao, W. Yang, Y. Huang, P. McKay, D. Yang, Q. Liu, H. Zeng, Techniques for Treating Slop Oil in Oil and Gas Industry: A Short Review, Fuel. 279 (2020) 118482.

[28] X. Zhu, D. Chen, G. Wu, Molecular Dynamic Simulation of Asphaltene Co-Aggregation with Humic Acid During Oil Spill, Chemosphere. 138 (2015) 412–421.

[29] L.A. Bernardez, S. Ghoshal, Solubilization Kinetics for Polycyclic Aromatic Hydrocarbons Transferring from A Non-Aqueous Phase Liquid to Non-Ionic Surfactant Solutions, J. Colloid Interface Sci. 320 (2008) 298–306.

[30] Z. Grenoble, S. Trabelsi, Mechanisms, Performance Optimization and New Developments in Demulsification Processes for Oil and Gas Applications, Adv. Colloid Interface Sci. 260 (2018) 32–45.

[31] G. Gelardi, S. Mantellato, D. Marchon, M. Palacios, A.B. Eberhardt, R.J. Flatt, Chemistry of Chemical Admixtures, in: Sci. Technol. Concr. Admix., Elsevier, 2016: pp. 149–218.

[32] A.O. Adilbekova, K.I. Omarova, A. Karakulova, K.B. Musabekov, Nonionic Surfactants Based on Polyoxyalkylated Copolymers Used as Demulsifying Agents, Colloids Surf. Physicochem. Eng. Asp. 480 (2015) 433–438.

[33] Z. Li, H. Geng, X. Wang, B. Jing, Y. Liu, Y. Tan, Noval Tannic Acid-Based Polyether as An Effective Demulsifier For Water-In-Aging Crude Oil Emulsions, Chem. Eng. J. 354 (2018) 1110–1119.

[34] E.I. Hernández, L.V. Castro-Sotelo, J.R. Avendaño-Gómez, C.A. Flores, F. Alvarez-Ramírez, F. Vázquez, Synthesis, Characterization, and Evaluation of Petroleum Demulsifiers of Multibranched Block Copolymers, Energy Fuels. 30 (2016) 5363–5378.

[35] G. Cendejas, F. Arreguín, L.V. Castro, E.A. Flores, F. Vazquez, Demulsifying Super-Heavy Crude Oil with Bifunctionalized Block Copolymers, Fuel. 103 (2013) 356–363.

[36] Z. Zhang, G.Y. Xu, F. Wang, S.L. Dong, Y.M. Li, Characterization And Demulsification Of Poly(Ethylene Oxide)–Block–Poly(Propylene Oxide)–Block–Poly(Ethylene Oxide) Copolymers, J. Colloid Interface Sci. 277 (2004) 464–470.

[37] V.F. Pacheco, L. Spinelli, E.F. Lucas, C.R.E. Mansur, Destabilization of Petroleum Emulsions: Evaluation of the Influence of the Solvent on Additives, Energy Fuels. 25 (2011) 1659–1666.

[38] D. Pradilla, S. Simon, J. Sjöblom, Mixed Interfaces of Asphaltenes and Model Demulsifiers, Part II: Study of Desorption Mechanisms at Liquid/Liquid Interfaces, Energy Fuels. 29 (2015) 5507–5518.

[39] D. Pradilla, S. Simon, J. Sjöblom, Mixed Interfaces of Asphaltenes and Model Demulsifiers Part I: Adsorption and Desorption of Single Components, Colloids Surf. Physicochem. Eng. Asp. 466 (2015) 45–56.

[40] F. Gao, Z. Xu, G. Liu, S. Yuan, Molecular Dynamics Simulation: The Behavior of Asphaltene In Crude Oil and At the Oil/Water Interface, Energy Fuels. 28 (2014) 7368–7376.

[41] C. Jian, M.R. Poopari, Q. Liu, N. Zerpa, H. Zeng, T. Tang, Reduction of Water/Oil Interfacial Tension by Model Asphaltenes: The Governing Role of Surface Concentration, J. Phys. Chem. B. 120 (2016) 5646–5654.

[42] T. Kuznicki, J.H. Masliyah, S. Bhattacharjee, Aggregation and Partitioning of Model Asphaltenes at Toluene−Water Interfaces: Molecular Dynamics Simulations, Energy Fuels. 23 (2009) 5027–5035.

[43] S. Hezaveh, S. Samanta, G. Milano, D. Roccatano, Molecular Dynamics Simulation Study of Solvent Effects on Conformation and Dynamics of Polyethylene Oxide and Polypropylene Oxide Chains in Water and in Common Organic Solvents, J. Chem. Phys. 136 (2012) 124901.

[44] Z. Niu, X. Ma, R. Manica, T. Yue, Molecular Destabilization Mechanism of Asphaltene Model Compound C5Pe Interfacial Film by EO-PO Copolymer: Experiments and MD Simulation, J. Phys. Chem. C. 123 (2019) 10501–10508.

[45] F. Shehzad, I.A. Hussein, M.S. Kamal, W. Ahmad, A.S. Sultan, M.S. Nasser, Polymeric Surfactants and Emerging Alternatives used in the Demulsification of Produced Water: A Review, Polym. Rev. 58 (2018) 63–101.

[46] M. Tomšič, M. Bešter-Rogač, A. Jamnik, W. Kunz, D. Touraud, A. Bergmann, O. Glatter, Nonionic Surfactant Brij 35 in Water and in Various Simple Alcohols: Structural

Investigations by Small-Angle X-ray Scattering and Dynamic Light Scattering, J. Phys. Chem. B. 108 (2004) 7021–7032.

[47] A.B. Andrews, A. McClelland, O. Korkeila, A. Demidov, A. Krummel, O.C. Mullins, Z. Chen, Molecular Orientation of Asphaltenes and PAH Model Compounds in Langmuir−Blodgett Films Using Sum Frequency Generation Spectroscopy, Langmuir. 27 (2011) 6049–6058.

[48] D. Liu, C. Li, X. Zhang, F. Yang, G. Sun, B. Yao, H. Zhang, Polarity Effects of Asphaltene Subfractions on the Stability and Interfacial Properties of Water-In-Model Oil Emulsions, Fuel. 269 (2020) 117450.

[49] J. Dufour, J.A. Calles, J. Marugán, R. Giménez-Aguirre, J.L. Peña, D. Merino-García, Influence of Hydrocarbon Distribution in Crude Oil and Residues on Asphaltene Stability †, Energy Fuels. 24 (2010) 2281–2286.

[50] J.M. Sheremata, M.R. Gray, H.D. Dettman, W.C. McCaffrey, Quantitative Molecular Representation and Sequential Optimization of Athabasca Asphaltenes, Energy Fuels. 18 (2004) 1377–1384.

[51] C. Jian, T. Tang, S. Bhattacharjee, Probing the Effect of Side-Chain Length on the Aggregation of a Model Asphaltene Using Molecular Dynamics Simulations, Energy Fuels. 27 (2013) 2057–2067.

[52] C. Jian, T. Tang, Molecular Dynamics Simulations Reveal Inhomogeneity-Enhanced Stacking of Violanthrone-78-Based Polyaromatic Compounds in *n* -Heptane–Toluene Mixtures, J. Phys. Chem. B. 119 (2015) 8660–8668.

[53] A.D. Becke, A New Mixing of Hartree–Fock and Local Density-Functional Theories, J. Chem. Phys. 98 (1993) 1372–1377.

[54] A.K. Malde, L. Zuo, M. Breeze, M. Stroet, D. Poger, P.C. Nair, C. Oostenbrink, A.E. Mark, An Automated Force Field Topology Builder (ATB) and Repository: Version 1.0, J. Chem. Theory Comput. 7 (2011) 4026–4037.

[55] L.D. Schuler, X. Daura, W.F. van Gunsteren, An Improved GROMOS96 Force Field for Aliphatic Hydrocarbons in the Condensed Phase, J. Comput. Chem. 22 (2001) 1205–1218.

[56] C.M. Breneman, K.B. Wiberg, Determining Atom-Centered Monopoles from Molecular Electrostatic Potentials. The Need for High Sampling Density in Formamide Conformational Analysis, J. Comput. Chem. 11 (1990) 361–373.

[57] M.J. Frisch, G.W. Trucks, H.B. Schlegel, G.E. Scuseria, M.A. Robb, J.R. Cheeseman, G. Scalmani, V. Barone, G.A. Petersson, H. Nakatsuji, et al., Gaussian 16 Rev. C.01, Wallingford, CT, 2016.

[58] T. Lan, H. Zeng, T. Tang, Molecular Dynamics Study on the Mechanism of Graphene Oxide to Destabilize Oil/Water Emulsion, J. Phys. Chem. C. 123 (2019) 22989–22999.

[59] J. Zielkiewicz, Structural properties of water: Comparison of the SPC, SPCE, TIP4P, and TIP5P models of water, J. Chem. Phys. 123 (2005) 104501.

[60] T. Kuznicki, J.H. Masliyah, S. Bhattacharjee, Molecular Dynamics Study of Model Molecules Resembling Asphaltene-Like Structures in Aqueous Organic Solvent Systems, Energy Fuels. 22 (2008) 2379–2389.

[61] D.V.D. Spoel, E. Lindahl, B. Hess, G. Groenhof, A.E. Mark, H.J.C. Berendsen, GROMACS: Fast, Flexible, and Free, J. Comput. Chem. 26 (2005) 1701–1718.

[62] E. Lindahl, B. Hess, D. van der Spoel, GROMACS 3.0: A Package for Molecular Simulation and Trajectory Analysis, J. Mol. Model. 7 (2001) 306–317.

[63] H.J.C. Berendsen, D. van der Spoel, R. van Drunen, GROMACS: A Message-Passing Parallel Molecular Dynamics Implementation, Comput. Phys. Commun. 91 (1995) 43–56.

[64] C. Oostenbrink, A. Villa, A.E. Mark, W.F.V. Gunsteren, A Biomolecular Force Field Based on the Free Enthalpy of Hydration and Solvation: The GROMOS Force-Field Parameter Sets 53a5 and 53a6, J. Comput. Chem. 25 (2004) 1656–1676.

[65] B. Hess, P-LINCS: A Parallel Linear Constraint Solver for Molecular Simulation, J. Chem. Theory Comput. 4 (2008) 116–122.

[66] U. Essmann, L. Perera, M.L. Berkowitz, T. Darden, H. Lee, L.G. Pedersen, A Smooth Particle Mesh Ewald Method, J. Chem. Phys. 103 (1995) 8577–8593.

[67] Z. Niu, T. Yue, X. He, R. Manica, Changing the Interface Between an Asphaltene Model Compound and Water by Addition of an EO–PO Demulsifier through Adsorption Competition or Adsorption Replacement, Energy Fuels. 33 (2019) 5035–5042.

[68] E. Pensini, D. Harbottle, F. Yang, P. Tchoukov, Z. Li, I. Kailey, J. Behles, J. Masliyah, Z. Xu, Demulsification Mechanism of Asphaltene-Stabilized Water-in-Oil Emulsions by a Polymeric Ethylene Oxide–Propylene Oxide Demulsifier, Energy Fuels. 28 (2014) 6760–6771.

[69] J.J. Sheng, Surfactant-Polymer Flooding, in: Mod. Chem. Enhanc. Oil Recovery, Elsevier, 2011: pp. 371–387.

[70] S. Liu, Cooperative Adsorption on Solid Surfaces, J. Colloid Interface Sci. 450 (2015) 224–238.

[71] T. Aste, T. Di Matteo, Nanometric Architectures: Emergence of Efficient Non-Crystalline Atomic Organization in Nanostructures, in: Nanostructure Control Mater., Elsevier, 2006: pp. 32–56.

[72] O.V. de Oliveira, L.T. Costa, E.R. Leite, Molecular Modeling of a Polymer Nanocomposite Model in Water and Chloroform Solvents, Comput. Theor. Chem. 1092 (2016) 52–56.

[73] P.M. Spiecker, K.L. Gawrys, C.B. Trail, P.K. Kilpatrick, Effects of Petroleum Resins on Asphaltene Aggregation and Water-In-Oil Emulsion Formation, Colloids Surf. Physicochem. Eng. Asp. 220 (2003) 9–27.

[74] J.D. McLean, P.K. Kilpatrick, Effects of Asphaltene Aggregation in Model Heptane–Toluene Mixtures on Stability of Water-in-Oil Emulsions, J. Colloid Interface Sci. 196 (1997) 23–34.

[75] S. Simon, J. Jestin, T. Palermo, L. Barré, Relation between Solution and Interfacial Properties of Asphaltene Aggregates, Energy Fuels. 23 (2009) 306–313.

[76] X. Sun, H. Zeng, T. Tang, Molecular Simulation of Folding and Aggregation of Multi-Core Polycyclic Aromatic Compounds, J. Mol. Liq. 310 (2020) 113248.

[77] N. Anton, T.F. Vandamme, P. Bouriat, Dilatational Rheology of a Gel Point Network Formed by Nonionic Soluble Surfactants at The Oil–Water Interface, Soft Matter. 9 (2013) 1310–1318.

[78] Y. Mikami, Y. Liang, T. Matsuoka, E.S. Boek, Molecular Dynamics Simulations of Asphaltenes at the Oil–Water Interface: From Nanoaggregation to Thin-Film Formation, Energy Fuels. 27 (2013) 1838–1845.

[79] Y. Aray, R. Hernández-Bravo, J.G. Parra, J. Rodríguez, D.S. Coll, Exploring the Structure–Solubility Relationship of Asphaltene Models in Toluene, Heptane, and Amphiphiles Using a Molecular Dynamic Atomistic Methodology, J. Phys. Chem. A. 115 (2011) 11495–11507.

[80] Z. Li, S. Yin, G. Tan, S. Zhao, Z. Shi, B. Jing, L. Zhai, Y. Tan, Synthesis and Properties of Novel Branched Polyether as Demulsifiers for Polymer Flooding, Colloid Polym. Sci. 294 (2016) 1943–1958.

Chapter 6. Free Energy of Interaction between Adsorbate-Stabilized Water Droplets

6.1 Introduction

Water droplet coalescence is a phenomenon in many environmental and industrial processes. [1–8] Understanding water droplet coalescence in gas phase is crucial for studying atmosphere science, such as the cloud droplet growth, rain droplet formation etc. [9,10] Water droplets dispersed in immiscible liquids (e.g. oil) are thermodynamically unstable and tend to coalesce. [11,12] Interface-active materials could be adsorbed on the interface between water and the other liquid, making the water droplets kinetically stable in water-in-oil emulsion. [13,14] A stable emulsion is desirable in many applications, such as cosmetics, pharmaceutical, and food industries. While in petroleum industry, separating water from oil phase remains a key challenge because the presence of water in oil could cause severe problems such as corrosion and fouling. [15]

By investigating water droplets with the adsorption of various interfacially-active materials, the stability of emulsified droplets can be understood and manipulated. For example, asphaltenes, a fraction in crude oil, are the main contributors to unwanted water in crude oil emulsion [11]. Shi et al. [16] measured the surface interaction between micrometer-size water droplets stabilized by asphaltenes with different concentrations in toluene, heptane and heptol (mixtures of toluene and heptane). Drop probe atomic force microscopy (AFM) was used to quantitatively measure the interaction force during the coalescence of water droplets in water-in-oil emulsion. [15] Adhesion between two water droplets during their separation were induced by the interpenetration and aggregation of interfacially adsorbed asphaltenes. [15] The strength of adhesion increased with increasing asphaltenes concentration up to a threshold and then significantly decreased with further

increase of asphaltenes concentration. [15] The water in crude oil emulsion, which is stabilized by interfacially-active components, can be destabilized by adding non-ionic surfactants as chemical demulsifiers. Pensini et al. [16] studied the demulsification of asphaltenes-stabilized water-in-toluene emulsion by PEO-PPO copolymers. The amount of water resolved in the bottle test reached its maximum of ~85% by applying 2.3 ppm of PEO-PPO copolymer in the asphaltenes is stabilized water-in-toluene emulsion. [16] With lower than 0.1 ppm of demulsifiers, the water in toluene could not be separated; as well the resolved water decreased with the increase of PEO-PPO concentration from 2.3 ppm to 288.4 ppm. [16] By adding only PEO-PPO copolymers to the emulsion without asphaltenes, the amount of resolved water was 100% when the concentration of demulsifiers was 2.3 ppm. [16] Similar to the systems with a mixture of demulsifiers and PACs, the water resolved in systems with only demulsifiers decreased as the PEO-PPO concentration increased from 2.3 ppm to 230.7 ppm. [16]

Experimental investigation on water droplet coalescence has encountered many challenges, such as the inability to capture the rapidity of the phenomenon [17] and nanometer size water droplets [18]. Molecular dynamics (MD) simulations have been carried out to provide molecular-level evidence on water droplet coalescence [4,19–21]. Jian et al. studied the adsorption of model asphaltenes on water droplets and its effect on water droplet coalescence in toluene by using MD simulations. [22,23] At low concentration, the adsorption of model asphaltenes on the water droplets was incomplete. The dispersed model asphaltenes acted as barriers to prevent water droplet coalescence. [22,23] Evident adsorption of model asphaltenes was observed when the model asphaltenes concentration was sufficiently high. [22,23] A protective film of model asphaltenes was formed on the surface of water droplets and prevented the coalescence. [22,23] In a quantitative way, Pak et al. performed MD simulations to calculate the free energy profile for

the coalescence of water droplets uncoated [24] and coated by organic compounds (benzoic acid, heptanoic acid, and pimelic acid) [25]. Negative free energy profiles were obtained for all the systems, which indicated the spontaneous coalescence of water droplets with and without coated materials. [24,25] These free energy calculations were carried out for water droplets in the atmosphere [24,25]. It is demanding to provide quantitative analysis on water droplet coalescence coated with interfacially-active components in liquid solutions.

In this work, MD simulations were performed on water droplets with the adsorption of interfacially active components in toluene, which represented the immiscible phase for water. The adsorbates of interest included a model asphaltenes, violenthrane-79 (VO-79), and two non-ionic surfactants, PEO-PPO triblock copolymer and Brij-93. Model asphaltenes, including VO-79, have been frequently considered as a stabilizer for water droplets in oil phase. PEO-PPO triblock copolymers have been extensively used as demulsifiers. A model PEO-PPO triblock copolymer, $(EO)_5(PO)_{10}(EO)_5$, was employed and compared with another low molecular weight non-ionic surfactant Brij-93, which has also been studied as a demulsifier [26,27]. The process of water droplet coalescence was analyzed through adsorbate film formation on a single water droplet, non-equilibrium head-on coalescence of two water droplets, and the equilibrium (quasi-static) state free energy calculations. This molecular level study provided useful quantitative insights into the free energy of coalescence and interaction force between adsorbates stabilized water droplets. Practically, this work gives useful implication on water droplet related problems such as emulsification and demulsification.

6.2 Methods

6.2.1 Molecule models and system details.

Three types of interfacially-active molecules were used as adsorbates at water and toluene interface. As shown in Fig. 6.1a, violenthrane-79 (VO-79, $C_{50}H_{48}O_4$, molecular weight (MW): 712 g/mol) is a polycyclic aromatic compound (PAC) with a PA core (marked in dash blue square) and two peripheral chains. PEO-PPO-PEO copolymer, one of the non-ionic surfactants, had a triblock structure of $(EO)_5(PO)_{10}(EO)_5$ (MW: 1039 g/mol) as shown in Fig. 6.1b, referred to as NisP in this work. Hydrophilic PEO groups are marked in dash blue squares as shown in Fig. 6.1b. Another non-ionic surfactant simulated was polyethylene glycol oleyl ether Brij-93 ($C_{22}H_{44}O_3$, MW: 357 g/mol), referred to as NisB in this work and shown in Fig. 6.1c where the hydrophilic group is marked. Force field parameters of the three molecules have been validated and directly adopted from our previous works. [28–30] Briefly, chemical structures for the non-ionic surfactants were drawn in ChemDraw Prime 16.0. The geometry and force field parameters were optimized by using Gaussian 16 [31] at the B3LYP [32]/6-31G + (d,p) level, with partial charge calculated with CHELPG (CHarges from ELectrostatic Potentials using a Grid based method) [33]. Automated Topology Builder (ATB) [34] was used to further optimize the obtained geometry and to generate the topology compatible with GROMOS parameter sets [35].

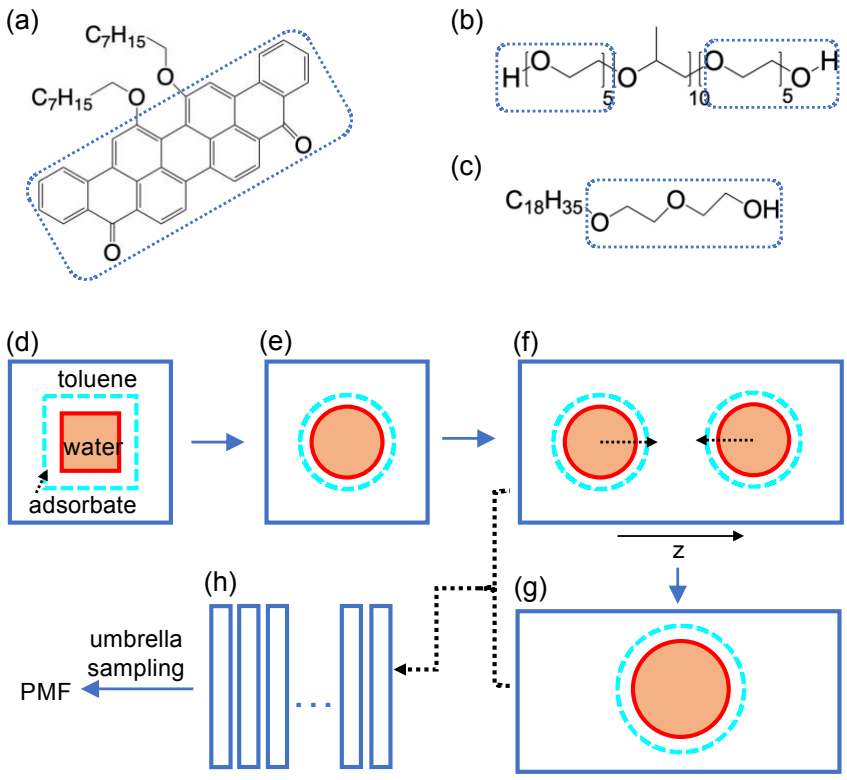

Figure 6.1. Molecular structure for (a) VO-79, (b) NisP ($(EO)_5(PO)_{10}(EO)_5$), and (c) NisB (Brij-93); (d-h) schematics of simulation procedure.

Details of the simulated systems are shown in Table 6.1. Sys. A0 represented the control system with no adsorbates. The systems with adsorbate were named by the type of adsorbates, e.g. sys. V1 contained VO-79 molecules. The adsorbate concentration was lower in sys. V1, P1, and B1 than in sys. V2, P2, and B2, respectively. Each system had two water droplets that were built by duplicating a system with a single water droplet. The systems with a single water droplet were named with "-S" appending to the name of their corresponding system with two water droplets. There were 96 VO-79 in sys. V1-S, 34 in sys. P1-S, and 77 in sys. B1-S. These numbers were chosen to obtain a similar surface coverage of the water droplet (approximately 46-47%) in V1-S, P1-S and B1-S, as shown in Appendix D1. There were 196 VO-79 molecules in sys. V2-S, so that

the mass concentration of VO-79 in sys. V2 was approximately twice that in sys. V1. Similarly, the mass concentration of NisP in sys. P2 was about twice the concentration of NisP in sys. P1. The mass concentration of NisB in sys. B2 was comparable to the mass concentration of NisP in sys. P2.

Table 6.1. System details. Surface coverage fraction was obtained from the equilibrated system containing a single water droplet.

sys.	adsorbate	mass concentration of adsorbate (ppm)	single water droplet		
			sys.	# of adsorbates	surfaces coverage fraction
A0	-	-	A0-S	-	-
V1	VO-79	44,789	V1-S	96	47%
P1	NisP	22,568	P1-S	34	47%
B1	NisB	17,553	B1-S	77	46%
V2	VO-79	97,558	V2-S	196	61%
P2	NisP	46,027	P2-S	66	72%
B2	NisB	45,807	B2-S	192	78%

6.2.2 Simulation details.

All simulations were performed by using GROMACS package [36-38] (version 5.0.7) with GROMOS force field parameter set 54A7 [39]. There were three phases in the simulations. First phase was the simulation for a single water droplet in sys. A0-S, V1-S, P1-S, B1-S, V2-S, P2-S, or B2-S, as shown in Fig. 6.1d (initial configuration) and Fig. 6.1e (final configuration). Second phase was the steered molecular dynamics (SMD) simulations where two water droplets were pulled towards each other till coalescence, as shown in Fig. 6.1f (initial configuration) and Fig. 6.1g (final configuration). Third phase was the umbrella sampling (US) simulations to generate the potential of mean force (PMF), as shown in Fig. 6.1h.

In each simulation of a single water droplet, as shown in Fig. 6.1d, a water box with dimension of 5×5×5 nm^3 was constructed and centered in a 14×14×14 nm^3 box. For the control system with no adsorbates, the water box was then solvated by toluene molecules. For systems with adsorbates, the adsorbate molecules were placed in arrays on the six sides of the water box, as shown Fig. 6.1d. The rest of the box was then solvated by toluene molecules. Each system with a single water droplet underwent energy minimization (EM) using steepest descent method, NVT equilibration, and production simulation in NpT ensemble. NVT equilibration was performed for 100 ps with position-restraints, where harmonic potential of force constant 1000 kJ/(mol·nm^2) was applied on the non-hydrogen atoms in adsorbate molecules. With the restraint removed, production simulation was carried out at 300 K and 1 bar. Pressure coupling was applied by using Parrinello-Rahman barostat with time constant (τ_p) of 1.0 ps. Velocity rescaling thermostat with a time constant (τ_T) of 0.1 ps was used for temperature coupling. LINCS [40] algorithm, Particle Mesh Ewald method for full electrostatics [41], and periodic boundary conditions in (x, y, z) directions were applied. Twin-range cut-offs were used for van der Waals and electrostatic interactions with cut-off of 1.4 nm. All simulations had a time step of 2 fs, and the simulation time for each system with a single droplet was 60 ns. After equilibrium, a single water droplet was formed and surrounded by the adsorbate molecules, as shown in Fig. 6.1e.

SMD simulations were performed to expedite the coalescence of two water droplets by applying external force on their centers of mass (COMs). To obtain two water droplets, the configuration of an equilibrated single droplet (as shown in 1e) was duplicated along z direction, forming a simulation box approximately 14×14×28 nm^3 in dimension, as shown in Fig. 6.1f. After EM and NVT equilibration following the same procedure as described above, SMD was carried out. The parameters in SMD were similar to those in the production MD in phase 1 with the

following exceptions. Firstly, the pressure coupling was removed and NVT ensemble was used in the SMD. [24,25] Secondly, COM pulling was applied on the water droplets, which were defined based on the initial configuration of the SMD (Fig. 6.1f). Specifically, each droplet contained a large cluster of water molecules where any water molecule had at least one neighboring water molecule within 0.35 nm [42]. The atom indices in this cluster were used to define the COM of the droplet, and a harmonic potential was applied on the two COMs with spring constant of 1000 kJ/(mol·nm^2). It was noteworthy that after EM and NVT equilibration just before SMD, the COMs of two water droplets may not be aligned exactly along z direction. The reaction coordination (ζ) was selected as the distance between the two COMs, i.e., along the head-on direction. COMs of both water droplets were pulled together along ζ at a net pull rate of 0.01 nm/ps. Such rate was selected based on the following considerations. Firstly, in Lemkul and Bevan's work [43] of dissociating two peptides, the trajectory and force profile resulted from pull rate of 0.01 nm/ps was almost identical to those resulted from the pull rate of 0.005 and 0.001 nm/ps. Secondly, the primary aim of SMD here was to generate the trajectory of water droplet coalescence, while more quantitative analysis on PMF was performed by US. The total pull time was 1.4 ns and a total of 140 configurations were obtained from every 10 ps of the 1.4 ns simulation. Since the COM distance in the initial configuration (Fig. 6.1f) was 14 nm, the two droplets merged into a single droplet (Fig. 6.1g) at the end of the SMD, with the final COM separation of approximately 0 nm.

US was carried out to compute the PMF along the reaction coordinate (ζ). The range of ζ was selected to sample from the maximum COM separation (~14 nm) to the separation where the water droplets merged. A total of 43-50 US windows were used, in order to render good overlap (Appendix D2) between the probability distributions from neighboring US simulations. [43,44] During each US simulation, an external biasing potential with spring constant of 2000 kJ/(mol·nm^2)

was applied on the COMs of the two droplets, at the corresponding US window. After a brief NVT equilibration, the US simulation was run for 2 ns by using an SMD at zero pull rate. Data collected from US was analyzed by weighted histogram analysis method (WHAM) [43,45] to generate the unbiased PMF as a function of the reaction coordinate (ζ).

6.3 Results and Discussion

6.3.1 Adsorbate film on water droplet

Fig. 6.2a shows the final configurations for systems containing a single water droplet. Without adsorbates (sys. A0-S), a sphere-like water droplet was formed in toluene. As shown Appendix D1, the diameter for the droplet (4074 water molecules) was estimated to be D_p = 6.18 nm (radius R_p = 3.09 nm). For sys. V1-S, most of the VO-79 molecules (90 out of 96) were adsorbed on the water droplet, forming a patchy film. In sys. P1-S and sys. B1-S, all the 34 NisP and 77 NisB molecules were adsorbed on the water droplets, resulting in surface coverage fraction comparable to sys. V1-S, as explained in Appendix D1 and shown in Table 6.1.

The thickness of the films was analyzed by the radial distribution function (RDF) of all atoms in the adsorbate molecules with respect to the COM of the water droplet. The results obtained by averaging data over the last 5 ns of simulation are shown in Fig. 6.2b for sys. V1-S, P1-S and B1-S, and in Fig. 6.2d for sys. V2-S, P2-S and B2-S. The distance (d) from the water droplet COM was normalized by the radius of the water droplet (R_p) on the horizontal axis of the plots. For each system in Fig. 6.2b, a single pronounced peak was located at d/R_p around 1.0-1.2, indicating the formation of a film on the surface of the water droplet. As shown in Appendix D3, the thickness of the adsorbate film was represented by the width of RDF peak in Fig. 6.2b, which from the thickest to thinnest followed: sys. V1 > sys. P1 > sys. B1.

RDFs for different atom groups in the adsorbates with respect to the COM of water droplet are plotted in Fig. 6.2c for sys. V1-S, P1-S and B1-S, and in Fig. 6.2e for sys. V2-S, P2-S and B2-S. The group of atoms located closer to the water phase was named group 1 (g1) for each type of adsorbates, which corresponded to the PA core in VO-79 and hydrophilic groups in NisP and NisB as marked in Fig. 6.1a-c. The other atom group, i.e. side chains in VO-79 and hydrophobic groups in NisP and NisB, was named group 2 (g2). The location and width of the RDF peaks are also summarized in Appendix D3. As shown in Fig. 6.2c and Appendix D3, the peak for group 1 of VO-79 was located at $d/R_p = 1.15$, which was closer to the droplet COM than the peak for group 2 ($d/R_p = 1.24$). This was attributed to the fact that the oxygen functionality in the PA core formed hydrogen bonds with the water molecules [46]. Similarly, the RDF peaks for group 1 in sys. P1-S and B1-S were closer to the water phase than the peaks for the hydrophobic groups. The surfactants had amphiphilic feature and the hydrophilic groups tend to interact with the water molecules. Comparing group 1 in sys. V1-S, sys. P1-S and B1-S, the location of RDF peak from highest to lowest was ranked: sys. V1-S > sys. P1-S (slightly) > sys. B1-S. It indicated that the hydrophilic group in NisP and NisB molecules were located closer to water phase than the core group in VO-79. For group 2 in sys. V1-S, sys. P1-S and B1-S, the location and width of RDF peak also followed the ranking of sys. V1-S > sys. P1-S > sys. B1-S.

For systems with higher concentration of adsorbates (sys. V2-S, P2-S, B2-S), as shown in Fig. 6.2a, protective films were also formed at the droplet surface. In Fig. 6.2d, a single peak was observed in each RDF curve, and the width of RDF peak for sys. V2-S, P2-S, B2-S was larger than the corresponding systems with less adsorbates, as shown in Appendix D3. Comparing different adsorbates, the thickness of the film followed the ranking of sys. V2-S > P2-S > B2-S. Observations in Fig. 6.2e were similar to those in Fig. 6.2c.

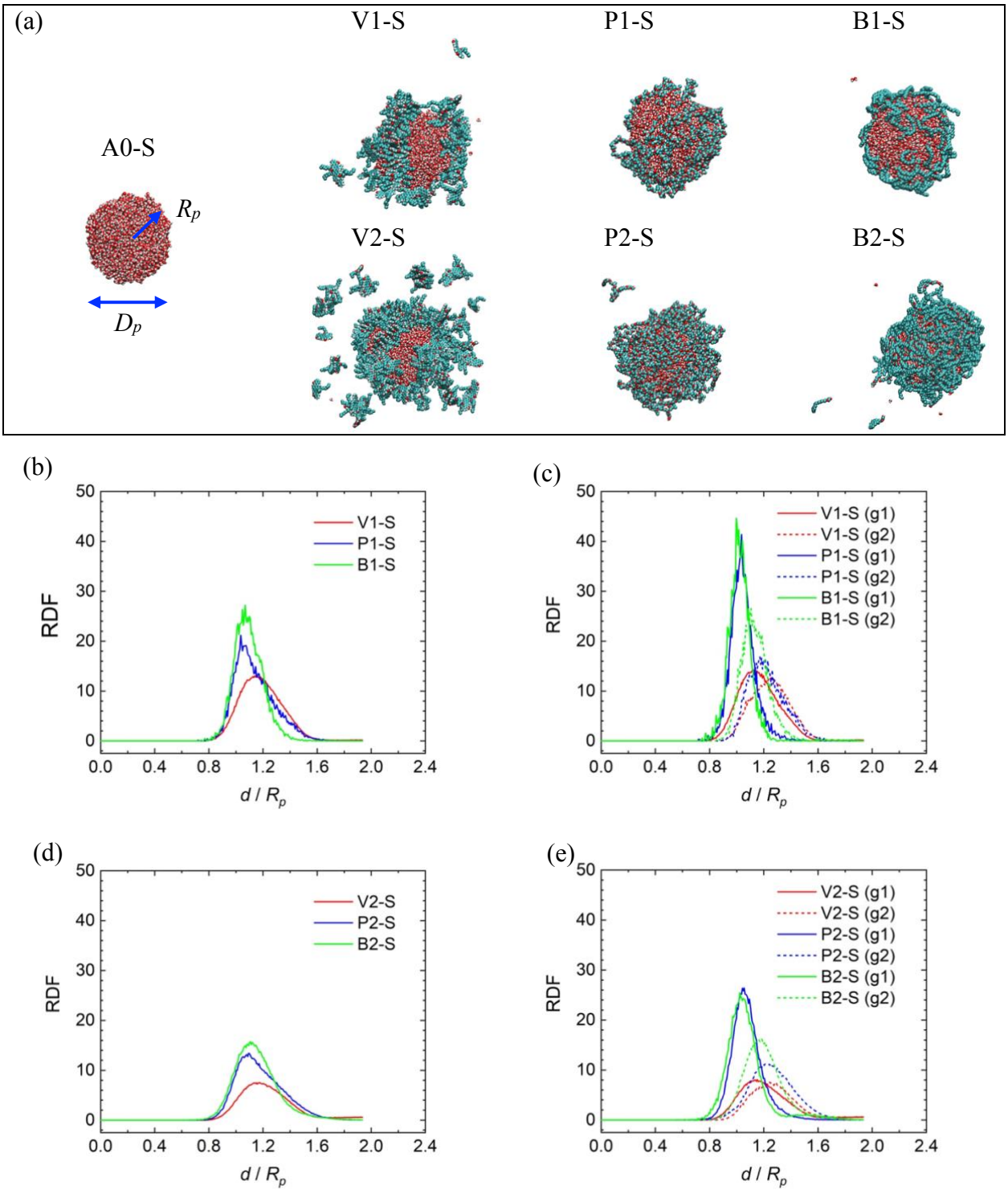

Figure 6.2. (a) Snapshot of final configurations for all systems containing a single water droplet (atoms were shown as van der Waals spheres, oxygen atoms: red; hydrogen atoms: grey; carbon atoms: cyan; toluene molecules eliminated for clarity); RDF for all atoms in adsorbate molecules

with respect to COM of water droplet for (b) sys. V1-S, P1-S, B1-S, and (d) sys. V2-S, P2-S, B2-S; RDF for atoms in PA core (g1) and side chains (g2) of VO-79, in hydrophilic (g1) and hydrophobic (g2) groups of NisP and NisB, with respect to COM of water droplet for (c) sys. V1-S, P1-S, B1-S, and (e) sys. V2-S, P2-S, B2-S.

6.3.2 Coalescence of water droplets

During the SMD, the two water droplets were pulled along the reaction coordinate (ζ), i.e. their COM separation. The snapshots for 0 ns, 0.7 ns, 0.8 ns, 0.9 ns, and 1.0 ns in SMD are shown in Fig. 6.3 for sys. A0, V1, P1, and B1 (from left to right). The additional snapshots, e.g. 1.1-1.4 ns for sys. A0, V1, P1, and B1 and 0-1.4 ns for sys. V2, P2, and B2 are shown in Appendix D4.

As shown in Fig. 6.3a, at t = 0 ns, ζ was approximately 14 nm (half of box length in z direction). With constant pulling rate at 0.01 nm/ps, ζ at 0.7 ns was around 7 nm, where the two droplets were in close proximity of each other. For sys. A0, water molecules from the two droplets started to contact at 0.8 ns and continued to merge at 0.9 ns and 1 ns. In sys. V1 (VO-79 as adsorbates), as the water droplets approached each other, the adsorbed VO-79 molecules redistributed on the surface, leaving the droplets uncovered in the head-on direction. At 0.8-1.0 ns, the water droplets contacted each other and merged. As shown in Appendix D4, during 1.1-1.4 ns, a single spherical droplet formed due to coalescence, and VO-79 molecules initially from different droplets redistributed on the merged larger droplet. For sys. P1, the NisP molecules also redistributed on the droplet surface from 0 to 0.7 ns and drainage of the NisP film between the two droplets was observed. There was a still gap between the two droplets at 0.8 ns, coalescence initiated at 0.9 ns and continued at 1.0 ns. As shown in Appendix D4, redistribution of NisP molecules was also observed on the merged droplet during 1.1-1.4 ns. Observations in sys. B1

were similar, except that the initiation of coalescence was delayed to 1 ns, with some NisB molecules still interfering with the contact between water droplets at 0.9 ns.

In Fig. 6.3b, the number of hydrogen bonds (H-bonds) between water molecules in different droplets is plotted against the reaction coordinate ζ (normalized by D_p). Four data points in each curve were highlighted, which corresponded to t = 0.7 ns, 0.8 ns, 0.9 ns and 1.0 ns in the SMD. For sys. A0 at t = 0.7 and 0.8 ns, the number of H-bonds were zero when the water droplets were close and about to make contact ($\zeta/D_p \sim$ 1.1-1.3). At t = 0.9 ns, the number of H-bonds were 393 and it increased dramatically to 1286 at t = 1.0 ns. Similar trend was observed for sys. V1. The number of H-bonds was zero before contact (t = 0.7 ns) and increased after coalescence began (t = 0.8 ns) and progressed (t = 0.9 and 1.0 ns). The curves sys. P1 and sys. B1 share the same trend, but with a delayed increase in the number of H-bonds, consistent with the observations shown in Fig. 6.3a.

As shown in the snapshots for sys. V2 in Appendix D4, many VO-79 molecules were dispersed in toluene phase (0 ns). During the approaching of water droplets (0-0.7 ns), the dispersed molecules were gradually excluded from the space between the two droplets. Similar to sys. V1, the VO-79 molecules redistributed on the droplet surfaces, which left water molecules uncovered in the head-on direction (Appendix D4). H-bonds were formed after 0.8 ns when the droplets started to merge, as shown in Fig. 6.3c. For sys. P2 from 0-0.8 ns, the NisP film became thinner and the NisP molecules redistributed on the surface of water droplets as shown in Appendix D4. However, the exposed water surface after NisP redistribution of was less apparent at 0.9 ns, due to the high surface coverage of NisP. Droplet coalescence started after 0.9 ns and H-bonds formed between them, as shown in Fig. 6.3c. NisB in sys. B2 formed a very uniform coating on

the droplet surfaces, as shown in Appendix D4. The merging of water droplets initiated, and H-bonds were formed after 1.0 ns, as shown in Fig. 6.3c.

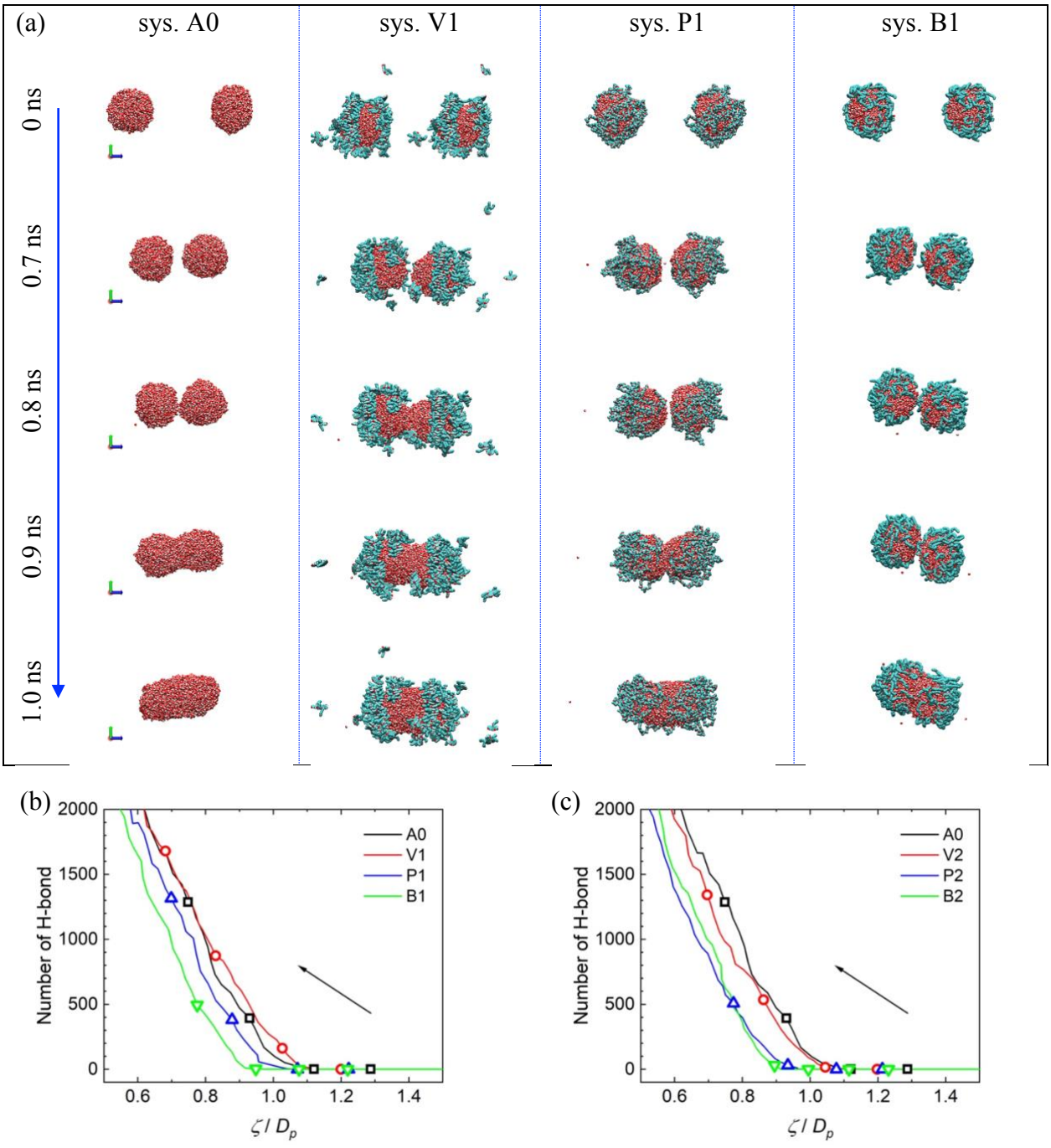

Figure 6.3. (a) Snapshots of the droplets at 0 ns, 0.7 ns, 0.8 ns, 0.9 ns, and 1.0 ns during SMD for sys. A0, V1, P1 and B1 (from left to right). Atoms are shown as van der Waals spheres, oxygen atoms: red; hydrogen atoms: grey; carbon atoms: cyan; toluene molecules eliminated for

clarity. Number of hydrogen bonds vs. the COM separation (normalized by diameter of water droplet) between two water droplets during SMD for (b) sys. V1, P1, B1; (c) sys. V2, P2, B2. (sys. A0 is shown as reference; data points at time = 0.7, 0.8, 0.9, 1.0 ns are highlighted; arrows show the direction of time evolution.)

6.3.3 Free energy and interaction force for water droplets coalescence.

PMF (ΔG) was plotted against the reaction coordinates ζ (normalized by D_p) in Fig. 6.4a. The range of reaction coordinate was selected to ensure sampling from the largest separation $\zeta / D_p \sim$ 2.25-2.27 to the point after the coalescence occurred. The largest separation in each system was used as the reference for zero potential ($G_0 = 0$). From the largest separation, PMF for sys. A0 slight decreased until $\zeta / D_p \sim 1.2$ and then drastically decreased. For sys. V1, the PMF increased to the maximum of ΔG_{max}=23.0 kcal/mol at $\zeta / D_p \sim 1.2$, followed by a rapid drop. The positive and increasing value of ΔG as the droplets approached each other (up to $\zeta / D_p \sim 1.2$) indicated repulsive interaction, and ΔG_{max} represented the energy barrier for droplet coalescence. Similar trend was also observed in the PMF for sys. P1 and sys. B1, and ΔG_{max} in these two systems were comparable to that in sys. V1., suggesting similar energy barrier caused by the three adsorbates. The difference among the three systems lied in the reaction coordinate at which ΔG_{max} occurred, which was $\zeta/D_p = 1.13$ in sys. P1 and $\zeta/D_p \sim 1.10$ in sys. B1.

As shown in Fig. 6.4b, the mean force (F) between the two water droplets was calculated from the negative derivative of the PMF curve as [47]:

$$F(\zeta) = -\frac{\partial \Delta G}{\partial \zeta} \tag{6.1}$$

Without adsorbates (sys. A0), the interaction between the water droplets was negligible (F close to zero) before $\zeta / D_p \sim 1.2$ but became attractive (negative F) as coalescence started. For the systems with adsorbates, F underwent three stages as the droplets approached. In the first stage where $\zeta/D_p > \sim 2.0$, F was positive (i.e., repulsive), and the repulsion was stronger in sys. V1 than in sys. P1 and B1. Within the second stage (transition point $< \zeta/D_p < 2.0$), F in each system gradually increased as ζ/D_p decreased, until a maximum (F_{max}) was reached. F_{max} was similar for sys. V1, P1, B1, being 37 pN, 35 pN, and 29 pN, respectively. And the transition points of ζ/D_p at F_{max} in sys. V1, P1, B1 was 1.47, 1.45, or 1.44, respectively. After the transition point, F started to decrease due to the attraction between water droplets and the formation of H-bonds between them as shown in Fig. 6.2b.

In Fig. 6.4a, similar increasing-decreasing trend was observed in the PMF curves for sys. V2, P2 or B2. The energy barrier for droplet coalescence was much higher for systems with more adsorbates (sys. V2, P2 or B2) than their counterparts that had less adsorbates (sys. V1, P1, or B1). Comparing different adsorbates, ΔG_{max} were ranked as sys. B2 > sys. V2 > sys. P2. As shown in Fig. 6.4b, the mean force F for sys. V2, P2 and B2 could also be distinguished in three stages, as was discussed for sys. V1, P1 and B2. In stage 1, F was again higher in sys. V2 than in sys. P2 or B2. However, in stage 2, F_{max} was quite different among the three systems and followed the same ranking for ΔG_{max}: sys. B2 (183 pN) > sys. V2 (98 pN) > sys. P2 (79 pN). The transition points at F_{max} were located at $\zeta/D_p \sim 1.41$ (sys. V2), 1.44 (sys. P2) and 1.16 (sys. B2), respectively.

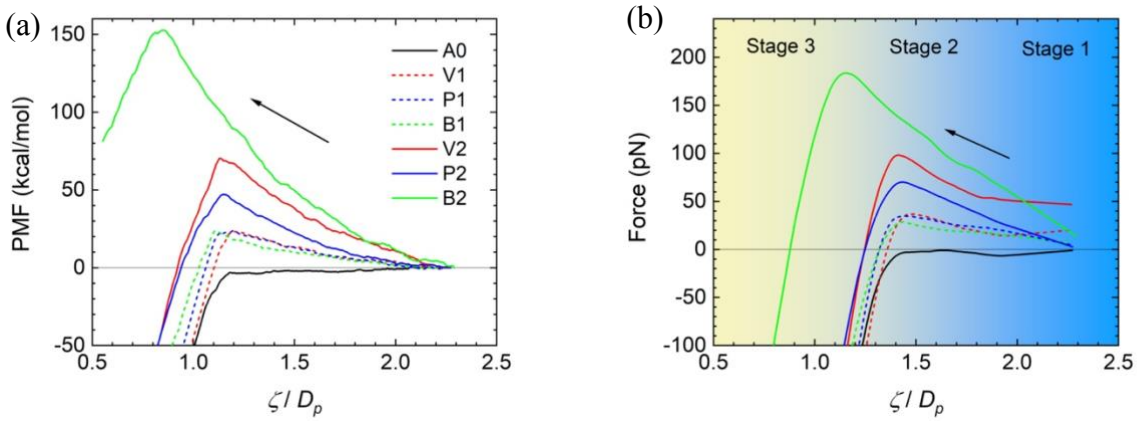

Figure 6.4. (a) PMF (ΔG) and (b) mean force (F) for between two water droplets as they approached each other (direction indicated by arrows).

6.3.4 Discussion

In this work, interfacially-active materials were adsorbed and formed barrier films on the surface of water droplets in toluene. As shown in Table 6.1 and Appendix D1, to achieve similar surface coverage, the mass concentration of VO-79 in sys. V1 had to be much higher than NisP in sys. P1 or NisB in sys. B1. With more adsorbates, the surface coverage by VO-79 (in sys. V2) was lower than the surface coverage by NisP (in sys. P2) or NisB (in sys. B2), even though the mass concentration of VO-79 was twice that of NisP or NisB. The more difficulty of coving the water droplet with VO-79 than with surfactants (NisP and NisB) was attributed to the following reasons. Firstly, VO-79 molecules were adsorbed mainly through the interaction between the PA cores in VO-79 and the water molecules, as shown in Fig. 6.2c and e. On the other hand, PA cores from different VO-79 molecules formed stackings through π–π interactions [22] as observed in Fig. 6.2a. Fig. 6.2c and e show that the atoms in the PA cores of VO-79 were located farther from the droplet surface than the hydrophilic groups in NisP and NisB, which indicates that the PA cores were almost perpendicular to the surface, as suggested by previous studies [23]. Such configuration

tended to provide a poorer surface coverage than one in which the PA cores are parallel to the surface. The hydrophilic chains in NisP and NisB were closely adsorbed (as shown in Fig. 6.2c and e) which facilitated coverage of the droplet surface. Secondly, VO-79 had high solubility in aromatic solvent (i.e. toluene) [23], thus, the VO-79 molecules were partially adsorbed and some remained dispersed in bulk toluene, as shown in Fig. 6.2a and 6.3a. Comparing the two surfactants, the hydrophilic groups in NisP and NisB were adsorbed at a similar distance from the COM of the droplet, while the hydrophobic groups in NisP were located farther than the hydrophobic groups in NisB (Fig. 6.2c and e). The NisP film was therefore less compact than the NisB film on the surface of water droplets, and the surface coverage was compromised. This can be seen from Table 6.1, where a higher mass concentration of NisP in sys. P1 was used to achieve a surface coverage comparable to sys. B1, and at similar mass concentration, surface coverage in sys. P2 was lower than that in sys. B2.

Based on the three stages of interaction force between water droplets, as shown in Fig. 6.4b, the mechanism of adsorbates stabilized water droplet coalescence is summarized as follows:

Stage 1: At large COM separation ($\zeta / D_p > 2.0$), water droplets were under influence of weak repulsive force, indicated by the positive mean force F in Fig. 6.4b. The repulsion in systems with VO-79 was stronger than that in systems with NisP or NisB, when comparing sys. V1 to P1 and B1, and sys. V2 to P2 and B2. The plausible explanation was that some VO-79 molecules were dispersed in the toluene phase and interfered with the approaching of water droplets. Thus, the repulsive force in this stage might be attributed to the hinderance from the dispersed molecules in the toluene phase.

Stage 2: When $\zeta/D_p < 2.0$ but greater than the transition point where F changes sign, steric repulsion between the adsorbate films hindered droplet coalescence and the repulsion became

stronger as the droplets got closer. Compared with the hydrophilic groups (g1), the hydrophobic groups (g2) in the adsorbates were located farther from the surface of water droplets, as shown in Fig. 6.2c and e. With water droplets approaching, the hydrophobic groups on different droplets came to contact first. At the same time, the steric repulsion pushed the adsorbate molecules away from the contact zone and drove them to redistribute on the droplet surface, as shown in the snapshots in Fig. 6.3a and Appendix D4. If the droplet surfaces were only partially covered (sys. V1, P1, B1), there was sufficient room for adsorbate redistribution, leaving the contact zone exposed, as shown in Fig. 6.3a. The attractive interaction between water molecules reduced the mean force F to zero at the transition point (ζ/D_p = 1.47, 1.45 and 1.44 for sys. V1, P1 and B1 respectively). Similar energy barrier (ΔG_{max}) and maximum force (F_{max}) was observed in sys. V1, P1 and B1, as shown in Fig. 6.4a-b, which might be attributed to the similar surface coverage fraction of adsorbates. For systems with higher surface coverage (sys. V2, P2, B2), the majority of the droplet surface was covered by the adsorbates, as shown in Fig. 6.2a. Consequently, the repulsive force was stronger in sys. V2, P2, B2 compared with sys. V1, P1, B1, respectively. ζ/D_p at the transition point was also smaller in V2, P2, B2, being 1.41, 1.44 and 1.16, respectively. However, there was still a limited surface for adsorbates to redistribute. As shown in Fig. 6.4b, sys. B2 had stronger repulsive force than sys. V2 and P2, probably due to the larger surface coverage in sys. B2 and less adsorbates drained between the water droplets. Additionally, the adsorbate film in sys. B2 was thinner and the hydrophobic groups were located closer to the water droplet as compared to sys. V2 and P2. Consequently, it was more difficult for NisB to redistribute (Appendix D4), resulting in higher F_{max} in sys. B2. Sys. P2 had higher surface coverage but lower F_{max} than sys. V2. One plausible explanation is that the long hydrophobic chains in NisP assisted the redistribution of molecules on the surface of water droplets. As shown in Fig. 6.3a, some NisB

molecules were still on the surface of water droplets at the head-on direction of coalescence in sys. B1 at 0.8 ns and 0.9 ns, while the surface of water droplets was uncovered in the head-on direction in sys. P1 at 0.8 ns.

Stage 3: At the final stage of coalescence, where ζ/D_p is smaller than the transition point, the exposed water molecules from the two droplets interacted and formed H-bonds. As shown in Fig. 6.3b-c, the number of H-bonds between two water droplets dramatically increased after the merging of water droplets. Strong H-bonds between water molecules counteracted with the steric repulsion between adsorbates, which led to decrease in the mean force (increasing attraction). Also, the adsorbate molecules on different water droplets tended to associate (as shown in Appendix D4), which further facilitated the coalescence.

From the PMF point of view (as shown in Fig. 6.4a), ΔG increased when water droplets were initially approaching, indicating that the coalescence was energetically unfavorable in stages 1 and 2. In the other word, the water droplets were stabilized by the adsorbates. At stage 3, the formation H-bond between water molecules and association of adsorbates molecules caused spontaneous coalescence as the PMF decreased from its peak value.

Understanding the process of coalescence between adsorbate stabilized water droplets provides useful implications on water-in-oil emulsification and demulsification. PAC molecules (VO-79) were adsorbed and formed patchy film at the water/toluene interface. The water droplets were stabilized by the adsorption of VO-79 molecules, due to the steric repulsion between the interfacial films. It was consistent with Shi et al.'s [15] AFM measurements that the interfacially adsorbed asphaltenes sterically hindered the water droplets coalescence. Also, this work proposed that the dispersed VO-79 molecules contributed to the long-range stability of water droplets, which was consistent with the previous hypothesis from Jian et al. [48] During chemical demulsification,

the non-ionic surfactants were adsorbed on the water/oil interface, break up the interfacial film and enhance the film drainage, which contributed to the destabilization of the asphaltenes-stabilized water droplets in oil. [49,50]. Comparing the two surfactants, the hydrophobic chains in triblock copolymer NisP were located farther from the water droplets than the hydrophobic chains of NisB. Thus, the NisP film was less compact than the NisB film at the surface of water droplets. Also, at similar mass concentration (sys. P2 and B2), the surface of water droplets was less covered in sys. P2 (72%) than in sys. B2 (78%), which resulted in lower energy barrier and repulsive force for water droplets coalescence. NisP molecules redistributed and were drained during head-on collision of water droplets. It suggested that molecular structure for NisP was beneficial for the destabilization of water droplets in emulsions.

6.4 Conclusion

This work used molecular dynamics simulations to quantitatively probe the free energy and interaction force for water droplets coalescence in toluene with the presence of adsorbates, including polycyclic aromatic compound (VO-79) and non-ionic surfactants (PEO-PPO triblock copolymer; Brij-93). Three stages of water droplets coalescence were distinguished as follows. Stage 1: When the center of mass (COMs) of water droplets were far separated (more than twice of the droplet diameter), weak repulsive force hindered the approaching of water droplets. The repulsion was enhanced if some molecules, e.g. VO-79, were dispersed in toluene phase. Stage 2: With the approaching of water droplets, the repulsion between them became stronger due to the increase of steric repulsion between the adsorbate films, mainly the hydrophobic parts. The steric repulsion also induced the redistribution of adsorbates on the water droplets, leaving uncovered water droplets surface facing each other. Stage 3: The uncovered water molecules tended to interact with the uncovered water molecules on the other droplets by forming H-bonds. Also, the

adsorbates became interconnect on the surface of merged water droplets. These interactions contributed to the attraction for the water droplets coalescence, which counteracted with the steric repulsion.

The energy barrier and maximum repulsion for water droplet coalescence was similar for systems with different adsorbate but similar surface coverage fraction (46-47%). At systems with higher surface coverage (61-78%), the hindrance for water droplets became more significant, indicated by the higher energy barrier and maximum repulsion. Among these systems, the loose structure of NisP film and the long hydrophobic chain in the NisP molecules enhanced the redistribution of NisP on the surface compared with NisB. It resulted in a lower energy barrier and repulsion during the water droplets coalescence, which was beneficial for the destabilization of water droplets in emulsions.

References

[1] R. Shimizu, H. Tanaka, A Novel Coarsening Mechanism of Droplets in Immiscible Fluid Mixtures, Nature Communications. 6 (2015) 7407.

[2] A.B. Pawar, M. Caggioni, R. Ergun, R.W. Hartel, P.T. Spicer, Arrested Coalescence in Pickering Emulsions, Soft Matter. 7 (2011) 7710.

[3] H. Fan, A. Striolo, Mechanistic Study of Droplets Coalescence in Pickering Emulsions, Soft Matter. 8 (2012) 9533.

[4] M.H. Factorovich, V. Molinero, D.A. Scherlis, Vapor Pressure of Water Nanodroplets, J. Am. Chem. Soc. 136 (2014) 4508–4514.

[5] J. Kamp, J. Villwock, M. Kraume, Drop Coalescence in Technical Liquid/Liquid Applications: A Review on Experimental Techniques and Modeling Approaches, Reviews in Chemical Engineering. 33 (2017) 1–47.

[6] D.J. Lee, H.M. Kim, Y.S. Song, J.R. Youn, Water Droplet Bouncing and Superhydrophobicity Induced by Multiscale Hierarchical Nanostructures, ACS Nano. 6 (2012) 7656–7664.

[7] M.-L. Liao, S.-P. Ju, S.-H. Yang, Coalescence Behavior of Water Nanoclusters: Temperature and Size Effects, J. Phys. Chem. C. 111 (2007) 6927–6932.

[8] S. Perumanath, M.K. Borg, M.V. Chubynsky, J.E. Sprittles, J.M. Reese, Droplet Coalescence is Initiated by Thermal Motion, Phys. Rev. Lett. 122 (2019) 104501.

[9] D.G.A.L. Aarts, H.N.W. Lekkerkerker, H. Guo, G.H. Wegdam, D. Bonn, Hydrodynamics of Droplet Coalescence, Phys. Rev. Lett. 95 (2005) 164503.

[10] P. Chakraborty, M.R. Zachariah, On the Structure of Organic-Coated Water Droplets: From "Net Water Attractors" To "Oily" Drops, Journal of Geophysical Research: Atmospheres. 116.D21 (2011).

[11] L. Zhang, L. Xie, X. Cui, J. Chen, H. Zeng, Intermolecular and Surface Forces at Solid/Oil/Water/Gas Interfaces in Petroleum Production, Journal of Colloid and Interface Science. 537 (2019) 505–519.

[12] Y. Qiu, V. Molinero, Morphology of Liquid–Liquid Phase Separated Aerosols, J. Am. Chem. Soc. 137 (2015) 10642–10651.

[13] L. Xie, C. Shi, X. Cui, H. Zeng, Surface Forces and Interaction Mechanisms of Emulsion Drops and Gas Bubbles in Complex Fluids, Langmuir. 33 (2017) 3911–3925.

[14] S. Zhang, L. Zhang, X. Lu, C. Shi, T. Tang, X. Wang, Q. Huang, H. Zeng, Adsorption Kinetics of Asphaltenes at Oil/Water Interface: Effects of Concentration and Temperature, Fuel. 212 (2018) 387–394.

[15] C. Shi, L. Zhang, L. Xie, X. Lu, Q. Liu, J. He, C.A. Mantilla, F.G.A. Van den berg, H. Zeng, Surface Interaction of Water-in-Oil Emulsion Droplets with Interfacially Active Asphaltenes, Langmuir. 33 (2017) 1265–1274.

[16] E. Pensini, D. Harbottle, F. Yang, P. Tchoukov, Z. Li, I. Kailey, J. Behles, J. Masliyah, Z. Xu, Demulsification Mechanism of Asphaltene-Stabilized Water-in-Oil Emulsions by a Polymeric Ethylene Oxide–Propylene Oxide Demulsifier, Energy Fuels. 28 (2014) 6760–6771.

[17] Y. Chen, C. Shen, G.P. Peterson, Hydrodynamics and Morphologies of Droplet Coalescence, Ind. Eng. Chem. Res. 54 (2015) 9257–9262.

[18] A.M. Dokter, S. Woutersen, H.J. Bakker, Inhomogeneous Dynamics in Confined Water Nanodroplets, Proceedings of the National Academy of Sciences. 103 (2006) 15355–15358.

[19] S. Vaitheeswaran, D. Thirumalai, Hydrophobic and Ionic Interactions in Nanosized Water Droplets, J. Am. Chem. Soc. 128 (2006) 13490–13496.

[20] B.-B. Wang, X.-D. Wang, W.-M. Yan, T.-H. Wang, Molecular Dynamics Simulations on Coalescence and Non-coalescence of Conducting Droplets, Langmuir. 31 (2015) 7457–7462.

[21] L. Zhao, P. Choi, Molecular Dynamics Simulation of The Coalescence of Nanometer-Sized Water Droplets In n-Heptane, The Journal of Chemical Physics. 120 (2004) 1935–1942.

[22] C. Jian, H. Zeng, Q. Liu, T. Tang, Probing the Adsorption of Polycyclic Aromatic Compounds onto Water Droplets Using Molecular Dynamics Simulations, J. Phys. Chem. C. 120 (2016) 14170–14179.

[23] C. Jian, Q. Liu, H. Zeng, T. Tang, Effect of Model Polycyclic Aromatic Compounds on the Coalescence of Water-in-Oil Emulsion Droplets, J. Phys. Chem. C. 121 (2017) 10382–10391.

[24] C.Y. Pak, W. Li, Y.-L. Steve Tse, Free Energy and Dynamics of Water Droplet Coalescence, J. Phys. Chem. C. 122 (2018) 22975–22984.

[25] C.Y. Pak, W. Li, Y.-L. Steve Tse, Free Energy and Dynamics of Organic-Coated Water Droplet Coalescence, J. Phys. Chem. C. 124 (2020) 8749–8757.

[26] D. Pradilla, S. Simon, J. Sjöblom, Mixed Interfaces of Asphaltenes and Model Demulsifiers, Part II: Study of Desorption Mechanisms at Liquid/Liquid Interfaces, Energy Fuels. 29 (2015) 5507–5518.

[27] D. Pradilla, S. Simon, J. Sjöblom, Mixed Interfaces of Asphaltenes And Model Demulsifiers Part I: Adsorption and Desorption of Single Components, Colloids and Surfaces A: Physicochemical and Engineering Aspects. 466 (2015) 45–56.

[28] X. Sun, H. Zeng, T. Tang, Effect of Non-Ionic Surfactants on the Adsorption of Polycyclic Aromatic Compounds at Water/Oil Interface: A Molecular Simulation Study, Journal of Colloid and Interface Science. 586 (2021) 766–777.

[29] X. Sun, H. Zeng, T. Tang, Molecular Simulation of Folding and Aggregation of Multi-Core Polycyclic Aromatic Compounds, Journal of Molecular Liquids. 310 (2020) 113248.

[30] T. Lan, H. Zeng, T. Tang, Molecular Dynamics Study on the Mechanism of Graphene Oxide to Destabilize Oil/Water Emulsion, J. Phys. Chem. C. 123 (2019) 22989–22999.

[31] M.J. Frisch, G.W. Trucks, H.B. Schlegel, G.E. Scuseria, M.A. Robb, J.R. Cheeseman, G. Scalmani, V. Barone, G.A. Petersson, H. Nakatsuji, et al., Gaussian 16 Rev. C.01, Wallingford, CT, 2016.

[32] A.D. Becke, A New Mixing of Hartree–Fock And Local Density-Functional Theories, The Journal of Chemical Physics. 98 (1993) 1372–1377.

[33] C.M. Breneman, K.B. Wiberg, Determining Atom-Centered Monopoles from Molecular Electrostatic Potentials. The Need for High Sampling Density in Formamide Conformational Analysis, Journal of Computational Chemistry. 11 (1990) 361–373.

[34] A.K. Malde, L. Zuo, M. Breeze, M. Stroet, D. Poger, P.C. Nair, C. Oostenbrink, A.E. Mark, An Automated Force Field Topology Builder (ATB) and Repository: Version 1.0, J. Chem. Theory Comput. 7 (2011) 4026–4037.

[35] L.D. Schuler, X. Daura, W.F. van Gunsteren, An Improved GROMOS96 Force Field for Aliphatic Hydrocarbons in The Condensed Phase, Journal of Computational Chemistry. 22 (2001) 1205–1218.

[36] D.V.D. Spoel, E. Lindahl, B. Hess, G. Groenhof, A.E. Mark, H.J.C. Berendsen, GROMACS: Fast, Flexible, And Free, Journal of Computational Chemistry. 26 (2005) 1701–1718.

[37] E. Lindahl, B. Hess, D. van der Spoel, GROMACS 3.0: A Package for Molecular Simulation and Trajectory Analysis, J Mol Model. 7 (2001) 306–317.

[38] H.J.C. Berendsen, D. van der Spoel, R. van Drunen, GROMACS: A Message-Passing Parallel Molecular Dynamics Implementation, Computer Physics Communications. 91 (1995) 43–56.

[39] C. Oostenbrink, A. Villa, A.E. Mark, W.F.V. Gunsteren, A Biomolecular Force Field Based on the Free Enthalpy of Hydration and Solvation: The GROMOS Force-Field Parameter Sets 53a5 and 53a6, Journal of Computational Chemistry. 25 (2004) 1656–1676.

[40] B. Hess, P-LINCS: A Parallel Linear Constraint Solver for Molecular Simulation, J. Chem. Theory Comput. 4 (2008) 116–122.

[41] U. Essmann, L. Perera, M.L. Berkowitz, T. Darden, H. Lee, L.G. Pedersen, A Smooth Particle Mesh Ewald Method, The Journal of Chemical Physics. 103 (1995) 8577–8593.

[42] E.M. Sevick, P.A. Monson, J.M. Ottino, Monte Carlo Calculations of Cluster Statistics in Continuum Models of Composite Morphology, The Journal of Chemical Physics. 88 (1988) 1198–1206.

[43] J.A. Lemkul, D.R. Bevan, Assessing the Stability of Alzheimer's Amyloid Protofibrils Using Molecular Dynamics, J. Phys. Chem. B. 114 (2010) 1652–1660.

[44] W. You, Z. Tang, C.A. Chang, Potential Mean Force from Umbrella Sampling Simulations: What Can We Learn and What Is Missed?, J. Chem. Theory Comput. 15 (2019) 2433–2443.

[45] J.S. Hub, B.L. de Groot, D. van der Spoel, g_wham—A Free Weighted Histogram Analysis Implementation Including Robust Error and Autocorrelation Estimates, J. Chem. Theory Comput. 6 (2010) 3713–3720.

[46] C. Jian, M.R. Poopari, Q. Liu, N. Zerpa, H. Zeng, T. Tang, Reduction of Water/Oil Interfacial Tension by Model Asphaltenes: The Governing Role of Surface Concentration, J. Phys. Chem. B. 120 (2016) 5646–5654.

[47] D.I. Kopelevich, One-dimensional Potential of Mean Force Underestimates Activation Barrier for Transport Across Flexible Lipid Membranes, The Journal of Chemical Physics. 139 (2013) 134906.

[48] C. Jian, Q. Liu, H. Zeng, T. Tang, Effect of Model Polycyclic Aromatic Compounds on the Coalescence of Water-in-Oil Emulsion Droplets, J. Phys. Chem. C. 121 (2017) 10382–10391.

[49] A. Le Follotec, I. Pezron, C. Noik, C. Dalmazzone, L. Metlas-Komunjer, Triblock Copolymers as Destabilizers of Water-In-Crude Oil Emulsions, Colloids and Surfaces A: Physicochemical and Engineering Aspects. 365 (2010) 162–170.

[50] D. Wang, D. Yang, C. Huang, Y. Huang, D. Yang, H. Zhang, Q. Liu, T. Tang, M. Gamal El-Din, T. Kemppi, B. Perdicakis, H. Zeng, Stabilization Mechanism and Chemical Demulsification Of Water-In-Oil and Oil-in-Water Emulsions in Petroleum Industry: A Review, Fuel. 286 (2021) 119390.

Chapter 7. Conclusion and Future Perspectives

7.1 Conclusion

In this dissertation, a series of molecular dynamics (MD) simulations was performed to investigate the colloidal behaviors of model asphaltenes. Mechanistic understanding on the aggregation and interfacial behaviors of model asphaltenes was provided at atomic level. Two questions on the aggregation of model asphaltenes were answered, firstly, the relations between intramolecular flexibility in archipelago asphaltenes and the aggregation; secondly, the effect of salinity in aqueous phase on the aggregation of model continental asphaltenes. The other two important topics in the interfacial behaviors of model asphaltenes were elucidated, including the effect of non-ionic surfactants on the adsorption of asphaltenes, and the interaction between stabilized water droplets with adsorbed asphaltenes or model demulsifiers.

In chapter 3, archipelago model asphaltenes had intramolecular flexibility and may exhibit folding between different polycyclic aromatic cores. In water, the single dispersed archipelago model asphaltene preferred unfolded states and had low internal flexibility. When multiple archipelago model asphaltenes formed aggregates in water, the folded stated became dominate. The folding behavior of archipelago model asphaltene was further altered if coaggregation between continental and archipelago model asphaltenes occurred in water. In heptane or toluene, the archipelago type asphaltenes had higher internal flexibility than in water and could easily change between folded and unfolded states whether a single archipelago molecule presented or multiple molecules aggregated. Co-aggregation between continental and archipelago model asphaltenes tended to make archipelago type asphaltenes more flexible in heptane, while the effect was insignificant in toluene. Chapter 4 unveiled the effect of NaCl concentration on the

aggregation of four continental model asphaltenes with different side chain length. For model asphaltenes with long side chain length, hydrophobic interactions contributed to the association between asphaltenes. NaCl concentration had non-monotonic effect on the hydrophobic interactions, thus the aggregation of asphaltenes with long side chains was promoted at low NaCl concentration and suppressed at high NaCl concentration. With moderate side chain length, the model asphaltenes were under influence of the mutual effect of NaCl concentration on the side chain-side chain, core-core, and core-side chain interactions. The NaCl had significant effect on the core-core interactions during the aggregation of model asphaltenes with shortest side chain length, while the effect on side chain-side chain interaction still played a role in the aggregation.

Chapter 5 illustrated the effect of non-ionic surfactants on the adsorption of model asphaltenes at water/oil interface. A comprehensive set of simulations was carried out by employing various important parameters, such as asphaltene types (archipelago or continental), solvent types to represent oil phase (toluene or heptane), model demulsifiers (PEO-PPO-PEO triblock copolymer or Brij-93), and demulsifier concentrations (low or high). Archipelago asphaltenes tended to form small and loosely structured aggregates at the interface. More archipelago asphaltenes were adsorbed at water/heptane interface than at water/toluene interface. While continental asphaltenes formed larger and more compact aggregates than archipelago asphaltenes, and all 32 continental asphaltenes were completely adsorbed at water/toluene and water/heptane interfaces. Model demulsifiers were adsorbed closer than the model asphaltenes to the water phase. The adsorbed demulsifiers interacted with the water phase and interfered the interaction between model asphaltenes and water phase. Thus, desorption of asphaltenes was induced in the systems with archipelago asphaltenes at water/toluene and water/heptane interfaces when Brij-93 added, and in systems with archipelago asphaltenes at water/toluene interface when

copolymer added. For archipelago asphaltenes at water/heptane interface with copolymer added, co-adsorption between asphaltenes and demulsifiers was observed. With continental asphaltenes adsorption, adding demulsifiers resulted in co-adsorption between asphaltenes and demulsifiers at both water/toluene and water/heptane interfaces. Chapter 6 investigated the interaction between water droplets with adsorption of continental model asphaltene (VO-79), model demulsifiers (PEO-PPO-PEO triblock copolymer or Brij-93). The water droplets coalescence was classified into three stages based on the interaction force derived from the potential of mean force. In the first stage, where the center of masses (COMs) separation between water droplets was greater than twice the droplet size, the water droplets underwent repulsive force, mainly attributing to the dispersed adsorbate molecules in toluene phase. Comparing systems with similar surface coverage, VO-79 molecules had more dispersed molecules in toluene phase, thus the repulsive force in the first stage was higher in the systems with VO-79 than the systems with model demulsifiers. In the second stage, the steric repulsion between the adsorbate film induced the increase of repulsive force during the approaching of water droplets. At the same time, the adsorbate molecules redistributed on the surface of water droplets, leaving the water molecules uncovered in the head-on direction. The maximum repulsive force for water droplets coalescence was positively correlated to the surface coverage of adsorbates on the surface. In the third stage, the repulsive force started to drop due to the formation of hydrogen bonds between water molecules in two water droplets. At similar concentration of model demulsifiers, copolymer coated water droplets had weaker repulsive force than Brij-93 coated water droplets, when the surface coverage of water droplets was high (71-78%).

Overall, the work in this dissertation provided mechanistic understanding of the colloidal properties of model asphaltenes at atomic level, which shed light to solving the problems in

petroleum industries related to the aggregation of asphaltenes and interfacial adsorption of asphaltenes.

7.2 Future Perspectives

The following studies are suggested to be investigated in the future.

(1) Stabilization of water-in-oil emulsions has been commonly attributed to the formation of rigid and solid film at the water/oil interface, as reviewed in Chapter 2. The interfacial behavior of asphaltene were dependent on their molecule structures, including the polarity, architecture of PA cores, and the presence of heteroatoms etc. Researchers have made hypothesis on the relations between polarity of asphaltenes and the stability of water-in-oil emulsions. While the effect of molecules structures of model asphaltenes on the formation of film at water/oil interface and the stability of water-in-oil emulsions has not been investigated. MD simulations could be used to study various model asphaltenes with different structures, whether as single component or in mixtures. It will help identity the effect of molecule structures of asphaltenes on the stability of emulsions.

(2) The interfacial properties of water/oil interface, such as interfacial tension, are dependent on the salinity in aqueous phase. Through MD simulations, the interfacial tension at the water/oil interface with presence of asphaltenes and demulsifiers could be obtained, which can be compared with the experimental measurements. Also, the interaction between asphaltenes and demulsifiers can be observed and investigated by using MD simulations, which could not be achieved by experimental measurements alone. The study could investigate the adsorption of model asphaltenes and demulsifiers at interface oil and brine water with various salinity, in order to illustrate the effect of salinity on the stability of water/oil interface with asphaltenes and demulsifiers.

(3) Various demulsifiers have been used to break up the stable water-in-oil emulsions, especially the PEO-PPO-PEO copolymers with different structures. It is demanding to probe the interaction force between water droplets with presence of asphaltenes and different polymeric demulsifiers. Beside quantifying the interaction force, MD simulations could also provide observation on the movement of demulsifiers on the surface of water droplets. It will provide mechanistic understanding on the demulsification mechanism and thus improve the efficiency in the demulsification.

Bibliography

Aarts, D. G. A. L., Lekkerkerker, H. N. W., Guo, H., Wegdam, G. H., & Bonn, D. (2005). Hydrodynamics of Droplet Coalescence. Physical Review Letters, 95(16), 164503.

Abdel-Shafy, H. I., & Mansour, M. S. (2016). A Review on Polycyclic Aromatic Hydrocarbons: Source, Environmental Impact, Effect on Human Health and Remediation. Egyptian Journal of Petroleum, 25(1), 107–123.

Acevedo, S., Castro, A., Vásquez, E., Marcano, F., & Ranaudo, M. A. (2010). Investigation of Physical Chemistry Properties of Asphaltenes Using Solubility Parameters of Asphaltenes and Their Fractions A1 and A2. Energy & Fuels, 24(11), 5921–5933.

Achten, C., & Andersson, J. T. (2015). Overview of Polycyclic Aromatic Compounds (PAC). Polycyclic Aromatic Compounds, 35(2–4), 177–186.

Adamson, B. D., Skeen, S. A., Ahmed, M., & Hansen, N. (2018). Detection of Aliphatically Bridged Multi-Core Polycyclic Aromatic Hydrocarbons in Sooting Flames with Atmospheric-Sampling High-Resolution Tandem Mass Spectrometry. The Journal of Physical Chemistry A, 122(48), 9338–9349.

Adilbekova, A. O., Omarova, K. I., Karakulova, A., & Musabekov, K. B. (2015). Nonionic Surfactants Based on Polyoxyalkylated Copolymers Used as Demulsifying Agents. Colloids and Surfaces A: Physicochemical and Engineering Aspects, 480, 433–438.

Alvariño, C., Pía, E., García, M. D., Blanco, V., Fernández, A., Peinador, C., & Quintela, J. M. (2013). Dimensional Matching of Polycyclic Aromatics with Rectangular Metallacycles: Insertion Modes Determined by [C-H···π] Interactions. Chemistry – A European Journal, 19(45), 15329–15335.

Andrews, A. B., McClelland, A., Korkeila, O., Demidov, A., Krummel, A., Mullins, O. C., & Chen, Z. (2011). Molecular Orientation of Asphaltenes and PAH Model Compounds in Langmuir−Blodgett Films Using Sum Frequency Generation Spectroscopy. Langmuir, 27(10), 6049–6058.

Anton, N., Vandamme, T. F., & Bouriat, P. (2013). Dilatational Rheology of a Gel Point Network Formed by Nonionic Soluble Surfactants at The Oil–Water Interface. Soft Matter, 9(4), 1310–1318.

Arantes, P. R., Polêto, M. D., John, E. B. O., Pedebos, C., Grisci, B. I., Dorn, M., & Verli, H. (2019). Development of GROMOS-Compatible Parameter Set for Simulations of Chalcones and Flavonoids. The Journal of Physical Chemistry B, 123(5), 994–1008.

Aray, Y., Hernández-Bravo, R., Parra, J. G., Rodríguez, J., & Coll, D. S. (2011). Exploring the Structure–Solubility Relationship of Asphaltene Models in Toluene, Heptane, and Amphiphiles Using a Molecular Dynamic Atomistic Methodology. The Journal of Physical Chemistry A, 115(42), 11495–11507.

Aste, T., & Di Matteo, T. (2006). Nanometric Architectures: Emergence of Efficient Non-Crystalline Atomic Organization in Nanostructures. In Nanostructure Control of Materials (pp. 32–56). Elsevier.

Aumaitre, C., & Morin, J.-F. (2019). Polycyclic Aromatic Hydrocarbons as Potential Building Blocks for Organic Solar Cells. The Chemical Record, 19(6), 1142–1154.

Barré, L., Jestin, J., Morisset, A., Palermo, T., & Simon, S. (2009). Relation between Nanoscale Structure of Asphaltene Aggregates and their Macroscopic Solution Properties. Oil & Gas Science and Technology – Rev. IFP, 64(5), 617–628.

Becke, A. D. (1993). A New Mixing of Hartree–Fock and Local Density-Functional Theories. The Journal of Chemical Physics, 98(2), 1372–1377.

Berendsen, H. J. C., van der Spoel, D., & van Drunen, R. (1995). GROMACS: A Message-Passing Parallel Molecular Dynamics Implementation. Computer Physics Communications, 91(1–3), 43–56.

Bernardez, L. A., & Ghoshal, S. (2008). Solubilization Kinetics for Polycyclic Aromatic Hydrocarbons Transferring from A Non-Aqueous Phase Liquid to Non-Ionic Surfactant Solutions. Journal of Colloid and Interface Science, 320(1), 298–306.

Borges, B., Rondón, M., Sereno, O., & Asuaje, J. (2009). Breaking of Water-in-Crude-Oil Emulsions. 3. Influence of Salinity and Water−Oil Ratio on Demulsifier Action. Energy & Fuels, 23(3), 1568–1574.

Breneman, C. M., & Wiberg, K. B. (1990). Determining Atom-Centered Monopoles from Molecular Electrostatic Potentials. The Need for High Sampling Density in Formamide Conformational Analysis. Journal of Computational Chemistry, 11(3), 361–373.

Byambajav, E., & Ohtsuka, Y. (2003). Cracking Behavior of Asphaltene in the Presence of Iron Catalysts Supported on Mesoporous Molecular Sieve with Different Pore Diameters. Fuel, 82(13), 1571–1577.

Cendejas, G., Arreguín, F., Castro, L. V., Flores, E. A., & Vazquez, F. (2013). Demulsifying Super-Heavy Crude Oil with Bifunctionalized Block Copolymers. Fuel, 103, 356–363.

Chaala, A., Benallal, B., & Hachelef, S. (1994). Investigation on the Flocculation of Asphaltenes and the Colloidal Stability of the Crude Oil Fraction. The Canadian Journal of Chemical Engineering, 72(6), 1036–1041.

Chakraborty, P., & Zachariah, M. R. (2011). On the Structure of Organic-Coated Water Droplets: From "Net Water Attractors" to "Oily" Drops. Journal of Geophysical Research: Atmospheres, 116(D21).

Chang, C.-C., Williams, I., Nowbahar, A., Mansard, V., Mecca, J., Whitaker, K. A., Schmitt, A. K., Tucker, C. J., Kalantar, T. H., Kuo, T.-C., & Squires, T. M. (2019). Effect of Ethylcellulose on the Rheology and Mechanical Heterogeneity of Asphaltene Films at the Oil–Water Interface. Langmuir, 35(29), 9374–9381.

Chávez-Miyauchi, T. E., Firoozabadi, A., & Fuller, G. G. (2016). Nonmonotonic Elasticity of the Crude Oil-Brine Interface in Relation to Improved Oil Recovery. Langmuir, 32(9), 2192–2198.

Chen, Y., Shen, C., & Peterson, G. P. (2015). Hydrodynamics and Morphologies of Droplet Coalescence. Industrial & Engineering Chemistry Research, 54(37), 9257–9262.

Choudhury, N. (2008). On the Manifestation of Hydrophobicity at The Nanoscale. Journal of Physical Chemistry B, 112(20), 6296–6300.

Choudhury, N., & Pettitt, B. M. (2005). On the Mechanism of Hydrophobic Association of Nanoscopic Solutes. Journal of the American Chemical Society, 127(10), 3556–3567.

Choudhury, N., & Pettitt, B. M. (2007). The Dewetting Transition and The Hydrophobic Effect. Journal of the American Chemical Society, 129(15), 4847–4852.

Cornellas, A., Perez, L., Comelles, F., Ribosa, I., Manresa, A., & Garcia, M. T. (2011). Self-Aggregation and Antimicrobial Activity of Imidazolium and Pyridinium Based Ionic Liquids in Aqueous Solution. Journal of Colloid and Interface Science, 355(1), 164–171.

de Oliveira, O. V., Costa, L. T., & Leite, E. R. (2016). Molecular Modeling of a Polymer Nanocomposite Model in Water and Chloroform Solvents. Computational and Theoretical Chemistry, 1092, 52–56.

Delahaije, R. J. B. M., Wierenga, P. A., Giuseppin, M. L. F., & Gruppen, H. (2014). Improved Emulsion Stability by Succinylation of Patatin Is Caused by Partial Unfolding Rather Than Charge Effects. Journal of Colloid and Interface Science, 430, 69–77.

Dobson, C. M. (2003). Protein Folding and Misfolding. Nature; London, 426(6968), 884–890.

Dokter, A. M., Woutersen, S., & Bakker, H. J. (2006). Inhomogeneous Dynamics in Confined Water Nanodroplets. Proceedings of the National Academy of Sciences, 103(42), 15355–15358.

Dong, B., Li, N., Zheng, L., Yu, L., & Inoue, T. (2007). Surface Adsorption and Micelle Formation of Surface Active Ionic Liquids in Aqueous Solution. Langmuir, 23(8), 4178–4182.

Dufour, J., Calles, J. A., Marugán, J., Giménez-Aguirre, R., Peña, J. L., & Merino-García, D. (2010). Influence of Hydrocarbon Distribution in Crude Oil and Residues on Asphaltene Stability †. Energy & Fuels, 24(4), 2281–2286.

Dutta Majumdar, R., Montina, T., Mullins, O. C., Gerken, M., & Hazendonk, P. (2017). Insights into Asphaltene Aggregate Structure Using Ultrafast MAS Solid-State 1 H NMR Spectroscopy. Fuel, 193, 359–368.

Essmann, U., Perera, L., Berkowitz, M. L., Darden, T., Lee, H., & Pedersen, L. G. (1995). A Smooth Particle Mesh Ewald Method. The Journal of Chemical Physics, 103(19), 8577–8593.

Eyssautier, J., Levitz, P., Espinat, D., Jestin, J., Gummel, J., Grillo, I., & Barré, L. (2011). Insight into Asphaltene Nanoaggregate Structure Inferred by Small Angle Neutron and X-ray Scattering. The Journal of Physical Chemistry B, 115(21), 6827–6837.

Factorovich, M. H., Molinero, V., & Scherlis, D. A. (2014). Vapor Pressure of Water Nanodroplets. Journal of the American Chemical Society, 136(12), 4508–4514.

Fan, H., & Striolo, A. (2012). Mechanistic Study of Droplets Coalescence in Pickering Emulsions. Soft Matter, 8(37), 9533.

Ferreira, R. J., Ferreira, M.-J. U., & dos Santos, D. J. V. A. (2012). Insights on P-Glycoprotein's Efflux Mechanism Obtained by Molecular Dynamics Simulations. Journal of Chemical Theory and Computation, 8(6), 1853–1864.

Fortuny, M., Oliveira, C. B. Z., Melo, R. L. F. V., Nele, M., Coutinho, R. C. C., & Santos, A. F. (2007). Effect of Salinity, Temperature, Water Content, and pH on the Microwave Demulsification of Crude Oil Emulsions †. Energy & Fuels, 21(3), 1358–1364.

Frisch, M. J., Trucks, G. W., Schlegel, H. B., Scuseria, G. E., Robb, M. A., Cheeseman, J. R., Scalmani, G., Barone, V., Petersson, G. A., Nakatsuji, H., Li, X., Caricato, M., Marenich, A. V., Bloino, J., Janesko, B. G., Gomperts, R., Mennucci, B., Hratchian, H. P., Ortiz, J. V., … Fox, D. J. (2016). Gaussian 16 Rev. C.01.

Fulazzaky, M. A. (2011). Determining the Resistance of Mass Transfer for Adsorption of The Surfactants onto Granular Activated Carbons from Hydrodynamic Column. Chemical Engineering Journal, 166(3), 832–840.

Gao, F., Xu, Z., Liu, G., & Yuan, S. (2014). Molecular Dynamics Simulation: The Behavior of Asphaltene in Crude Oil and at the Oil/Water Interface. Energy & Fuels, 28(12), 7368–7376.

Gelardi, G., Mantellato, S., Marchon, D., Palacios, M., Eberhardt, A. B., & Flatt, R. J. (2016). Chemistry of chemical admixtures. In Science and Technology of Concrete Admixtures (pp. 149–218). Elsevier.

Goliaei, A., Lau, E. Y., Adhikari, U., Schwegler, E., & Berkowitz, M. L. (2016). Behavior of P85 and P188 Poloxamer Molecules: Computer Simulations Using United-Atom Force-Field. The Journal of Physical Chemistry B, 120(33), 8631–8641.

González, J. A., Zawadzki, M., & Domanska, U. (2008). Thermodynamics of Mixtures Containing Polycyclic Aromatic Hydrocarbons. Journal of Molecular Liquids, 143(2–3), 134–140.

Grenoble, Z., & Trabelsi, S. (2018). Mechanisms, Performance Optimization and New Developments in Demulsification Processes for Oil and Gas Applications. Advances in Colloid and Interface Science, 260, 32–45.

Groenzin, H., & Mullins, O. C. (1999). Asphaltene Molecular Size and Structure. The Journal of Physical Chemistry A, 103(50), 11237–11245.

Groenzin, H., & Mullins, O. C. (2000). Molecular Size and Structure of Asphaltenes from Various Sources. Energy, 12, 677–684.

Hąc-Wydro, K., Połeć, K., & Broniatowski, M. (2019). The Impact of Selected Polycyclic Aromatic Hydrocarbons (pahs) on the Morphology, Stability and Relaxation of Ternary Lipid Monolayers Imitating Soil Bacteria Membrane. Journal of Molecular Liquids, 276, 409–416.

Heerdt, G., Tranca, I., Markvoort, A. J., Szyja, B. M., Morgon, N. H., & Hensen, E. J. M. (2018). Photoisomerization Induced Scission of Rod-Like Micelles Unravelled with Multiscale Modeling. Journal of Colloid and Interface Science, 510, 357–367.

Hernández, E. I., Castro-Sotelo, L. V., Avendaño-Gómez, J. R., Flores, C. A., Alvarez-Ramírez, F., & Vázquez, F. (2016). Synthesis, Characterization, and Evaluation of Petroleum Demulsifiers of Multibranched Block Copolymers. Energy & Fuels, 30(7), 5363–5378.

Hess, B. (2008). P-LINCS: A Parallel Linear Constraint Solver for Molecular Simulation. Journal of Chemical Theory and Computation, 4(1), 116–122.

Hezave, A. Z., Dorostkar, S., Ayatollahi, S., Nabipour, M., & Hemmateenejad, B. (2013). Investigating the Effect of Ionic Liquid (1-Dodecyl-3-Methylimidazolium Chloride ([C12mim] [Cl])) on the Water/Oil Interfacial Tension as A Novel Surfactant. Colloids and Surfaces A: Physicochemical and Engineering Aspects, 421, 63–71.

Hezaveh, S., Samanta, S., Milano, G., & Roccatano, D. (2012). Molecular Dynamics Simulation Study of Solvent Effects on Conformation and Dynamics of Polyethylene Oxide and Polypropylene Oxide Chains in Water and in Common Organic Solvents. The Journal of Chemical Physics, 136(12), 124901.

Hill, D. J., Mio, M. J., Prince, R. B., Hughes, T. S., & Moore, J. S. (2001). A Field Guide to Foldamers. Chemical Reviews, 101(12), 3893–4012.

Huang, X., Margulis, C. J., & Berne, B. J. (2003). Dewetting-Induced Collapse of Hydrophobic Particles. Proceedings of the National Academy of Sciences, 100(21), 11953–11958.

Hub, J. S., de Groot, B. L., & van der Spoel, D. (2010). g_wham—A Free Weighted Histogram Analysis Implementation Including Robust Error and Autocorrelation Estimates. Journal of Chemical Theory and Computation, 6(12), 3713–3720.

Hunter, C. A., & Sanders, J. K. M. (1990). The Nature of .pi.-.pi. Interactions. Journal of the American Chemical Society, 112(14), 5525–5534.

Jackson, N. E., Kohlstedt, K. L., Savoie, B. M., Olvera de la Cruz, M., Schatz, G. C., Chen, L. X., & Ratner, M. A. (2015). Conformational Order in Aggregates of Conjugated Polymers. Journal of the American Chemical Society, 137(19), 6254–6262.

Jain, V. P., Maldarelli, C., & Tu, R. S. (2009). Modeling the Dynamic Folding and Surface-Activity of a Helical Peptide Adsorbing to a Pendant Bubble Interface. Journal of Colloid and Interface Science, 331(2), 364–370.

Jarne, C., Cebolla, V. L., Membrado, L., Le Mapihan, K., & Giusti, P. (2011). High-Performance Thin-Layer Chromatography Using Automated Multiple Development for the Separation of Heavy Petroleum Products According to Their Number of Aromatic Rings. Energy & Fuels, 25(10), 4586–4594.

Jian, C., & Tang, T. (2014). One-Dimensional Self-Assembly of Polyaromatic Compounds Revealed by Molecular Dynamics Simulations. The Journal of Physical Chemistry B, 118(44), 12772–12780.

Jian, C., & Tang, T. (2015). Molecular Dynamics Simulations Reveal Inhomogeneity-Enhanced Stacking of Violanthrone-78-Based Polyaromatic Compounds in n -Heptane–Toluene Mixtures. The Journal of Physical Chemistry B, 119(27), 8660–8668.

Jian, C., Liu, Q., Zeng, H., & Tang, T. (2017). Effect of Model Polycyclic Aromatic Compounds on the Coalescence of Water-in-Oil Emulsion Droplets. The Journal of Physical Chemistry C, 121(19), 10382–10391.

Jian, C., Poopari, M. R., Liu, Q., Zerpa, N., Zeng, H., & Tang, T. (2016). Mechanistic Understanding of the Effect of Temperature and Salinity on the Water/Toluene Interfacial Tension. Energy & Fuels, 30(12), 10228–10235.

Jian, C., Poopari, M. R., Liu, Q., Zerpa, N., Zeng, H., & Tang, T. (2016). Reduction of Water/Oil Interfacial Tension by Model Asphaltenes: The Governing Role of Surface Concentration. The Journal of Physical Chemistry B, 120(25), 5646–5654.

Jian, C., Tang, T., & Bhattacharjee, S. (2013). Probing the Effect of Side-Chain Length on the Aggregation of a Model Asphaltene Using Molecular Dynamics Simulations. Energy & Fuels, 27(4), 2057–2067.

Jian, C., Tang, T., & Bhattacharjee, S. (2014). Molecular Dynamics Investigation on the Aggregation of Violanthrone78-Based Model Asphaltenes in Toluene. Energy & Fuels, 28(6), 3604–3613.

Jian, C., Tang, T., & Bhattacharjee, S. (2015). A Dimension Map for Molecular Aggregates. Journal of Molecular Graphics and Modelling, 58, 10–15.

Jian, C., Zeng, H., Liu, Q., & Tang, T. (2016). Probing the Adsorption of Polycyclic Aromatic Compounds onto Water Droplets Using Molecular Dynamics Simulations. The Journal of Physical Chemistry C, 120(26), 14170–14179.

Jin, H., Ding, W., Chen, B., Bai, B., Zhao, Q., & Cao, C. (2020). A Molecular Dynamics Simulation Investigation on the Solubility of Polycyclic Aromatic Hydrocarbons in Supercritical Water. Journal of Molecular Liquids, 301, 112464.

Kamp, J., Villwock, J., & Kraume, M. (2017). Drop Coalescence in Technical Liquid/Liquid Applications: A Review on Experimental Techniques and Modeling Approaches. Reviews in Chemical Engineering, 33(1), 1–47.

Katepalli, H., Bose, A., Hatton, T. A., & Blankschtein, D. (2016). Destabilization of Oil-in-Water Emulsions Stabilized by Non-ionic Surfactants: Effect of Particle Hydrophilicity. Langmuir, 32(41), 10694–10698.

Khadem, B., & Sheibat-Othman, N. (2019). Modeling of Double Emulsions Using Population Balance Equations. Chemical Engineering Journal, 366, 587–597.

Kim, F. S., Ren, G., & Jenekhe, S. A. (2011). One-Dimensional Nanostructures of π-Conjugated Molecular Systems: Assembly, Properties, and Applications from Photovoltaics, Sensors, and Nanophotonics to Nanoelectronics †. Chemistry of Materials, 23(3), 682–732.

Kopelevich, D. I. (2013). One-Dimensional Potential of Mean Force Underestimates Activation Barrier for Transport Across Flexible Lipid Membranes. The Journal of Chemical Physics, 139(13), 134906.

Kuznicki, T., Masliyah, J. H., & Bhattacharjee, S. (2008). Molecular Dynamics Study of Model Molecules Resembling Asphaltene-Like Structures in Aqueous Organic Solvent Systems. Energy & Fuels, 22(4), 2379–2389.

Kuznicki, T., Masliyah, J. H., & Bhattacharjee, S. (2009). Aggregation and Partitioning of Model Asphaltenes at Toluene−Water Interfaces: Molecular Dynamics Simulations. Energy & Fuels, 23(10), 5027–5035.

Lan, T., Wang, H., Liao, J., Yang, Y., Chai, Z., Liu, N., & Wang, D. (2016). Dynamics of Humic Acid and Its Interaction with Uranyl in the Presence of Hydrophobic Surface Implicated by Molecular Dynamics Simulations. Environmental Science & Technology, 50(20), 11121–11128.

Lan, T., Zeng, H., & Tang, T. (2018). Understanding Adsorption of Violanthrone-79 as a Model Asphaltene Compound on Quartz Surface Using Molecular Dynamics Simulations. The Journal of Physical Chemistry C, 122(50), 28787–28796.

Lan, T., Zeng, H., & Tang, T. (2019). Molecular Dynamics Study on the Mechanism of Graphene Oxide to Destabilize Oil/Water Emulsion. The Journal of Physical Chemistry C, 123(37), 22989–22999.

Lashkarbolooki, M., & Ayatollahi, S. (2016). Effect of Asphaltene and Resin on Interfacial Tension of Acidic Crude Oil/ Sulfate Aqueous Solution: Experimental Study. Fluid Phase Equilibria, 414, 149–155.

Lashkarbolooki, M., Ayatollahi, S., & Riazi, M. (2014). Effect of Salinity, Resin, and Asphaltene on the Surface Properties of Acidic Crude Oil/Smart Water/Rock System. Energy & Fuels, 28(11), 6820–6829.

Lashkarbolooki, M., Riazi, M., Ayatollahi, S., & Zeinolabedini Hezave, A. (2016). Synergy Effects of Ions, Resin, and Asphaltene on Interfacial Tension of Acidic Crude Oil and Low-High Salinity Brines. Fuel, 165, 75–85.

Lavabre, D., Pradines, V., Micheau, J.-C., & Pimienta, V. (2005). Periodic Marangoni Instability in Surfactant (CTAB) Liquid/Liquid Mass Transfer. The Journal of Physical Chemistry B, 109(15), 7582–7586.

Le Follotec, A., Pezron, I., Noik, C., Dalmazzone, C., & Metlas-Komunjer, L. (2010). Triblock copolymers as destabilizers of water-in-crude oil emulsions. Colloids and Surfaces A: Physicochemical and Engineering Aspects, 365(1–3), 162–170.

Lee, D. J., Kim, H. M., Song, Y. S., & Youn, J. R. (2012). Water Droplet Bouncing and Superhydrophobicity Induced by Multiscale Hierarchical Nanostructures. ACS Nano, 6(9), 7656–7664.

Lemkul, J. A., & Bevan, D. R. (2010). Assessing the Stability of Alzheimer's Amyloid Protofibrils Using Molecular Dynamics. The Journal of Physical Chemistry B, 114(4), 1652–1660.

Lemkul, J. A., Allen, W. J., & Bevan, D. R. (2010). Practical Considerations for Building GROMOS-Compatible Small-Molecule Topologies. Journal of Chemical Information and Modeling, 50(12), 2221–2235.

Li, X., Yoneda, M., Shimada, Y., & Matsui, Y. (2017). Effect of Surfactants on The Aggregation and Stability of TiO2 Nanomaterial In Environmental Aqueous Matrices. Science of The Total Environment, 574, 176–182.

Li, Z., Geng, H., Wang, X., Jing, B., Liu, Y., & Tan, Y. (2018). Noval Tannic Acid-Based Polyether as An Effective Demulsifier For Water-In-Aging Crude Oil Emulsions. Chemical Engineering Journal, 354, 1110–1119.

Li, Z., Yin, S., Tan, G., Zhao, S., Shi, Z., Jing, B., Zhai, L., & Tan, Y. (2016). Synthesis and Properties of Novel Branched Polyether as Demulsifiers For Polymer Flooding. Colloid and Polymer Science, 294(12), 1943–1958.

Liao, M.-L., Ju, S.-P., & Yang, S.-H. (2007). Coalescence Behavior of Water Nanoclusters: Temperature and Size Effects. The Journal of Physical Chemistry C, 111(19), 6927–6932.

Lin, M. Y., Lindsay, H. M., Weitz, D. A., Ball, R. C., Klein, R., & Meakin, P. (1989). Universality in Colloid Aggregation. Nature, 339(6223), 360–362.

Lindahl, E., Hess, B., & van der Spoel, D. (2001). GROMACS 3.0: A Package for Molecular Simulation and Trajectory Analysis. Journal of Molecular Modeling, 7(8), 306–317.

Liu, D., Li, C., Zhang, X., Yang, F., Sun, G., Yao, B., & Zhang, H. (2020). Polarity Effects of Asphaltene Subfractions on the Stability and Interfacial Properties of Water-In-Model Oil Emulsions. Fuel, 269, 117450.

Liu, J., Li, X., Jia, W., Li, Z., Zhao, Y., & Ren, S. (2015). Demulsification of Crude Oil-in-Water Emulsions Driven by Graphene Oxide Nanosheets. Energy & Fuels, 29(7), 4644–4653.

Liu, J., Zhang, L., Xu, Z., & Masliyah, J. (2006). Colloidal Interactions between Asphaltene Surfaces in Aqueous Solutions. Langmuir, 22(4), 1485–1492.

Liu, S. (2015). Cooperative Adsorption on Solid Surfaces. Journal of Colloid and Interface Science, 450, 224–238.

Long, J., Li, L., Jin, Y., Sun, H., Zheng, Y., & Tian, S. (2016). Synergistic Solubilization Of Polycyclic Aromatic Hydrocarbons by Mixed Micelles Composed of a Photoresponsive Surfactant and a Conventional Non-Ionic Surfactant. Separation and Purification Technology, 160, 11–17.

Maes, M., Trekels, M., Boulhout, M., Schouteden, S., Vermoortele, F., Alaerts, L., Heurtaux, D., Seo, Y.-K., Hwang, Y. K., Chang, J.-S., Beurroies, I., Denoyel, R., Temst, K., Vantomme, A., Horcajada, P., Serre, C., & De Vos, D. E. (2011). Selective Removal of N-Heterocyclic Aromatic Contaminants from Fuels by Lewis Acidic Metal–Organic Frameworks. Angewandte Chemie International Edition, 50(18), 4210–4214.

Malde, A. K., Zuo, L., Breeze, M., Stroet, M., Poger, D., Nair, P. C., Oostenbrink, C., & Mark, A. E. (2011). An Automated Force Field Topology Builder (ATB) and Repository: Version 1.0. Journal of Chemical Theory and Computation, 7(12), 4026–4037.

Manuel F. González, Clementina Sosa Stull, Francisco López-Linares, A., & Pereira-Almao*, P. (2007). Comparing Asphaltene Adsorption with Model Heavy Molecules over Macroporous Solid Surfaces. Energy & Fuels, 21(1), 234–241.

Mativetsky, J. M., Kastler, M., Savage, R. C., Gentilini, D., Palma, M., Pisula, W., Müllen, K., & Samorì, P. (2009). Self-Assembly of a Donor-Acceptor Dyad Across Multiple Length Scales: Functional Architectures for Organic Electronics. Advanced Functional Materials, 19(15), 2486–2494.

McLean, J. D., & Kilpatrick, P. K. (1997). Effects of Asphaltene Aggregation in Model Heptane–Toluene Mixtures on Stability of Water-in-Oil Emulsions. Journal of Colloid and Interface Science, 196(1), 23–34.

Mclean, J. D., & Kilpatrick, P. K. (1997). Effects of Asphaltene Solvency on Stability of Water-in-Crude-Oil Emulsions. Journal of Colloid and Interface Science, 189(189), 242–253.

Menger, F. M., Shi, L., & Rizvi, S. A. A. (2010). Self-Assembling Systems: Mining a Rich Vein. Journal of Colloid and Interface Science, 344(2), 241–246.

Mezzenga, R., & Fischer, P. (2013). The Self-Assembly, Aggregation and Phase Transitions of Food Protein Systems in One, Two and Three Dimensions. Reports on Progress in Physics, 76(4), 046601.

Mezzenga, R., Schurtenberger, P., Burbidge, A., & Michel, M. (2005). Understanding Foods as Soft Materials. Nature Materials, 4(10), 729–740.

Mikami, Y., Liang, Y., Matsuoka, T., & Boek, E. S. (2013). Molecular Dynamics Simulations of Asphaltenes at the Oil–Water Interface: From Nanoaggregation to Thin-Film Formation. Energy & Fuels, 27(4), 1838–1845.

Moeini, F., Hemmati-Sarapardeh, A., Ghazanfari, M. H., Masihi, M., & Ayatollahi, S. (2014). Toward Mechanistic Understanding of Heavy Crude Oil/Brine Interfacial Tension: The Roles of Salinity, Temperature and Pressure. Fluid Phase Equilibria, 375, 191–200.

Müllen, K., & Rabe, J. P. (2008). Nanographenes as Active Components of Single-Molecule Electronics and How a Scanning Tunneling Microscope Puts Them to Work. Accounts of Chemical Research, 41(4), 511–520.

Mullins, O. C. (2010). The Modified Yen Model †. Energy & Fuels, 24(4), 2179–2207.

Mullins, O. C., Sabbah, H., Eyssautier, J., Pomerantz, A. E., Barré, L., Andrews, A. B., Ruiz-Morales, Y., Mostowfi, F., McFarlane, R., Goual, L., Lepkowicz, R., Cooper, T., Orbulescu, J., Leblanc, R. M., Edwards, J., & Zare, R. N. (2012). Advances in Asphaltene Science and the Yen–Mullins Model. Energy & Fuels, 26(7), 3986–4003.

Nagrimanov, R. N., Samatov, A. A., & Solomonov, B. N. (2019). Additive Scheme of Solvation Enthalpy for Linear, Cyclic and Branched-Chain Aliphatic Compounds At 298.15 K. Journal of Molecular Liquids, 292, 111365.

Narita, A., Wang, X.-Y., Feng, X., & Müllen, K. (2015). New Advances in Nanographene Chemistry. Chemical Society Reviews, 44(18), 6616–6643.

Nenningsland, A. L., Gao, B., Simon, S., & Sjöblom, J. (2011). Comparative Study of Stabilizing Agents for Water-In-Oil Emulsions. Energy and Fuels, 25(12), 5746–5754.

Niu, Z., Ma, X., Manica, R., & Yue, T. (2019). Molecular Destabilization Mechanism of Asphaltene Model Compound C5Pe Interfacial Film by EO-PO Copolymer: Experiments and MD Simulation. The Journal of Physical Chemistry C, 123(16), 10501–10508.

Niu, Z., Yue, T., He, X., & Manica, R. (2019). Changing the Interface Between an Asphaltene Model Compound and Water by Addition of an EO–PO Demulsifier through Adsorption Competition or Adsorption Replacement. Energy & Fuels, 33(6), 5035–5042.

Oostenbrink, C., Villa, A., Mark, A. E., & Gunsteren, W. F. V. (2004). A Biomolecular Force Field Based on the Free Enthalpy of Hydration and Solvation: The GROMOS Force-Field Parameter Sets 53a5 and 53a6. Journal of Computational Chemistry, 25(13), 1656–1676.

Origuchi, S., Kishimoto, M., Yoshizawa, M., & Yoshimoto, S. (2018). A Supramolecular Approach to the Preparation of Nanographene Adlayers Using Water-Soluble Molecular Capsules. Angewandte Chemie International Edition, 57(47), 15481–15485.

Pacheco, V. F., Spinelli, L., Lucas, E. F., & Mansur, C. R. E. (2011). Destabilization of Petroleum Emulsions: Evaluation of the Influence of the Solvent on Additives. Energy & Fuels, 25(4), 1659–1666.

Pak, C. Y., Li, W., & Steve Tse, Y.-L. (2018). Free Energy and Dynamics of Water Droplet Coalescence. The Journal of Physical Chemistry C, 122(40), 22975–22984.

Pak, C. Y., Li, W., & Steve Tse, Y.-L. (2020). Free Energy and Dynamics of Organic-Coated Water Droplet Coalescence. The Journal of Physical Chemistry C, 124(16), 8749–8757.

Paul, N., Schrader, P., Enders, S., & Kraume, M. (2014). Effects of Phase Behaviour on Mass Transfer in Micellar Liquid/Liquid Systems. Chemical Engineering Science, 115, 148–156.

Pawar, A. B., Caggioni, M., Ergun, R., Hartel, R. W., & Spicer, P. T. (2011). Arrested Coalescence in Pickering Emulsions. Soft Matter, 7(17), 7710.

Penfold, J., Thomas, R. K., & Shen, H.-H. (2012). Adsorption and Self-Assembly of Biosurfactants Studied by Neutron Reflectivity and Small Angle Neutron Scattering: Glycolipids, Lipopeptides And Proteins. Soft Matter, 8(3), 578–591.

Pensini, E., Harbottle, D., Yang, F., Tchoukov, P., Li, Z., Kailey, I., Behles, J., Masliyah, J., & Xu, Z. (2014). Demulsification Mechanism of Asphaltene-Stabilized Water-in-Oil Emulsions by a Polymeric Ethylene Oxide–Propylene Oxide Demulsifier. Energy & Fuels, 28(11), 6760–6771.

Perumanath, S., Borg, M. K., Chubynsky, M. V., Sprittles, J. E., & Reese, J. M. (2019). Droplet Coalescence is Initiated by Thermal Motion. Physical Review Letters, 122(10), 104501.

Pisula, W., Feng, X., & Müllen, K. (2010). Tuning the Columnar Organization of Discotic Polycyclic Aromatic Hydrocarbons. Advanced Materials, 22(33), 3634–3649.

Pradilla, D., Simon, S., & Sjöblom, J. (2015a). Mixed interfaces of asphaltenes and model demulsifiers part I: Adsorption and desorption of single components. Colloids and Surfaces A: Physicochemical and Engineering Aspects, 466, 45–56.

Pradilla, D., Simon, S., & Sjöblom, J. (2015b). Mixed Interfaces of Asphaltenes and Model Demulsifiers, Part II: Study of Desorption Mechanisms at Liquid/Liquid Interfaces. Energy & Fuels, 29(9), 5507–5518.

Qiu, Y., & Molinero, V. (2015). Morphology of Liquid–Liquid Phase Separated Aerosols. Journal of the American Chemical Society, 137(33), 10642–10651.

Rahmani, N. H. G., Dabros, T., & Masliyah, J. H. (2004). Evolution of Asphaltene Floc Size Distribution in Organic Solvents Under Shear. Chemical Engineering Science, 59(3), 685–697.

Rajeshkumar, V., Courté, M., Fichou, D., & Stuparu, M. C. (2016). Synthesis and Properties of Large Polycyclic Aromatic Hydrocarbons with Planar and Non-Planar Structural Motifs. European Journal of Organic Chemistry, 2016(36), 6010–6014.

Rane, J. P., Pauchard, V., Couzis, A., & Banerjee, S. (2013). Interfacial Rheology of Asphaltenes at Oil–Water Interfaces and Interpretation of the Equation of State. Langmuir, 29(15), 4750–4759.

Rankin, B. M., Ben-Amotz, D., Van Der Post, S. T., & Bakker, H. J. (2015). Contacts between alcohols in water are random rather than hydrophobic. Journal of Physical Chemistry Letters, 6(4), 688–692.

Rezaeidoust, A., Puntervold, T., Strand, S., & Austad, T. (2009). Smart Water as Wettability Modifier in Carbonate and Sandstone: A Discussion of Similarities/Differences in The Chemical Mechanisms. Energy and Fuels, 23(9), 4479–4485.

Sakthivel, S., Velusamy, S., Nair, V. C., Sharma, T., & Sangwai, J. S. (2017). Interfacial tension of crude oil-water system with imidazolium and lactam-based ionic liquids and their evaluation for enhanced oil recovery under high saline environment. Fuel, 191, 239–250.

Sarkar, A., Horne, D. S., & Singh, H. (2010). Interactions of Milk Protein-Stabilized Oil-In-Water Emulsions with Bile Salts in A Simulated Upper Intestinal Model. Food Hydrocolloids, 24(2–3), 142–151.

Sayyad Amin, J., Nikooee, E., Ayatollahi, S., & Alamdari, A. (2010). Investigating Wettability Alteration Due to Asphaltene Precipitation: Imprints in Surface Multifractal Characteristics. Applied Surface Science, 256(21), 6466–6472.

Schuler, B., Meyer, G., Peña, D., Mullins, O. C., & Gross, L. (2015). Unraveling the Molecular Structures of Asphaltenes by Atomic Force Microscopy. Journal of the American Chemical Society, 137(31), 9870–9876.

Schuler, L. D., Daura, X., & Gunsteren, W. F. van. (2001). An improved GROMOS96 force field for aliphatic hydrocarbons in the condensed phase. Journal of Computational Chemistry, 22(11), 1205–1218.

Schüttelkopf, A. W., van Aalten, D. M. F., & IUCr. (2004). PRODRG: A Tool for High-Throughput Crystallography of Protein–Ligand Complexes. Acta Crystallographica Section D Biological Crystallography, 60(8), 1355–1363.

Sedghi, M., Goual, L., Welch, W., & Kubelka, J. (2013). Effect of Asphaltene Structure on Association and Aggregation Using Molecular Dynamics. The Journal of Physical Chemistry B, 117(18), 5765–5776.

Sevick, E. M., Monson, P. A., & Ottino, J. M. (1988). Monte Carlo Calculations of Cluster Statistics in Continuum Models of Composite Morphology. The Journal of Chemical Physics, 88(2), 1198–1206.

Sharghi, H., Khalifeh, R., & Salimi Beni, A. R. (2010). Synthesis of New Lariat Ethers Containing Polycyclic Phenols and Heterocyclic Aromatic Compound on Graphite Surface Via Mannich Reaction. Journal of the Iranian Chemical Society, 7(1), 275–288.

Shariatpanahi, S. F., Strand, S., & Austad, T. (2011). Initial Wetting Properties of Carbonate Oil Reservoirs: Effect of The Temperature and Presence of Sulfate in Formation Water. Energy and Fuels, 25(7), 3021–3028.

Shehzad, F., Hussein, I. A., Kamal, M. S., Ahmad, W., Sultan, A. S., & Nasser, M. S. (2018). Polymeric Surfactants and Emerging Alternatives used in the Demulsification of Produced Water: A Review. Polymer Reviews, 58(1), 63–101.

Sheng, J. J. (2011). Surfactant-Polymer Flooding. In Modern Chemical Enhanced Oil Recovery (pp. 371–387). Elsevier.

Sheng, J. J. (2014). Critical Review of Low-Salinity Waterflooding. Journal of Petroleum Science and Engineering, 120, 216–224.

Sheppard, E., & Tcheurekdjian, N. (1968). Monolayer Studies: Iv. Surface Films of Emulsion Latex Particles. Journal of Colloid and Interface Science, 28(3), 481–486.

Sheremata, J. M., Gray, M. R., Dettman, H. D., & McCaffrey, W. C. (2004). Quantitative Molecular Representation and Sequential Optimization of Athabasca Asphaltenes. Energy & Fuels, 18, 1377–1384.

Shi, C., Zhang, L., Xie, L., Lu, X., Liu, Q., He, J., Mantilla, C. A., Van den berg, F. G. A., & Zeng, H. (2017). Surface Interaction of Water-in-Oil Emulsion Droplets with Interfacially Active Asphaltenes. Langmuir, 33(5), 1265–1274.

Shi, C., Zhang, L., Xie, L., Lu, X., Liu, Q., Mantilla, C. A., van den Berg, F. G. A., & Zeng, H. (2016). Interaction Mechanism of Oil-in-Water Emulsions with Asphaltenes Determined Using Droplet Probe AFM. Langmuir, 32(10), 2302–2310.

Shimizu, R., & Tanaka, H. (2015). A Novel Coarsening Mechanism of Droplets In Immiscible Fluid Mixtures. Nature Communications, 6(1), 7407.

Simon, S., Jestin, J., Palermo, T., & Barré, L. (2009). Relation between Solution and Interfacial Properties of Asphaltene Aggregates. Energy & Fuels, 23(1), 306–313.

Somekawa, N., Yamauchi, A., Eda, K., & Osakai, T. (2019). Computational Prediction of Adsorption Equilibrium for Nonionic Surfactants at the Oil/Water Interface. Langmuir, 35(35), 11345–11350.

Speight, J. G. (2004). Petroleum Asphaltenes—Part 1: Asphaltenes, Resins and the Structure of Petroleum. Oil & Gas Science and Technology, 59(5), 467–477.

Spiecker, P. M., Gawrys, K. L., Trail, C. B., & Kilpatrick, P. K. (2003). Effects of Petroleum Resins on Asphaltene Aggregation And Water-In-Oil Emulsion Formation. Colloids and Surfaces A: Physicochemical and Engineering Aspects, 220(1–3), 9–27.

Srivastava, A., & Ismail, K. (2014). Solubilization of Polycyclic Aromatic Hydrocarbons in Aqueous Sodium Dioctylsulfosuccinate Solutions. Journal of Molecular Liquids, 195, 105–109.

Steinchen, A., Sefiane, K., & Sanfeld, A. (2011). Nano-Encapsulation as High Pressure Devices for Folding–Unfolding Proteins. Journal of Colloid and Interface Science, 355(2), 509–511.

Sun, X., Zeng, H., & Tang, T. (2020). Molecular Simulation of Folding and Aggregation of Multi-Core Polycyclic Aromatic Compounds. Journal of Molecular Liquids, 310, 113248.

Sun, X., Zeng, H., & Tang, T. (2021). Effect of non-ionic surfactants on the adsorption of polycyclic aromatic compounds at water/oil interface: A molecular simulation study. Journal of Colloid and Interface Science, 586, 766–777.

Sztukowski, D. M., Jafari, M., Alboudwarej, H., & Yarranton, H. W. (2003). Asphaltene Self-Association and Water-In-Hydrocarbon Emulsions. Journal of Colloid and Interface Science, 265(1), 179–186.

Taheri-Shakib, J., Saadati, N., Esfandiarian, A., Hosseini, S. A., & Rajabi-Kochi, M. (2020). Characterizing the Wax-Asphaltene Interaction and Surface Morphology Using Analytical Spectroscopy and Microscopy Techniques. Journal of Molecular Liquids, 302, 112506.

Tchoukov, P., Yang, F., Xu, Z., Dabros, T., Czarnecki, J., & Sjöblom, J. (2014). Role of Asphaltenes in Stabilizing Thin Liquid Emulsion Films. Langmuir, 30(11), 3024–3033.

Tirjoo, A., Bayati, B., Rezaei, H., & Rahmati, M. (2019). Molecular Dynamics Simulation of the Effect of Ions in Water on the Asphaltene Aggregation. Journal of Molecular Liquids, 277, 40–48.

Tomšič, M., Bešter-Rogač, M., Jamnik, A., Kunz, W., Touraud, D., Bergmann, A., & Glatter, O. (2004). Nonionic Surfactant Brij 35 in Water and in Various Simple Alcohols: Structural

Investigations by Small-Angle X-ray Scattering and Dynamic Light Scattering. The Journal of Physical Chemistry B, 108(22), 7021–7032.

Vaitheeswaran, S., & Thirumalai, D. (2006). Hydrophobic and Ionic Interactions in Nanosized Water Droplets. Journal of the American Chemical Society, 128(41), 13490–13496.

Van Der Spoel, D., Lindahl, E., Hess, B., Groenhof, G., Mark, A. E., & Berendsen, H. J. C. (2005). GROMACS: Fast, Flexible, And Free. Journal of Computational Chemistry, 26(16), 1701–1718.

van Gunsteren, W. F., Daura, X., & Mark, A. E. (2002). Computation of Free Energy. Helvetica Chimica Acta, 85(10), 3113–3129.

Verruto, V. J., Le, R. K., & Kilpatrick, P. K. (2009). Adsorption and Molecular Rearrangement of Amphoteric Species at Oil-Water Interfaces. The Journal of Physical Chemistry B, 113(42), 13788–13799.

Volkov, A. G. (2001). Liquid Interfaces in Chemical, Biological and Pharmaceutical Applications. CRC Press.

von Wandruszka, R. (2000). Humic Acids: Their Detergent Qualities and Potential Uses in Pollution Remediation. Geochemical Transactions, 1(1), 10.

Wallqvist, A., & Berne, B. J. (1995). Molecular Dynamics Study of the Dependence of Water Solvation Free Energy on Solute Curvature and Surface Area. J. Phys. Chem, 99, 2885–2892.

Wang, B.-B., Wang, X.-D., Yan, W.-M., & Wang, T.-H. (2015). Molecular Dynamics Simulations on Coalescence and Non-coalescence of Conducting Droplets. Langmuir, 31(27), 7457–7462.

Wang, D., Yang, D., Huang, C., Huang, Y., Yang, D., Zhang, H., Liu, Q., Tang, T., Gamal El-Din, M., Kemppi, T., Perdicakis, B., & Zeng, H. (2021). Stabilization Mechanism and Chemical Demulsification Of Water-In-Oil and Oil-In-Water Emulsions in Petroleum Industry: A review. Fuel, 286, 119390.

Wang, D., Zhao, Z., Qiao, C., Yang, W., Huang, Y., McKay, P., Yang, D., Liu, Q., & Zeng, H. (2020). Techniques for Treating Slop Oil in Oil and Gas Industry: A Short Review. Fuel, 279, 118482.

Wang, J., Gayatri, M., & Ferguson, A. L. (2018). Coarse-Grained Molecular Simulation and Nonlinear Manifold Learning of Archipelago Asphaltene Aggregation and Folding. The Journal of Physical Chemistry B, 122(25), 6627–6647.

Wang, X., & Alvarado, V. (2012). Effects of Aqueous-Phase Salinity on Water-in-Crude Oil Emulsion Stability. Journal of Dispersion Science and Technology, 33(2), 165–170.

Wasserfallen, D., Kastler, M., Pisula, W., Hofer, W. A., Fogel, Y., Wang, Z., & Müllen, K. (2006). Suppressing Aggregation in a Large Polycyclic Aromatic Hydrocarbon. Journal of the American Chemical Society, 128(4), 1334–1339.

Wu, A., Lu, F., Sun, P., Gao, X., Shi, L., & Zheng, L. (2016). Photoresponsive Self-Assembly of Surface Active Ionic Liquid. Langmuir, 32(32), 8163–8170.

Wu, C., De Visscher, A., & Gates, I. D. (2017). Molecular Interactions Between 1-Butyl-3-Methylimidazolium Tetrafluoroborate and Model Naphthenic Acids: A DFT Study. Journal of Molecular Liquids, 243, 462–471.

Wu, G., Wang, C.-Y., Jiao, T., Zhu, H., Huang, F., & Li, H. (2018). Controllable Self-Assembly of Macrocycles in Water for Isolating Aromatic Hydrocarbon Isomers. Journal of the American Chemical Society, 140(18), 5955–5961.

Wu, J., Pisula, W., & Müllen, K. (2007). Graphenes as Potential Material for Electronics. Chemical Reviews, 107(3), 718–747.

Xie, L., Shi, C., Cui, X., & Zeng, H. (2017). Surface Forces and Interaction Mechanisms of Emulsion Drops and Gas Bubbles in Complex Fluids. Langmuir, 33(16), 3911–3925.

You, W., Tang, Z., & Chang, C. A. (2019). Potential Mean Force from Umbrella Sampling Simulations: What Can We Learn and What Is Missed? Journal of Chemical Theory and Computation, 15(4), 2433–2443.

Yuan, S. Y., Wei, S. H., & Chang, B. V. (2000). Biodegradation of Polycyclic Aromatic Hydrocarbons by A Mixed Culture. Chemosphere, 41(9), 1463–1468.

Zangi, R., & Berne, B. J. (2006). Aggregation and Dispersion of Small Hydrophobic Particles in Aqueous Electrolyte Solutions. Journal of Physical Chemistry B, 110(45), 22736–22741.

Zekri, A. Y., & Shedid, S. A. (2004). The Effect of Fracture Characteristics on Reduction of Permeability by Asphaltene Precipitation in Carbonate Formation. Journal of Petroleum Science and Engineering, 42(2–4), 171–182.

Zhang, D., Ronson, T. K., Lavendomme, R., & Nitschke, J. R. (2019). Selective Separation of Polyaromatic Hydrocarbons by Phase Transfer of Coordination Cages. Journal of the American Chemical Society, 141(48), 18949–18953.

Zhang, L., Shi, C., Lu, Q., Liu, Q., & Zeng, H. (2016). Probing Molecular Interactions of Asphaltenes in Heptol Using a Surface Forces Apparatus: Implications on Stability of Water-in-Oil Emulsions. Langmuir, 32(19), 4886–4895.

Zhang, L., Xie, L., Cui, X., Chen, J., & Zeng, H. (2019). Intermolecular and Surface Forces At Solid/Oil/Water/Gas Interfaces In Petroleum Production. Journal of Colloid and Interface Science, 537, 505–519.

Zhang, L., Xie, L., Shi, C., Huang, J., Liu, Q., & Zeng, H. (2017). Mechanistic Understanding of Asphaltene Surface Interactions in Aqueous Media. Energy & Fuels, 31(4), 3348–3357.

Zhang, S., Zhang, L., Lu, X., Shi, C., Tang, T., Wang, X., Huang, Q., & Zeng, H. (2018). Adsorption Kinetics of Asphaltenes At Oil/Water Interface: Effects of Concentration and Temperature. Fuel, 212, 387–394.

Zhang, Z., Kim, D. S., Lin, C.-Y., Zhang, H., Lammer, A. D., Lynch, V. M., Popov, I., Miljanić, O. Š., Anslyn, E. V., & Sessler, J. L. (2015). Expanded Porphyrin-Anion Supramolecular Assemblies: Environmentally Responsive Sensors for Organic Solvents and Anions. Journal of the American Chemical Society, 137(24), 7769–7774.

Zhang, Z., Xu, G. Y., Wang, F., Dong, S. L., & Li, Y. M. (2004). Characterization and Demulsification Of Poly(Ethylene Oxide)–Block–Poly(Propylene Oxide)–Block–Poly(Ethylene Oxide) Copolymers. Journal of Colloid and Interface Science, 277(2), 464–470.

Zhao, L., & Choi, P. (2004). Molecular Dynamics Simulation of The Coalescence of Nanometer-Sized Water Droplets in N -Heptane. The Journal of Chemical Physics, 120(4), 1935–1942.

Zhao, W., Chiuman, W., Lam, J. C. F., McManus, S. A., Chen, W., Cui, Y., Pelton, R., Brook, M. A., & Li, Y. (2008). DNA Aptamer Folding on Gold Nanoparticles: From Colloid Chemistry to Biosensors. Journal of the American Chemical Society, 130(11), 3610–3618.

Zheng, Z., & Obbard, J. P. (2001). Effect of Non-Ionic Surfactants on Elimination of Polycyclic Aromatic Hydrocarbons (PAHs) in Soil-Slurry by Phanerochaete Chrysosporium. Journal of Chemical Technology & Biotechnology, 76(4), 423–429.

Zhou, W., & Zhu, L. (2005). Distribution of Polycyclic Aromatic Hydrocarbons in Soil–Water System Containing A Nonionic Surfactant. Chemosphere, 60(9), 1237–1245.

Zhu, X., Chen, D., & Wu, G. (2015). Molecular Dynamic Simulation of Asphaltene Co-Aggregation with Humic Acid During Oil Spill. Chemosphere, 138, 412–421.

Zhu, X., Wu, G., & Chen, D. (2016). Molecular Dynamics Simulation of Cyclodextrin Aggregation and Extraction of Anthracene from Non-Aqueous Liquid Phase. Journal of Hazardous Materials, 320, 169–175.

Zielkiewicz, J. (2005). Structural Properties of Water: Comparison of the SPC, SPCE, TIP4P, and TIP5P Models of Water. The Journal of Chemical Physics, 123(10), 104501.

Appendix A: Supporting Information for Chapter 3

A1. Density of M molecules in solid state and size of their aggregates in organic solvents.

An MD simulation was performed on a system containing 44 M molecules in a cubic box with an initial length of 6 nm in each direction. No solvent was added so this system represented M molecules in solid state. Energy minimization and subsequent NVT and NpT (production run) simulations were performed, in the same way as described in the Method section of the Chapter 4. During the NpT simulation, the simulation box shrunk to approximately 4.4 nm in each direction. Using the final equilibrated volume, the density of the M molecules was calculated to be 1092 kg/m^3. This is in good agreement with the results of Duran et al. [1], where the density of asphaltene samples from Western Canada bitumen was measured to be 1008.8 to 1153.5 kg/m^3.

The size of the largest aggregate in organic solvents (systems 5, 6, 8, 9) was quantified by calculating its radius of gyration (R_g) through the following equation:

$$R_g = \left(\frac{\sum_i m_i r_i}{\sum_i m_i}\right)^{1/2} \quad \text{(B1)}$$

where m_i is the mass of atom i, and r_i is the distance between atom i and the center of mass of the aggregate. The results for the largest aggregate at the end of the simulations are shown in Table A1. R_g of asphaltene nanoaggregates has been measured by many researchers using the small angle neutron and X-ray scattering technique [2,3]. The reported R_g ranged from 3.0 to 5.2 nm in toluene and from 5.1 to 11.8 nm in toluene/heptane mixture [4,5], which is in overall agreement with our simulation data. Because the asphaltic samples precipitated in heptane, the aggregate size was not obtained experimentally for pure heptane solutions. Theoretically, Teklebrhan et al. performed MD simulations on five types of model asphaltenes (molecular weight 689-762 g/mol) in heptane

and toluene [6]. In heptane, R_g was found to be 0.93-2.62 nm, and the number of molecules in the largest nanoaggregates (N_m) ranged from 4 to 21. In toluene, R_g was between 0.76-1.29 nm and N_m was 3-8 [6]. While N_m from our simulations compare well with Teklebrhan et al. (see Table A1), our R_g is larger probably because the M molecule is much larger (molecular weight: 1303 g/mol) than the models in Teklebrhan et al. [6]. The trend of having smaller R_g (and N_m) in toluene than in heptane was captured in all works.

Table A1 Radius of gyration (R_g) and number of molecules (N_m) in the largest aggregate.

solvent	sys.	R_g (nm)	R_g in S4-5 (nm)	R_g in S6 (nm)	N_m	N_m in S6
heptane	5	4.94	N/A	0.93-2.62	3	4-21
	8	7.17			6	
toluene	6	3.31	3.0-5.2	0.76-1.29	2	3-8
	9	0.92			2	

A2. Root-mean-square deviation (RMSD) for a single M molecule.

As shown in Fig. A1, for system 1 with one M molecule in water, the curve increases rapidly and reaches a plateau. The curves for one M molecule in toluene and heptane show a similar trend but the fluctuation in RMSD is higher throughout the simulations. It indicates that after a short time (~ 4 ns), the structure of the single M molecule became relatively stable in water, while the molecule in toluene and heptane underwent more dynamic but reversible structural changes.

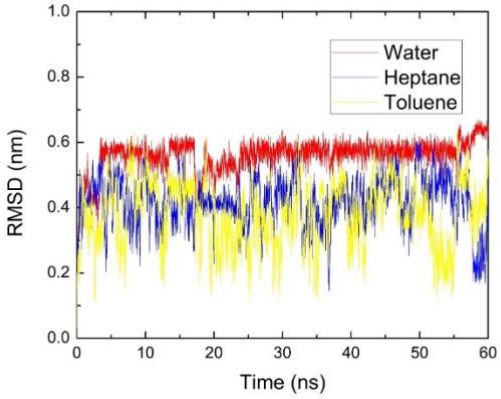

Figure A1 Root-mean-square deviation (RMSD) as a function of simulation time for systems with a single molecule in water, heptane and toluene.

A3. Interaction between core1 and core3.

Fig. A2 shows the distance (D) between centers of geometries (COGs) of core1 and core3 versus the angle (θ) between the two cores over the last 50 ns. Compared with Fig. 4.3 in the main texts (between core1 and core2), the separation between core1 and core 3 is generally larger, indicating weaker interactions.

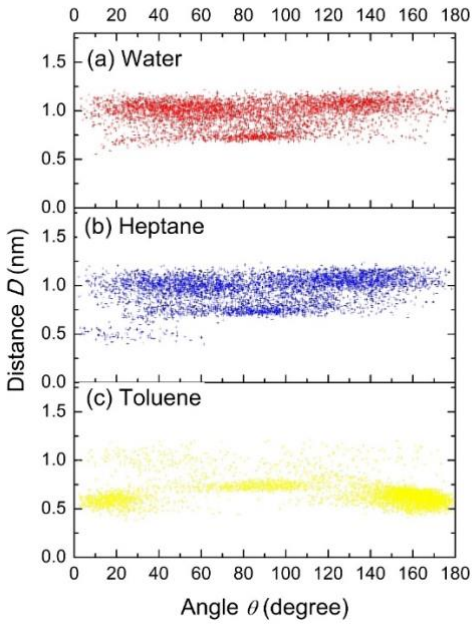

Figure A2 Distance D between COGs of core1 and core3 versus angle θ between the two cores. Data are from simulations of a single M molecule in (a) water, (b) heptane and (c) toluene.

A4. Additional discussion on the folded configurations.

Fig. A3a-b shows representative configurations for the single molecule in toluene in unfolded state. In Fig. A3a, core1 and core2 are each represented by three atoms, one sulfur in yellow, and two carbon in blue and pink respectively. These three atoms form a plane and Fig. A3b shows the calculation of the normal vectors of the planes. Specifically, each normal vector was determined using the right-hand-rule based on the following order of atoms: yellow-blue-pink. The cosine of the angle θ between the two planes was calculated from the dot product of the two normal vectors as shown in Fig. A3b. Fig. A3c-d show the molecule in folded states with angle θ close to 180° and 0°, respectively. Core1 and core2 are nearly parallel in both scenarios. In Fig. A3c, the normal vector of core2 is pointing outwards and the angle θ is close to 180°. If core2 flips, the normal vector will point inwards and the angle θ is close to 0°, as shown in Fig. A3d.

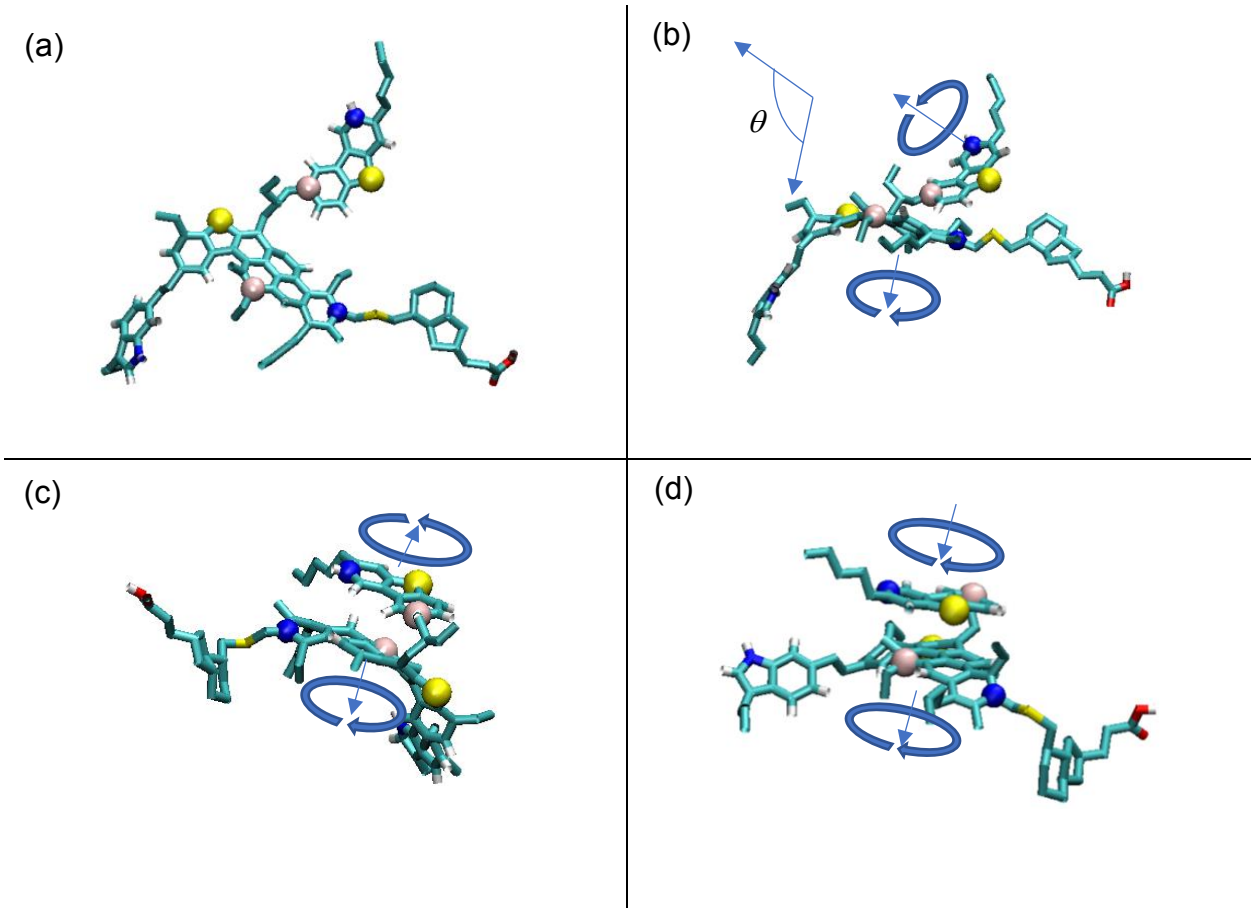

Figure A3 Snapshots of a single M molecule in toluene in unfolded state: D = 1.0 nm and θ = 137° (a) top view and (b) side view; in folded states: (c) D = 0.4 nm and θ = 173°, (d) D = 0.4 and θ = 5°.

A5. Cut-off distance for folded states.

The distance between COGs of core1 and core2 for single M molecule in water was plotted in Fig. 3.3 in Chapter 3, which separated into two bands. The probability distribution of distance was calculated and shown in Fig. A4. The two peaks correspond to the two bands observed in Fig. 3.3, and the dashed line (at 0.55 nm) locates the first minimum in the distribution between the two peaks. This value was therefore chosen to define folded, unfolded and partially folded states.

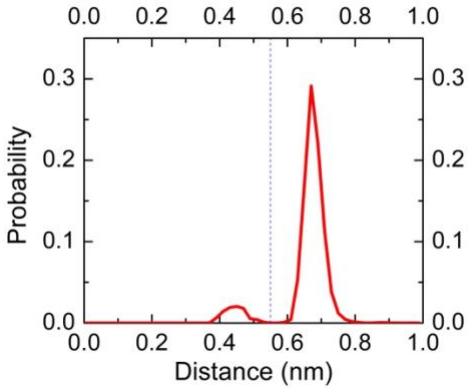

Figure A4 Probability distribution of distance between COGs of core1 and core2 for system 1.

A6. Evolution of angle between core1 and core2.

Fig. A5 shows the angle between core1 and core2 over the simulation time of 60 ns for systems with a single M molecule. In Fig. A5a, the angle fluctuates in a range of 20°-100° with only a few data points below 20° during the first 56 ns. The curve then jumps to a higher range of angle between 140°-180° in the last 4 ns. It suggests an energy barrier for the transition between unfolded and folded states for a single molecule in water. In heptane (Fig. A5b) and toluene (Fig. A5c), the angle evolutions have large fluctuations throughout the simulations.

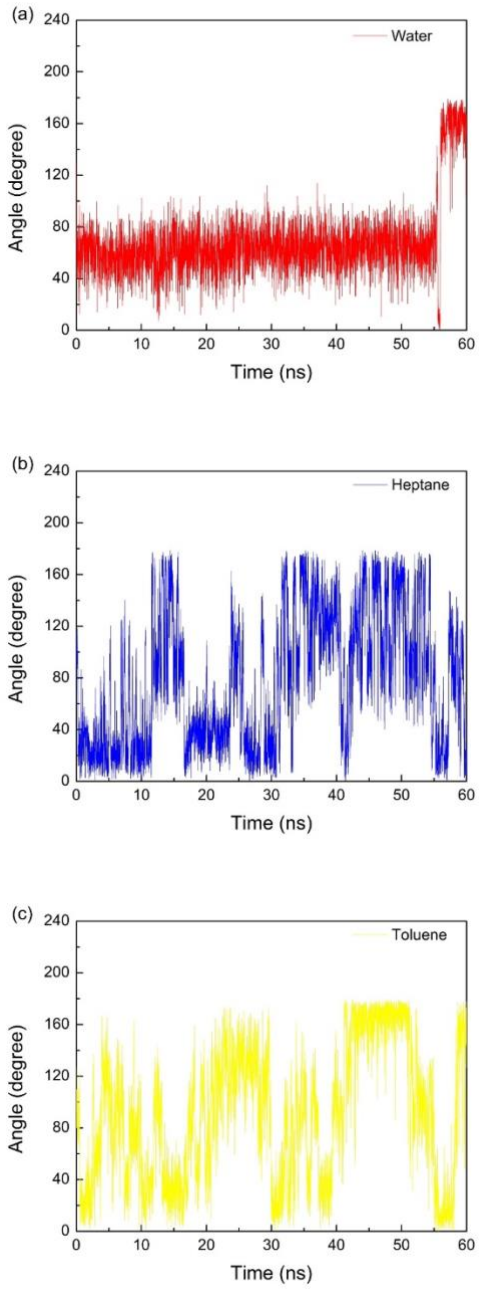

Figure A5 Angle between core1 and core2 over the simulation of 60 ns for systems containing a single molecule in (a) water, (b) heptane and (c) toluene.

A7. Interaction between M molecule and solvent molecules.

For systems with a single M molecule in solutions, the radial distribution functions (RDF) were obtained for water and toluene with respect to the oxygen atoms (in -COOH group) and the nitrogen atom (in -NH- group), as plotted in Fig. A6. The curve for water with respect to oxygen has a distinct peak at 0.18 nm, which corresponds to direct hydrogen bonding between water and the carboxyl group of the M molecule. A peak at such short distance is absent for the non-polar toluene, indicating its lack of short-ranged interaction with the carboxyl group. For both water and toluene, the first peak in the radial distribution function with respect to nitrogen occurs around 0.36 - 0.40 nm, suggesting only weak contact between both solvents and the -NH- group.

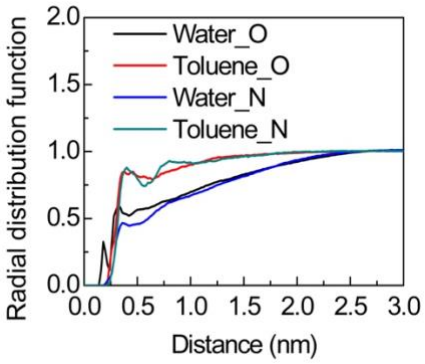

Figure A6 Radial distribution function of solvent (water and toluene) with respect to the oxygen atoms (in -COOH group) and the nitrogen atom (in -NH- group).

A8. Definition of cut-off distance for aggregate.

We used 0.35 nm as a cut-off minimum distance for two M molecules, below which they were considered to be in an aggregate. The choice of this value was based on two considerations. First of all, 0.35 nm is a common cut-off for hydrogen bonds because it is the location of the first minimum in the RDF of SPC water [7]. Secondly, for the system with 12 M molecules in water, the minimum distance between any pair of molecules were calculated for the simulation time from

40 to 60 ns, and the probability distribution for these distances is plotted in Fig. A7. The dashed line shows the distance of 0.35 nm. Clearly, there is a natural gap in the distribution from 0.35 nm to 0.45 nm. We therefore considered two molecules to be aggregated when the minimum distance between them was less than 0.35 nm.

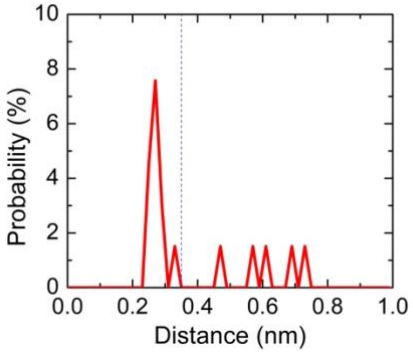

Figure A7 Probability distribution of minimum distance between every pair of M molecules in water.

A9. Snapshots of association between two M molecules.

Fig. A8a shows a snapshot of two M molecules in the largest aggregate in water. In each molecule, two carbon and one sulfur represent the plane of core1, and the two planes are highlighted by blue lines. Core1 in the bottom molecule is horizontal and the core1 in the top molecule is almost perpendicular to it, i.e., the two cores form a T-stacking with a distance of 0.8 nm between their COGs. Fig. A8b shows a snapshot of two M molecules in the largest aggregate in heptane. The two carboxyl groups have close contact and the distance between the oxygen atoms is about 0.3 nm (see enlarged image in the black box). The association between carboxyl groups has limited the interaction between the polyaromatic cores at close proximity. Specifically, the distance between the COGs of the two core1 (planes highlighted by blue lines) is 1.0 nm.

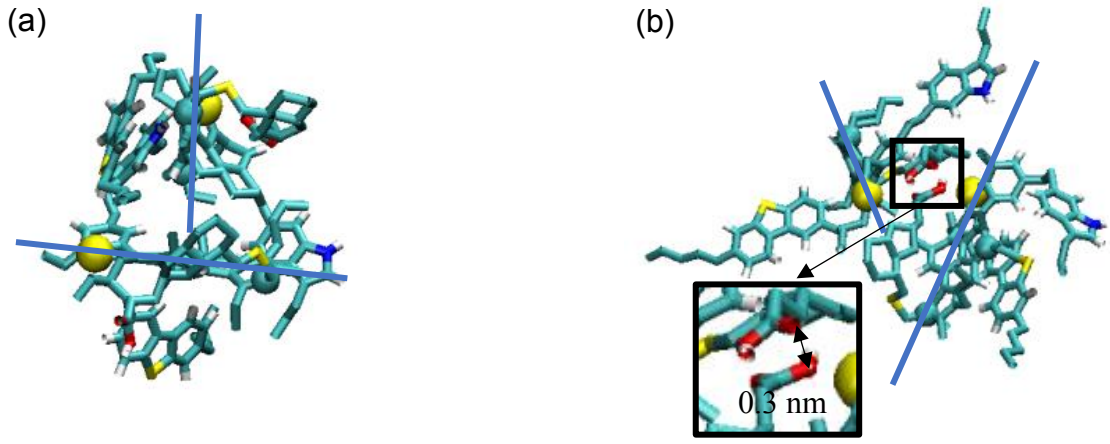

Figure A8 Snapshots for the association between two M molecules (a) in water, and (b) in heptane.

A10. Free energy change for individual M molecules in water.

Table A2 shows the free energy change (see Eqn. 3.1 in Chapter 3) for individual M molecules in the largest aggregates in water (systems 4 and 7) to transit from one state to another. In system 4, molecules W2, W3, W4 and W6 have negative ΔG from unfolded to folded states with large absolute values, implying the high stability of the preferred folded configuration. W5 was exclusively in the unfolded state (100% probability) and therefore ΔG was reported as N/A. These 5 molecules had large energy barrier to transit from one state to another. Only molecule W1 had a small $|\Delta G|$ and was relatively flexible to switch between the states. In system 7, molecules W1, W2 and W3 were highly constrained in the unfolded state (89% and more; large ΔG to come out of the unfolded states), while W4, W5 and W6 had noticeable probability for both folded and unfolded states.

Table A2 Probabilities that individual M molecules are in unfolded, partially folded and folded states, as well as free-energy change estimated from the probabilities, for systems 4 and 7.

mol.	probability (%)			free energy change (kJ/mol)	
	unfolded	partially folded	folded	unfolded to partially folded	unfolded to folded
system 4: 12 M molecules in water, 6 in the largest aggregate					
W1	35.7	2.7	61.6	6.4	-1.4
W2	0.4	4.3	95.3	-5.9	-13.6
W3	6.8	14.4	78.8	-1.9	-6.1
W4	17.8	2.2	80.0	5.2	-3.7
W5	100.0	0.0	0.0	N/A	N/A
W6	1.9	76.7	21.4	-9.2	-6.0
system 7: 6 M and 12 S molecules in water, all aggregated					
W1	100.0	0.0	0.0	N/A	N/A
W2	98.7	0.2	1.1	15.5	11.2
W3	89.8	1.2	9.0	10.8	5.7
W4	75.5	4.8	19.7	6.9	3.3
W5	70.6	0.7	28.7	11.5	2.2
W6	38.8	8.6	52.6	3.8	-0.8

A11. Folding of M molecules in vacuum.

An MD simulation was done for a single M molecule in vacuum (system V1), following the same procedure as described in the main text except that there was no pressure coupling in the production stage. As shown in Fig. A9, the D-θ plot indicated that during the last 50 ns the single M molecule had more folded states. The probabilities for unfolded, partially folded, and folded states were found to be respectively 26%, 1%, and 73%, as shown in Table A3. Though in the initial

configuration the molecule was unfolded, without solvents the through-space interactions led to the preference of folded state. Comparison with data in Table 3.2 of Chapter 3 indicates that all three solvents have, to some degree, suppressed the intramolecular folding of M molecule, and the effect was most significant in water. Such suppression may be caused by the interaction of M molecule with the solvent, as well as the more dynamic motion of the smaller solvent molecules (especially water) which hinders the stabilization of the folded configuration.

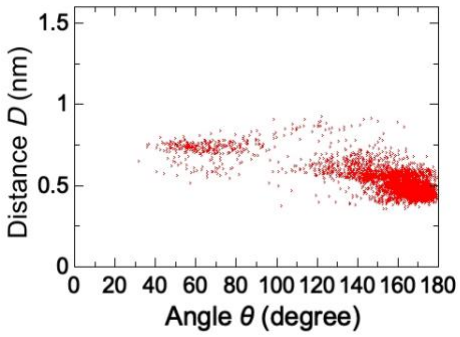

Figure A9 Distance D between COGs of core1 and core2 versus angle θ between the two cores for a single M molecule in vacuum in the last 50 ns.

Table A3 Probabilities of states for systems V1-V3.

sys.	# of M molecules	initial state	probability (%)		
			unfolded	partially folded	folded
V1	1	unfolded	26	1	73
V2	12	unfolded	53	10	37
V3	12	folded	62	6	32

Two additional systems, V2 and V3, were simulated with 12 M molecules in vacuum, following the same procedure as described above. In the initial configuration of system V2, the M molecules were all in the unfolded state and randomly dispersed in the simulation box. Whereas,

in the initial configuration of system V3, the M molecules were all in the folded state. At the end of the simulations, all 12 M molecules formed a single large aggregate in both systems V2 and V3, and the folding characteristics (to be discussed next) were similar in the two systems. This suggests the independence of the simulation results on the initial configurations. During the last 50 ns of simulations, all molecules in systems V2 or V3 were flexible enough to explore the three different states (Fig. A10), with the unfolded state being more favorable (Table A3). The results are qualitatively similar to those for systems 5 and 6 in Chapter 3 but quite different from system 4 (Table 3.2), where the M molecules were much less flexible and the folded state was more dominant.

RDFs for the COG distance between core1 of any two M molecules are shown in Fig. A11a. The first predominant peak is located at ~ 0.64 nm for system V2 and ~ 0.82 nm for system V3, close to the first peak (~ 0.8 nm) in the curve for system 4 in Fig. 3.5a of Chapter 3. However, the RDFs for the distance between the carboxyl groups of any two M molecules (Fig. A11b) are very different from the curve for system 4 in Fig. 3.5b. There is a sharp peak located at ~ 0.28 nm for system V2 and ~ 0.26 nm for system V3, corresponding to the hydrogen bonding between carboxyl groups. The height of the first peaks in Fig. A11b is not only 100 times more than the values for system 4 in Fig. 3.5b, but also more than 10 times the RDF values in Fig. A11a, indicating that the interaction between carboxyl groups played a significant role in the association of M molecules in vacuum. In contrast, in system 4 the hydrophobic polyaromatic cores repelled water while the carboxyl groups were attracted to water. This led to the formation of aggregates with interior polyaromatic cores and exterior carboxyl groups. The carboxyl groups on the outer surface interacted with water while having little interaction amongst themselves. In the final configuration, R_g of the largest aggregate was found to be 5.42 nm for system V2 (12 molecules), 5.09 nm for

system V3 (12 molecules), and 1.13 nm for system 4 (6 molecules). If the spatial density of the M molecules were the same in the aggregates, then R_g would be expected to scale with the cubic root of the number of molecules within. In other words, R_g of systems V2 and V3 would only be $(12/6)^{\frac{1}{3}} = 1.26$ time R_g of system 4. Instead, R_g values of systems V2 and V3 are more than 4 times R_g of system 4. This indicates that the aggregate in system 4 is much more compact than those in systems V2 and V3. Two consequences arise from the significantly more compact structure in system 4: the molecules tend to be folded, and they are much less flexible. The folding behaviors in systems V2 and V3 are closer to system 5 (heptane as solvent) and system 6 (toluene as solvent), where carboxyl-carboxyl interaction was more important in driving aggregation, the aggregates had less compact structure than in water and the molecules within were more flexible.

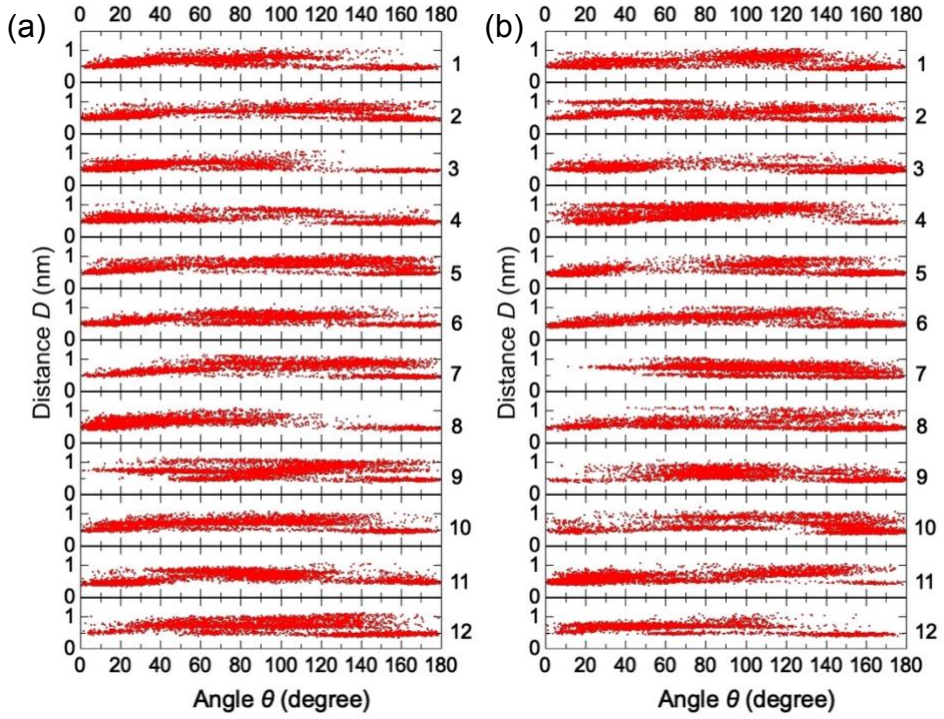

Figure A10 Distance D between COGs of core1 and core2 versus angle θ between the two cores, for the 12 M molecules (labeled from 1 to 12) aggregated in systems (a) V2 and (b) V3.

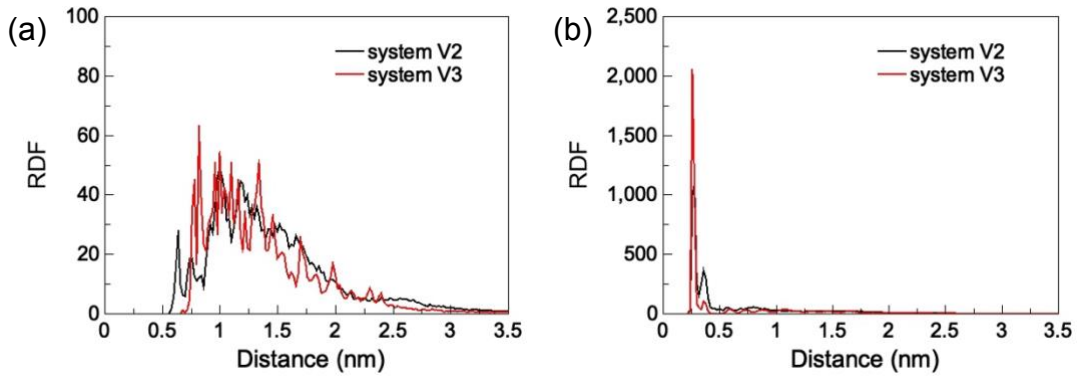

Figure A11 RDFs for (a) the COG distance between core1 of any two M molecules and (b) distance between the carboxyl groups of any two M molecules, where each carboxyl group is represented by the COG of the two oxygen atoms. Results are shown for systems V2 and V3 from the averages over the last 5 ns.

References

[1] J.A. Duran, Y.A. Casas, L. Xiang, L. Zhang, H. Zeng, H.W. Yarranton, Nature of Asphaltene Aggregates, Energy & Fuels. 33 (2019) 3694–3710.

[2] J. Eyssautier, P. Levitz, D. Espinat, J. Jestin, J. Gummel, I. Grillo, L. Barré, Insight into Asphaltene Nanoaggregate Structure Inferred by Small Angle Neutron and X-Ray Scattering, Journal of Physical Chemistry B. 115 (2011) 6827–6837.

[3] L. Barré, S. Simon, T. Palermo, Solution Properties of Asphaltenes, Langmuir. 24 (2008) 3709–3717.

[4] K.L. Gawrys, G.A. Blankenship, P.K. Kilpatrick, Solvent Entrainment in and Flocculation of Asphaltenic Aggregates Probed by Small-Angle Neutron Scattering, Langmuir. 22 (2006) 4487–4497.

[5] J.N. Roux, D. Broseta, B. Demé, SANS Study of Asphaltene Aggregation: Concentration and Solvent Quality Effects, Langmuir. 17 (2001) 5085–5092.

[6] R.B. Teklebrhan, L. Ge, S. Bhattacharjee, Z. Xu, J. Sjöblom, Probing Structure-Nanoaggregation Relations of Polyaromatic Surfactants: A Molecular Dynamics Simulation and Dynamic Light Scattering Study, Journal of Physical Chemistry B. 116 (2012) 5907–5918.

[7] M.J. Abraham, D. van der Spoel, E. Lindahl, B. Hess, the GROMACS development team, GROMACS User Manual version 2016, 2018.

Appendix B: Supporting Information for Chapter 4

B1. Partial atomic charges

The default partial atomic charges generated from PRODRG was not used directly because it may lead to unreliable simulation results. [1] Instead, these charges were modified based on analogue structures in GROMOS96 force field 53A6. [2] Jian et al. [3] adopted the partial atomic charges from residues dipalmitoylphosphatidylcholine, phenylalanine and peptide bond, and used them for the aromatic carbon and hydrogen in the polyaromatic (PA) core, carbonyl groups in the PA core, ester groups and united hydrocarbon groups in the side chains. As shown in Fig. B1, the oxygen atoms in carbonyl groups of the PA core and ester groups of the side chains carry negative charges. Aromatic carbon and hydrogen carry small partial charges. The united atoms in the side chains do not carry any partial charges.

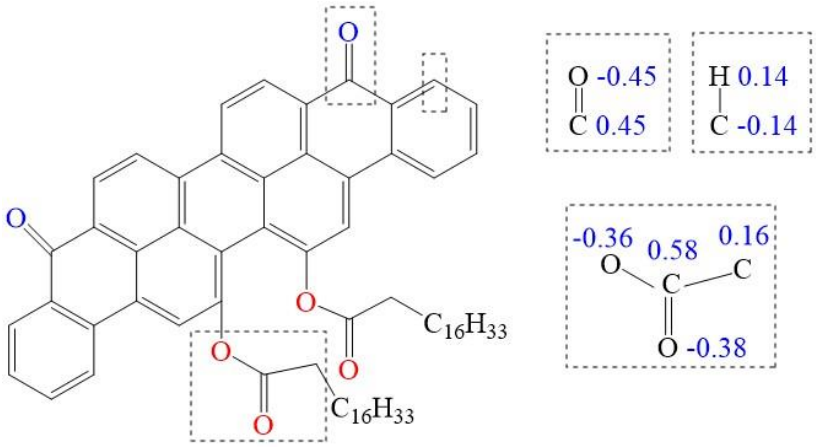

Figure B1. Charge groups (shown in dashed square) in the molecular structure of VO-16C (left) and their partial atomic charges (right, value in unit of e). Only one group is shown to represent each type of charge groups.

B2. Time evolution of number of molecules in the largest aggregates

As shown in Fig. B2, the largest aggregates become stable in the last 10 ns of simulations for all systems.

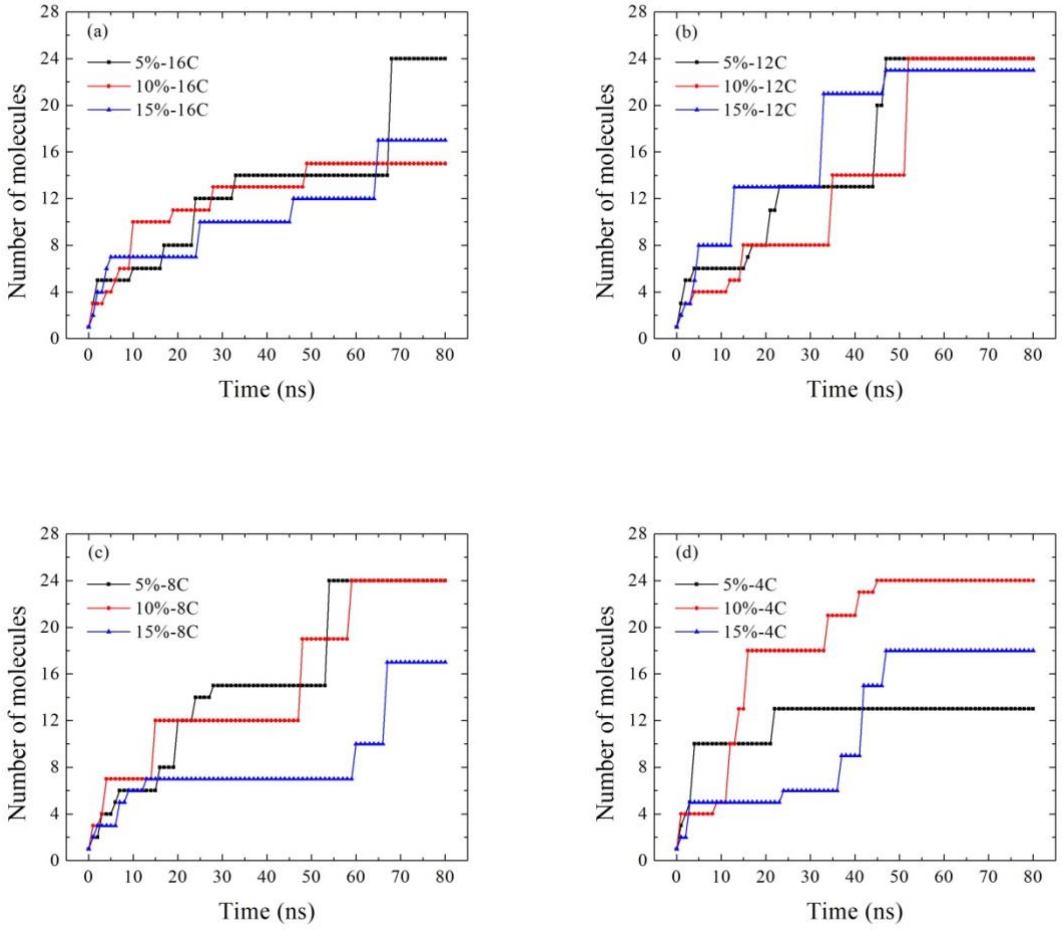

Figure B2. Time evolution of number of molecules in the largest aggregates for systems containing (a) VO-16C, (b) VO-12C, (c) VO-8C and (d) VO-4C.

B3. Radial distribution functions (RDFs) for the center of geometry (COG) distance between PA cores

Each subfigure below plots the RDFs for the COG distance between PA cores in a particular simulated system. There are five curves representing the average over different 2 ns time windows, e.g., curve "70-72 ns" represents the average RDF over simulation time from 70 ns to 72 ns.

(a1) 5%-16C

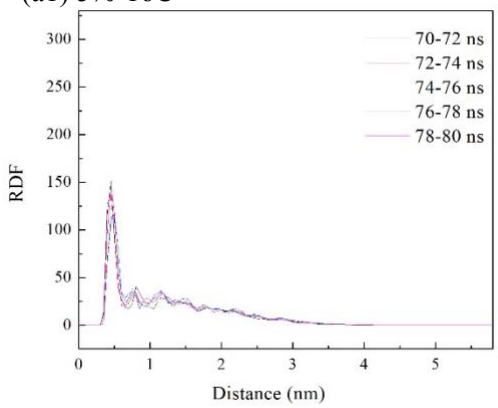

(b1) 5%-12C

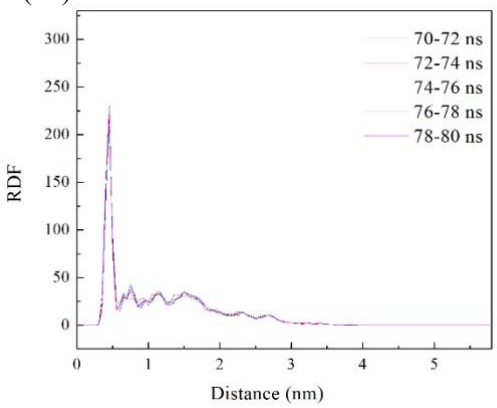

(a2) 10%-16C

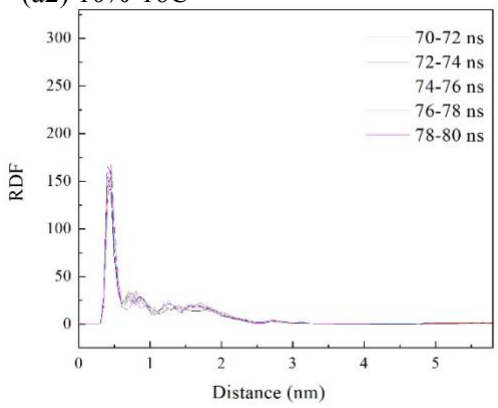

(b2) 10%-12C

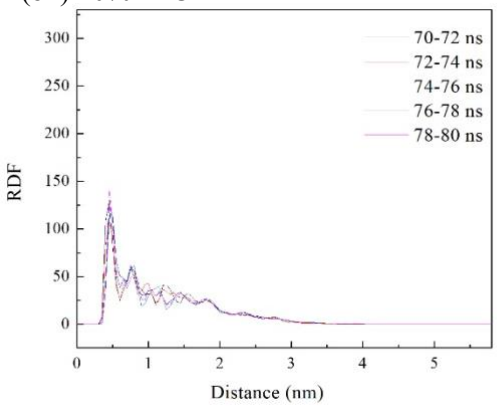

(a3) 15%-16C

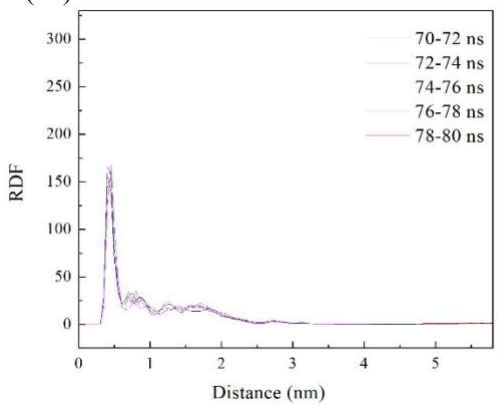

(b3) 15%-12C

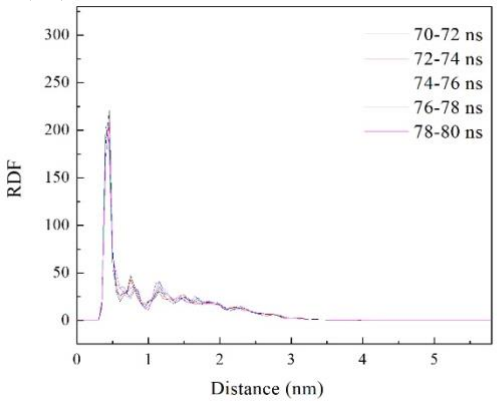

(c1) 5%-8C

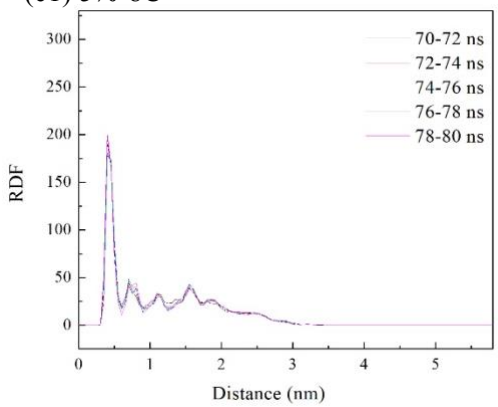

(d1) 5%-4C

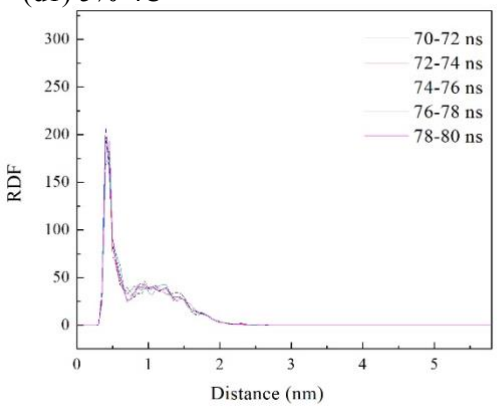

(c2) 10%-8C

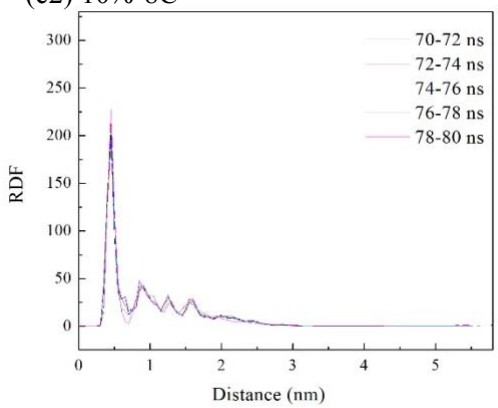

(d2) 10%-4C

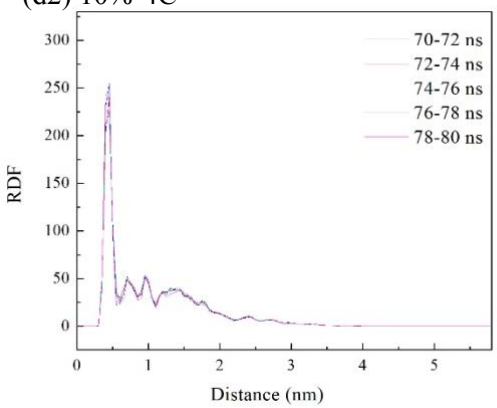

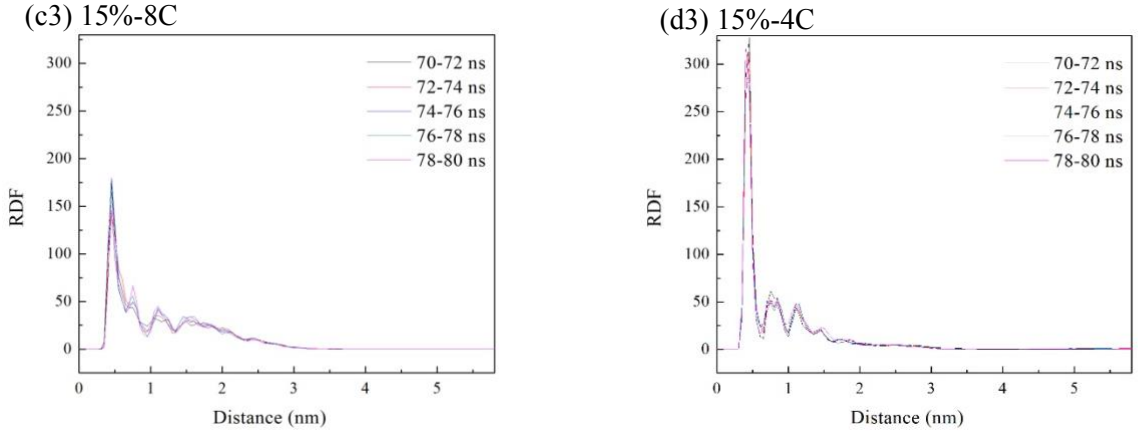

Figure B3. RDFs of COG between PA cores of VO-16C: (a1) 5%-16C, (a2) 10%-16C, (a3) 15%-16C; VO-12C: (b1) 5%-12C, (b2) 10%-12C, (b3) 15%-12C; VO-8C: (c1) 5%-8C, (c2) 10%-8C, (c3) 15%-8C; and VO-4C: (d1) 5%-4C, (d2) 10%-4C, (d3) 15%-4C.

B4. Time evolution of π−π, π−θ and θ−θ contacts

As shown in Fig. B4, the counts of the three types of contacts become stable in the last 10 ns for all systems. As explained in the main text, the numbers of π−θ contacts have been scaled by a factor of 1/2.

(a1) 5%-16C

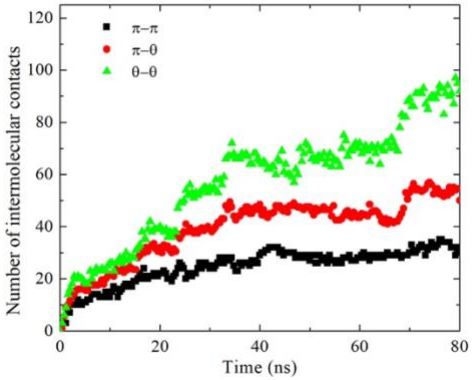

(b1) 5%-12C

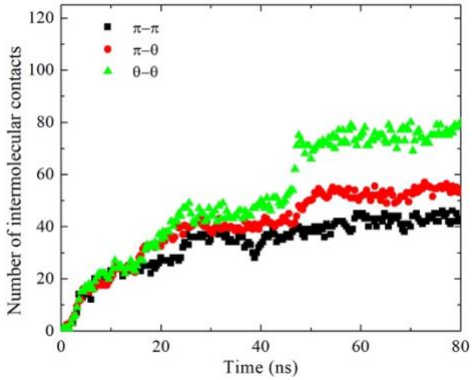

(a2) 10%-16C

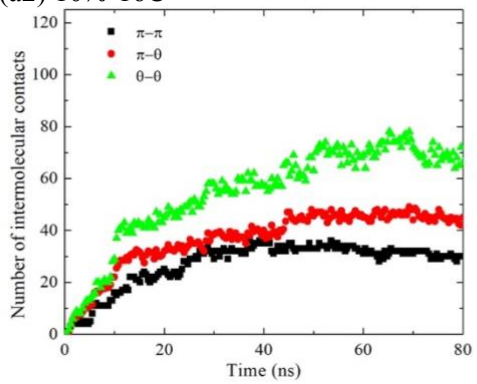

(b2) 10%-12C

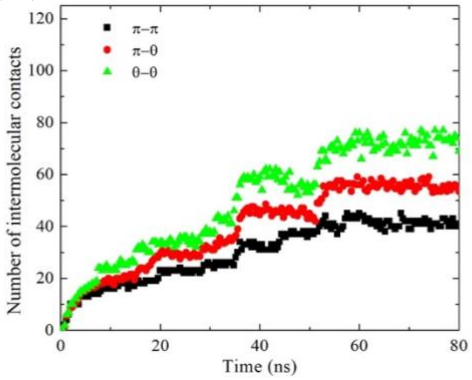

(a3) 15%-16C

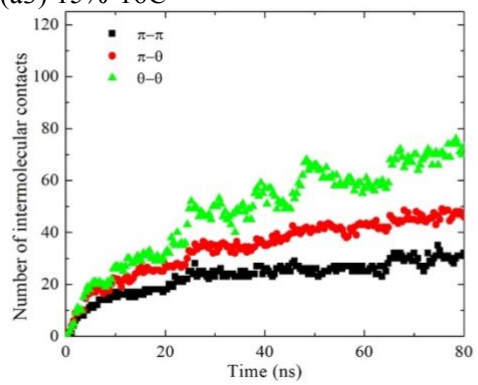

(b3) 15%-12C

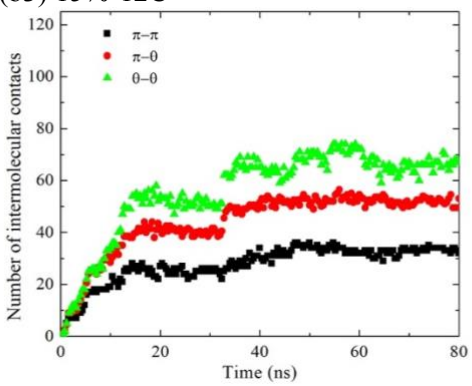

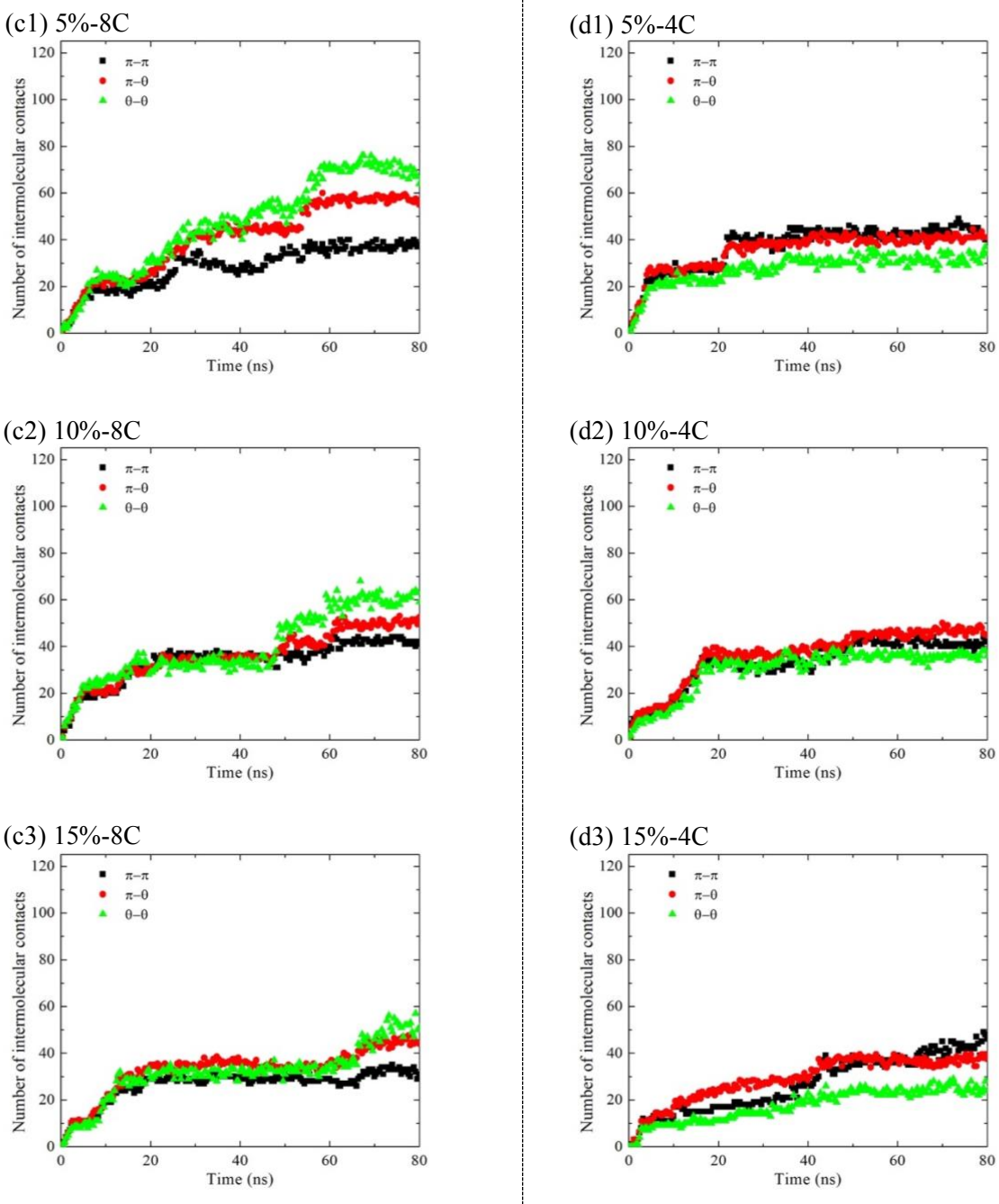

Figure B4. Time evolution of π– π, π–θ (scaled) and θ–θ contacts in systems containing VO-16C: (a1) 5%-16C, (a2) 10%-16C, (a3) 15%-16C; VO-12C: (b1) 5%-12C, (b2) 10%-12C, (b3) 15%-12C; VO-8C: (c1) 5%-8C, (c2) 10%-8C, (c3) 15%-8C; and VO-4C: (d1) 5%-4C, (d2) 10%-4C, (d3) 15%-4C.

B5. Details of simulations on PA cores

The structure of the PA core was created by removing the side chains from VO-16C (Fig. B5). The coordinates of the PA core were imported to GlycoBioChem PRODRG2 server [4], where the topology file was generated. The partial charges and charge groups in the topology were manually adjusted to be compatible with the GROMOS96 53A6 force field [2]. Six PA cores were randomly dispersed in a cubic box with edge length of 7.56 nm. The volume of the box is 1/4 of the volume of the box used to simulate 24 molecules with side chains; hence the number concentration of molecules is the same for the two sets of simulations. For the simulation in pure water the box was randomly filled with simple-point-charge (SPC) water [5–7]. Appropriate amount of NaCl was then added into the solvent to generate concentration of 5% wt., 10% wt. and 15%wt. respectively. MD simulations were performed by using GROMACS (version 5.0.6) package. Periodic boundary conditions and full electrostatics with particle mesh Ewald summation method [8] were used. SETTLE algorithm was used to constrain all bonds of water molecules and LINCS algorithm was applied to constrain all bonds of solute molecules. The total potential energy was first minimized by static structure optimization. Then, the solvent molecules were relaxed around the solutes for 1 ns (300 K, 1 bar) with harmonic restraint (1000 kJ/(mol nm^2)) on the non-hydrogen atoms. After removing the restraint, an NpT ensemble was performed on each system for 20 ns. Full trajectory was obtained, and coordinates were recorded every 10 ps.

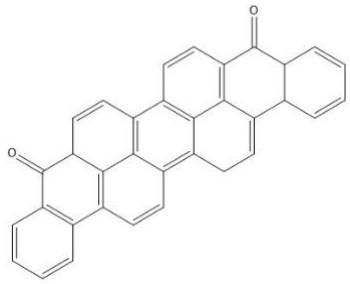

Figure B5. Molecular structure of the PA core.

B6. RDFs of Na^+ around oxygen atoms

The RDFs of Na^+ ions with respect to oxygen atoms are shown in Fig. B6. The solid curves represent the RDFs of Na^+ with respect to the two oxygen atoms on the PA cores, whereas the dash curves are the corresponding RDFs with respect to four oxygen atoms in the side chains. In each plot, the solid curves have two peaks, located at 0.24 nm and 0.48 nm respectively. Whereas, the dash curves stay close to zero at short distance. It indicates that the oxygen atoms on the core have more attractive interaction with neighbouring Na^+ ions.

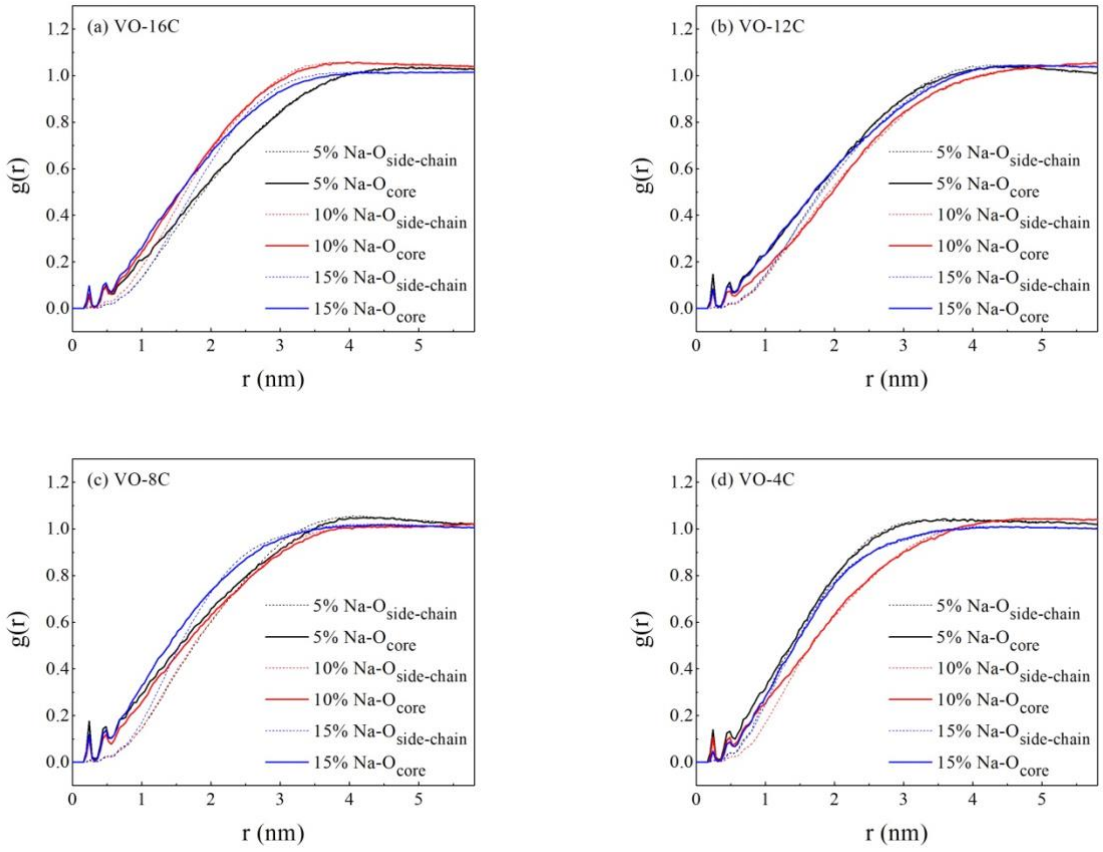

Figure B6. RDFs of Na^+ ions with respect to oxygen atoms in the PA cores (solid lines) and on the side chains (dash lines): (a) VO-16C, (b) VO-12C, (c) VO-8C, and (d) VO-4C. Each subfigure contains data that correspond to 5% wt., 10% wt. and 15% wt. NaCl solutions. All data are averaged over the last 10 ns of the simulations.

B7. Snapshot of aggregates in 5%-8C and 10%-8C systems.

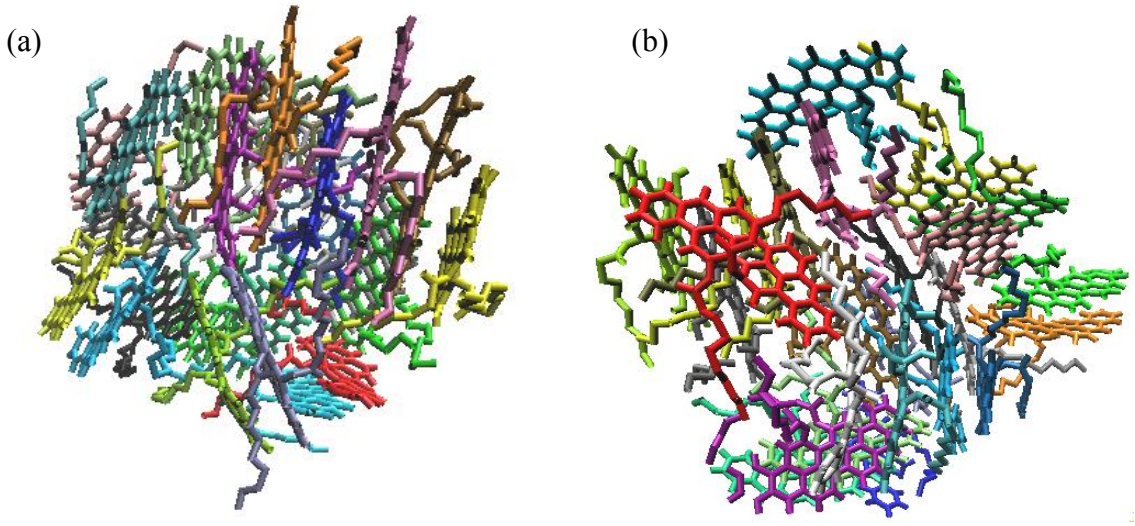

Figure B7. Snapshot of aggregates in (a) 5%-8C and (b) 10%-8C.

References

[1] J.A. Lemkul, D.R. Bevan, Assessing the Stability of Alzheimer's Amyloid Protofibrils Using Molecular Dynamics, J. Phys. Chem. B. 114 (2010) 1652–1660.

[2] C. Oostenbrink, A. Villa, A.E. Mark, W.F. Van Gunsteren, A Biomolecular Force Field Based on the Free Enthalpy of Hydration and Solvation: The GROMOS Force-Field Parameter Sets 53A5 and 53A6, J. Comput. Chem. 25 (2004) 1656–1676.

[3] C. Jian, T. Tang, S. Bhattacharjee, Probing the Effect of Side-Chain Length on the Aggregation of a Model Asphaltene Using Molecular Dynamics Simulations, Energy Fuels. 27 (2013) 2057–2067.

[4] A.W. Schüttelkopf, D.M.F. van Aalten, IUCr, *PRODRG* : A Tool For High-Throughput Crystallography of Protein–Ligand Complexes, Acta Crystallogr. D Biol. Crystallogr. 60 (2004) 1355–1363.

[5] T. Kuznicki, J.H. Masliyah, S. Bhattacharjee, Molecular Dynamics Study of Model Molecules Resembling Asphaltene-Like Structures in Aqueous Organic Solvent Systems, Energy Fuels. 22 (2008) 2379–2389.

[6] T. Kuznicki, J.H. Masliyah, S. Bhattacharjee, Aggregation and Partitioning of Model Asphaltenes at Toluene−Water Interfaces: Molecular Dynamics Simulations, Energy Fuels. 23 (2009) 5027–5035.

[7] X. Zhu, D. Chen, G. Wu, Molecular Dynamic Simulation of Asphaltene Co-Aggregation With Humic Acid During Oil Spill, Chemosphere. 138 (2015) 412–421.

[8] U. Essmann, L. Perera, M.L. Berkowitz, T. Darden, H. Lee, L.G. Pedersen, A Smooth Particle Mesh Ewald Method, J. Chem. Phys. 103 (1995) 8577–8593.

Appendix C: Supporting Information for Chapter 5

C1. Thermodynamic properties of model molecules.

Additional MD simulations were performed to calculate the density of pure model molecules, as shown in Table C1. In each system, a number of model molecules (see Table C1 for details) were randomly placed in a cubic simulations box of initial dimension $6\times6\times6$ nm^3 for systems with PacM, PacS and NisB, and $8\times8\times8$ nm^3 for the system with NisP. The system was then subjected to energy minimization, NVT (100 ps) and finally NpT (30 ns) simulations, using simulation parameters described in the main text. During the NpT simulation, the box size changed, and the density was calculated by averaging over the last 5 ns of the simulation.

The PacM molecule is a hypothetical model and the exact same molecule is not available for direct comparison. Therefore, experimental data for naturally existing mixture of polycyclic aromatic compounds (PACs) were used as reference. The density of PacM was calculated to be 1092 kg/m^3, in good agreement with the experimental density of 1008.8 to 1153.5 kg/m^3 reported by Duran et al. [1] for asphaltene samples from Western Canada bitumen. In our previous work [2], the radius of gyration (R_g) of PacM molecules in water, toluene and heptane were compared with experimental and theoretical references. For example, using small angle neutron and X-ray scattering experiments, R_g for nanoaggregates of natural mixture of PACs was measured to range from 3.0 to 5.2 nm in toluene, and from 5.1 to 11.8 nm in toluene/heptane mixture [3,4]. Our simulations [2] predicted that R_g for PacM was 3.31 nm in toluene and 4.94 nm in heptane, which showed good agreement. The density of PacS calculated from simulation was 1141 kg/m^3, which also agreed with the density of naturally existing PAC mixtures, 1008.8 to 1153.5 kg/m3 [1]. Previous work [5] also reported other behaviours of the PacS model that aligned with experimental

observations, such as its aggregation in bulk solvent and interfacial activity reducing the water/toluene interfacial tension.

The density of NisB was found to be 904 kg/m^3 from our simulation. As a commercially available surfactant, the density of Brij-93 is 0.912 g/mL (912 kg/m^3) at 25°C as reported by Sigma-Aldrich. Clearly, our simulation result showed good consistency with the real material. The PEO-PPO triblock copolymer $(EO)_5(PO)_{10}(EO)_5$, NisP in our work, is a hypothetical model, thus it was compared with a group of poloxamer copolymers. The density of poloxamer copolymers (Poloxamer 124, Poloxamer 184, Poloxamer 188, Poloxamer 407) reported by BASF is between 1050 and 1060 kg/m^3, and our result of 1085 kg/m^3 for NisP was close to this range.

Table C1 System details for density calculation and comparison with experimental data.

molecule	# of molecules	final box side length (nm)	density (kg/m^3)	reference (kg/m^3)
PacM	44	4.43	1092	1008.8 - 1153.5 [a]
PacS	76	4.29	1141	1008.8 - 1153.5 [a]
NisB	171	4.83	904	912 [b]
NisP	72	4.86	1085	1050 - 1060 [c]

[a] data for natural mixtures of PACs from Duran et al. [S1]

[b] data for Brij-93 from Sigma-Aldrich.

[c] data for poloxamer polymers from BASF.

C2. Equilibration of systems.

Fig. C1 shows the total energy vs. time during the production runs for all systems. Since sys. 1 was simulated longer (120 ns) than any other systems (60 ns), data for sys. 1 was only presented from the last 60 ns of the simulation. All curves reached a plateau after a few nanoseconds and fluctuated around this value afterwards.

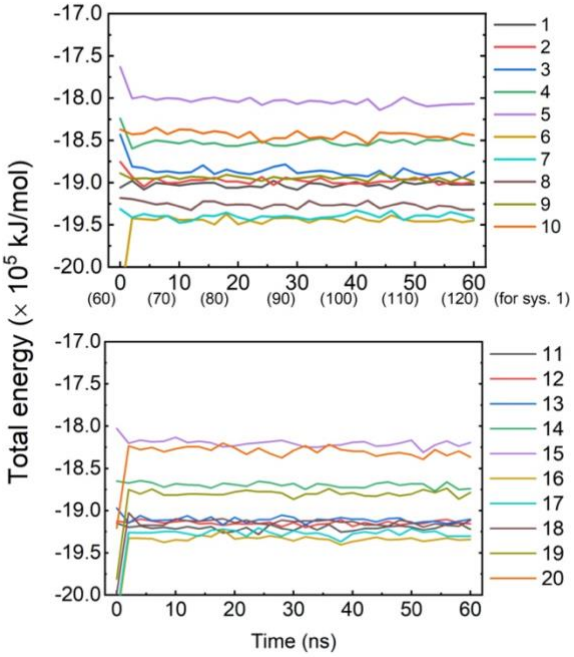

Figure C1 Time evolution of total energy during the production runs. For sys. 1, the last 60 ns of the 120 ns simulation was shown.

In order to verify that the adsorption of PacM was equilibrated before adding non-ionic surfactants, the density profiles of PacM were examined during the last 10 ns of the simulations for sys. 1 and sys. 6. Fig. C2 shows the profiles plotted for every 1 ns during that time interval. The two peaks in each subfigure correspond to the accumulation of PacM at the interfaces, whereas the region between the peaks corresponds to the bulk organic phase (toluene or heptane). On

water/toluene interface as shown in Fig. C2a, the two sharp peaks from different curves were overlapping during the last 5 ns of simulation. This indicated the stabilization of PacM adsorption on the interface, although some PacM molecules remained in bulk toluene and exhibited more dynamic feature. As shown in Fig. C2b for sys. 6 with PacM on water/heptane interface, the peaks also converged in the 10 ns window. There were slight fluctuations near the lower peak on the right interface, caused by the configurational changes of adsorbed PacM.

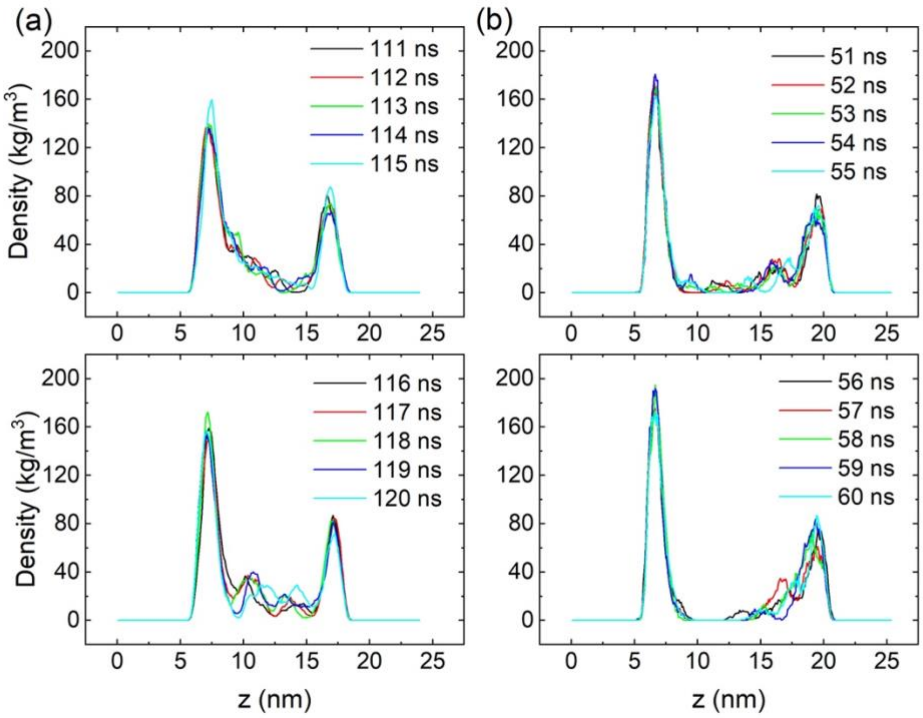

Figure C2 Density profiles for PacM molecules in (a) sys. 1 (water/toluene interface) and (b) sys. 6 (water/heptane interface), plotted at every 1 ns during the last 10 ns.

C3. Criterion for defining adsorbed PAC molecules.

To define a criterion for adsorbed PAC molecules, the first consideration is the common cut-off distance used to define hydrogen bonding, 0.35 nm, which is the location of the first minimum in the radial distribution function (RDF) of single point charge (SPC) water [6]. Secondly, the criterion should be able to identify close contacts between PACs and the water phase. The minimum distance between every PAC molecule and the water phase in the control systems, sys. 1, 6, 11 and 16, was averaged over the last 5 ns of simulation. The distribution of the minimum distance is shown in Fig. C3. For sys. 1, 6, 11 and 16, the first peak in the distribution reduced to minimum at 0.25 nm, 0.3 nm, 0.25nm and 0.20 nm, respectively. All control systems have a clear gap in the distributions immediately after 0.35 nm, as shown by the dashed line. As a result, 0.35 nm was used as the cut-off distance to determine the number of adsorbed PACs on the interface.

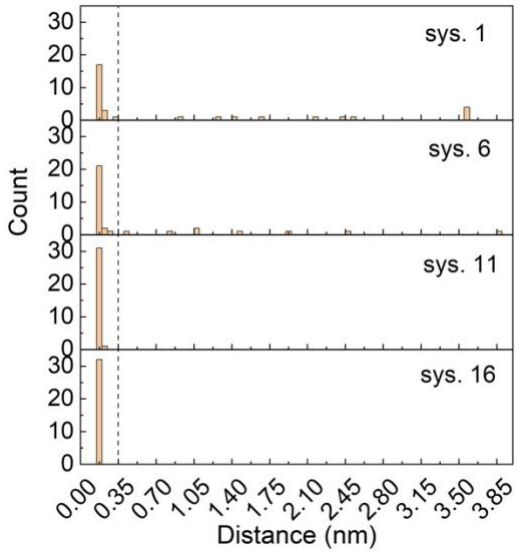

Figure C3 Histogram of the minimum distance between PacM molecules and the water phase, averaged over the last 5 ns of the simulations on the control systems.

C4. Number of adsorbed PacM molecules at the interface.

The number of adsorbed PacM molecules were quantified as shown in Fig. C4. In the last 5 ns of simulation, the number of adsorbed molecules became stable and the average values are given in the insets.

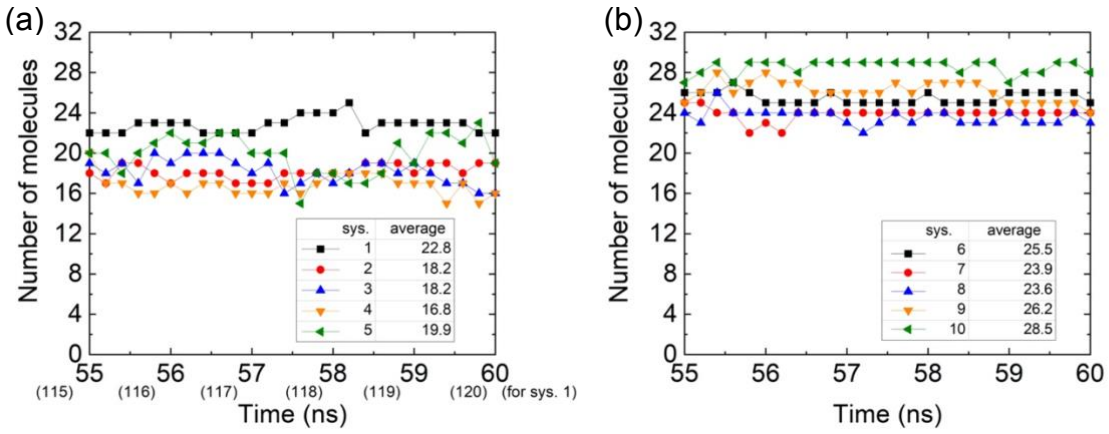

Figure C4 Number of adsorbed PacM molecules during the last 5 ns of simulation and the average values for (a) sys.1-5 (water/toluene interface), and (b) sys. 6-10 (water/heptane interface). Black: control system; red: NisB at low concentration; blue: NisB at high concentration; orange: NisP at low concentration; olive: NisP at high concentration.

C5. Locations of interfaces and peaks in the PAC density profiles.

Table C2 shows, for each system simulated, the final box length in z direction; the z-positions of the two interfaces (interface-L, interface-R) after shifting the configuration in -z direction for 6 nm; the z-positions of the two peaks in the PAC density profile, one near interface-L (peak-L) and the other near interface-R (peak-R); the distance from peak-L to interface-L (dist.-L) and the distance from peak-R to interface-R (dist.-R); and the total distance calculated from the sum of dist.-L and dist.-R. After adding the non-ionic surfactants, an increase in dist.-L as compared to the control system corresponded to a shift of the left peak towards the bulk organic phase, while a decrease corresponded to a shift towards the water phase. The same applies to the right peak quantified by dist.-R.

Table C2 Box length in z direction, z-positions of the interfaces (interface-L and interface-R), z-positions of the peaks in the density profiles of PACs (peak-L and peak-R), the distance from the peaks to the nearest interface (dist.-L and dist.-R), and the total distance (dist.-L + dis.-R).

sys.	z (nm)	interface-L (nm)	interface-R (nm)	peak-L (nm)	peak-R (nm)	dist.-L (nm)	dist.-R (nm)	total dist. (nm)
1	24.01	6.15	18.01	7.08	17.08	0.93	0.93	1.86
2	23.99	6.15	17.94	7.00	17.00	0.85	0.94	1.79
3	23.82	6.24	17.56	7.50	16.31	1.26	1.25	2.51
4	23.94	6.17	17.85	7.62	16.72	1.45	1.13	2.58
5	23.81	6.22	17.56	7.26	16.47	1.04	1.11	2.15
6	25.42	5.94	20.29	6.65	19.44	0.71	0.85	1.56
7	25.41	5.98	20.30	6.73	19.52	0.77	0.78	1.55
8	25.48	6.01	20.33	6.84	19.66	0.83	0.67	1.50
9	25.44	5.93	20.26	6.57	19.33	0.64	0.93	1.57
10	25.46	5.99	20.30	6.58	19.65	0.59	0.65	1.24
11	24.18	6.20	18.21	6.57	17.85	0.37	0.36	0.73
12	24.41	6.16	18.60	6.63	18.27	0.47	0.33	0.80
13	24.34	6.20	18.45	6.53	18.12	0.33	0.33	0.66
14	24.33	6.19	18.45	6.61	18.13	0.42	0.32	0.74
15	24.22	6.26	18.26	6.58	17.81	0.32	0.45	0.77
16	25.43	5.97	20.34	6.23	20.05	0.26	0.29	0.55
17	26.69	5.82	22.41	6.18	21.93	0.36	0.48	0.84
18	26.53	5.87	22.08	6.23	21.62	0.36	0.46	0.82
19	26.63	5.79	22.26	6.08	21.87	0.29	0.39	0.68
20	26.53	5.74	21.97	6.05	21.70	0.31	0.27	0.58

C6. Interaction between non-ionic surfactants and PacM in bulk organic phase.

Radial distribution functions (RDF) of all atoms in dispersed non-ionic surfactants with respect to atoms in all PacM molecules for sys.4 (PacM and NisP at low concentration, toluene as the organic phase) and sys. 7 (PacM and NisB at low concentration, heptane as the organic phase) are plotted in Fig. C5. Data were averaged over the last 5 ns of the simulations. There was only 1 NisP molecules in bulk toluene in sys. 4, the RDF increased gradually indicating there was no obvious short-range interaction between dispersed NisP and PacM molecules. In sys. 7, the first predominant peak was located at ~ 0.56 nm, indicating interaction of dispersed NisB with PacM molecules in bulk heptane.

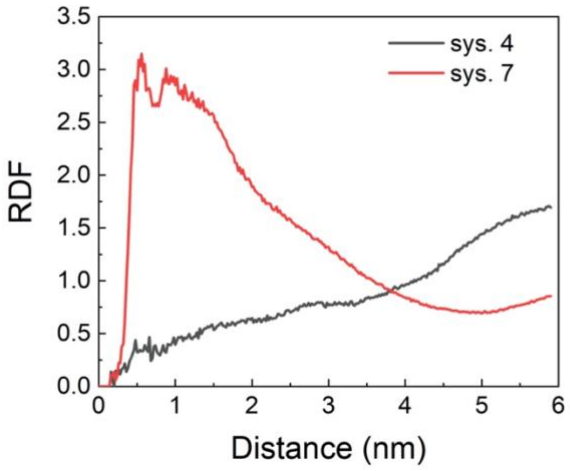

Figure C5 RDF for atoms in dispersed non-ionic surfactants with respect to atoms in all PacM molecules, averaged over the last 5 ns of simulation for sys. 4 (PacM and NisP at low concentration, toluene as the organic phase) and sys. 7 (PacM and NisB at low concentration, heptane as the organic phase).

C7. Probability distribution of aggregate size.

Two molecules were considered in aggregated form if the minimum distance between any atoms from one molecule and any atoms from the other was below 0.35 nm, the same criterion as discussed in C3. The number of molecules in the PAC aggregates was used to represent the aggregate size, which were collected during the last 5 ns of the simulations. All the data were used to generate the probability distribution for the aggregate size, as plotted in Fig. C6. In sys. 1-10, more than 70% of PacM existed in monomer form. Adding non-ionic surfactants (sys. 2-5 and sys. 7-10) increased the probability of monomers compared to the control systems, sys. 1 and sys. 6. In sys. 11-20, the aggregates were larger and the probability for monomers was below 50%. Adding non-ionic surfactant reduced the probability of monomers in sys. 12-15 compared to sys. 11. For sys. 17-20, the probability of monomers was increased by adding non-ionic surfactants.

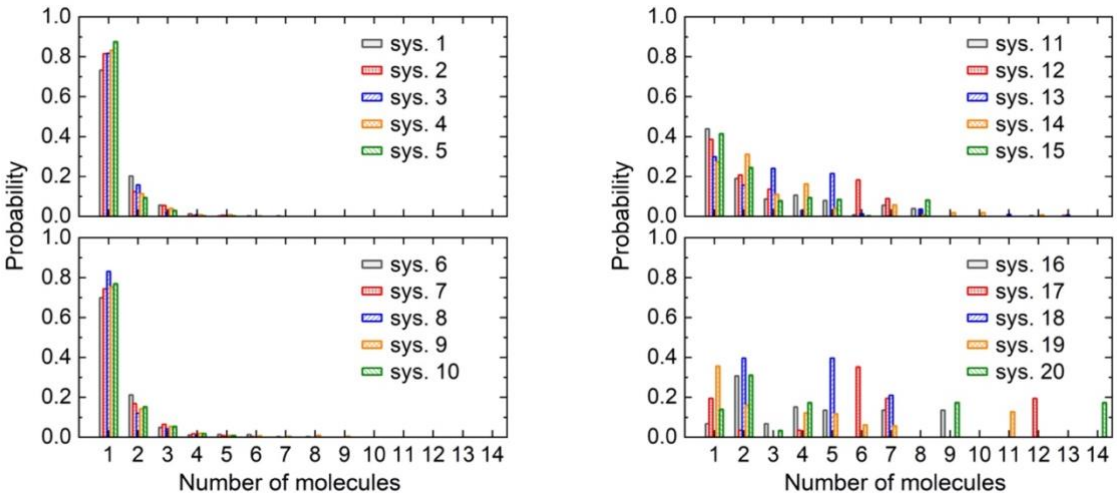

Figure C6 Probability distribution for the number of PAC molecules in aggregates over the last 5 ns of the simulations.

C8. Size of the largest aggregates.

Fig. C7 shows the size of the largest aggregates, averaged over the last 5 ns. With PacM in systems with water/toluene interface (black symbols), the largest aggregates were small regardless of whether NisB or NisP were added. There were on average 2.7-3.5 molecules in the largest aggregates, and adding the surfactant slightly decreased the size. Increasing the concentration of NisB or NisP tended to decrease the size, although the effect was not significant. With PacM and water/heptane interface (red symbols), the size of the largest PacM aggregates was larger than the case of water/toluene interface (black symbols). While the addition of NisB reduced the size of the largest aggregates, the addition of NisP increased it. There appeared to be a correlation between the size of the largest aggregates and adsorption on the water/heptane interface: the higher the adsorption, the larger the aggregates. For systems with PacS and water/toluene interface (green), the size of the largest PacS aggregates was slightly reduced by adding NisB but increased by adding NisP. In the case of water/heptane interface (blue symbol), the size of the largest aggregates was increased by adding either type of non-ionic surfactant at low or high concentrations.

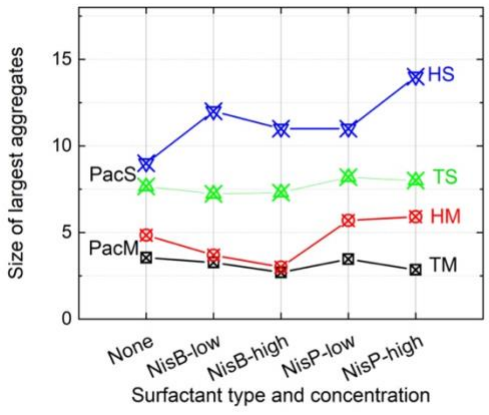

Figure C7 Number of molecules in the largest PAC aggregates averaged over the last 5 ns of the simulations. PacM in toluene (black), PacM in heptane (red), PacS in toluene (green), PacS in

heptane (blue). Horizontal labeling: (None) control systems 1, 6, 11, 16; (NisB-low) sys. 2, 7, 12, 17; (NisB-high) sys. 3, 8, 13, 18; (NisP-low) sys. 4, 9, 14, 19; (NisP-high) sys. 5, 10, 15, 20.

C9. Final configurations for the control systems and RDF between PACs.

Fig. C8 shows the final configurations for sys. 1, 6, 11, and 16 (left panel, also shown in Fig. 5.3) along with the top view on interface-L (right panel). The oxygen atoms in the PACs are highlight in red, including the two oxygen atoms in carboxyl groups of PacM, and the two oxygen atoms on the core of PacS without attaching to the aliphatic chains. As shown on the left, for sys. 1 and 6, most of the adsorbed PacM molecules had the oxygen atoms close to the water phase. Similarly, the oxygen atoms in PacS had close contact with water phase for sys. 11 and 16. As shown on the right, the largest aggregates were located on the interface-L, highlighted with thickened bonds. The PacM aggregates were loosely structured (sys. 1 and 6), while the PacS aggregates (sys. 11 and 16) were more compact due to stacking through π-π interaction. As shown in Fig. C9, the RDF between different PAC molecules had sharp peaks around 0.5 nm. The intensity of the peaks was higher in sys. 11 and sys. 16 than in sys. 1 and sys. 6, indicating more aggregation between PacS molecules than PacM molecules. In all 4 systems, the interface was sparsely covered by the PAC molecules, leaving ample surface area exposed. A quantification of the surface coverage can be found in Appendix C11.

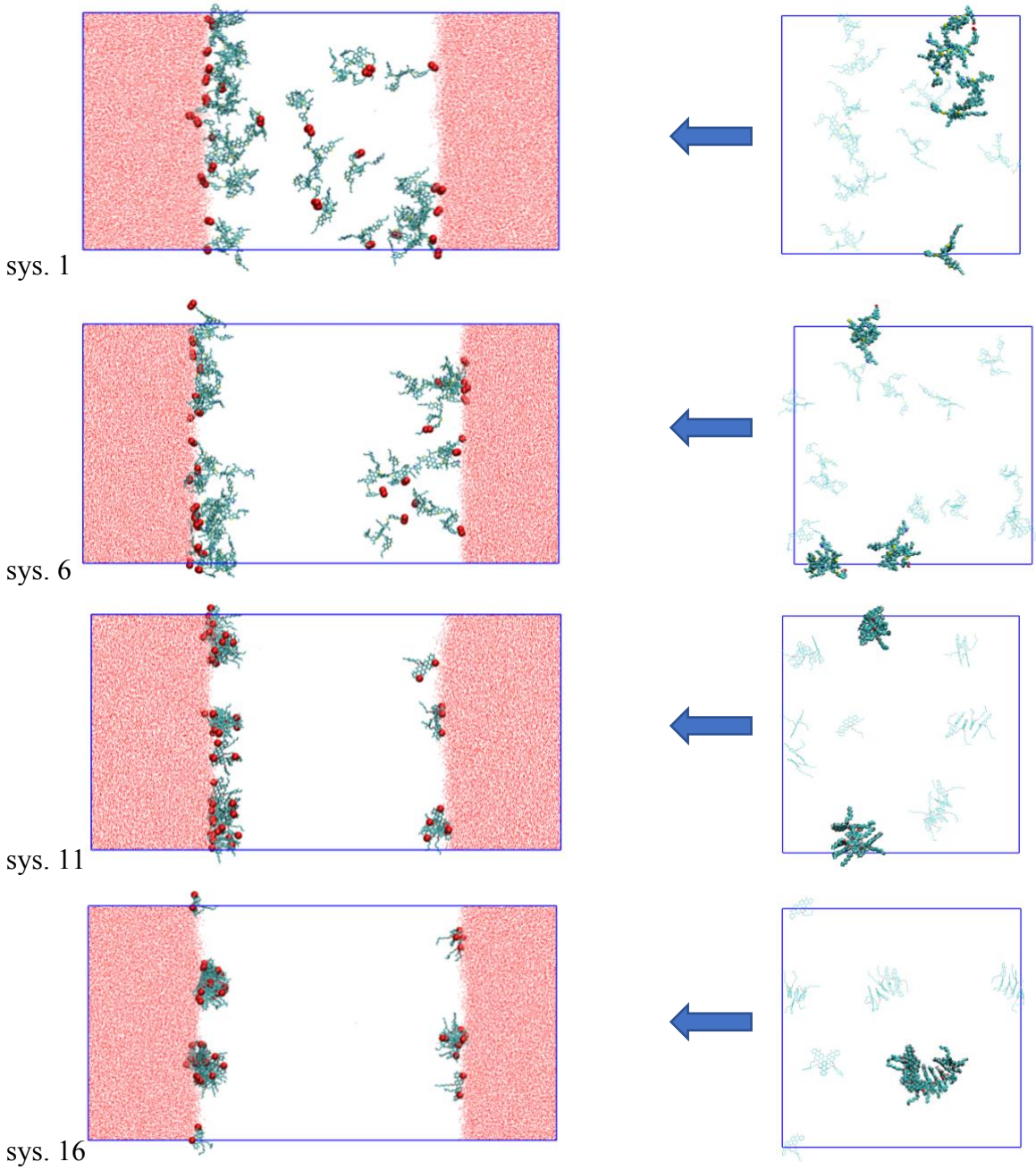

Figure C8 (Left panel) final configurations of the control systems, sys. 1, 6, 11 and 16 (red: water; cyan: PacM or PacS; organic solvent molecules removed for clarity; oxygen atoms in PacM and PacS (not including those attached to aliphatic chains) highlighted in red). (Right panel) top view of PACs on interface-L (the largest aggregates were shown in thickened bonds).

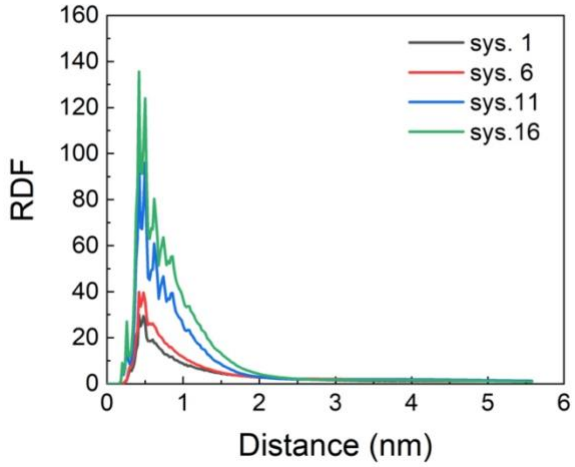

Figure C9 RDF between different PAC molecules, averaged over the last 5 ns of simulations for the control systems, sys. 1 (PacM at water/toluene interface), sys. 6 (PacM at water/heptane interface), sys. 11 (PacS at water/toluene interface), and sys. 16 (PacS at water/heptane interface). All atoms in each PAC molecule were included in the calculation.

C10. Final configurations for simulation sys. 2-5 and sys. 7-10.

Final configurations for systems with non-ionic surfactants and PacM are shown in Fig. C10. the non-ionic surfactants (blue) were located closer to the water phase than PacM molecules.

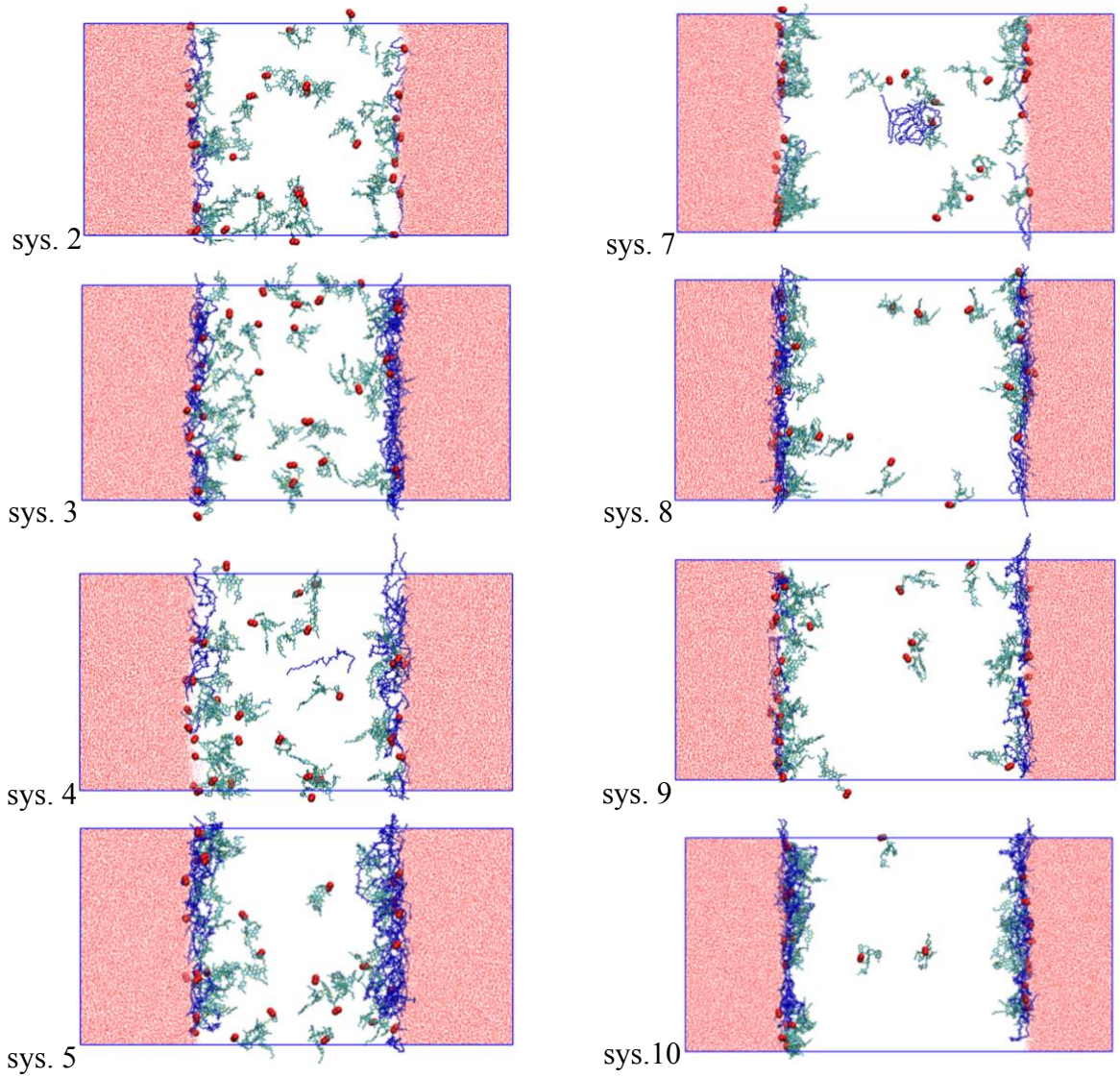

Figure C10 Final configurations of sys. 2-5 and 7-10, red: water; cyan: PacM (oxygen atoms in PacM highlighted in red); blue: NisB/P; organic solvent molecules removed for clarity.

C11. Fraction of surface coverage by PACs in control systems.

The fraction of interface covered by PacM and PacS in the control systems was quantified using an approach similar to what was proposed by Rabanel et al. [7] to calculate the surface coverage of nanoparticle by PEG chains. The projected area of each PEG chain on the nanoparticle surface was determined from $\pi {R_F}^2$, where RF is the Flory radius of the PEG chain. [7] Here, the projected area (A_p) of a PAC molecule on the interface provided an estimation on the surface area covered by the PAC, as illustrated in Fig. C11. A_p depended not only on the number of atoms in the molecule, but also on its adsorbed configuration. For example, a PacS with its polyaromatic (PA) core perpendicular to the interface would result in a lower surface coverage than a PacS with its PA core lying flat on the interface. To calculate A_p for each control system, all the atoms in the adsorbed molecules were represented by van der Waals spheres and projected onto the interface. The fraction of surface coverage was obtained as the ratio of Ap to the area of the interfaces (both interface-L and interface-R). The surface coverage fraction was found to be 15% for sys. 1 (PacM at water/toluene interface), 18% for sys. 6 (PacM at water/heptane interface), and 11% for both sys. 11 (PacS at water/toluene interface) and sys. 16 (PacS at water/heptane interface).

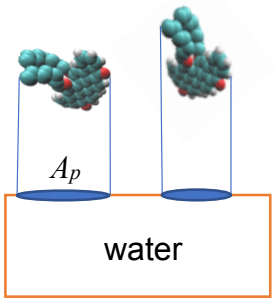

Figure C11 Schematic of projecting a PAC molecule on the interface. Atoms are represented by van der Waals spheres.

References

[1] J.A. Duran, Y.A. Casas, L. Xiang, L. Zhang, H. Zeng, H.W. Yarranton, Nature of Asphaltene Aggregates, Energy Fuels. 33 (2019) 3694–3710.

[2] X. Sun, H. Zeng, T. Tang, Molecular Simulation of Folding and Aggregation of Multi-Core Polycyclic Aromatic Compounds, Journal of Molecular Liquids. 310 (2020) 113248.

[3] K.L. Gawrys, G.A. Blankenship, P.K. Kilpatrick, Solvent Entrainment in and Flocculation of Asphaltenic Aggregates Probed by Small-Angle Neutron Scattering, Langmuir. 22 (2006) 4487–4497.

[4] J.-N. Roux, D. Broseta, B. Demé, SANS Study of Asphaltene Aggregation: Concentration and Solvent Quality Effects, Langmuir. 17 (2001) 5085–5092.

[5] T. Lan, H. Zeng, T. Tang, Molecular Dynamics Study on the Mechanism of Graphene Oxide to Destabilize Oil/Water Emulsion, J. Phys. Chem. C. 123 (2019) 22989–22999.

[6] M.J. Abraham, D. van der Spoel, E. Lindahl, B. Hess, the GROMACS development team, GROMACS User Manual version 2016, 2018.

[7] J.-M. Rabanel, P. Hildgen, X. Banquy, Assessment of PEG on Polymeric Particles Surface, A Key Step in Drug Carrier Translation, Journal of Controlled Release. 185 (2014) 71–87.

Appendix D: Supporting Information for Chapter 6

D1. Quantification of surface coverage fraction.

As shown in Fig. 6.2a in the main text, the water droplet in toluene (sys. A0-S) is sphere like with toluene surrounding. If the water droplet (4074 molecules) is treated as sphere with density of 997 kg/m^3, the radius for the sphere is proposed to be R_p = (3*4074*18*10^{-26}/(4*pi*6.022*997))$^{1/3}$ = 3.08 nm, where the diameter D_p = 6.18 nm.

The surface coverage fraction of adsorbates on water droplets was calculated by the following procedures. 1. Treat the water drop as a sphere with radius of r; 2. Place the center of mass (COM) for the water drop located at (0, 0, 0), and obtain the translated coordination of the adsorbed molecules; 3. Project the coordination of each atoms in the adsorbed molecules to the sphere, as shown in Fig. D1 (a) and (d). Each coordination is a point on the sphere surface, as shown in Fig. S1 (b) and (e); 4. During the projection, the atom is treated as a sphere with its van der Waals (VDW) radius r_W as shown in Fig. D1 (b). The sphere will be projected as an area on the surface, which is like a "footprint" [1], as shown in Fig. D1 (c); 5. Generate sufficient (e.g. 100,000) random points on the sphere surface. If the point fit into any projected area, that the distance between the random point and any projected atom is less than r_{max}, it is counted as covered.

It should be noted that the radius r is determined by the distance between COM of water drop and the nearest atom in the adsorbed molecule. Because the coordination is projected, the actual value of radius r does not affect the fraction. This value is selected to facilitate the calculation. The distance r_{max} was calculated by the equations as follows:

$$\theta = \sin^{-1}\left(\frac{r_w}{D}\right) \quad (1)$$

$$r_{max} = 2 \times r \times \sin(\theta/2) \quad (2)$$

Where rw is the VDW radius, D is the distance between COM of the atom and the COM of the water droplet.

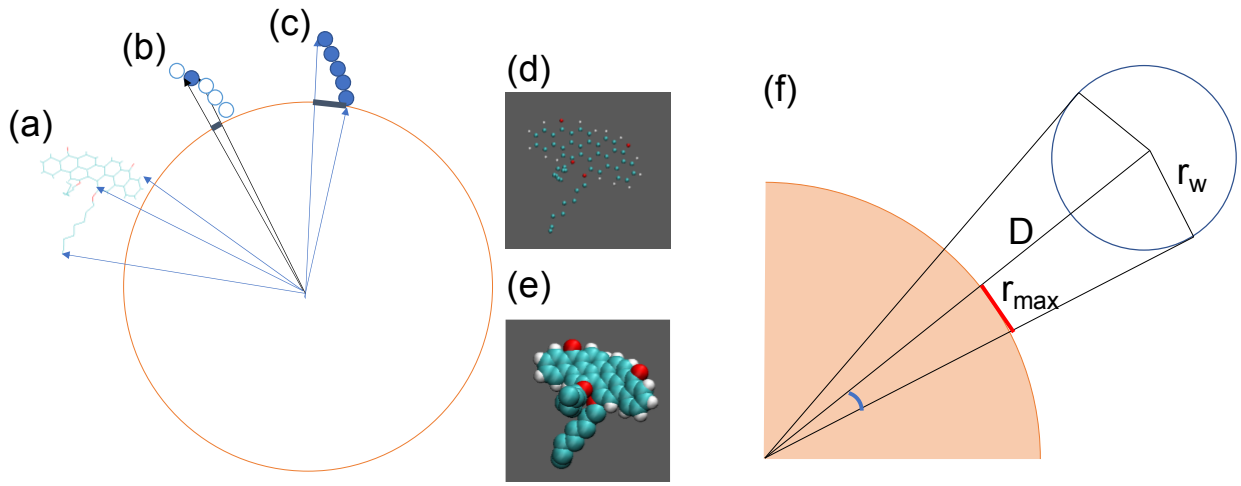

Figure D1. Illustration on the calculation of surface coverage fraction.

D2. Details of umbrella sampling

Details of sampling windows are shown in Table D1. The histogram for 43-50 umbrella simulations was plotted against the reaction coordinate ζ (normalized by D_p) in the bottom panel of Fig. D2. The corresponding potential of mean force (PMF) was plotted in the top panel. As shown in the bottom panels, the sampling windows were overlapping their neighboring window, reproducing the unbiased potential by removing the biasing potential. Around the start point of dramatic drop of PMF, the histogram for some sampling windows has more than one peaks.

Table D1 Details of umbrella sampling windows.

sys.	# of windows	range of ζ / D_p
A0	50	0.93 - 2.27
V1	49	0.83 - 2.25
P1	43	0.84 - 2.26
B1	45	0.55 - 2.25
V2	50	0.84 - 2.27
P2	45	0.74 - 2.27
B2	48	0.55 - 2.29

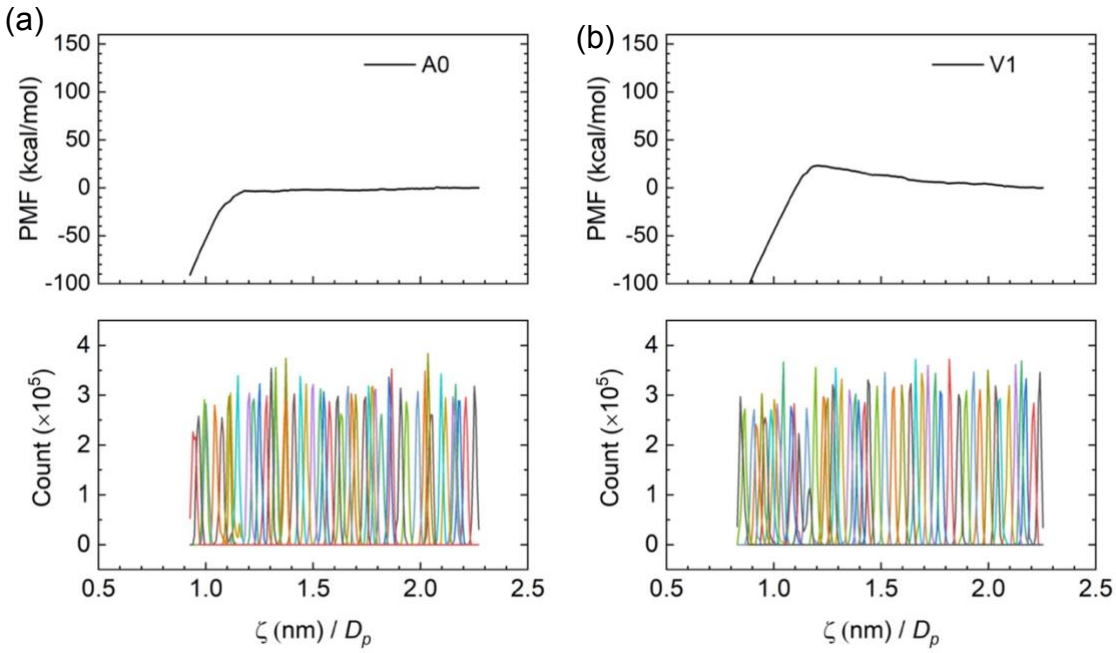

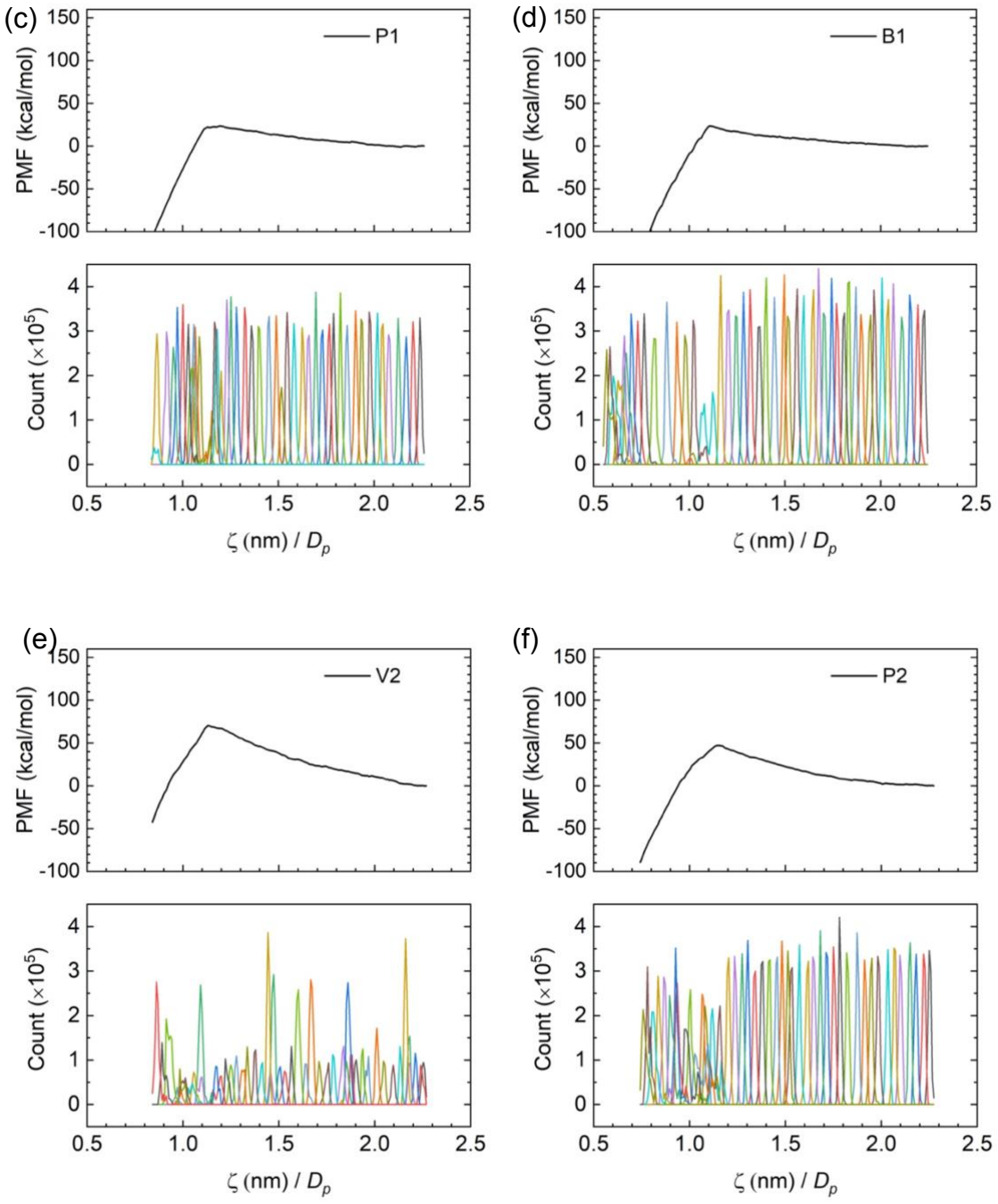
(c)
P1
PMF (kcal/mol)
Count (×10^5)
ζ (nm) / D_p
(d)
B1
PMF (kcal/mol)
Count (×10^5)
ζ (nm) / D_p
(e)
V2
PMF (kcal/mol)
Count (×10^5)
ζ (nm) / D_p
(f)
P2
PMF (kcal/mol)
Count (×10^5)
ζ (nm) / D_p

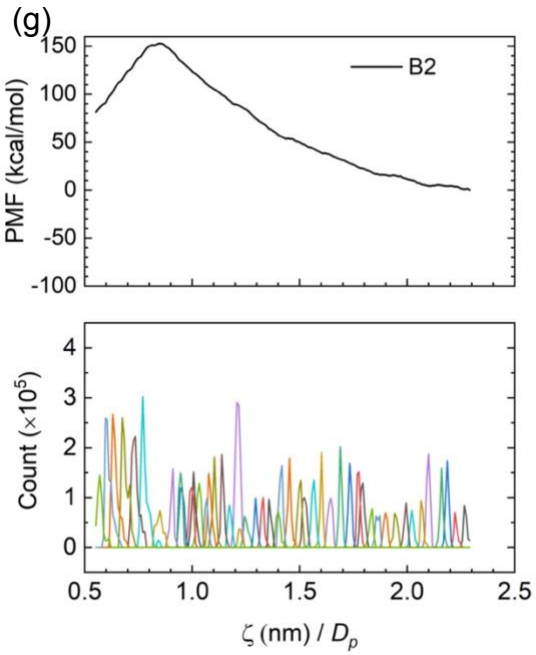

Figure D2. PMF (top) and umbrella histograms (bottom) of the COM separation between two water droplets in toluene for (a) sys. A0 without adsorbates, (b) sys. V1, (c) sys. P1, (d) sys. B1, (e) sys. V2, (f) sys. P2, (g) sys. B2.

D3. Location and width of RDF peaks.

Estimation on the location the width of the RDF peaks is performed by fitting the peaks by Gaussian functions. As an example of curve fitting in Fig. D3a, the thickness of the adsorbate layers is determined by the width of the fitting Gaussian curves. Total width of RDF peak (w_{all}), as shown in Fig. D3b, is calculated by:

$$w_{all} = \frac{w_1}{2} + \frac{w_2}{2} + (L_2 - L_1) \quad \text{(D3)}$$

where, w_1 and w_2 are the width of RDF peak for group 1 and group 2 with respect to COM of water droplets, respectively; L_1 and L_2 are the center of the RDF peaks, as shown in Fig. D3b. The location and width of peaks in Fig. 6.2c and e, and the width of the peaks in Fig. 6.2b and d

are presented in Table D2. The thickness of the adsorbate films was represented by the width (w_{all}) of RDF peaks for all atoms in adsorbates with respect to the COM of water droplets, as:

$$A_{film} = w_{all} * R_p = 3.09 w_{all}\ (nm) \quad (4)$$

As shown in Table D2, the thickness of film was thickest for sys. V1 compared with sys. P1 and B1. The film became thicker when there were more adsorbates in the system, e.g. comparing sys. V2 to V1, P2 to P1, B2 to B1.

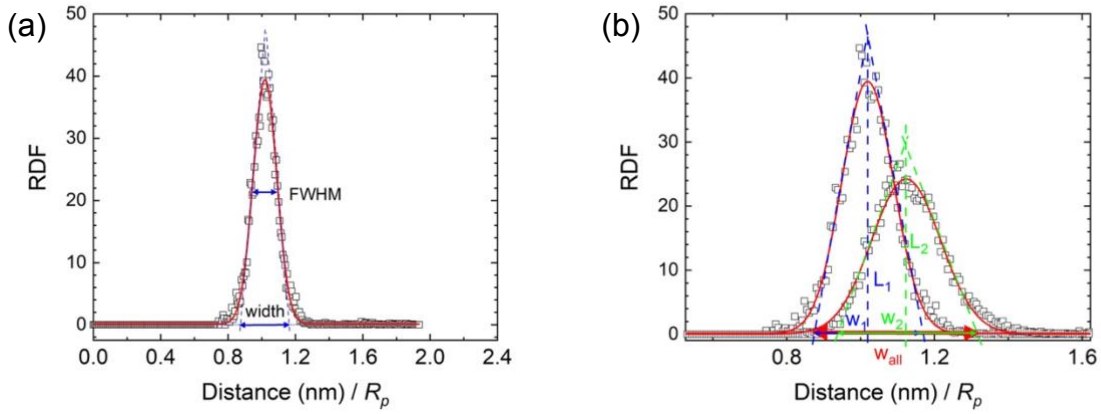

Figure D3 (a) Example of RDF curve fitting; scattered data is the RDF of group1 in sys. B1-S with respect to COM of water droplet (B1-S (g1) as shown in Fig 6.2c of the main text); red curve is the fitting Gaussian curve; full width at half maximum (FWHM) and the width of Gaussian curve are obtained; and (b) calculation of peak width (w_{all}) for RDF of all atoms with respect to COM of water droplets. Scattered data are from B1-S (g1) and B1-S (g2) in Fig 6.2c of the main text.

Table D2 Location and width of RDF peaks in Fig. 6.2. Values are normalized by R_p.

sys.	g1			g2			w_{all}	A_{film} (nm)
	L_1	FWHM	w_1	L_2	FWHM	w_2		
V1-S	1.15	0.34	0.58	1.24	0.35	0.59	0.68	2.11
P1-S	1.04	0.18	0.30	1.20	0.31	0.52	0.58	1.79
B1-S	1.02	0.17	0.28	1.12	0.22	0.37	0.43	1.33
V2-S	1.17	0.38	0.64	1.25	0.36	0.62	0.71	2.19
P2-S	1.06	0.22	0.37	1.25	0.37	0.63	0.69	2.13
B2-S	1.04	0.23	0.39	1.18	0.29	0.50	0.58	1.79

D4. Additional snapshots during steered molecular dynamics (SMD).

The snapshots of 1.1 ns - 1.4 ns in SMD for sys. A0, V1, P1 and B1 are shown in Fig. 6.4a. With the merging of water droplet, a single water droplet is gradually formed in each system. The adsorbates on different water droplets before coalescence are approaching to contact and interact. As shown in the snapshot of last frame (1.4 ns) in each system, some adsorbates are interconnecting the adsorbates on each side of the single large droplet.

As shown in Fig. D4b for sys. V2, some of the VO-79 molecules are adsorbed on the water droplets and some are dispersed in toluene phase. The water droplets are approaching each other at time t = 0-0.7 ns and VO-79 molecules are redistributing on the surface of water droplets. There is gap between the two water droplets at =0.7 ns. The merging of water droplets in sys. V2 is observed at t=0.8 ns and later. In sys. P2, with the water droplets getting closer from t=0 ns to 0.8 ns, NisP films on the surface of water droplets on the head-on direction are thinned, and the NisP molecules are redistributing on the surface. The water droplets merge at t=0.9 and 1.0 ns in sys. P2. similar observation can be obtained for sys. NisB, except that the thinning of NisB film is insignificant. With the merging of water droplets, a single large droplet is formed from 1.1 ns to 1.4 ns. In the sys. V2, P2, B2 with more adsorbates compared with sys. V1, P1, B1 respectively,

it is similar that the adsorbates on each side of the water droplets are interconnecting each other during the merging.

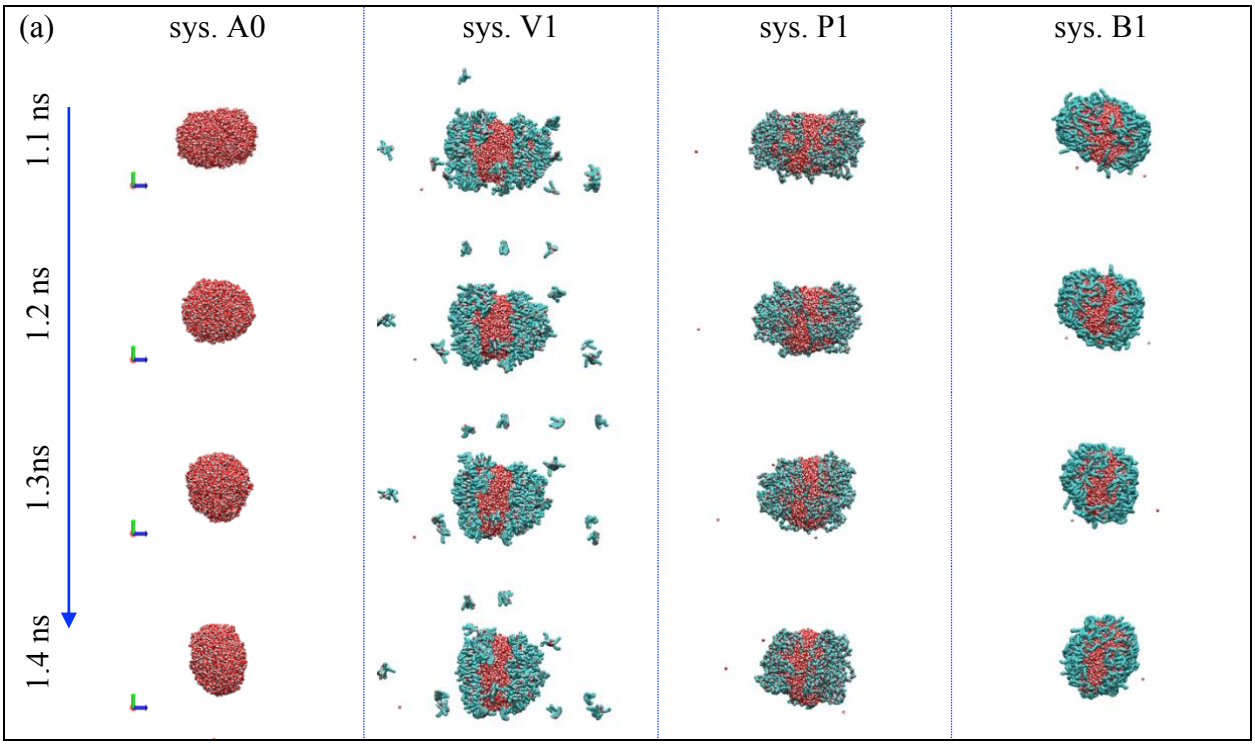

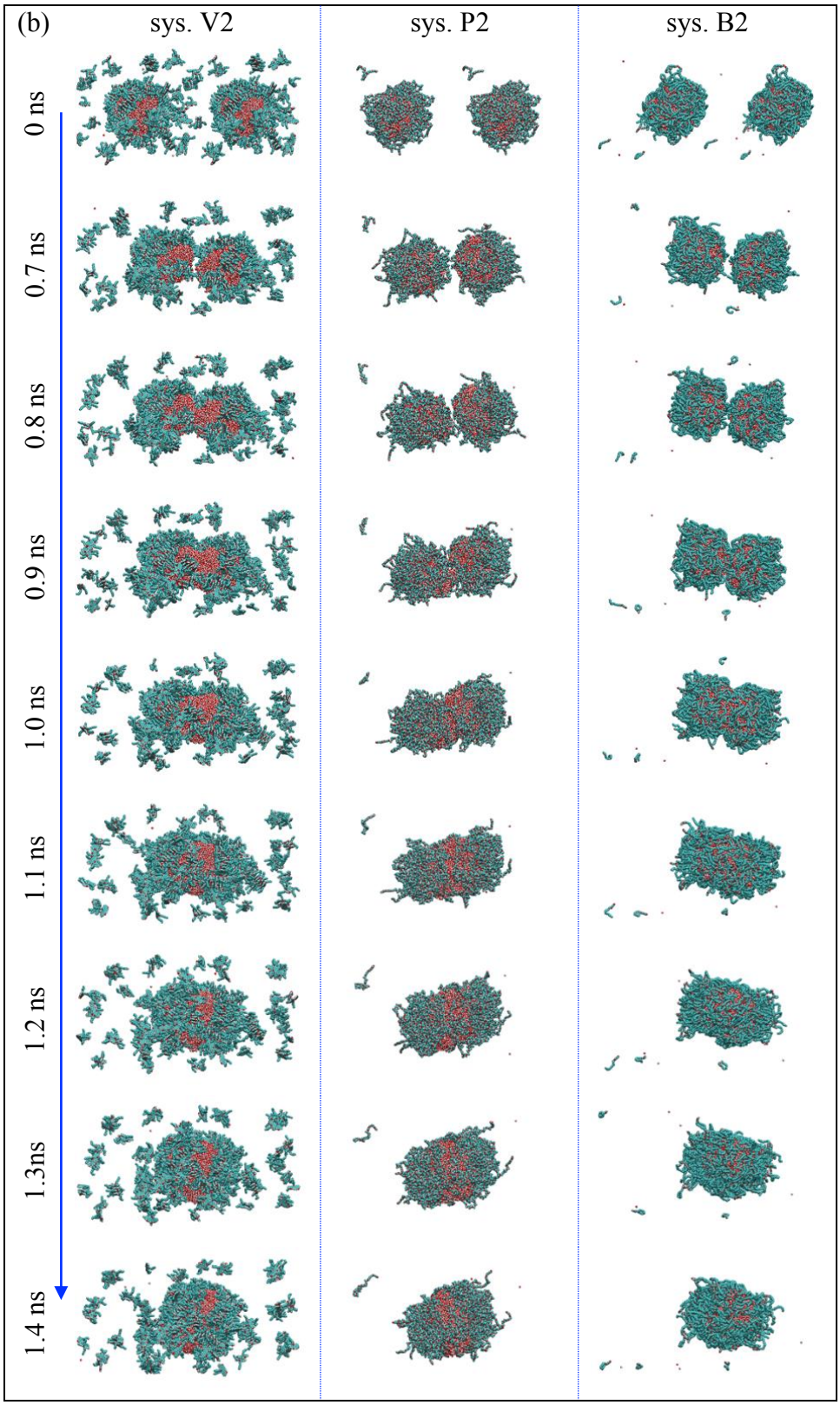

Figure D4. Snapshots of (a) 1.1 ns - 1.4 ns during SMD for sys. A0, V1, P1, and B1; (b) 0 ns, 0.7 ns - 1.4 ns during SMD for sys. V2, P2 and B2. Atoms were shown as van der Waals spheres,

oxygen atoms: red; hydrogen atoms: grey; carbon atoms: cyan; toluene molecules are eliminated for clarity.

References

[1] J.-M. Rabanel, P. Hildgen, X. Banquy, Assessment of PEG on Polymeric Particles Surface, A Key Step in Drug Carrier Translation, Journal of Controlled Release. 185 (2014) 71–87.